# THEORETICAL AND EXPERIMENTAL STUDY OF CONCENTRATED PHOTOVOLTAIC (CPV) SYSTEM WITH HYDROGEN PRODUCTION AS ENERGY STORAGE

**MUHAMMAD BURHAN**

(*BSc Eng, UET Lahore, Pakistan)*

A THESIS SUBMITTED

FOR THE DEGREE OF DOCTOR OF PHILOSOPHY

DEPARTMENT OF MECHANICAL ENGINEERING

NATIONAL UNIVERSITY OF SINGAPORE

2015

# DECLARATION

I hereby declare that the thesis is my original work and it has been written by me in its entirety. I have duly acknowledged all the sources of information which have been used in the thesis.

This thesis has also not been submitted for any degree in any university previously.

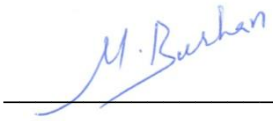

Muhammad Burhan
25 December 2015

## ACKNOWLEDGEMENTS

*Bismillah Hir Rahman Nir Raheem (In the name of ALLAH, the most Gracious, the most Merciful).* First of all, I am grateful to ALLAH, the God Almighty, for His blessing and strength that made me able to complete this thesis.

I would like to convey my heartiest and deepest gratitude to my supervisor, Prof. Ng Kim Choon who believed in me and gave me opportunity to work on this project. I am truly thankful to him for his guidance, time and ideas with encouragement and motivation throughout the project and providing me funding to complete this project. I would like to extend my gratitude to Prof. Chua Kian Jon Ernest for his support, advice and guidance in my research.

I am thankful to Dr. Oh Seung Jin for his kind help and efforts throughout my project and without which, it was difficult for me to finish this project. I am greatly thankful to my closet lab mates Dr. Muhammad Wakil Shahzad, Dr. Li Ang and Dr. Azhar Bin Ismail for providing me motivation and encouragement during my entire PhD and helping me during hard times. I am also thankful to Dr. Kyaw Thu, Dr. M. Kumja and Dr. Loh Wai Soong for their inspiration as seniors during my PhD. I would also like to express my appreciation for Mr. Scadevan Raghvan for his technical and moral help during my project. I would like to thank to my lab fellows Chen Qien and Lin Jie for memorable moments and time.

Most importantly, I am truly grateful to my beloved and respected parents, my father, Muhammad Muazzam and my mother, Naila Nighat, for their prayers, motivation and support. My parents are my life and all of my happiness and

achievements belong to them. I would also like to thank my beloved sisters, Aisha Shoaib and Zunaira Awais, for their love and support. I dedicate my thesis to my family.

Muhammad Burhan
25 December 2015

# List of Publications

Journal Publications

1. **Muhammad Burhan**, Chua Kian Jon Ernest, Ng Kim Choon. Sunlight to hydrogen conversion: Design optimization and energy management of concentrated photovoltaic (CPV-Hydrogen) system using micro genetic algorithm. *Energy* 2016, **99**, 115-128.

2. **Muhammad Burhan**, Chua Kian Jon Ernest, Ng Kim Choon. Simulation and development of a multi-leg homogeniser concentrating assembly for concentrated photovoltaic (CPV) system with electrical rating analysis. *Energy Conversion and Management* 2016, **116**, 58-71.

3. **Muhammad Burhan**, Oh Seung Jin, Chun Wongee, Chua Kian Jon Ernest, Ng Kim Choon. Development of Compact and Low Cost Two axis Solar Tracker using Master Slave Configuration for CPV Applications. *Solar Energy* 2016. **(accepted)**

4. **Muhammad Burhan**, Chua Kian Jon Ernest, Ng Kim Choon. Electrical rating of concentrated photovoltaic (CPV) systems: long-term performance analysis and comparison to conventional PV systems. *International Journal of Technology* 2016, **7(2)**, 189-196.

5. **Muhammad Burhan**, Oh SJ, Ng KC, Chun W. Experimental investigation of Multijunction Solar Cell using Two Axis Solar Tracker. *Applied Mechanics and Materials* 2016, **819**, 536-540.

6. S. J. Oh, **Muhammad Burhan**, K.C. Ng, Y. Kim, W. Chun. Development and performance analysis of a two-axis solar tracker for concentrated photovoltaics. *International Journal of Energy Research* 2015. **39(7)**, 965-976.

7. **Muhammad Burhan**, Chua Kian Jon Ernest, Ng Kim Choon. Long Term Electrical Rating of Concentrated Photovoltaic (CPV) Systems in Singapore. *Applied Energy* 2015. (under review)

8. **Muhammad Burhan**, Chua Kian Jon Ernest, Ng Kim Choon. Long Term Hydrogen Production Potential of CPV System in Tropical Weather of Singapore. *International Journal of Hydrogen Energy* 2015. (under review)

9. **Muhammad Burhan**, Chua Kian Jon Ernest, Ng Kim Choon. Performance Comparison of Conventional Concentrated Photovoltaic (CPV) Systems with Ray Tracing Simulation and Experimentation. *Renewable and Sustainable Energy Reviews* 2015. (Manuscript under Preparation)

10. **Muhammad Burhan**, Chua Kian Jon Ernest, Ng Kim Choon. Energy Output of Concentrated Photovoltaic: Performance Simulation Model and Field Experimentation. *Energy Conversion and Management* 2015. (Manuscript under Preparation)

Conference Publications

1. **Muhammad Burhan**, Chua Kian Jon Ernest, Ng Kim Choon. Electrical Rating of Concentrated Photovoltaic (CPV) Systems: Long Term Performance Analysis and Comparison with Conventional PV Systems. *The 8th International Meeting on Advanced Thermofluids (IMAT)* 2015, Jakarta, Indonesia.

2. **Muhammad Burhan**, Chua Kian Jon Ernest, Oh Seung Jin, Muhammad Wakil Shahzad, Ng Kim Choon. Electrical Rating Analysis for Long Term Performance of Concentrated Photovoltaic (CPV) System. First Pacific Rim Thermal Engineering Conference (PRTEC) 2016, Hawaii, USA.

3. **Muhammad Burhan**, Oh Seung Jin, Muhammad Wakil Shahzad and Kim Choon Ng, Electrical Rating of Concentrated Photovoltaic (CPV) Systems for Long Term Performance. *The 6$^{th}$ International Symposium on Physics of Fluids (ISPF6)* 2015, Xining, China.

4. **Muhammad Burhan**, Oh SJ, Shahzad MW, Kim YD, Ng KC, Chun W. Prediction of Annual Performance of CPV Systems using Multi-Junction Solar Cells, *The 7th International Meeting on Advanced Thermofluids (IMAT)* 2014, Kuala Lumpur, Malaysia.

5. **Muhammad Burhan**, Oh SJ, Ng KC, Chun W. Experimental investigation of Multijunction Solar Cell using Two Axis Solar Tracker. *International Conference on Energy and Thermal Science (ICETS)* 2014, Skudai, Malaysia.

6. **Muhammad Burhan**, S. J. Oh, K. C. Ng. Analysis of Concentrated Photovoltaic System with Two Axis Solar Tracker For Hydrogen Production. *The 6th International Symposium on Microchemistry and Microsystems (ISMM)* 2014, Singapore.

7. **Muhammad Burhan**, Oh SJ, Ng KC, Chun W. Experimental investigation of Multijunction Solar Cell using Two Axis Solar Tracker. *The 6th International Meeting on Advanced Thermofluids (IMAT)* 2013, Singapore.

# Table of Contents

# Summary

Owing to concerns over the increasing global warming issues from the extensive use of fossil fuels, the use of solar energy especially photovoltaic system has gained escalating interest as a sustainable energy source to meet the global energy demand. This is due to their capability to directly convert solar energy into electricity with simple configuration. The concentrated photovoltaic (CPV) system is emerging as a highly efficient photovoltaic technology. The aim of this thesis is to conduct extensive theoretical and experimental study of the concentrated photovoltaic system for development of a compact and cost effective system design, with the hydrogen production as energy storage to handle solar intermittency. The compact system design with cost effective approach, will eliminate the installation limitations related to conventional CPV system. Furthermore, the CPV-Hydrogen study will show the real CPV hydrogen production potential and will introduce the design methodology for steady operation of CPV.

A CPV field based upon the compact concentrated photovoltaic (CPV) systems is developed, utilizing the cost effective master slave configuration through wireless control communication. The developed system performance is investigated for long term outdoor operation at the rooftop of Engineering building (EA). In master slave configuration, the required tracking information from expensive devices is transmitted wirelessly through one master tracker. While, the rest of the slave trackers are only equipped with minimum hardware and operate according to the tracking information received from master tracker. The compact, smart but highly accurate and sensitive two axis

solar trackers are designed and developed utilizing hybrid tracking algorithm. All the trackers are equipped with novel and low cost solar feedback tracking sensor utilizing double lens collimator and photo-sensor array, with tracking accuracy of $0.1^{o}$. The accuracy of the tracker is verified for long term field operation.

The developed CPV field based upon four prototypes of compact CPV systems; three of them are based upon the conventional concentrating assemblies designs and utilizing mini parabolic dish in cassegrain arrangement and Fresnel lens with glass and reflective homogeniser. While the fourth CPV system is based upon the novel design of multi-leg homogeniser concentrating assembly which unlike conventional design, concentrates solar radiations on four solar cells with a single set of concentrator. The detailed design model and the selection criteria for the concentrating assemblies is proposed and verified through ray tracing simulation in TracePro. The simulated and experimental performance of the developed CPV systems is verified and compared for short term and long term operation.

An electrical rating methodology is proposed to rate the real field potential of the photovoltaic systems and the highest long term electrical rating of 240.21 $kWh/m^2$.year is recorded for CPV systems, which is 2-3 folds higher than the conventional PV even in tropical weather conditions of Singapore.

To handle solar intermittency and to operate CPV for steady power production, the potential of the CPV system is first experimentally analyzed for hydrogen production. A hydrogen production system based upon PEM electrolysers and a hydrogen storage system based upon the mechanical

compressor, are designed and developed. The CPV-Hydrogen system showed solar to hydrogen maximum efficiency of 18-19% and average efficiency of 15-16% for whole day operation. In addition, for standalone operation of CPV, a detailed performance model and design optimization strategy is first time developed and verified for CPV system with hydrogen production as energy storage. Using micro-GA, the techno-economic optimization of the CPV-Hydrogen system is carried out for uninterrupted power supply at minimum system cost, according to the proposed energy management and control strategy. The developed model can also be used to estimate the long term performance of any component of CPV-Hydrogen system for design purpose, which is already verified for the long term CPV performance. In addition, the proposed model and strategy can be integrated into the commercial analyzing tools, to enhance their analyzing capability for CPV.

# List of Tables

# List of Figures

# Nomenclature

| Symbol | Description | Units |
|---|---|---|
| EOT | Equation of time | min |
| $L_{st}$ | Standard longitude of local time zone | deg |
| $L_{loc}$ | Longitude of local observer position | deg |
| $\omega$ | Hour angle | deg |
| $\delta$ | Declination Angle | deg |
| $\theta_z$ | Zenith Angle | deg |
| $\theta_{az}$ | Azimuth Angle | deg |
| $\varphi$ | Latitude of local observer position | deg |
| $T_{SR}$/ $T_{SS}$ | Sun rise/sun set time | hour |
| $\alpha$ | Right ascension angle | deg |
| n | Number of day | - |
| SD | Sensor dimension | mm |
| $\theta_a$ | Angular offset in the position of the sun or Angular deviation of solar rays from concentrator axis | deg |
| CH | Column Height for Shadow Purpose | mm |
| d | Distance between photo-sensors | mm |
| $f_{cx}$ | Focal length of convex lens | mm |
| $f_{cn}$ | Focal length of concave lens | mm |
| $D_{cx}$ | Convex lens diameter | mm |
| S | Distance between collimating lenses | mm |
| $b_t$ | Collimated beam thickness | mm |
| h | Distance between collimating lens assembly and photo-sensor array | mm |
| $L_m$ | Maximum Depth of ZigBee Network | - |
| $R_m$ | Maximum number of routing cable children | - |
| $C_m$ | Maximum number of non-routing cable children | - |
| $f_{pr}$ | Focal length of mini parabolic dish | mm |

| Symbol | Description | Units |
|---|---|---|
| $\theta_r$ | Rim angle | deg |
| $D_{pr}$ | Diameter of mini parabolic dish | mm |
| $d_{pr}$ | Diameter of centre hole of mini parabolic dish | mm |
| $t_{pr}$ | Parabolic Curvature depth of mini parabolic dish | mm |
| $t_d$ | Thickness of mini parabolic dish | mm |
| $CR_g$ | Geometric concentration ratio | - |
| $A_{con}$ | Effective area of primary concentrator | $m^2$ |
| $A_C$ | Area of solar cell (MJC) | $m^2$ |
| $\theta_{a\_CPC}$ | Acceptance angle of CPC | deg |
| $n_{CPC}$ | Refractive index of CPC material | - |
| L | Overall length of CPC | mm |
| a | Half of inter aperture size of CPC | mm |
| a' | Half of outlet aperture size of CPC | mm |
| $\theta_e$ | Tracking error of angular deviation of parallel rays from concentrator axis | deg |
| $D_{hp}$ | Diameter of mini hyper dish | mm |
| $f1_{hp}$ | First focal length of mini hyperbolic dish | mm |
| $f2_{hp}$ | Second focal length of mini hyperbolic dish | mm |
| $M_t$ | MJC thickness | mm |
| $f_{FL}$ | Focal length of Fresnel lens | mm |
| $C_L$ | Curvature of conical surface of lens | mm |
| $R_{FL}$ | Radius of curvature of Fresnel lens | mm |
| k | Conical surface constant | - |
| $A_i$ | Aspheric coefficients | - |
| $Z_L$ | Lens dimension variable towards lens sag direction | mm |
| $r_L$ | Lens dimension variable towards lens radial direction | mm |
| $D_{FL}$ | Diameter of Fresnel Lens | mm |
| $S_{FL}$ | Fresnel lens rings height | mm |

| Symbol | Description | Units |
|---|---|---|
| $t_{FL}$ | Fresnel lens thickness | mm |
| $L_{FL}$ | Linear side dimension of square Fresnel lens | mm |
| $n_{FL}$ | Refractive index of Fresnel lens material | - |
| $P_{CPV}$ | Power output of CPV | W |
| $V_{CPV}$ | Voltage output of CPV | V |
| $I_{CPV}$ | Current output of CPV | A |
| DNI | Direct Normal Irradiance | $W/m^2$ |
| $\eta_{CPV}$ | Efficiency of CPV system | % |
| $n_{E,H2}$ | Rate of Hydrogen production | mol/s |
| $\eta_{EF}$ | Faraday Efficiency of Electrolyser | % |
| $N_{EC}$ | Total number of Electrolyser cells | - |
| $I_E$ | Electrolyser current | A |
| $U_E$ | Electrolyser voltage | V |
| $n_E$ | No. of electrons required for electrolysis | - |
| F | Faraday Constant | A.s/mol |
| $\eta_{EL}$ | Electrolyser Efficiency | % |
| $\eta_{CPV\_H2}$ | Overall solar to hydrogen conversion efficiency | % |
| $R_{e,m}$ | Monthly electrical rating | $kWh/m^2$.year |
| $R_e$ | Overall electrical rating | $kWh/m^2$.year |
| m | Maximum number of days in month | - |
| q | Total number of experimental days | - |
| E | Daily total energy yield of CPV | $kWh/m^2$ |
| $D_m$ | Daily total solar energy received | $kWh/m^2$ |
| GHI | Global Horizontal Irradiance | $W/m^2$ |
| $d_1$ | Dimension of square primary reflector of multi-leg homogeniser concentrating assembly | mm |
| $d_2$ | Dimension of square secondary reflector of multi-leg homogeniser concentrating assembly | mm |

| Symbol | Description | Units |
|---|---|---|
| f1 | Focal length of primary reflector of multi-leg homogeniser concentrating assembly | mm |
| f2 | Focal length of secondary reflector of multi-leg homogeniser concentrating assembly | mm |
| $t_1$ | Depth of primary reflector of multi-leg homogeniser concentrating assembly | mm |
| $t_2$ | Depth of secondary reflector of multi-leg homogeniser concentrating assembly | mm |
| $A_{HO}$ | Area of centre hole in primary reflector of multi-leg homogeniser concentrating assembly | $m^2$ |
| D1 | Corresponding diameter of primary reflector of multi-leg homogeniser concentrating assembly | mm |
| $\theta_C$ | Critical angle of optical material | deg |
| $I_C$ | Solar cell current | A |
| $C_C$ | Solar concentration at solar cell area | Suns |
| $V_C$ | Solar cell voltage | V |
| $N_{CM}$ | Number of solar cells in one panel | - |
| $NP_{CPV}$ | Number of CPV panels | - |
| $I_{SC}$ | Solar cell short circuit current | A |
| $EL_C$ | Electrical load demand of consumer | W |
| $V_{OC}$ | Solar cell open circuit voltage | V |
| $T_C$ | Solar cell temperature | $^oC$ |
| $I_{mppt}$ | Solar cell maximum power point current | A |
| $V_{mppt}$ | Solar cell maximum power point voltage | V |
| $P_C$ | Solar cell power | W |
| $P_{mppt}$ | Solar cell maximum power point power | W |
| $P_{Load}$ | Total load demand | W |
| $P_{excess}$ | Excess available power from CPV | W |

| Symbol | Description | Units |
|---|---|---|
| $P_{Tr}$ | Solar tracker power requirement | W |
| $P_{com}$ | Hydrogen compressor power | W |
| $P_{MJC,max}$ | MJC maximum rated power | W |
| $N_{E,O2}$ | Oxygen production flow rate from electrolyser | mol/s |
| $T_E$ | Electrolyser Temperature | $^oC$ |
| $A_E$ | Electrolyser Cell Area | $m^2$ |
| $V_{EC,max}$ | Electrolyser Cell Maximum Voltage | V |
| $I_{EC,max}$ | Electrolyser Cell Maximum Current | A |
| $P_{EL,max}$ | Electrolyser Cell Maximum Power | W |
| $L_{min}$ | Minimum Electrical Load Requirement | W |
| $U_{rev}$ | Reversible Voltage of Electrolysis | V |
| $n_{F,H2}$ | Hydrogen Consumption Flow Rate from Fuel Cell | mol/s |
| $n_{F,O2}$ | Oxygen Consumption Flow Rate from Fuel Cell | mol/s |
| $I_F$ | Fuel Cell Current | mA |
| $A_F$ | Cell Area of Fuel Cell | $cm^2$ |
| $U_F$ | Cell Voltage of Fuel Cell | mV |
| $N_{FC}$ | Number of Cells of Fuel Cell | - |
| $P_{FC,max}$ | Cell Maximum Power of Fuel Cell | W |
| $L_{max}$ | Maximum Electrical Load Requirement | W |
| $P_{req}$ | Electrical Power Deficiency not supplied by the CPV | W |
| $U_o$ | Reversible Voltage of Fuel Cell | mV |
| $ST_{H2}$ | State of Hydrogen Storage | kg |
| $ST_{O2}$ | State of Oxygen Storage | kg |
| $ST_W$ | State of Water Storage | kg |
| $STM_{H2}$ | Maximum Hydrogen Storage Capacity | kg |
| $STM_{O2}$ | Maximum Oxygen Storage Capacity | kg |
| $\eta_{OP}$ | Optical Efficiency of Concentrating Assembly | % |
| $\eta_{mppt}$ | Efficiency of Maximum Power Point Tracking Device | % |

| Symbol | Description | Units |
|---|---|---|
| $\eta_{DC/AC}$ | Efficiency of DC to AC Converter | % |
| $\eta_{EF}$ | Faraday Efficiency of Electrolyser | % |
| $\eta_{CDC}$ | Efficiency of DC to DC Converter | % |
| $\eta_{FF}$ | Faraday Efficiency of Fuel Cell | % |
| $\eta_{com}$ | Efficiency of Compressor | % |
| $P_{ta}$ | Instantaneous Pressure of Hydrogen Tank | Pa |
| $P_E$ | Pressure of Hydrogen Production from Electrolyser | Pa |
| $M_{H2}$ | Molar Mass of Hydrogen | g/mol |
| $CP_H$ | Specific Heat Capacity of Hydrogen | J/kg.K |
| $T_{com}$ | Hydrogen Compressor Temperature | K |
| $T_{ta}$ | Temperature of Hydrogen Storage Tank | K |
| $n_{ta}$ | Instantaneous Number of Moles of Hydrogen Gas in Storage Tank | mol |
| r | Isentropic Exponent of Hydrogen | - |
| R | Universal Gas Constant | J/mol.K |
| $Z_H$ | Compressibility Factor of Hydrogen | - |
| V | Volume of Storage Tank of Hydrogen | $m^3$ |
| $n_H$ | Number of Hydrogen Stage Tank | - |
| $P_H$ | Pressure of Hydrogen Storage Tank | Pa |
| L1 | Minimum Limit for Cyclic Hydrogen Storage | kg |
| L2 | Maximum Limit for Cyclic Hydrogen Storage | kg |
| $t_{PF}$ | Time for Power Failure | sec |
| PSFT | Power Supply Failure Time Factor | sec |
| CC | Capital Cost | $ |
| $C_{AT}$ | Total Annual System Cost | $ |
| $C_{CPV}$ | CPV Total Cost | $ |
| $C_{EL}$ | Electrolyser Total Cost | $ |
| $C_{FC}$ | Fuel Cell Total Cost | $ |

| Symbol | Description | Units |
|---|---|---|
| $C_{STH2}$ | Hydrogen Storage Total Cost | $ |
| $C_{STO2}$ | Oxygen Storage Total Cost | $ |
| $C_{com}$ | Hydrogen Compressor Total Cost | $ |
| OMC | Operation and Maintenance Cost | $ |
| RC | Replacement Cost | $ |
| CRF | Capital Recovery Factor | - |
| SPPW | Single Payment Present Worth | - |
| y | Payment Duration | years |
| *i* | Compound Interest Rate | % |
| w | Lifetime Period of System | years |

## Subscript

| | |
|---|---|
| SR | Sun rise |
| SS | Sunset |
| (H) | Angle Value in hours units |
| cx | Convex |
| cn | Concave |
| pr | Parabolic |
| hp | Hyperbolic |
| FL | Fresnel Lens |
| L | Lens |
| E | Electrolyser |
| F | Fuel Cell |
| ta | Tank |
| com | Compressor |
| H | Hydrogen |
| H2 | Hydrogen Gas |
| O2 | Oxygen Gas |

# Abbreviation

| | |
|---|---|
| CPV | Concentrated Photovoltaic |
| MJC | Multi-junction Solar Cell |
| BOS | Balance of System |
| GMT | Greenwich Mean Time |
| C | Coordinator |
| R | Router |
| ED | End Device |
| USART | Universal Synchronous/Asynchronous Receiver/Transmitter |
| RTC | Real Time Clock |
| ISP | In System Programming |
| ADC | Analogue to Digital Converter |
| CTS | Colour Tracking Sensor |
| CPC | Compound Parabolic Concentrator |
| MPPT | Maximum Power Point Tracking |
| TIR | Total Internal Reflection |
| DNI | Direct Normal Irradiance |
| STC | Standard Testing Conditions |
| NOCT | Nominal Operating Cell Temperature |
| AM | Air Mass |
| LTER | Long Term Electrical Rating |
| GHI | Global Horizontal Irradiance |
| MHCA | Multi-leg Homogeniser Concentrating Assembly |
| PSFT | Power Supply Failure Time |
| PEM | Proton Exchange Membrane |

# Chapter 1: Introduction

Energy is a resource needed for the survival of human beings and its importance permeates all human activities. The world's current energy consumption is about 12.477 GTOE and its demand is expected to increase by 41% when the world population hits 8.7 billion in 2035 **[1,2]**. Of this total primary energy consumption, the generation of electricity and heating have the highest share of 42% **[3]**. It has been reported that about 82% of the world's energy consumption is derived from the fossil fuels, namely oil, natural gas and coal. Consequently, the burning of these fuels has led to high emission of $CO_2$ into the atmosphere causing the drastic effects of global warming **[4]**. From environmental sustainability, only by switching to renewable energy resources as primary energy supply can mitigate the effects from global warming situation. Among all renewable energy resources, solar energy has the highest potential to meet our energy demand **[5]** as the daily irradiance received is 10,000 times more than the global energy consumption **[6]**.

The main advantage for solar energy systems is their energy conversion efficiency yet at relatively low cost with simple system configuration. The photovoltaic system or solar cell provides the simple, elegant and direct method of electricity production from solar energy **[7-9]**. The current installed capacity of photovoltaic systems in the world has reached $183GW_P$ **[10]**. Despite the increase in the total installed capacity of photovoltaic systems, it ranks third in the renewable energy utilization share, after hydro and wind energy resources **[11,12]**. The current photovoltaic market is almost fully dominated by the single junction crystalline silicon cells and thin film solar

cells, which offer low efficiencies at the cell level of 20-25% and 19-20% respectively, and under the single flash test conditions **[13]**. The single junction solar cell absorbs only a certain portion of the solar spectrum while the remaining portion is dissipated as heat loss, thereby offering lower efficiency **[14]**. Multi-junction solar cell, on the other hand, offers the highest efficiency up to 46% due to having cell materials that are responsive to a wider solar spectrum **[16]**. However, due to the high cost of multi-junction solar cells, cost effective concentrated photovoltaic (CPV) concept is used in which low cost concentrators are used to concentrate solar radiations onto a small area of solar cell material, thus reducing the use of expensive solar cell material **[17-18]**.

Solar concentrators operate for parallel rays or beam solar radiation and require solar tracking to face the sun at all times. Therefore, the two axis solar tracker is a key component of the CPV system. The conventional CPV systems are designed as big units containing multiple CPV modules mounted onto a two axis solar tracker. These gigantic CPV systems are only suitable to be installed in open fields especially desert areas with clear sky conditions and high beam radiations availability. It must be noted here that the rooftop installed PV panels, on the residential or commercial buildings and housing units, make a very large share of the global PV capacity and most of the countries are aiming for a share of 40-50% **[19]**. However, the current large CPV system design is not suitable for installation as a rooftop unit and the development of small and compact units for rooftop, was not considered with an intention of low power production due to low solar beam radiations availability in the urban region. Therefore, beside higher conversion

efficiency, the CPV system could not get much customers and popularity like the conventional PV systems.

Solar energy, while having the highest energy potential, is intermittent in nature due to changing weather conditions throughout the day **[20]**. In addition, there is no solar radiation during the night. An important requirement of the electricity industry is to provide continuous power supply and meet any demand load **[21]**. This feature of steady power supply gives the leading edge to conventional power plants running on fossil fuel. Therefore, beside solar energy utilization, energy storage is mandatory for steady and standalone operation of the solar energy systems, to eliminate to the solar intermittency. In the literature, there are many studies based upon the stand-alone operation of the photovoltaic systems, but considering the conventional PV system **[22-24]**. However, besides highest conversion efficiency, studies are lacking for the consideration of CPV system for standalone operation along with its design modelling, optimization tools and strategy. Solar energy systems are designed to operate for long term operation with a lifespan of 20-25 years **[25]**. Therefore, for long term operation, hydrogen production from water electrolysis provides a sustainable, clean and reliable energy storage solution in comparison with the conventional electrochemical electricity storage options i.e. battery which is only reliable for short term operation **[26]**.

The main motive of this research is to conduct extensive theoretical and experimental study for the development of concentrated photovoltaic system, to eliminate the design and performance related concerns and to operate it as a steady power source.

## 1.1 Objectives

The dissertation aims, firstly, to develop compact and cost effective design of concentrated photovoltaic (CPV) systems with theoretical and outdoor testing over a long period of operation. Secondly, to experimentally analyze the potential of CPV for hydrogen production, serving as energy storage, with development of theoretical design model for steady power operation of CPV. The main objectives of this thesis are:

1. To design and develop a compact and smart two-axis solar tracker for CPV applications. A tracking algorithm is developed using hybrid technique of astronomical and optical tracking methods. It also includes a novel and low cost solar tracking sensor utilizing double lens collimator with an array of photo-sensors, having sensitivity of $\pm 0.1^{o}$. The performance of two axis solar tracker is tested and verified outdoor on the rooftop of Engineering building (EA).
2. To develop a CPV field of compact solar trackers based upon the Master Slave control configuration. In a CPV field of many tracking units, only one master unit is equipped with expensive electronic modules and do the key computation. The required tracking information is then transmitted wirelessly to the slave units, containing less expensive hardware thereby reducing overall system cost.
3. To model, design and analyze the performance of the CPV concentrating assemblies using ray tracing simulation. Three concentrating assemblies, one is based upon mini parabolic dish in cassegrain arrangement and the other two are based upon the Fresnel lens (aspheric surface) with glass

homogeniser and with reflective homogeniser, are designed according to the small MJC concentration requirement of x500. The performance of the designed concentrating assemblies is analyzed and compared through ray tracing simulation in TracePro.

4. To investigate the experimental performance of CPV field, comprising in-house built CPV systems with designed mini dish and Fresnel lenses. The experimental and simulated performance of the CPV systems are compared and analyzed.
5. To develop and analyze the CPV-Hydrogen system to investigate the performance of the CPV system for hydrogen production. A hydrogen production system, based upon PEM electrolyser and a hydrogen compression system with the storage, are designed and fabricated. The CPV-Hydrogen system is investigated for instantaneous and average performance to analyze the real potential of the CPV-Hydrogen production in outdoor weather conditions of Singapore.
6. To analyze the long term electrical rating of the concentrated photovoltaic (CPV) systems. The proposed electrical rating methodology is used to investigate the long term power output of the developed CPV systems for one year field operation and the performance is compared with the conventional PV systems.
7. To design, develop and analyze the novel multi-leg homogeniser concentrating assembly (MHCA) for CPV system. The proposed concentrating assembly can concentrate solar radiations onto four MJCs using single set of concentrators.

8. To develop the performance model of CPV system with design optimization and energy management strategy for stand-alone operation of CPV system with hydrogen production as energy storage. An optimization code based upon CPV-Hydrogen system performance model is developed in FORTRAN with micro-GA. The multi-variable and the multi-objective techno-economic optimization of CPV-Hydrogen system is conducted for uninterrupted power supply and minimum overall system cost.

## 1.2 Thesis Outline

This thesis consists of nine chapters to the conduct theoretical and experimental study of concentrated photovoltaic (CPV) system with hydrogen production as energy storage. The contents of each chapter are summarized as follows.

In Chapter 1, as opening chapter, the aims and objectives of this research are outlined according to the main motivation of this study as described in the introduction section. The thesis outline is also presented in this chapter.

In Chapter 2, a detailed literature review is provided to highlight the scope of existing studies and the gaps that are needed to be addressed. First, the need of CPV system with its significance and impact on the energy demand is highlighted, followed by the limitations of the existing CPV systems designs. The gaps needed to be filled by current research are then highlighted in theoretical and experimental framework to make CPV system a reliable and steady power source without any application restrictions.

In Chapter 3, a compact two axis solar tracker is developed based upon a hybrid tracking algorithm using a novel, cheap and highly accurate in-house built solar tracking sensor. Using the solar tracker, a tracking system for CPV

field is proposed and developed based upon the master slave control configuration.

In Chapter 4, the detailed design modelling and the ray tracing simulation of the concentrating assemblies of developed CPV systems are discussed. Based upon the verified design using the ray tracing simulation, the performance of each of the CPV design is compared and analyzed.

In Chapter 5, the main focus is the development and the experimental investigation of the CPV and CPV-Hydrogen system. The design and development of three CPV systems are discussed, followed by a performance investigation of the systems in outdoor weather conditions. In the second part of the chapter, the design and the development of the CPV-Hydrogen system are discussed with maximum and average performance for hydrogen production in outdoor weather conditions.

In Chapter 6, the long term performance of the three developed CPV systems is analyzed using proposed electrical rating methodology. The long term electrical rating (LTER) is presented for tropical weather conditions of Singapore.

In Chapter 7, a novel design of the CPV system is proposed based upon the multi-leg homogeniser concentrating assembly (MHCA). The proposed MHCA is designed and developed, which can concentrate solar radiations on the four MJCs using single set of concentrators. The performance of developed CPV system is analyzed through ray tracing simulation and outdoor field experimentation.

In Chapter 8, an energy management and multi-objective techno-economic optimization methodology for standalone operation of CPV system with

hydrogen production as energy storage is developed, analyzed and verified. The CPV performance model is developed and the CPV-Hydrogen system design is optimized using micro-GA for uninterrupted power supply at minimum cost. The developed performance model can also be used to evaluate the long term performance of the CPV-Hydrogen system.

In Chapter 9, the conclusion and the major findings of the study are presented with future recommendations.

# Chapter 2: Literature Review

## 2.1 World Energy Scenario and $CO_2$ Emissions

Energy has become a key part in the economic and social development of the countries. Beside economic advancements, global population is also continuously growing thereby increasing the global energy demand. In addition, a remarkable shift in the living standard of the people and the urbanization are expected to significantly affect the global energy needs. The trend of global energy demand and the world population growth are shown in Figure 2.1. World's current energy demand has reached to 12476.63 MTOE and further 41% increase in energy demand is expected till 2035. In addition, the current global population is increasing at a rate of around 800 million per year. However, the world energy demand is growing at a faster rate than the global population **[1,27,28]**.

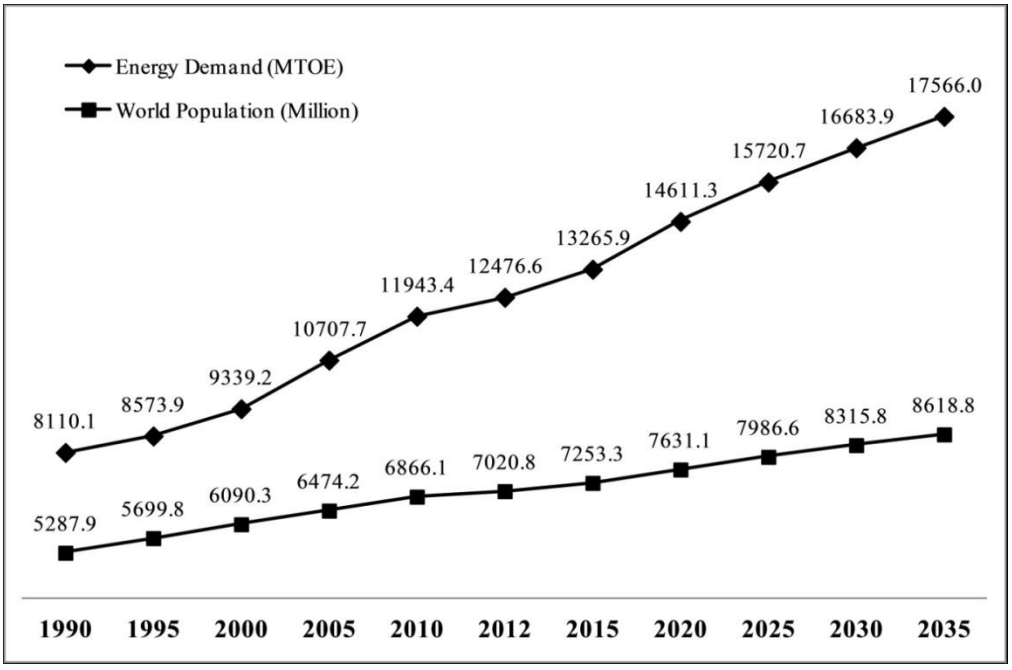


Figure 2.1: World Population and Energy Demand

To meet the global the energy need, the world is mainly relying on fossil fuels. In the global energy mix, the fossil fuels contribute to 82% of the global energy supply. Oil has the largest share in the energy mix with share of 31.5%, followed by coal with 29% and natural gas with 24% share. However, the bio-energy, nuclear energy and hydro-energy have a comparatively very small energy share of only 10%, 5.1% and 2.3% respectively. The share of the renewable energy resources, including solar, wind and geothermal energy, in the global energy supply is only about 1%, as shown in Figure 2.2 **[2]**. The Figure 2.3 shows the consumption of the primary energy supply according to sector and source. It can be seen that the highest share of the global energy supply, 39.3% is used for electricity generation and followed by the transport sector with share of 27% **[3]**. One of the main reasons for this high consumption of electricity is the advancement in the information technology field and as a result, electricity consumption share is increasing rapidly at a rate faster than the primary energy supply **[29]**.

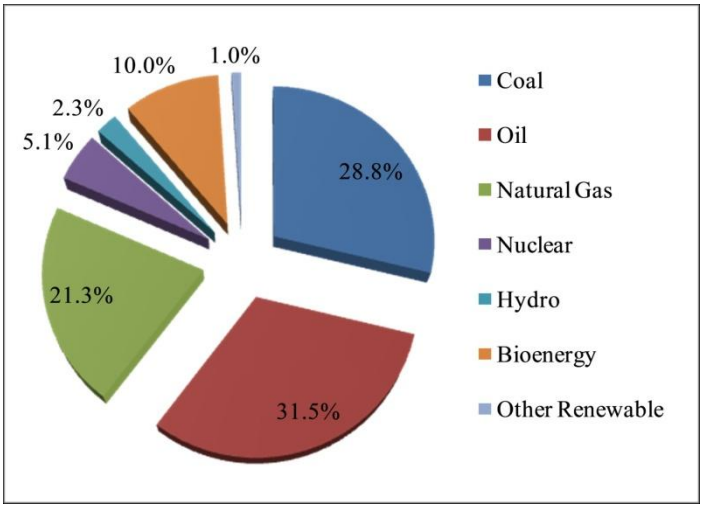


Figure 2.2: Global Energy Mix

Because of the huge dependency on fossil fuels, sustainability of the earth ecosystem is at risk. The energy generated from the combustion of the fossil

fuels has created numerous environmental issues and the emissions of green house gases are a primary concern **[30]**. Carbon dioxide is the main contributor in the greenhouse gas emissions , with very high growth rate **[31]**. $CO_2$ emissions have increased from 23.7Gt to 31.2Gt in a period from 2000 to 2011 and if current energy scenario prevails, it is expected to increase to 43.1Gt in 2035. The history of growth of $CO_2$ emissions is shown in Figure 2.4 **[32]**.

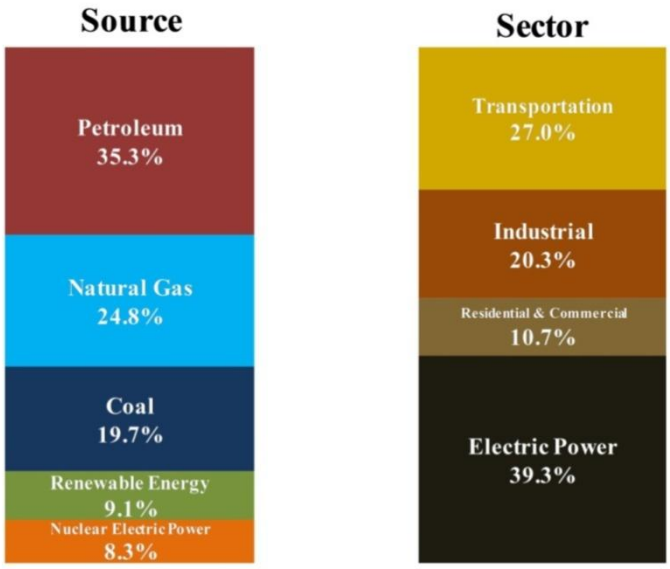


Figure 2.3: Primary Energy Supply Consumption by Sector

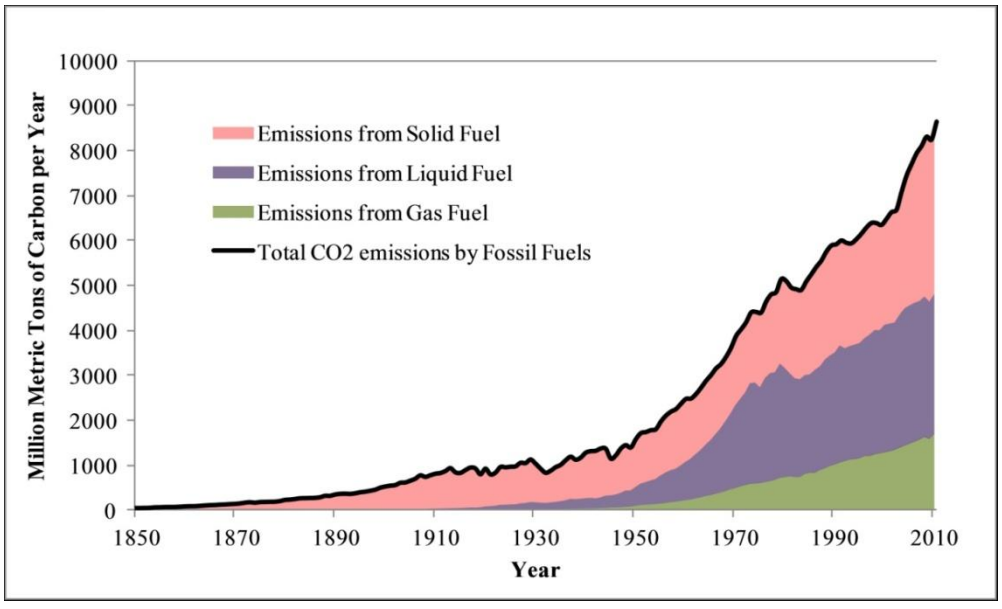


Figure 2.4: $CO_2$ Emission Trend by Fossil Fuels

Since electricity generation and transportation sectors have the largest consumption of the global energy supply, these two sectors also have highest share to $CO_2$ emissions. From Figure 2.5, it can be seen that the electricity generation sector contributes 42% of the $CO_2$ emissions, followed by the transport sector with 22% share. The share of $CO_2$ emissions from electricity generation has almost become doubled since 1990 due to dependence on fossil fuels for electricity generation **[7]**.

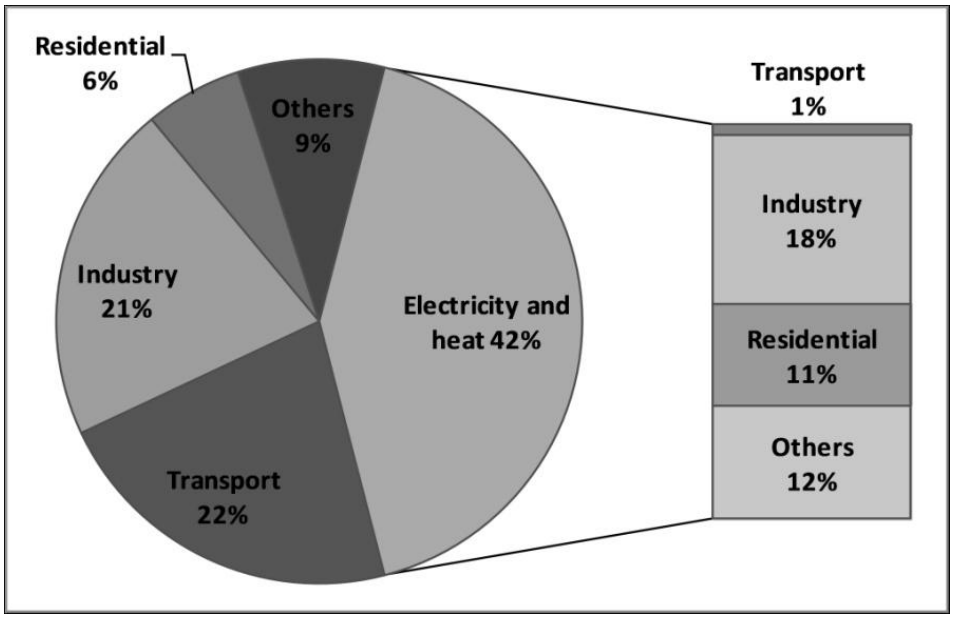


Figure 2.5: World $CO_2$ Emissions by Sector

The level of $CO_2$ in the atmosphere has already exceeded 400 ppm **[33]**. If current situation prevails, a 3.6$^{o}$C to 5.3$^{o}$C global temperature rise is expected in the long term. To control the $CO_2$ emissions in long term, different policies have been proposed to limit the global temperature rise and the main emphasis is given to have the largest share of renewable energy resources in the global energy mix **[4]**. Among all the available energy resources, solar energy has the highest potential of energy. The comparison of the energy potential for different energy resources, is shown in Figure 2.6.

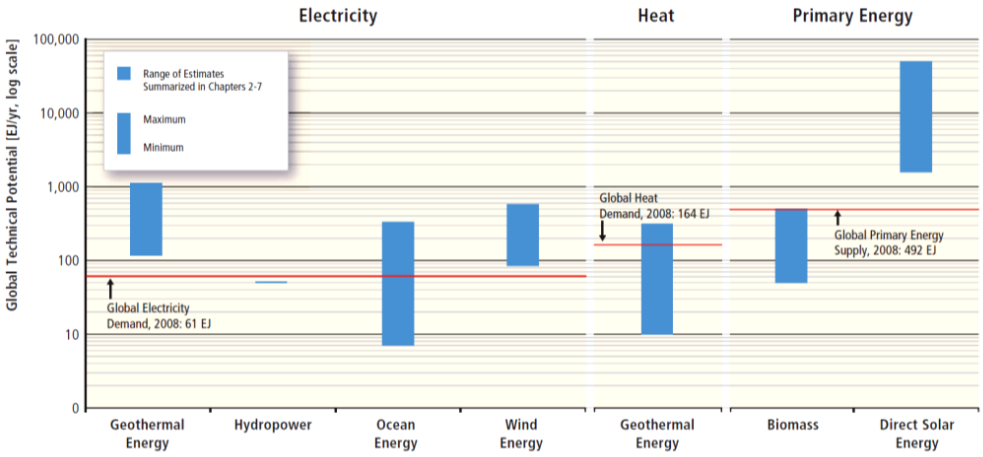


Figure 2.6: Global Technical Potential of Energy Sources (log scale, $10^{18}$J/year) **[5]**

## 2.2 Solar Resource Potential

The solar energy resource potential is far higher than the current global energy consumption. The solar energy received by the earth is in form of the electromagnetic radiations, generated due to nuclear fusion reaction of hydrogen and helium at sun surface. Figure 2.7 shows the total solar resource potential in comparison with the total fossil fuel resources, nuclear resources, renewable energy resources and annual global energy consumption **[34]**.

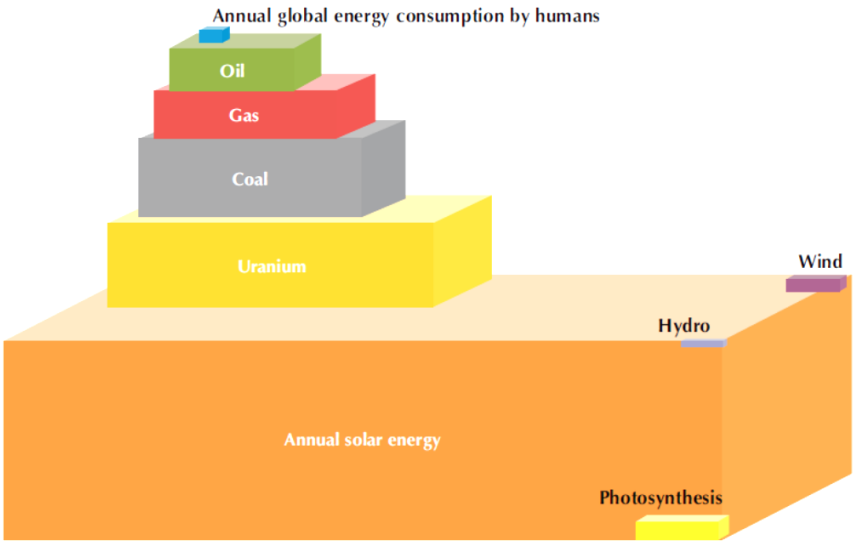


Figure 2.7: Total Energy Resources

After covering a distance of about 150 million kilometre, only a small fraction of solar energy reaches the earth **[34]**. However, there is a further loss of solar radiations as it passes through earth's atmosphere, due to further reflection and radiation through different components present in the earth atmosphere. The earth's atmosphere consists of a stable composition of gases, 78% nitrogen, 21% oxygen and remaining 1% contains noble gases like argon. Many other components like water vapour, carbon dioxide, nitrous oxide and methane are also present in the atmosphere, causing loss in the received solar energy. Figure 2.8 shows the schematic representation of scattering of the solar radiations while passing through the earth atmosphere. The solar radiation received by the earth surface is divided into three forms; direct, diffuse and global radiation **[35]**.

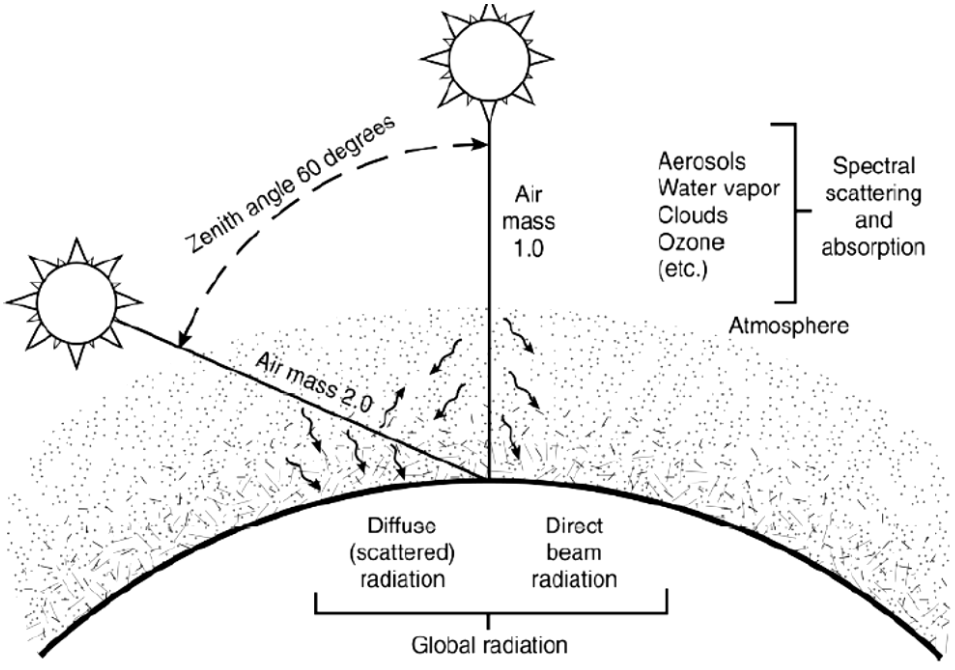


Figure 2.8: Scattering of Solar Radiation by Atmosphere

The thickness or amount of atmosphere through which solar radiations has to pass through to reach the earth surface, is defined by Air Mass (AM). The

value of AM0 represents the solar spectrum measurements taken outside of the earth surface. While AM1 represents the solar spectrum measurements taken when sun is overhead, directly at sea level **[35]**. The effect of the air mass (AM) on the measured solar spectrum is shown in Figure 2.9 **[36]**. Higher value of the air mass depicts more scattering, reflection and absorbance of the solar radiations through the earth atmosphere. Based upon the wavelength, the major portion of solar spectrum contains ultraviolet, visible and infrared radiations.

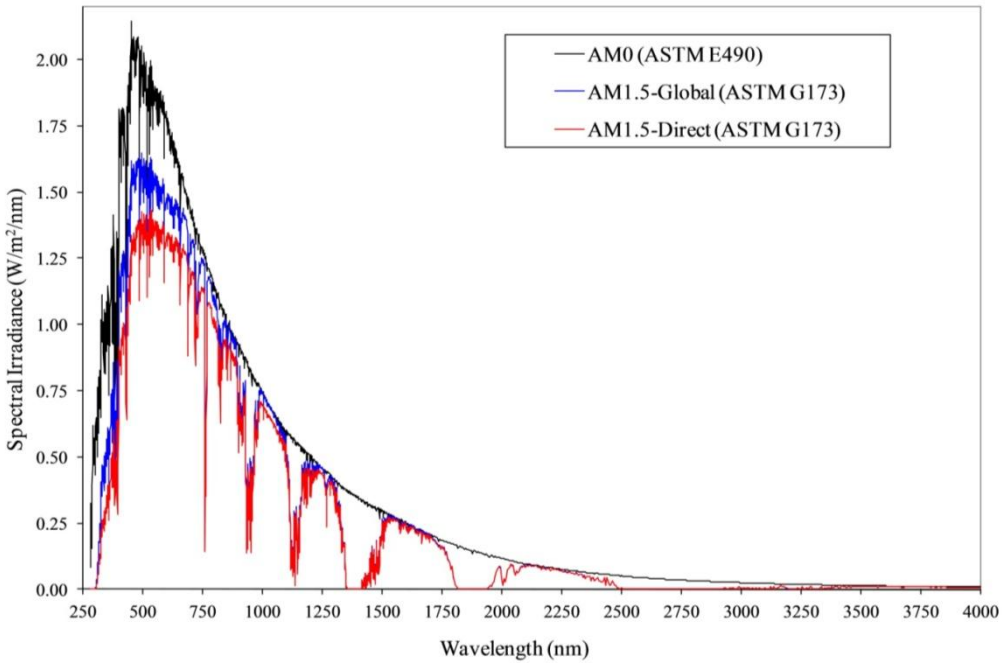


Figure 2.9:Solar Spectrum

Solar radiation received outside of the earth atmosphere, at AM0, is called Extraterrestrial radiation. The intensity of extraterrestrial radiations changes with change in earth-sun distance due to elliptical nature of the earth's orbit. The extraterrestrial radiations intensity or solar irradiance at any day of the year can be found using Equation (2.1) **[37]**. The parameter $E_{xt}$ represents the amount of extraterrestrial solar irradiance received outside the earth surface

and 'n' is the day number starting from 1st of January. The is the solar constant which is equal to solar irradiance received outside of the earth atmosphere when distance between earth and sun is 1AU (Astronomical Unit = 149,597,870,700 km). Various scientists have undertaken studies to calculate the value of the solar constant. NASA and ASTM have accepted solar constant value of 1353 W/m$^2$ proposed by Thekaekara **[38]**. However, World Radiation Centre (WRC) is adopting value of 1357 W/m$^2$ for solar constant.

$$E_{xt} = E_{SC}[1 + 0.033\cos\left(\frac{360n}{365}\right)] \qquad (2.1)$$

## 2.3 Solar Photovoltaic

Solar photovoltaic systems utilize solar cells which convert solar energy directly into the electricity through photo-reaction. Solar cells are made of semiconductor material and under the solar radiations, electron-hole pairs are generated which are separated by the internal electric field around the junction. In the presence of external load across the solar cell, it can provide current and voltage through internal electric field. Multiple solar cells can be easily combined in form of solar modules to generate hundred of watts. Photovoltaic systems can be used for a wide variety of applications with any power requirement and with excellent weather resistance. However, one of the main reason of the huge gap between solar energy potential and its use is the very low energy conversion efficiencies of most of the commercial photovoltaic systems.

Based upon the semiconductor material and the manufacturing method, the solar cell are divided into three generations, as shown in Figure 2.10. First

generation of the solar cells is based upon silicon wafer based photovoltaic systems which currently dominate 85% of the photovoltaic market. Single-crystalline and multi-crystalline wafers, both types of the solar cells are in commercial use and so far highest efficiencies of 25.6% and 20.4% are obtained at laboratory scale for single crystalline and multi-crystalline silicone based solar cells **[13]**. Second generation solar cells are based upon the deposits of the thin film of semiconductor material. This manufacturing technique provides very cost effective photovoltaic systems with reduced cost per watt of the electrical energy produced, which dominate rest of the photovoltaic market. However, the conversion efficiency offered by the second generation photovoltaic systems is lower than the first generation silicon based solar cells, with highest efficiencies of 20.5% for CIGS and 19.6% for CdTe thin film solar cell at laboratory scale **[13]**.

Currently, most of the research is based upon the third generation solar cells, to achieve high conversion efficiency while maintaining low cost feature of the second generation solar cells. Third generation solar cell includes hot carrier solar cell, multi-junction solar cell, organic polymer-based solar cell, Gratzel solar cell, multiband and thermo photovoltaic solar cell **[14].** However, in this study multi-junction solar cells are considered in form of concentrated photovoltaic systems for high efficiency power system with low cost.

### 2.3.1 Multi-Junction Solar cell (MJC)

The conventional solar cells of both first and second generations are based upon the single junction of the semiconductor material that responds to only a

certain portion of the solar spectrum for electricity production, while remaining portion of solar energy is dissipated as heat. In order to have higher efficiency, solar cell respond to maximum of the solar spectrum with minimum lost.

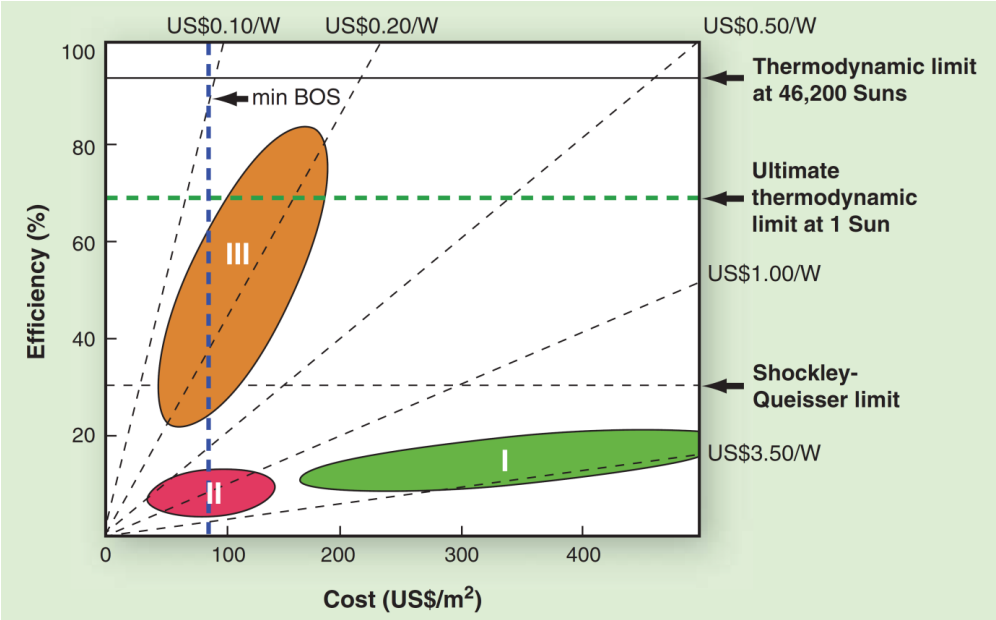


Figure 2.10: Three Generations of Solar Cell **[39]**

Multi-junction solar cells are basically a stack of the single junction solar cell such that each junction absorbs certain portion of the solar spectrum. This stack of the band gaps is selected such that the wide range of the solar spectrum is absorbed by the solar cell. From top to bottom of the stack, the band gap of each of the junction becomes smaller and smaller. However, the difference between each band gap must be as small as possible to have minimum spectrum loss as higher the band gap difference depicts the higher solar energy loss in form of heat **[14]**. So far the maximum efficiency of 46% is achieved by the multi-junction solar cell at laboratory scale **[15]**. The concept of the multi-junction solar cell as compared to single junction solar cell, is shown in Figure 2.11 **[16].**

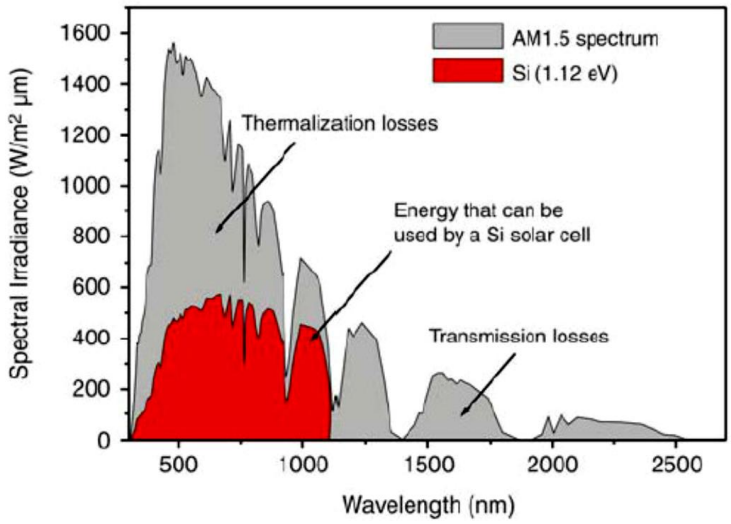


(a)

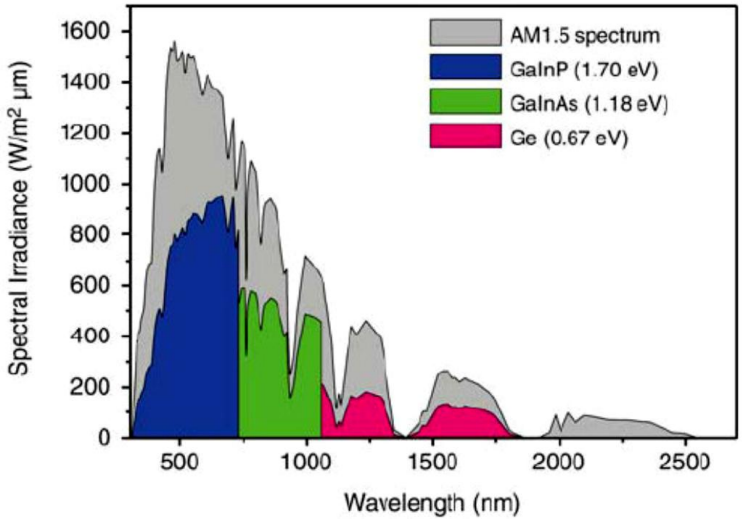


(b)

Figure 2.11: Part of Solar Spectrum Absorbed by (a) Si Solar Cells and (b) Multi-Junction Solar Cells

Another important factor of comparison between single junction and multi-junction solar cells is the maximum achievable thermodynamic efficiency. Shockley and Queisser first analyzed the solar cell classic limiting efficiency. The thermodynamic efficiency limit for a single junction solar cell under non-concentrated radiations is 31% **[40]**. This thermodynamic efficiency of single junction solar cell is limited by the photons transmission losses, having energy lower than the band gap and by the thermal relaxation of the photons with

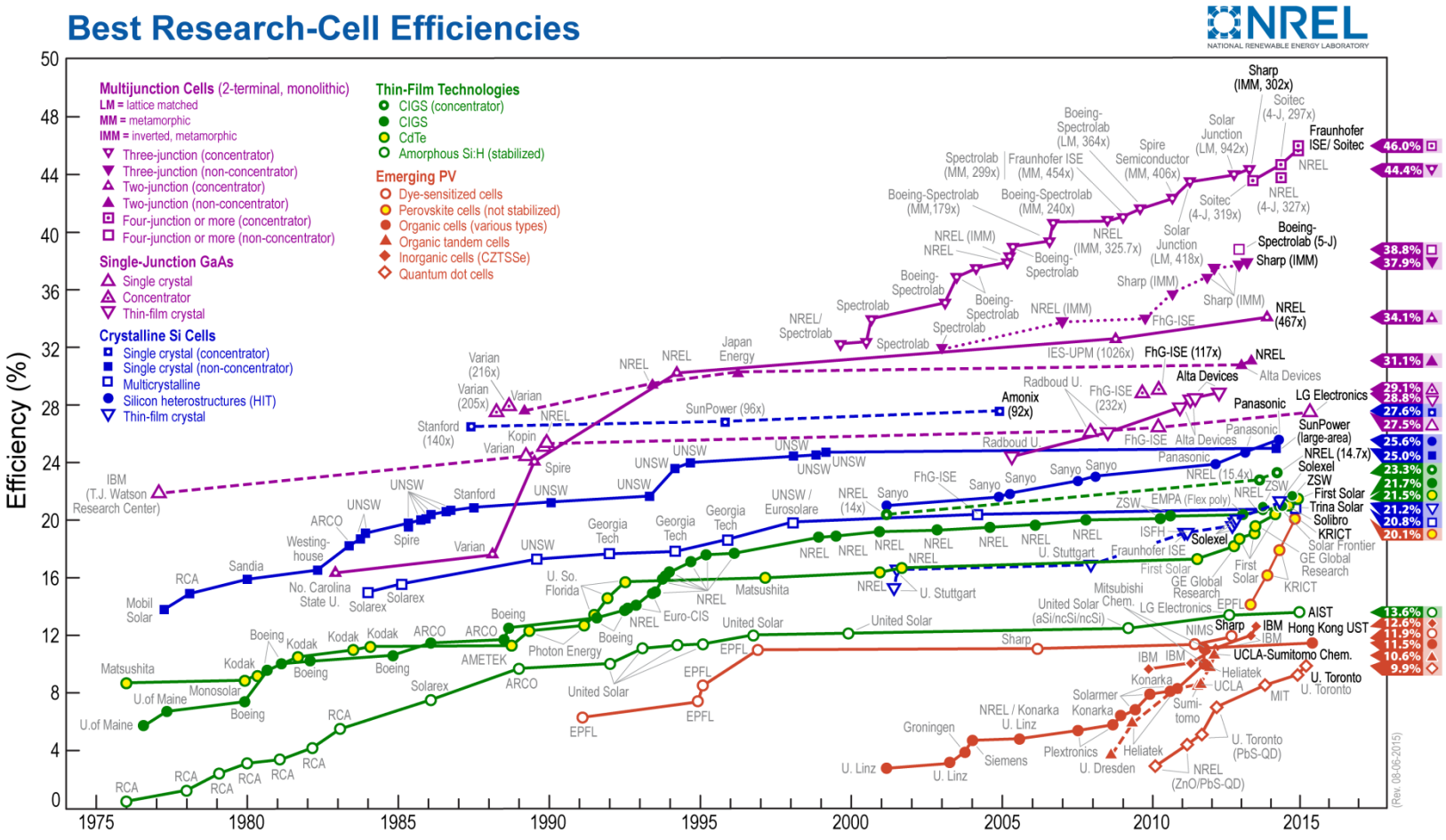


Figure 2.12: Best Research-Cell Efficiencies

energy higher than the band gap created carriers. While for the multi-junction solar cells, this limiting efficiency depends upon the number of the junctions in the stack. For the four junctions solar cell, the maximum achievable thermodynamic efficiency limit is 68.5%. However, this limit can be increased to 81% under concentrated solar radiations of intensity x10,000 **[41]**. Figure 2.12 shows the chart for the best efficiencies of different solar cell materials and technologies obtained at laboratory scale and the multi-junction solar cells can be seen at the top of the chart with highest efficiency among all the solar cells **[42]**.

## 2.4 Concentrated Photovoltaic and Two axis Solar Tracker

Besides highest conversion efficiency, the multi-junction solar cells are expensive to fabricate for large scale applications. In order to make them cost effective, concentrated photovoltaic concept is used in which low cost solar concentrators are used to concentrate the sunlight onto a small area of the solar cell, thereby reducing the use of the expensive semiconductor material **[43]**. Refractive optics like Fresnel Lens or reflective optics comprising of reflective mirrors, either flat or curved, are used to concentrate sunlight on the solar cell to intensity from 200 to 1000 suns; which allows 200 to 1000 times less use of photovoltaic material than non-concentrated system **[43,44]**. Figures 2.13 and 2.14 show the simplest arrangement of a CPV system using lens and reflectors as concentrators respectively, to concentrate the sunlight onto a multi-junction solar cell **[45]**. The lenses or reflectors are designed to concentrate sunlight of required intensity. The concentrators increase the amount of solar energy falling onto the solar cell like the cell is facing

multiple suns and as a result, the power output and efficiency of solar cell or photovoltaic system increases as compared to solar cell of same are but without concentration **[46]**.

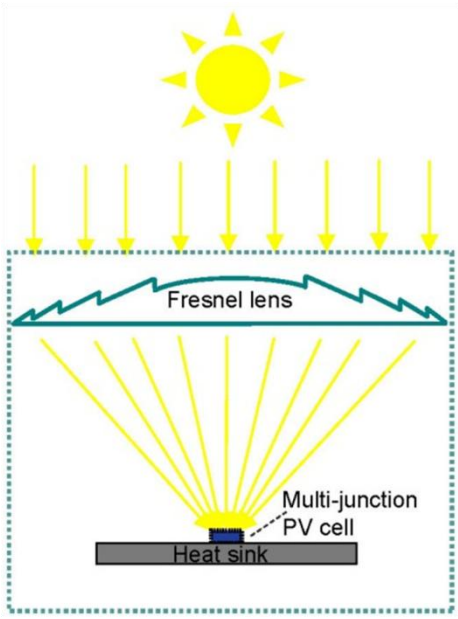


Figure 2.13: CPV System arrangement using Lens Concentrator

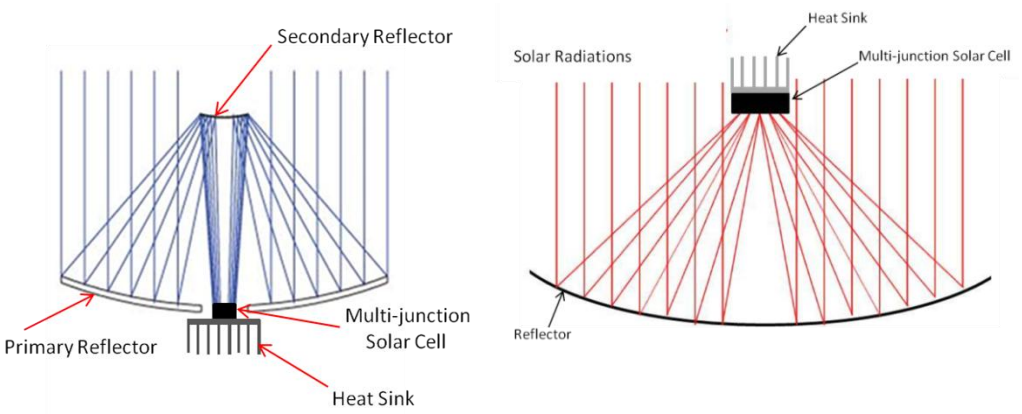


(a) (b)

Figure 2.14: CPV System arrangement using (a) Single Dish and (b) Double Dish, Cassegrain

The most basic form of CPV system consists of the concentrator, solar cell and the heat sink. As the concentrated sunlight falls onto the multi-junction solar cell, there is also a need to dissipate the waste heat from the solar cell to allow it to operate within the optimum efficiency limit, as the efficiency of the solar

cell decreases with increase in cell temperature. Therefore, heat sink or other cooling devices are utilized to dissipate heat to cool down MJC temperature within certain limits. Beside the shown schematic arrangement of the CPV system, another main component of CPV system is the two axis solar tracker. As solar concentrators are for solar beam radiations i.e. rays parallel to the concentrator axis, which demand CPV system to face towards sun all the time with high accuracy. In the concentrating assembly design of modern CPV, a secondary or tertiary optical glass component, called homogenizer, is attached optically to the MJC which not only increases the acceptance angle of the concentrating assembly but also guide the solar radiations towards the MJC with uniform distribution over the cell area. The CPV concentrating assemblies of refractive and reflective concentrators and with homogeniser, are shown in Figures 2.15 **[47]** and 2.16 **[48-49]**.

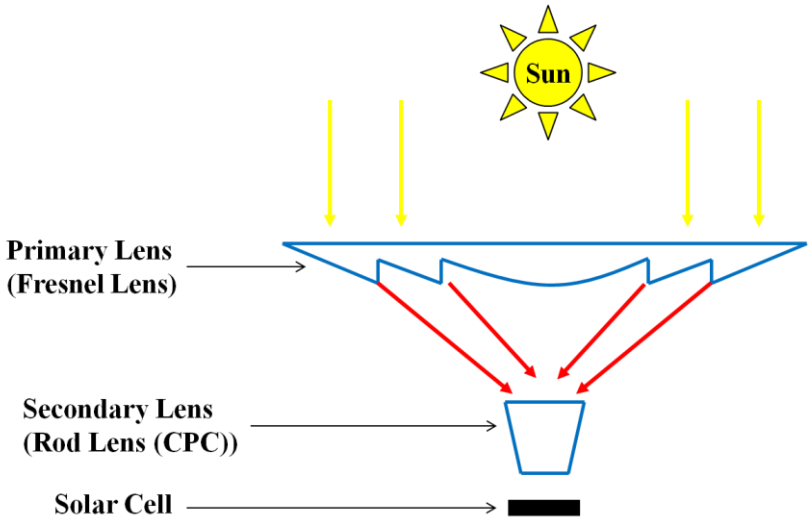


Figure 2.15: CPV System arrangement with Fresnel Lens and Homogeniser

The development of concentrated photovoltaic system (CPV) technology started in 1976 at National Sandia Laboratories, with the development of a 1KW CPV system **[50]**. This system showed satisfactory performance, which

later led to development of several prototypes of 500-1000 W power capacity in different countries **[51-53].**

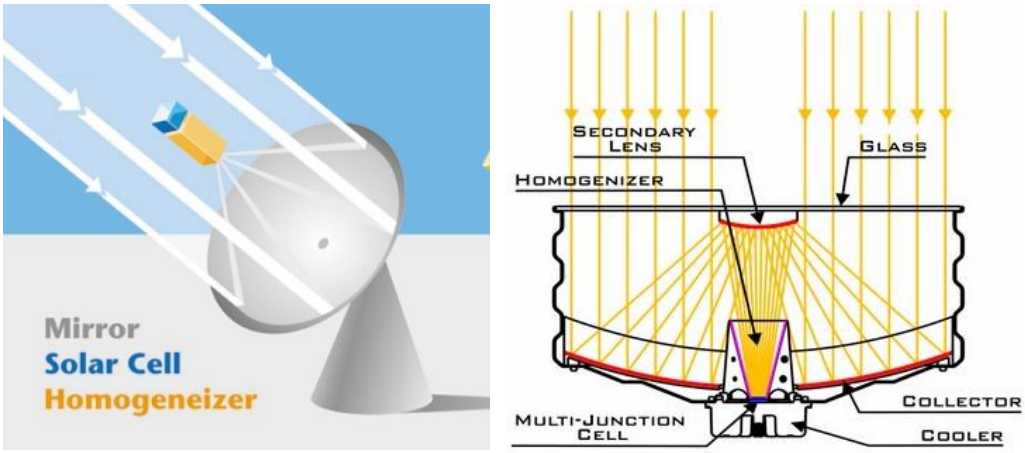


(a) (b)

Figure 2.16: CPV System arrangement with (a) Single Dish, (b) Double Dish and Homogeniser

Then in 1981, Martin Marietta developed another pre-industrial and demonstrational 350 KW CPV plant and installed in Saudi Arabia **[54]**. Although, the developed system showed satisfactory performance but the performance degradation issues with high solar cells temperature were observed. For reliable performance, spectrum splitting technology was also used using two cells at 800 suns concentration. However, all of these efforts could not pave the way for commercialization of the CPV system **[55,56]**. One of the main reason of poor reliability of the CPV system was the use of the conventional single junction silicone solar cells, which are not suitable and designed to operate under high concentration. The main focus was then given to the development of solar cell to have reliable performance under high temperature and concentration **[57]**. Later, multi-junction cells were considered for high concentration because of their high temperature tolerance

and response to broader spectrum of solar radiations that resulted in to achieve higher efficiency and field reliability.

With the reliable and mature solar cell development, now the main focus is on the development of concentrating assembly and overall system design. Initially, large reflective concentrating dishes were used for the CPV system **[58,59]**. Some CPV systems were also developed for linear concentration using parabolic trough and linear Fresnel lens, instead of point concentration **[60,61]**. In addition, some researchers also proposed the design of the CPV field using multiple flat reflectors focussing at single common receiver of the solar cell **[62-66]**. The first concern with these initial designs of CPV systems is the use of large reflective concentrators, which are difficulty to manufacture. Secondly, because of high heat flux at the cell areas and larger size of the solar cell, the heat rejection from the cell becomes another issue, which requires liquid based active cooling to keep MJC temperature within efficient operating limit. To reduce the manufacturing cost and cooling issues, CPV systems were then developed with relatively small size of refractive concentrators i.e. Fresnel lenses **[67,68]**. As mentioned before, concentrators are designed for parallel or beam radiations, so they are always pointed towards the sun by using two axis solar tracker. For the CPV system, tracking is very important, If the solar radiations are not properly focussed then the power output drops to zero. Although for non-concentrating PV, the solar tracker can increase the power output of the system. However, for CPV system, it is the essential part, which also consumes the power. Some designs of the concentrating assembly were developed then to reduce the tracking requirements with acceptance angle of concentrating assemblies $\pm 5^{o}$ and 80-

85% optical efficiency **[69]**. Lens-based concentrators mostly have higher focal length to accommodate homogeniser or secondary optics. This overall height of the lens based CPV system increases the instability and the shipping cost of the system. Different designs of the homogenises and concentrators are also developed to reduce the overall concentrator height and the acceptance angle **[70-72]**. Due to advantages of mini lens based concentrators designs, there is also a CPV design developed based upon the miniaturization of the dish concentrators with secondary reflector as a flat mirror to reduce the overall height of concentrator assembly **[73]**. However, all of these studies and designs finally led to the current commercial CPV system designs, which are based upon the single stage concentration using small Fresnel lenses and the double stage concentration using mini parabolic and hyperbolic reflectors in the cassegrain arrangement **[74-76]**. So far, all of the CPV concentrating assemblies are designed with a dedicated concentrator for each of the solar cell, which requires a large number of concentrators in case of the mini-concentrator CPV system design . Thus, there is a need to reduce the number of mini dishes, with concentrating assembly that can concentrate solar radiations onto multiple solar cells with single set of concentrator without increasing the cell size and temperature issues, as proposed in this thesis.

Beside concentrating assembly, one of the most important concern related to these CPV systems is that they are designed as big units with too many CPV modules installed on a large two axis solar tracker, which are only suitable to be installed in open desert like regions with high DNI availability **[77]**. The CPV appeared to be some of those technologies that few people bought, with less market and customers. It must be noted that the rooftop installations of

conventional flat plate PV make a significant share of the total PV installed capacity. For most the countries, the rooftop PV installation on commercial and residential buildings, is aimed to contribute to 40-50% of the total PV installations **[19].** On the other side, the commercial CPV systems are not so far designed to be installed on the rooftop, which gives motivation for the development of our new CPV field design based upon the master and slave configuration of the compact, smart, small and highly accurate two axis solar trackers which can be easily installed on the rooftop. As the trackers are proposed to be small and compact, large number of trackers will be required. However, with the proposed master and slave configuration, minimum hardware will be required by the slave trackers as they will receive required tracking information from the master tracker. The expensive sensors and devices will be supplied to the master tracker which will further distribute the information to the slave trackers. It is also worthy to mention here that the solar trackers required for the CPV system are different than the PV systems, as CPV need very high accuracy. The high accuracy of the tracking is ensure through hybrid tracking technique, utilizing optical tracking sensor. Most of the optical sensors developed for the solar tracking systems, does not offer tracking according to the required accuracy of the CPV. These sensors use classical approach of the shadow, tilt surface and the collimating tube, with an array of the photo-sensors. From the closed control loop and the comparison of the output signal of the photo-sensors, the position of the sun is determined. Due to requirement of the large shadow device or collimating tube for high accuracy, these conventional sensors are not suitable for the CPV applications **[78]**. However, the optical tracking sensor based upon the position sensitive

diode (PSD) is used for most of the current commercial large CPV trackers **[79,80]**. However, these PSD based tracking sensors are not suitable for the small systems due to their high cost for many small tracking units. Therefore, a cheap but highly accurate optical tracking sensor is also needed for proposed cheap CPV tracking system.

It is a conception that highly efficient CPV systems are suitable for desert regions with high DNI availability as the CPV systems only respond to beam radiations (DNI). That is why big units of CPV systems are designed for desert regions **[77]**. However, conventional PV system can operate in beam and diffuse radiations but with lower efficiency. Ultimately, the consumer is interested in true total long-term power produced by the photovoltaic system. Therefore, a methodology is also needed that can rate the system based upon its long-term power output, instead of the maximum conversion efficiency. In this thesis, an electrical rating methodology is also proposed and the developed CPV systems performance is evaluated for long-term operation and compared with the conventional PV systems, installed in the tropical weather of the Singapore. This study will also help to analyze the CPV system performance in low DNI regions, which may help to remove the conception that CPV systems are only suitable in desert regions.

## 2.5 Hydrogen Energy Storage

Owing to the alarming level of the green-house gas emissions and their drastic effect on the global environment, renewable energy resources are proved to be viable option under current global warming condition. Most of the renewable energy resources are proved to have the potential more than the global energy

demand. The major global energy need is in form of electrical energy and the main attractiveness of most of the popular renewable energy systems, especially solar, wind and hydro energy, is that the electricity can be produced easily through simple system configuration using these renewable energy resources. However, one of the core requirement of the electricity or power production system is the continuous supply of the electricity to the consumer without any interruption. The availability and the potential of all of the above mentioned renewable energy systems, varies largely from region to region especially for wind and hydro energy. However, solar energy is easily available and accessible around most of the regions and the photovoltaic system provides simplest way for electricity production directly from the solar energy **[7-9]**. As discussed before, solar energy has the highest energy potential among all energy resources and it can alone supply 10,000 times more energy than current global energy demand **[5,6]**. Like many other renewable energy systems **[20]**, solar energy is not available all the time and at a constant rate. Beside higher energy potential, in order to be proved to be a practical power production system, a steady supply of the power at a constant rate is required **[21]**. Solar energy is only available during diurnal period but not all the time and at constant rate due to cloud cover and weather changes. Moreover, the continuous motion of the sun also results in the variable solar intensity during different periods of time in a day, due to changing Air Mass (AM). Therefore, due to intermittent nature of the solar energy, an energy storage system is needed such that the energy during the time of excess power production is stored and then supplied back to the system during the time of low or no power production.

The common energy storage method employed for most of the photovoltaic systems, is the electrochemical storage using batteries. The battery bank provides convenient energy storage option for the systems with small capacity and short-term energy storage requirements due to convenience in charging and discharging and high round trip efficiency **[81-83]**. For most of the solar energy systems, the design is based upon the long term operation of 20-25 years lifetime period **[25]**. For long term storage, the batteries do not provide technically and economically feasible option especially for medium to large capacity systems **[26],** due to their self-discharging, low energy density and the leakage problems. Some other energy storage techniques of compressed air, pumped hydro, thermal storage and super-capacitors also provide the storage for the short term operation of only few day, hours or seconds **[84]**. Moreover, the application of these energy storage techniques is also not proved to be reliable especially for photovoltaic systems. Therefore, for the utilization of intermittent energy resources like solar energy, hydrogen production provides reliable and most-suitable energy storage option for medium to long term storage.

Hydrogen is considered as the promising alternate fuel of the future due to its sustainable nature and capability to store high quality energy; electricity from the fuel cell or heat from the direct combustion. Beside energy storage, hydrogen can also be used as energy carrier in form of the independent energy source as it can be easily transmitted anywhere with convenience **[85]**. In this scenario, hydrogen is believed to be considered as feasible option for sustainable and reliable operation of the energy systems. There are many methods for the production of the hydrogen using solar energy in form of

thermal energy, electrical energy, bio-energy and photon energy. Different process are developed for the production of hydrogen from above mentioned energy types **[86]**. However, the cheapest and widely used method for production of hydrogen for industrial need is the steam reforming of the fossil fuels especially methane or natural gas, followed by the oil and coal as hydrogen is one of the main constituent of the fossil fuels. This method contributes to the 96% of the total global hydrogen production **[87]**. Beside the production of hydrogen, greenhouse gases like CO and $CO_2$ are also produced through steam reforming of fossil fuels thereby making it not suitable option to be used for sustainable energy system. Another popular and simple process, that shares remaining 4% of the total global hydrogen production, is the electrolysis of water that uses electricity to split the water molecules for generation of hydrogen, with oxygen as by-product **[88]**. However, electrolysis provides viable and sustainable option for the production of hydrogen if the electricity is generated through renewable energy resources and the photovoltaic systems provide simple and convenient production of the electricity directly from the solar energy.

### 2.5.1 Water Electrolysis Theory

Water electrolysis is a simplest and popular process to split up the water molecule to produce hydrogen and oxygen. The main component of the electrolysis unit is the electrochemical cell, called as the electrolyser, as shown in Figure 2.17. In electrolyser, electrodes are separated by the electrolyte either liquid based or solid based, and connected to the external electrical power source. When a voltage higher than a certain minimum value is applied across the electrodes, the electrolysis process starts and hydrogen starts

producing at the negative electrode (cathode) and oxygen at the positive electrode (anode). The amount of the current passing through the electrolyser determines the amount and rate of production of hydrogen and oxygen **[89]**.

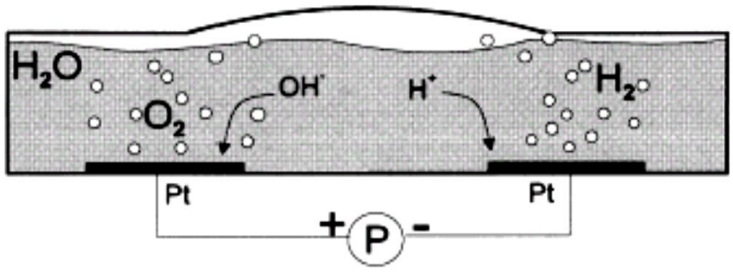


Figure 2.17: Sketch of Electrolyser

In electrolytic water, $H^+$ and $OH^-$ ions are always present in a certain percentage of equilibrium, represented by:

$$H_2O\ (l) \longleftrightarrow H^+\ (aq) + OH^-\ (aq)$$

When electricity is supplied to the electrolyser through electrodes, the positive ions ($H^+$) are attracted towards cathode and negative ions ($OH^-$) towards anode and hydrogen and oxygen gases are released at the cathode and anode respectively, due to oxidation and reduction reactions as shown below:

$$4OH^- \longleftrightarrow 2H_2O + O_2 + 4e^-$$

$$2H^+\ (aq) + 2e^- \longleftrightarrow H_2\ (g)$$

When electrolysis is done in an acidic or basic electrolytic medium, the reaction equations are slightly different due to presence of catalyst and some other ions. However, overall reaction for the electrolysis of water is given by the following equation:

$$2H_2O \longrightarrow (4e^-) \longrightarrow O_2 + 2H_2$$

In order to find the minimum voltage required for the electrolysis process to start-up, first there is a need to clear some basic ideas. Water electrolysis is a reverse process of the fuel cell reaction. In electrolysis, water molecule is split up into hydrogen and oxygen by application of the electrical energy. While in fuel cell, hydrogen and oxygen gases combine together to form water molecule and produce electricity equal to 237.2 kJ/mol. This energy is called as Gibbs free energy for fuel cell which is the net work done produced by system. Fuel cell reaction equation is given by.

$$H_2 + 1/2\ O_2 \longrightarrow H_2O_{(liquid)}$$

This equation is similar to that for calculation of the heat of combustion of hydrogen, which is 285.8 kJ/mol. However, electrical energy produced by fuel cell is 237.2 kJ/mol and remaining 48.6 kJ/mol is released as heat. So fuel cell complete reaction equation can be written as:

$$H_2 + 1/2\ O_2 \longrightarrow H_2O_{(liquid)} + 237.2\ kJ/mol\ (Electricity) + 48.6\ kJ/mol\ (Heat)$$

Gibbs free energy can be converted into corresponding thermodynamic voltage from following equation:

$$E^o = \frac{Gibbs\ Free\ Energy}{n_e F} = \frac{237200}{2 \times 96485} = 1.23V \qquad (2.2)$$

Where $n_e$=2 i.e. the number of electrons needed to create one molecule of hydrogen and F=96485 coulombs/mole (Faraday constant). Thermodynamic voltage of 1.23 volts are produced when a water molecule forms. Similarly, same amount of the voltage should be needed to split the water molecule. But during the water molecule formation, some amount of energy is released in form of the heat which also must be supplied at the same time. Therefore, at

least total 285.8 kJ/mol energy is needed to be supplied to split the water molecule. The voltage corresponding to the heat of combustion of the hydrogen is given by the Equation (2.3).

$$E_o = \frac{\Delta H^o}{nF} = \frac{285840}{2 \times 96485} = 1.481\ V$$

This is the minimum voltage that is theoretically required to split the water molecule into hydrogen and oxygen. However, practically more amount of voltage is needed due to some losses **[90]**. Based upon the electrolytic medium, there are two types of the electrolysers, alkaline and proton exchange membrane (PEM).

### 2.5.2 Alkaline Electrolyser

Alkaline electrolyser is based upon a well established technology which normally use 25-30 %wt. KOH aqueous solution as the electrolytic medium. Other solutions like NaOH and NaCl can also be used based upon the reaction environment. The electrolytic solution acts as catalyst which only helps to conduct the ions between two electrodes and is not consumed during the reaction. However, there is still a need to replenish it periodically due to other system losses. Basic form of the alkaline electrolyser consists of a tank containing electrolyte and electrodes which are fully dipped into electrolytic solution. The electrodes are separated by a diaphragm which allows the ions to pass through it but prevents the gases from mixing, produced at the electrodes which are separated be a very small distance. Based upon the design configuration, there are further two types of the alkaline electrolysers, unipolar and bipolar as shown in the Figures 2.18 and 2.19 **[91]**.

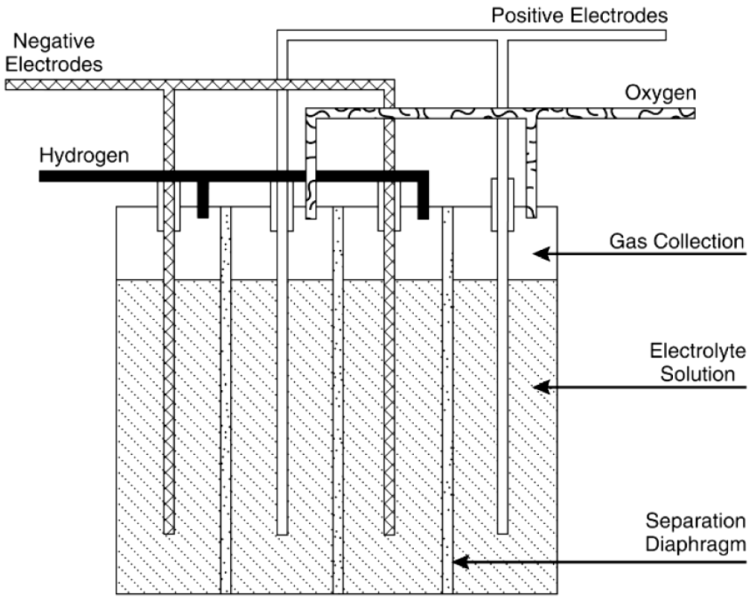


Figure 2.18: Unipolar Electrolyser

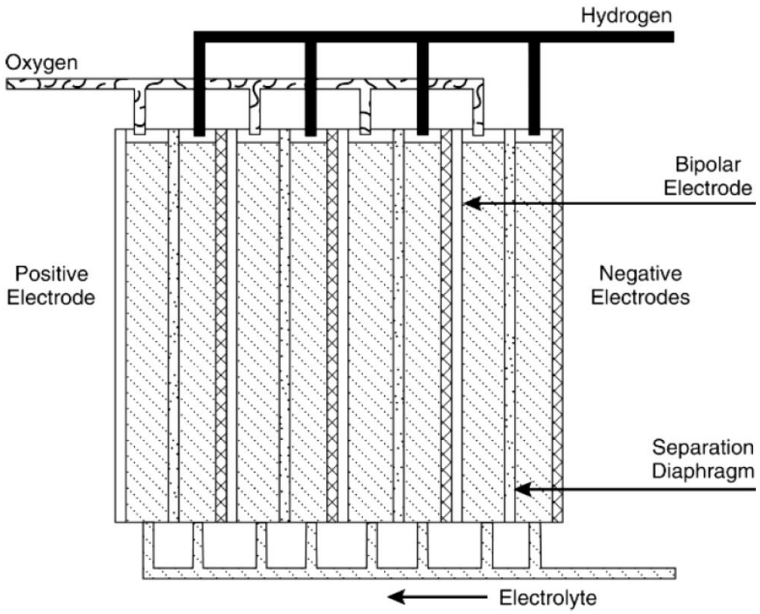


Figure 2.19: Bipolar Electrolyser

Each of the design configurations has its own significance. Unipolar electrolyser design requires very few parts with simple construction and easy maintenance as each the electrode pair is working independently and electrodes can be easily replaced while the others are still in operation. Bipolar design consists of alternate layers of the electrodes with diaphragm for the

gases separation. As the electrolyser cells are connected in series in bipolar design, so there is a need for high stack voltages. However, the size of the bipolar electrolyser is thinner than the unipolar. For the repairing work, the whole stack is removed and serviced **[91]**.

### 2.5.3 Proton Exchange Membrane (PEM) Electrolyser

PEM electrolyser is another commonly used commercial electrolyser, also referred as SPE (solid polymer electrolyte) or PEM ( polymer electrolyte membrane), as the solid electrolyte is used as the conducting medium. The catalyst and the electrolyte materials are coated onto a solid membrane with two electrodes at the extreme sides. Membrane is not electrically conductive but allows the ions to pass through. It serves as a separator to separate the produced gases at the electrodes from mixing. Unlike the alkaline electrolyser, deionised (DI) water is only used in PEM electrolysers. PEM electrolysers can operate at high current densities then the alkaline electrolysers and are the main focus for future research. Simple construction of PEM electrolyser is shown in Figure 2.20 **[91]**.

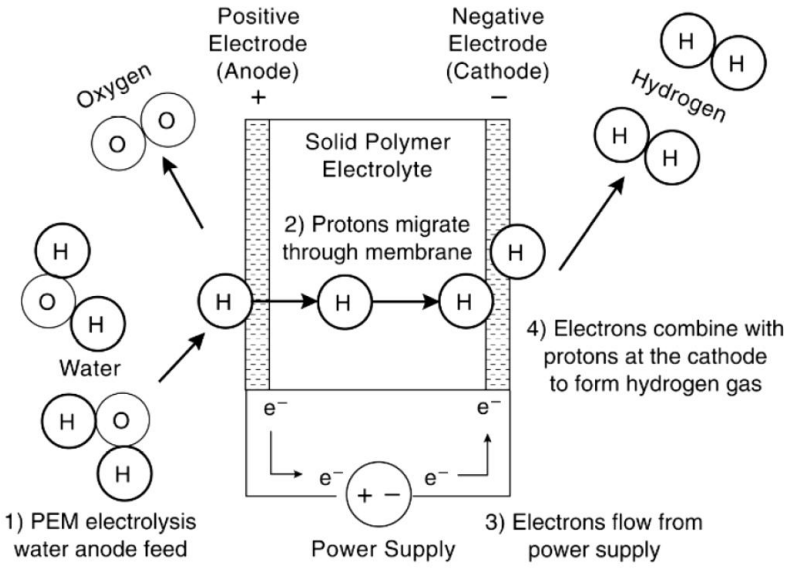


Figure 2.20: Sketch of PEM Electrolyser

## 2.6 Standalone Systems and Design Optimization

Hydrogen production is proved to be a sustainable option for the energy storage. However, the stored hydrogen, to be used as an energy storage, must be supplied back to the consumer in form of the primary energy when needed. The systems with this type of configuration are called standalone systems, which can supply electricity without any interruption and external supply. The schematic of the simple operation loop of a standalone solar energy system is shown in Figure 2.21. The electricity produced by the solar energy system is supplied to the consumer or load. While after fulfilling the consumer load requirement, the excess electricity is supplied to the hydrogen production system and the produced hydrogen is later sent to the storage system. When the electricity produced by the solar energy system is not enough to meet the consumer load requirements, then the stored hydrogen is supplied back to the hydrogen utilization unit that supply electricity to consumer according to the power deficiency. Therefore, in order to tackle the intermittency and steady power production, the solar energy systems must operate as a standalone system and the hydrogen production provides the most reliable, sustainable and long-term energy storage solution.

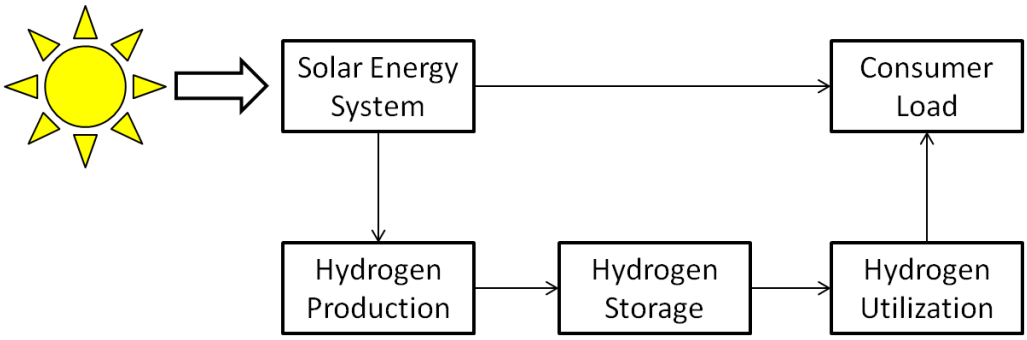


Figure 2.21: Simple Schematic of Standalone Solar Energy System with Hydrogen Production as Energy Storage

As the solar energy system provides electricity to the consumer, so the hydrogen production system in the shown schematic of standalone system is the electrolyser that converts water into hydrogen and oxygen. Similarly, the energy from the storage is also needed in form of the electricity. Therefore, the hydrogen utilization system is based upon the fuel cell that converts stored hydrogen and oxygen into electricity with water production as by-product. Another important aspect of standalone energy systems is the storage of hydrogen. The most common methods of hydrogen storage are liquefaction of hydrogen, high pressure compression storage, adsorption storage and metal hydride storage **[92]**. Among all the storage techniques, the compression storage of the hydrogen at high pressure provides simple and the convenient option such that hydrogen is readily available without any pre-processing **[93]**. The only concern raised for the compressed hydrogen storage is the volumetric capacity **[94]** at conventional storage pressure of 200-350 bar. However, the volume is not considered as the constraint for standalone system especially based upon solar energy. Beside volumetric capacity, another very important factor that is needed to be considered is the storage capacity (Gravimetric Capacity) corresponding to the overall mass and size of the system. The volumetric capacity can be increased to competent level if storage pressure is increased to 700 bar, but the gravimetric capacity may slightly reduce **[95]**. The volumetric capacity can be increased through liquefaction of the hydrogen. However, due to very low temperature requirement, this method is not very efficient and boiling of the hydrogen (above 20K) is also another issue **[96]**. The adsorption and metal hydride storage techniques provide high volumetric capacity and solution related to the high pressure storage problems.

In comparison, the adsorption storage technique offers comparatively low gravimetric capacity than the metal hydrides **[97]**. Although the metal hydrides offer storage at low pressure, but the main issue is also the gravimetric density offered by them. At very low pressure and temperature, metal hydrides offer very low gravimetric capacity of about 1% or less, which can be increased to 2.5-3% at pressure of 350bar **[98]**. This means, in order to have storage of 50kg of hydrogen, 2000-2500 kg of storage material is needed for gravimetric capacity of 2-2.5%. In the literature, very high gravimetric capacity of above 10% is reported for metal hydrides **[99,100]**, but at very high pressure and temperature. However, this demands extra work of compression and extra thermal energy input, along with the big and complex configuration of the system with regeneration requirement. Therefore, the compressed hydrogen storage at high pressure in the storage tanks provides the simple, most convenient and reliable long-term energy storage option.

The main aspect of the standalone energy system development is the design optimization, which includes the size optimization of each of the component of the standalone system along with energy management and control strategies. The system size is optimized such that it has enough capability to fulfil the energy requirements of the consumer load along with the enough energy storage to handle the power interruptions for long-term operation. The system performance is simulated based upon the long term weather data to optimize the system size for uninterrupted power with enough energy storage to meet the load requirements. There are many studies in the literature regarding the standalone energy system optimization with hydrogen production, based upon the size **[101]**, techno-economic optimization with

optimum efficiency and control strategy of each of component of the system **[102,103]**. In order to handle small power ripples with better system management and control, PV-hydrogen system was hybridized. The purpose of the techno-economic optimization is to get the optimum system size while keeping the overall system cost minimum. However, the cost and the size of the system can be reduced by capturing most of the available renewable energy and converting into electricity. In the literature, all of the studies are based upon the photovoltaic systems considering the conventional PV system, which offers very low energy conversion efficiency. Many researchers have considered to adopt the hybridized system of PV and wind turbine with hydrogen production **[104-106]** or along with the small capacity battery storage **[107-109]** to reduce the overall system cost and the size of the system. Some authors also proposed and analyzed the PV system in hybridization with the diesel generator system to significantly reduce the overall system cost and the energy storage **[110,111]**, but the main concern of green house gas emission is still there. Despite of highest solar energy conversion efficiency, the literature is lacking for study related to standalone system with CPV which can reduce the overall size of the system. In this thesis, the optimization algorithm and energy management technique for standalone operation of CPV are also developed with hydrogen production as energy storage.

Therefore, based upon the literature, it is found that a compact and cheap design of the CPV is needed with the development of complete theoretical and experimental framework for consideration of CPV as reliable steady power system or stand alone system, for which hydrogen production provides sustainable energy storage option.

# Chapter 3: Development of Two Axis Solar Tracker with Master Slave Configuration for CPV Field

## 3.1 Introduction

The two-axis solar tracker is one of the key components of a concentrating photovoltaic (CPV) system. The solar concentrators can only respond to solar beam radiations and that is why CPV systems need two axis solar tracking system to face towards the sun during their operation. Therefore, the performance of the CPV system, to some extent, is dependent on the accuracy and precision of the solar tracking system as very high tracking accuracy is required for CPV system operation and poor or inaccurate solar tracking may lead to 100% power loss.

Most of the commercial CPV units are available in large size with corresponding larger tracking units, designed for open fields in desert areas but not suitable for urban or residential areas or rooftops of residential buildings, unlike conventional PV systems. In this chapter, a novel master and slave configuration of the CPV field tracking system is proposed with small, compact and smart but cheap two-axis hybrid solar trackers, which are designed, developed and experimentally tested. The developed two-axis solar tracker is based upon the hybrid tracking algorithm, utilizing both active and passive tracking methods. By following the passive technique as main tracking algorithm, the tracking accuracy is ensured through active tracking algorithm. The passive tracking follows predefined solar geometry and active tracking utilizes photo-sensors for solar position feedback. Due to expensive

design of conventional solar feedback sensor, a novel and cheap but highly accurate solar feedback sensor design is also discussed in this chapter with tracking accuracy of $\pm 0.1^{o}$. In addition, a microcontroller based tracker control box is developed for tracker operation and is tested for long term operation. For tracking system of CPV field, the overall tracking algorithm is based upon master slave control in which all the slave trackers receive tracking information from master tracker thereby eliminating the need of expensive modules for each tracker. The tracking code is developed using C-programming language such that the solar tracker can operate at any location by using coordinates obtained through GPS module.

## 3.2 Development of Solar Tracking Technique

The two-axis solar tracker is developed based upon hybrid algorithm of passive and active tracking techniques as each tracking technique has certain limitations and if relied only on one method, accurate solar tracking is difficult to achieve. Passive tracking, also called as astronomical tracking, follows the predefined solar movement path using solar geometry equations and the tracker is rotated according to calculated solar angles, defined from certain reference point. However, the mechanical driving assemblies are prone to backlash or wear and tear, which can cause tracking error as passive/astronomical tracking works on open loop, without any feedback. In order to ensure the accurate tracking, the feedback is necessary.

The active tracking, also called as optical tracking, uses photo-sensors and the solar position is determined according to feedback from photo-sensors. However, in case of cloud cover, the optical tracking doesn't work as there is

no feedback from photo-sensors. That is why, accurate tracking cannot be achieved by relying purely on single tracking method. Therefore, a hybrid tracking algorithm is utilized for accurate solar tracking of concentrated photovoltaic (CPV) systems. The tracker follows the astronomical tracking in first stage and the accurate tracking is ensured by optical feedback.

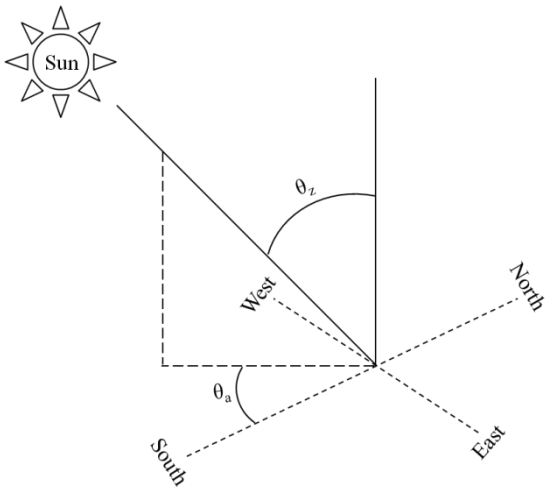


Figure 3.1: Plan View Showing Azimuth and Zenith Angles

### 3.2.1 Astronomical Tracking

The sun's movement in actual is because of rotation of earth around the sun and about its own axis. Due to this relative motion, the angle of solar beam radiations hitting the surface of earth changes continuously. The apparent motion of the sun follows a certain path and geometry that can be traced and predicted with extreme accuracy for years at any part of the world **[112]**. Azimuth and zenith are two angles that define the sun position with respect to horizontal and vertical planes respectively, as shown in Figure 3.1. The calculation of azimuth and zenith angles depends upon the other astronomical values such as declination angle, hour angle, solar time, latitude, longitude, date and time of certain place where solar position is needed to be determined.

Solar time is like 24-hour clock where 12:00 is called as solar noon when sun is at the meridian of the observer. The solar time is different from local time and depends upon the longitude of local position. Therefore, the conversion of local time into solar time is of high importance and needs two corrections.

First correction is based upon a constant depending upon the longitude difference of the standard meridian, at which local time is based, and the meridian of observer. For Singapore, local time is based upon GMT+8. As it takes 1 hour for sun to rotate $15^o$ (4 min/degree), so longitude for standard meridian is $120^o$. Second correction for the solar time is based upon the difference between mean solar time, which is average solar time because of elliptical earth's orbit and apparent solar time or real solar time, and is given by error of time (EOT) equation. The relation between solar time and local time (in minutes) is given by Equation (3.1).

$$Solar\,Time - Local\,Time = 4(L_{st} - L_{loc}) + EOT \qquad (3.1)$$

Wherre $L_{st}$ is standard longitude of local time zone and $L_{loc}$ is longitude of local observer position. However, reference for longitudes is west in degrees. Error of time (EOT) in minutes is given by Equation (3.2).

$$EOT = 229.2(0.000075 + 0.001868\cos B - 0.032077\sin B - 0.14615\cos 2B - 0.04089\sin 2B) \qquad (3.2)$$

where factor B depends upon the corresponding day of the year:

$$B = \frac{(n-1)360}{365} \qquad (3.3)$$

The angular displacement of the sun with respect to local meridian east or west due to rotation of earth, is given by hour-angle (ω) in Equation (3.4).

There is change of $15^o$/hour in hour-angle. At solar noon or at the lowest value of zenith angle, the hour angle is zero and is considered negative before solar noon and positive after solar noon.

$$\omega = \left(\frac{360}{24}\right) \bullet (Solar\,time - 12) \qquad (3.4)$$

At solar noon, the angular position of sun with respect to equator is defined by declination angle (δ) and depends upon factor B, given by Equation (3.5) **[37]**.

$$\delta = 0.006918 - 0.399912\cos B + 0.070257\sin B - 0.006758\cos 2B + 0.000907\sin 2B - 0.002679\cos 3B + 0.00148\sin 3B \qquad (3.5)$$

Now, the zenith angle, which is the angle between the direction of solar radiations and the vertical of local observer, is given by Equation (3.6). During day time, the zenith angle varies from $0^o$ to $90^o$. For a zenith angle greater than $80^o$, there is a difference of $0.834^o$ in the apparent position of the sun due to refraction of solar rays through atmosphere. However, for engineering application, this difference can be neglected for low latitudes.

$$\cos\theta_z = \sin\phi\sin\delta + \cos\phi\cos\delta\cos\omega \qquad (3.6)$$

Where ϕ is latitude of local position. The other tracking angle needed to describe solar position is the azimuth angle, which can be found using Equations (3.7) or (3.8) depending upon the hour angle.

If ω>0,

$$\cos\theta_{az} = 360 - \left[90 + \frac{\sin\delta - \sin(90-\theta_z)\sin\phi}{\cos(90-\theta_z)\cos\phi}\right] \qquad (3.7)$$

If ω<0,

$$\cos\theta_{az} = 90 + \frac{\sin\delta - \sin(90-\theta_z)\sin\phi}{\cos(90-\theta_z)\cos\phi} \qquad (3.7)$$

Where the value '90' is to change the reference plane from north to south. Another important parameter in solar tracking is the time at which the tracker must start or stop solar operation and it should be the sunrise and sunset timings at that particular location, given by Equations (3.9A) and (3.9B) **[113]**.

$$T_{SR} = \omega + \alpha - (0.06571 \times t_{SR}) - 6.622 \qquad (3.9A)$$

$$T_{SS} = \omega + \alpha - (0.06571 \times t_{SS}) - 6.622 \qquad (3.9B)$$

Where α is the sun right ascension and the values of factors $t_{SR}$ and $t_{SS}$ are given by the Equations (3.10) and (3.11) for sunrise and sunset respectively.

$$t_{SR} = n + \left[\frac{(6 - L_{loc(H)})}{24}\right] \qquad (3.10)$$

$$t_{SS} = n + \left[\frac{(18 - L_{loc(H)})}{24}\right] \qquad (3.11)$$

The $L_{loc(H)}$ is the local longitude considered in the form of hours ($15^o$=1 hour). The significance of the above mentioned tracking method is that it can be easily applied with high accuracy and simple programming. However, care must be taken during initialization from reference planes. As explained before, due to backlash problems of the mechanical assembly, tracking error can occur for astronomical tracking, which can be corrected through active or optical tracking method, as explained in the next section.

### 3.2.2 Active Tracking

Unlike passive tracking, the active tracking technique is based on the actual position of the sun. In active tracking, a certain arrangement of photo-sensors is utilized such that their output feedback is interpreted to determine the position of the sun. The important performance parameters for active tracking are accuracy and sensitivity. The tracking requirements, related to accuracy and stability, of CPV applications are very high as the tracking error may cause the CPV power output to drop from 100% to 0% within a short range of error. The basic concept for the working of conventional feedback sensor is explained in Figures 3.2 and 3.3.

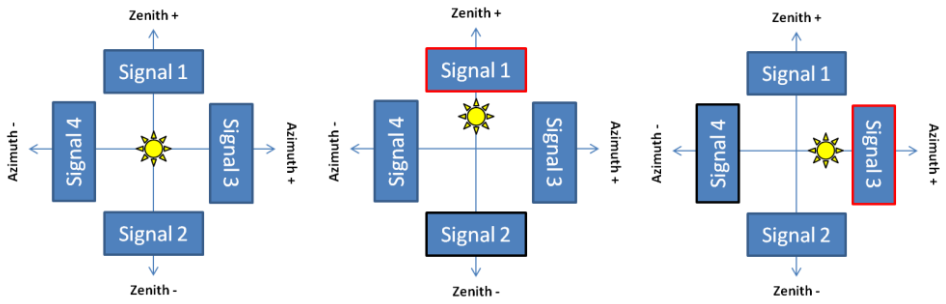


Figure 3.2: Active Tracking Sun Position Sensing Schematic

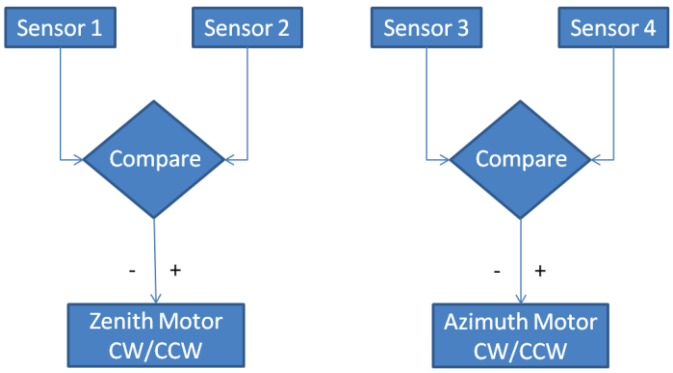


Figure 3.3: Active Tracking Algorithm

The view plane for solar feedback sensor is divided into four quadrants: zenith positive, zenith negative and azimuth positive and azimuth negative. One

photo-sensor is dedicated to each quadrant and by comparing the output of the two respective photo-sensors, the tracking position is determined. In the case of the accurately tracked sun, the output signals from all the sensors are equal. If the sun position is towards positive zenith or positive azimuth then the outputs of 'sensor 1' and 'sensor 3' are higher than the 'sensors 2' and 'sensor 4', and vice versa. Therefore, the tracker is rotated such that the output signals of opposite sensors become equal. In order to sense the solar movement, a rod type component is used to create shadow on photo-sensors if sun is not properly tracked, as shown in Figure 3.4. for this purpose, normally CdS sensors are used as the photo-sensors, for which the electrical resistance varies with change in the light intensity. The main drawback for this design is the poor accuracy and the low sensitivity. Equation (3.12) gives the height of column against the angular offset $\theta_a$ in the position of the sun.

$$CH = \frac{SD}{\tan \theta_a} \qquad (3.12)$$

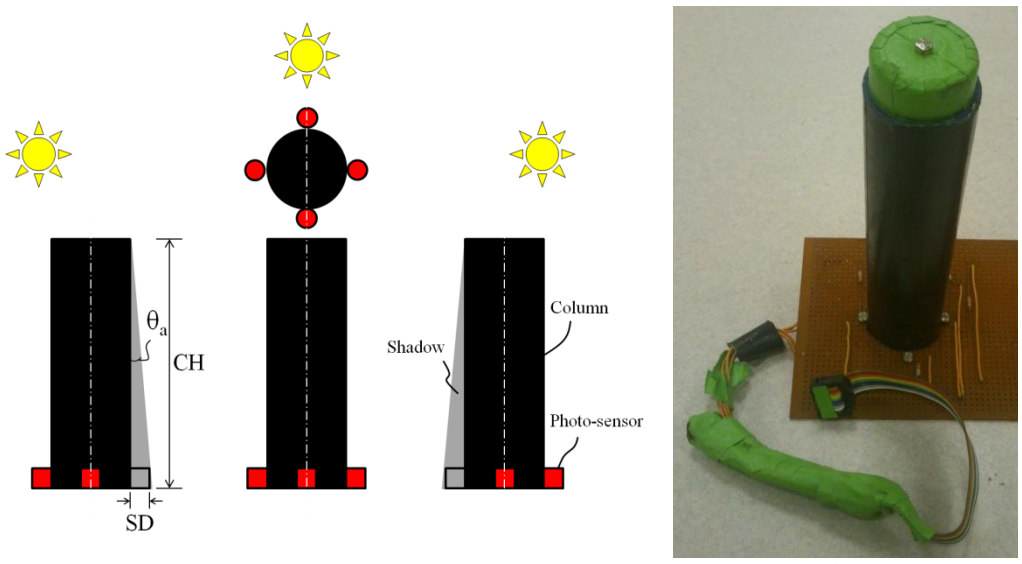


(a) (b)

Figure 3.4: Rod Type Solar Feedback Sensor (a) Design (b) Prototype

For 4 mm as the width of CdS sensors, the effect of angular offset on the height of column for shadow is shown in Figure 3.5. It can be seen that the extraordinary height of column is required for very high accuracy 0.1-0.3$^{o}$, making this design impractical for high accuracy CPV application. In addition, non-uniform and non-linear response of CdS sensors was observed even at the same irradiance level, resulting in inaccurate feedback.

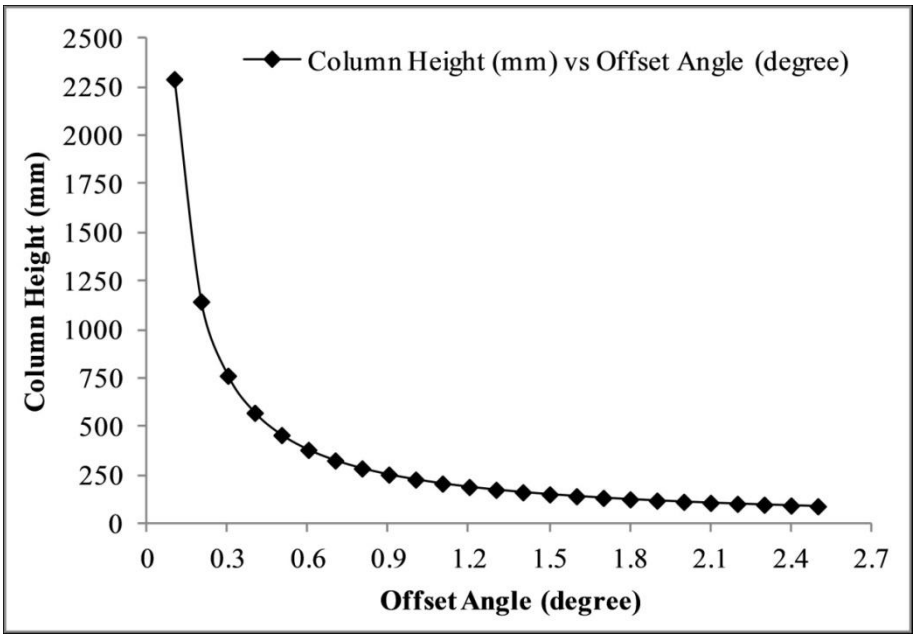


Figure 3.5: The Effect of Angular Offset on the Height of Shadow Column

Due to non-linear and non-uniform response of CdS sensors even at the same irradiance level, another solar feedback sensor was designed using the single convex lens and an array of photo-sensors, as shown in Figure 3.6. The principle of operation is that the sunlight is focused exactly in the centre of array of photo-sensors for perfect tracking and ray parallel to lens axis. However, with the tracking error induced, the solar radiations hitting the convex lens does not remain parallel to axis of lens and as a result the focused sunlight spot deviates linearly from the centre of photo-sensor array. When the tracking error exceeds a certain limit, the focussed sunlight spot hits any of the

photo-sensor, resulting higher output feedback indicating non-accuracy of tracking. In response to the feedback, the tracker is rotated such that to bring the concentrated sunlight spot again in the centre of the photo-sensor array, which indicates that the tracker is again facing towards the sun accurately and the output of all photo-sensors goes low.

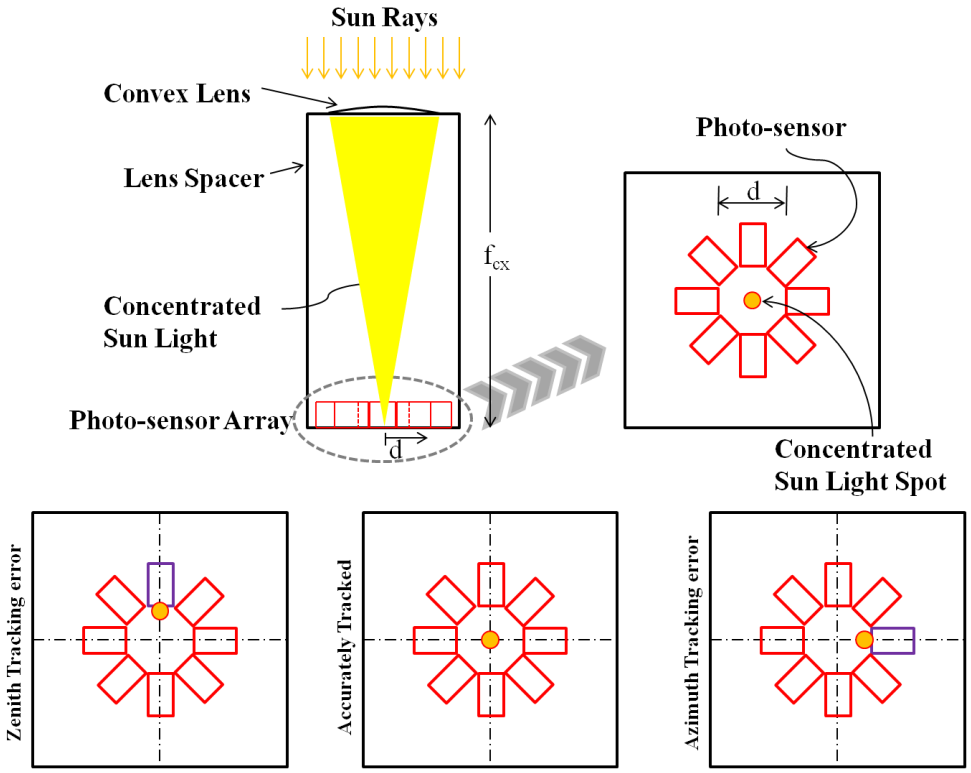


Figure 3.6: Schematic of Single Lens Solar Feedback Sensor

The main advantage of this configuration of feedback sensor is that it eliminates issues related to the non-linear response of the photo-sensor as the intensity of sunlight hitting the photo-sensor is always higher than the maximum range of photo-sensor. The distance 'd' between photo-sensors is adjusted according to the required tracking accuracy. Higher value of 'd' results in lower tracking accuracy and vice versa. However, the most important parameters are the sensitivity and response of solar feedback sensor against the tracking error or angular deviation of incident ray. The sensitivity

of the feedback sensor is defined as the angular deviation of concentrated rays against a very small angular deviation in incident rays or tracking error. The response of the feedback sensor corresponds to linear deviation of concentrated sunlight spot against angular deviation of incident rays. In order to determine the sensitivity and response of single lens solar feedback sensor, the ray tracing simulation of convex lens of diameter 20 mm and focal length of 80 mm was carried out using TracePro software, as shown in Figure 3.7.

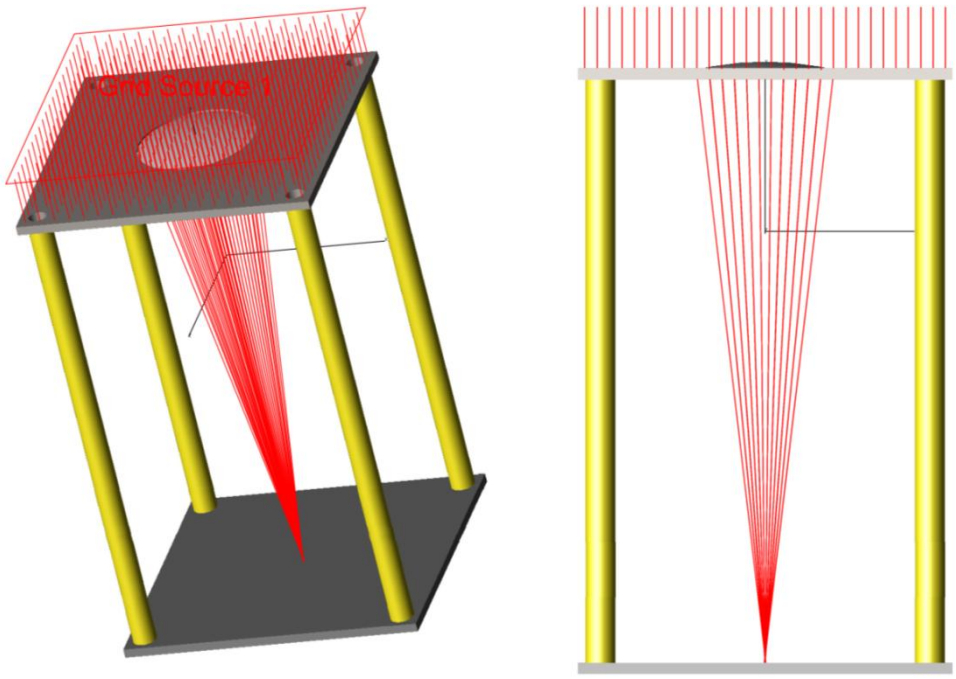


Figure 3.7: Ray Tracing Simulation of Single Lens Solar Feedback Sensor

The variation of angular deviation of concentrated beam against the angular deviation of incident rays for single lens solar feedback sensor is shown in Figure 3.8. It can be seen that the slope of the graph is almost 1, which corresponds to poor sensitivity of the single lens solar feedback sensor. However, Figure 3.9 shows the response of the feedback sensor for different focal lengths against the angular deviation of incident rays. It can be seen that response of feedback sensor is high for higher focal length. It can be seen that

for focal length of 250mm or above, the response of the feedback sensor is considerable for tracking accuracy of $0.1^{o}$ or $0.3^{o}$. As focal length determine the overall height of feedback sensor but larger height is not suitable for practical design. For the same response but with high sensitivity and overall height, the double lens collimating feedback sensor was finally developed, tested and operated for current CPV project.

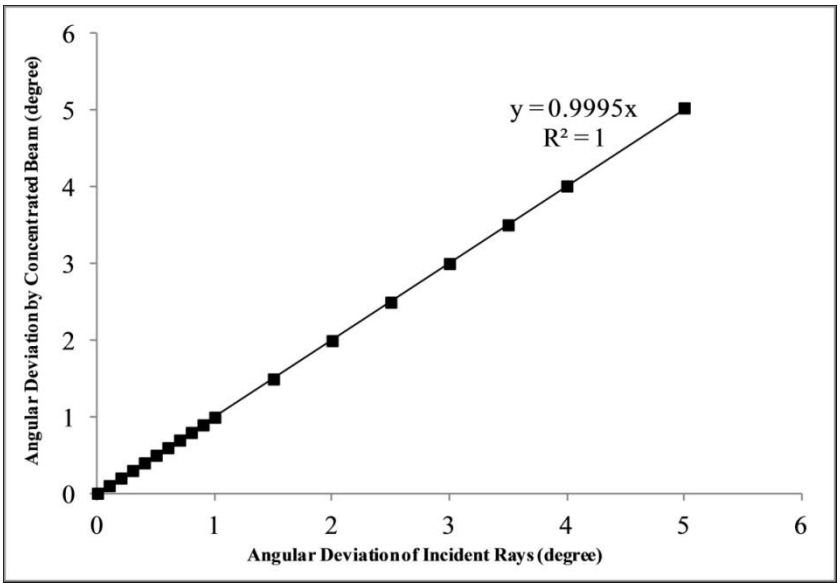


Figure 3.8: The Angular Deviation of Incident Rays through Single Lens Solar Feedback Sensor

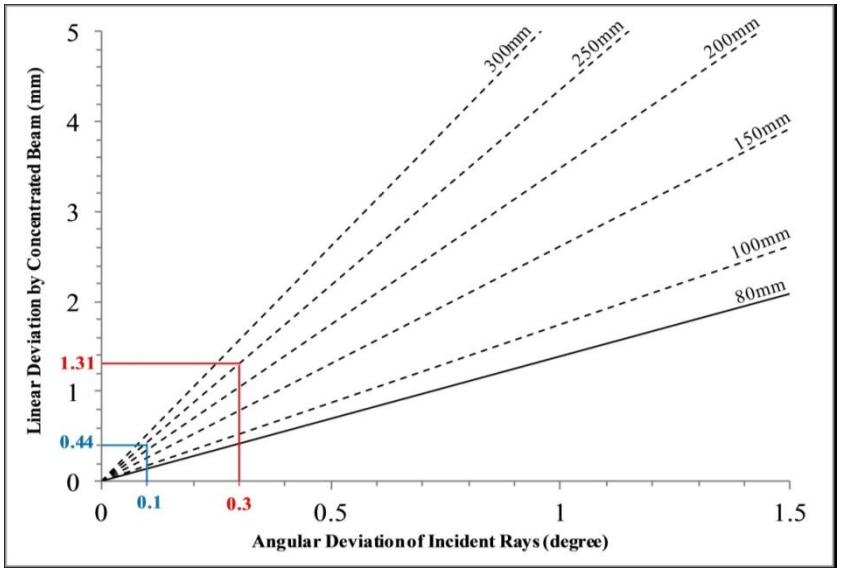


Figure 3.9: The Response of Single Lens Feedback Sensor for Different Focal Length against Angular Deviation Of Incident Rays

### 3.2.3.1 Development of Double Lens Collimating Solar Feedback Sensor

In order to have higher sensitivity and accuracy of optical feedback tracking, a solar feedback sensor was developed based upon double lens collimator design. The operating principle of double lens collimating solar feedback sensor, as shown in Figure 3.10, is same as described for single lens solar feedback sensor. However, the certain arrangement of convex and concave lenses gives collimated concentrated beam. The converging rays from the convex lens become parallel again with the concave lens placed on the way. As far as the collimated beam remains in the middle of photo-sensors array, the sun is considered to be tracked accurately; otherwise it is adjusted accordingly against feedback. If $D_{cx}$ is the diameter of the convex lens with focal length $f_{cx}$ and focal length of concave lens is $f_{cn}$, then Equations (3.13) and (3.14) give the distance between two lenses S and the thickness of the collimated beam $b_t$ after the concave lens, respectively.

$$S = f_{cx} + (-f_{cn}) \qquad (3.13)$$

$$b_t = \frac{D_{cx}}{f_{cx}} \bullet f_{cn} \qquad (3.14)$$

The Equation (3.14) is derived from corresponding right angle triangle, made by converging beam within the lens spacing 'S'. Based upon convex lens of 20mm diameter with 80 mm focal length and concave lens of 12 mm diameter and 12 mm focal length, the current solar feedback sensor was developed. By using Equations (3.13) and (3.14), the distance between lenses and thickness of collimated beam were calculated to be 68 mm and 3mm, respectively.

However, the distance between photo-sensors will be decided according to response of feedback sensor and the required tracking accuracy.

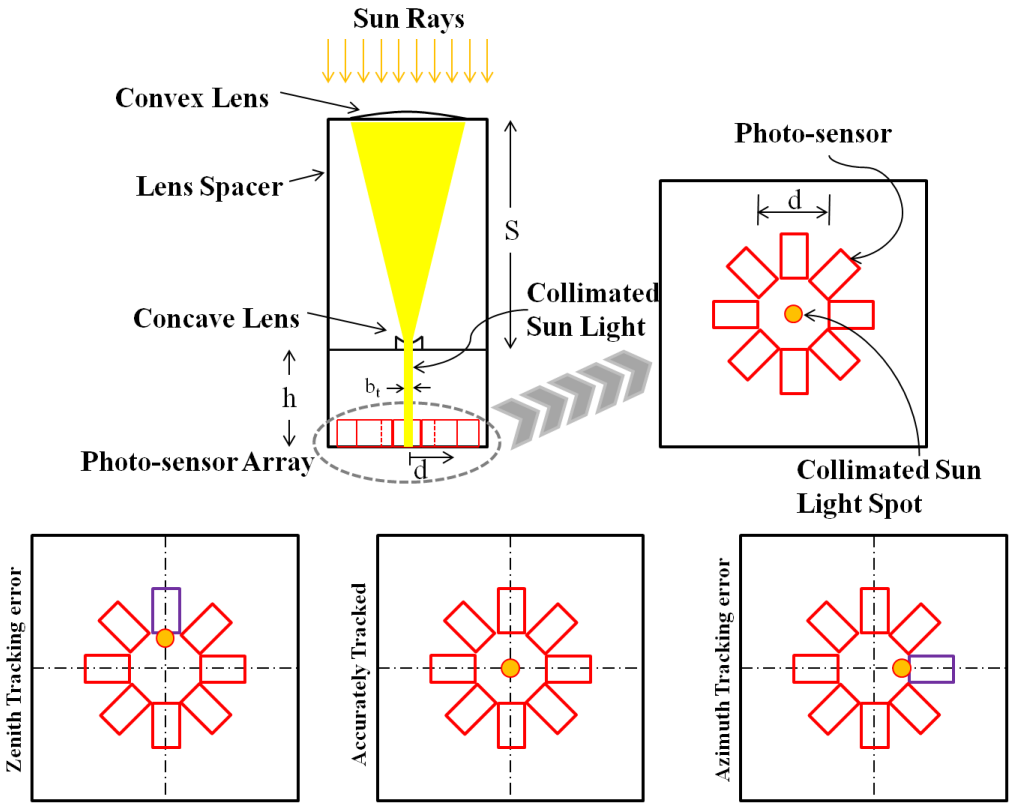


Figure 3.10: Schematic of Double Lens Solar Feedback Sensor

The ray tracing simulation results of double lens solar feedback sensor for above mentioned dimensions and with the parallel ray grid source, are shown in Figure 3.11. A perfect collimated beam of parallel rays can be seen after the concave lens. However, due to chromatic and spherical aberration of the lenses, the thickness of collimated beam from simulation was found to be 3.4mm instead of designed value of 3 mm. Although, convex and concave surfaces of the lens are optimized to minimize this effect, but due to wide range of wavelength in the solar spectrum and the corresponding refractive index variations, these effects cannot be completely eliminated using single convex/concave lens only. That is why, instead of perfect designed point

focus, the focus point becomes slightly bigger which causes the discrepancy in the collimated beam size, than the designed value. However, it does not affect the operation as the displacement in the collimated beam is sensed. For sensitivity and response analysis of developed feedback sensor, the angular and linear deviation of collimated beam are plotted against the angular deviation of incident rays, as shown in Figure 3.12 and 3.13. It can be seen in Figure 3.12 that the proposed double lens has sensitivity of 7.45, which depicts the deviation of 7.45 units in the collimated beam against the one unit deviation of incident rays, which is much higher than the single lens design. Moreover, the response of the feedback sensor was investigated for spacing of 30 mm, 40 mm and 50 mm between photo-sensor array and the concave lens, as shown in Figure 3.13. It can be seen that the linear deviation of collimated beam at $0.3^{o}$ for 30 mm spacing is almost same as 250 mm spacing for single lens feedback sensor design.

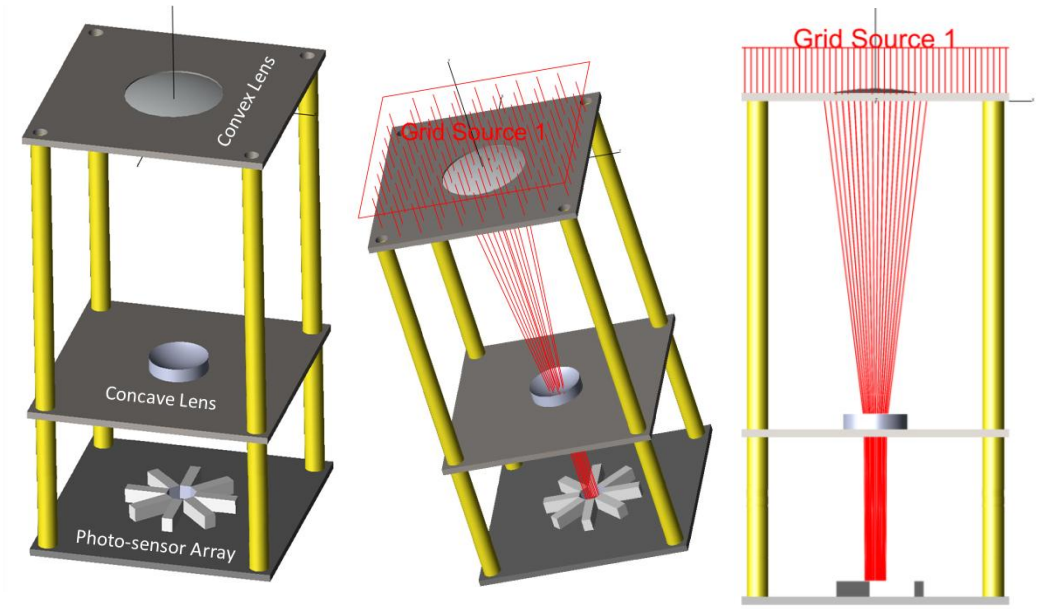


Figure 3.11: The Ray Tracing Simulation Results of Double Lens Feedback Sensor with Parallel Ray Grid Source

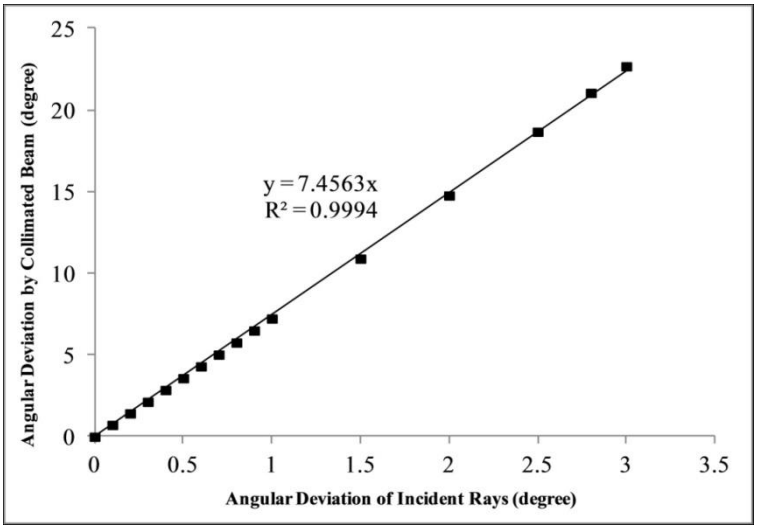


Figure 3.12: The Angular Deviation of Incident Rays through Double Lens Solar Feedback Sensor

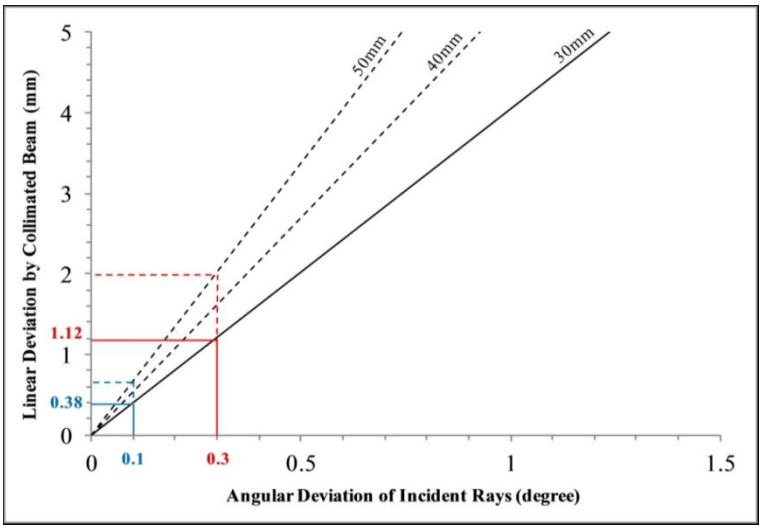


Figure 3.13: The Response of Double Lens Feedback Sensor for Different Lens-Sensor Plate Distance against Angular Deviation of Incident Rays

From Figure 3.13, it can be seen that for angular deviation of $0.3^{o}$, the linear deviation of collimated beam is 1.12 mm. this indicates that in order to design a feedback sensor for tracking accuracy of $0.3^{o}$ and collimated beam thickness of 3.4 mm, the spacing between sensors 'd' should be near to 5.64 mm. For the developed solar feedback sensor, the sensor spacing of 6mm was selected for tracking accuracy slightly higher than $0.3^{o}$. However, for angular deviation higher than $0.3^{o}$, the collimated beam hit the photo-sensor and the tracker position is adjusted accordingly, as shown in Figure 3.14. Thus, with the

proposed double lens collimated design, higher sensitivity with tracking accuracy of $0.1^{o}$ can be achieved.

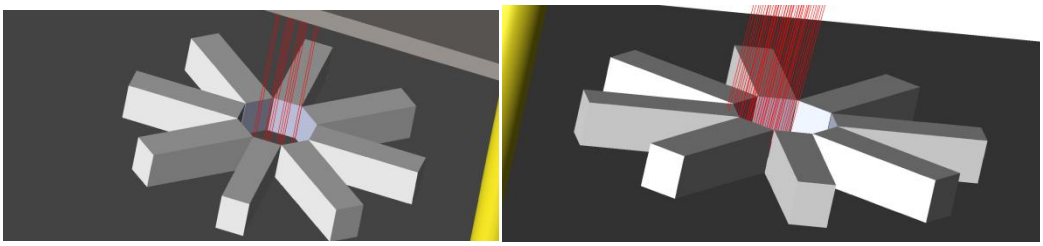

(a) (b)

Figure 3.14: Collimating Beam Position for Tracking Error (a) $0^{o}$ (b) $0.3^{o}$

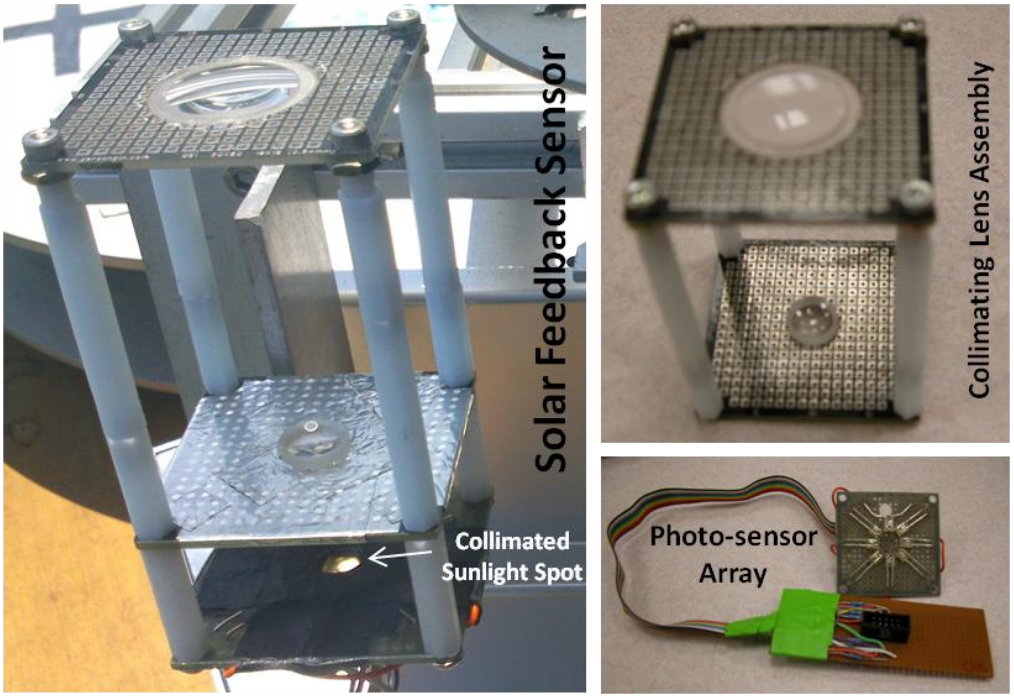


Figure 3.15: Developed Prototype of Double Lens Solar Feedback Sensor

The developed prototype of the double lens collimating solar feedback sensor, designed for $0.3^{o}$ tracking accuracy, is shown in Figure 3.15. A perfect concentrated and collimated bright spot of sunlight can be seen in middle of photo-sensors array. The photo-sensors array is connected to a 10 pin connector for feedback communication with a microcontroller. As the resistance of photo-sensor changes when light hits the sensing part; it is

connected in voltage divider configuration with constant resistor to translate this resistance change into voltage change. The electrical circuit configuration of solar feedback sensor is shown in Figure 3.16. If a constant voltage is applied to series combination of photo-sensor and resistance, then a certain amount of voltage drop occurs across each component. When bright light spot hits the photo-sensor, the voltage drop across it changes. If the voltage drop is above threshold value, then the tracker is adjusted accordingly.

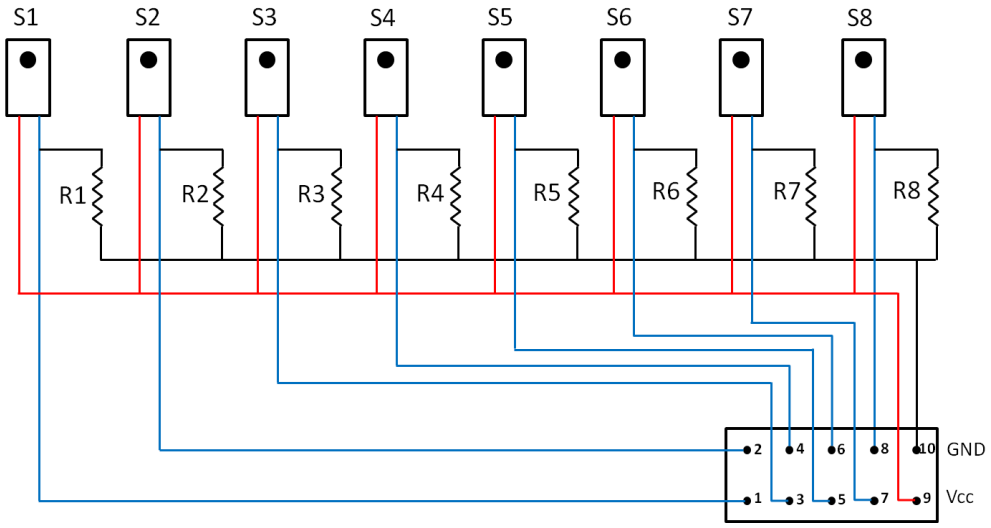


Figure 3.16: Electrical Connection arrangement for Photo-Sensors Array

## 3.3 Development of Tracking System for CPV Field - Master and Slave Configuration

The CPV field consists of many units of CPV systems, whose power output are combined to meet the larger energy requirement. In a CPV field, a separate solar tracker is dedicated for each CPV system unit. In order to provide a cost effective and simple control technique for CPV field, a master and slave configuration is proposed. In a master slave configuration, the master tracker sends the necessary information required for the operation of slave trackers. Each of the tracker in CPV field operates on same tracking algorithm.

However, only the master tracker is equipped with sophisticated and expensive modules and the required tracking data, which after receiving and sorting, is transmitted wirelessly to slave trackers in the field. Therefore, instead of equipping each tracker with the expensive devices, these are replace with a wireless transceiver.

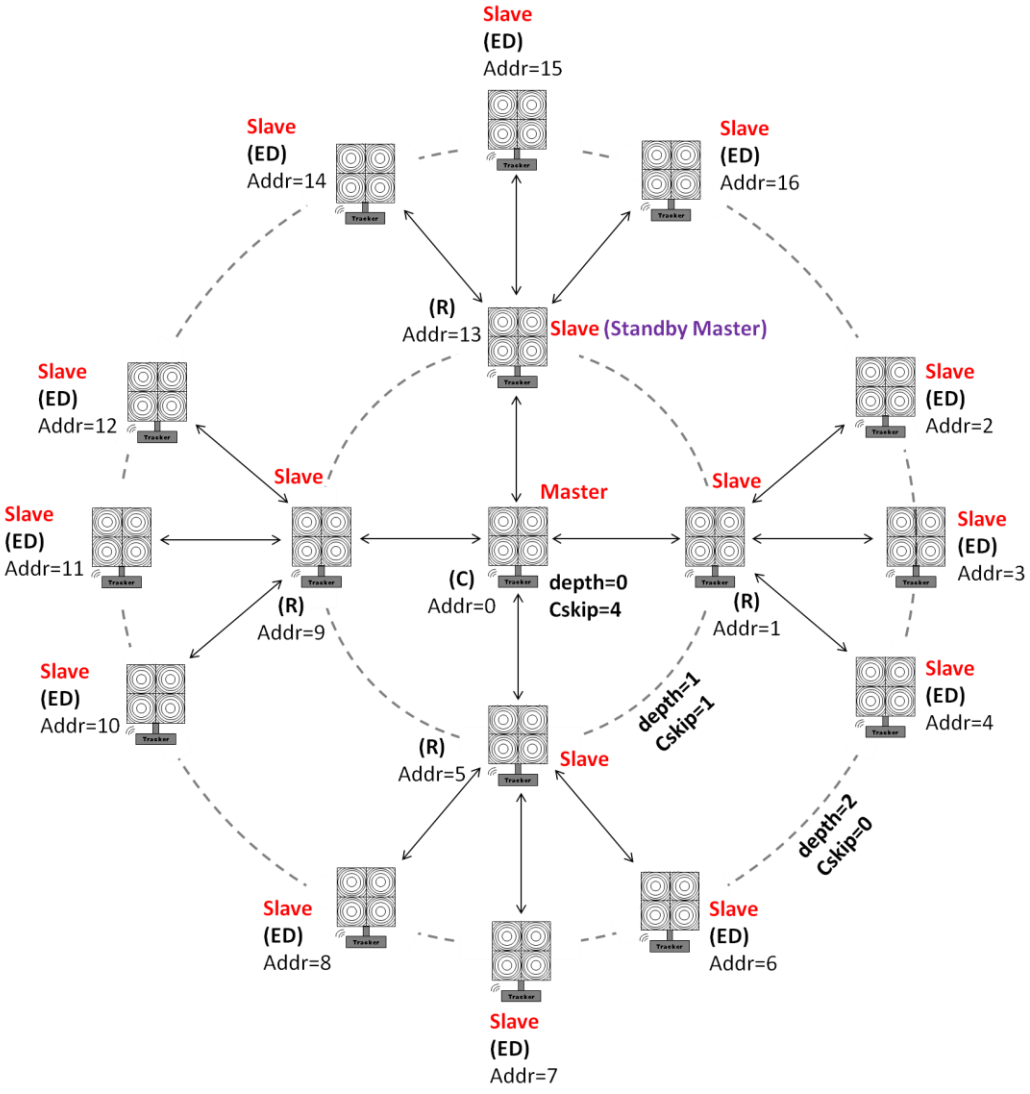


Figure 3.17: Master and Slave Network arrangement using ZigBee

A wireless control technique using ZigBee protocol, is proposed for master slave configuration as ZigBee offers low cost communication technique using radio frequency based upon IEEE 802.15.4 physical radio specification. In

ZigBee communication, the coordinator (C) device, in master tracker, creates the network and rest of the slave ZigBee devices, routers (R) and end devices (ED), join the network. A schematic of master and slave configuration of solar trackers is shown in Figure 3.17. In this ZigBee network, coordinator transmits information to the routers, which transmit it further to end devices. The shown network has maximum depth ($L_m$) of '2' and the maximum number of routing capable children ($R_m$) and non-routing capable children ($C_m$) a parent can have, are '4' and '3' respectively. Equation (3.15a) or (3.15b) **[114]** gives the Cskip factor, which is a factor used to allocate the address to Zigbee in a certain sequence, in each depth or ring. The reference for Cskip value is taken as zero (0) for the outermost ring with maximum depth. Then the rest of the values for Cskip factor are calculated using Equations (3.15a) and (3.15b).

$$Cskip = 1 + C_m\left(L_m - d - 1\right) \qquad if\ R_m = 1, \qquad for, d < L_m \tag{3.15a}$$

$$Cskip = \frac{1 + C_m - R_m - \left(C_m R_m^{\,(L_m - d - 1)}\right)}{1 - R_m}, \quad otherwise, \quad for, d < L_m \tag{3.15b}$$

The address to the devices are given in series from coordinator to end device. However, for multiple routing children, the address of next parent child is the value of Cskip of its parent plus the address of other previous child of same parent. For zero Cskip, all the children act as non-routing children or end devices. For the current CPV system, the master slave configuration is applied to 4 developed trackers with one master tracker and three slave trackers as end nodes, as shown in Figure 3.18.

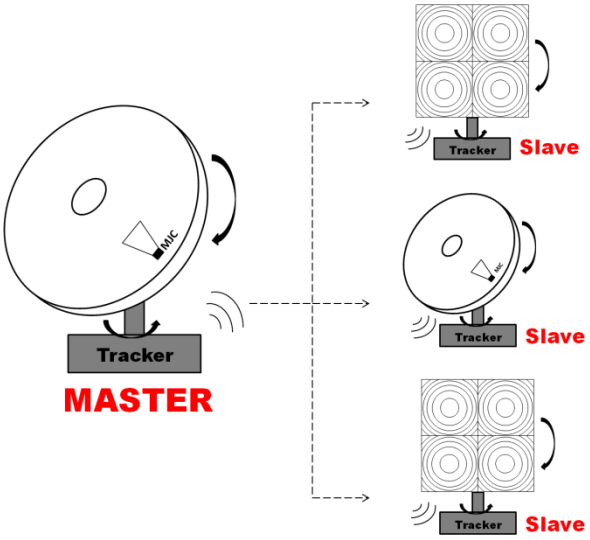


Figure 3.18: Master and Slave arrangement of Developed CPV Field

## 3.4 Solar Tracker Hardware Development

Hardware development of two axis solar tracker is based upon the electrical circuit and mechanical structure with driving assembly. Electronic circuit is responsible for implementation of tracking algorithm and control, while mechanical assembly consists of supporting structure and driving assemblies for rotation of tracker. Further details are given in the following sections.

### 3.4.1 Electrical Circuit Development

The block diagram of electrical circuit or control box for the developed two axis solar tracking system is shown in Figure 3.19. The electrical circuit is divided into three main blocks: power supply, master tracker control box and slave tracker control box. The power supply unit is responsible to supply power to microcontroller and the driving motors. The control box for master tracker contains all the required modules for tracker operation and the device to receive and transmit the required tracking information. The heart of the tracker control box is ATmega2560 microcontroller which executes the

developed tracking code and also acts as link between other electrical components and devices.

In the master tracker, the main information required for astronomical tracking, local location and the current time and date, is obtained through GPS. The GPS module is connected to microcontroller through Universal Synchronous/Asynchronous Receiver/Transmitter (USART) port, which transfers data through serial communication. Information obtained from GPS is also used to initialize Real Time Clock (RTC) module. The RTC module provides information of real time to microcontroller through I2C protocol. The battery backup of RTC keeps clock running in case power supply is switched off. Solar feedback sensor is connected to the microcontroller through ADC (Analogue to Digital Converter) to convert analogue voltage value to corresponding digital value for the microcontroller to understand. In System Programming (ISP) and serial communication are used by microcontroller to communicate with computer using ISP-USB and Serial-USB device. The LCD provides onsite display of tracking parameters to verify tracker operation. The driving stepper motors are controlled by the microcontroller through motor drivers. Motor drivers translate the digital signal of microcontroller to control rotation of motors. The ZigBee module is connected to microcontroller through USART port and transmits the required tracking information of latitude, longitude, date and time or tracking coordinates to control box of slave trackers.

The slave tracker control boxes are equipped with only microcontroller, motor drivers, solar feedback sensor and ZigBee module. The Zigbee eliminates the need of other modules by receiving required tracking from slave tracker.

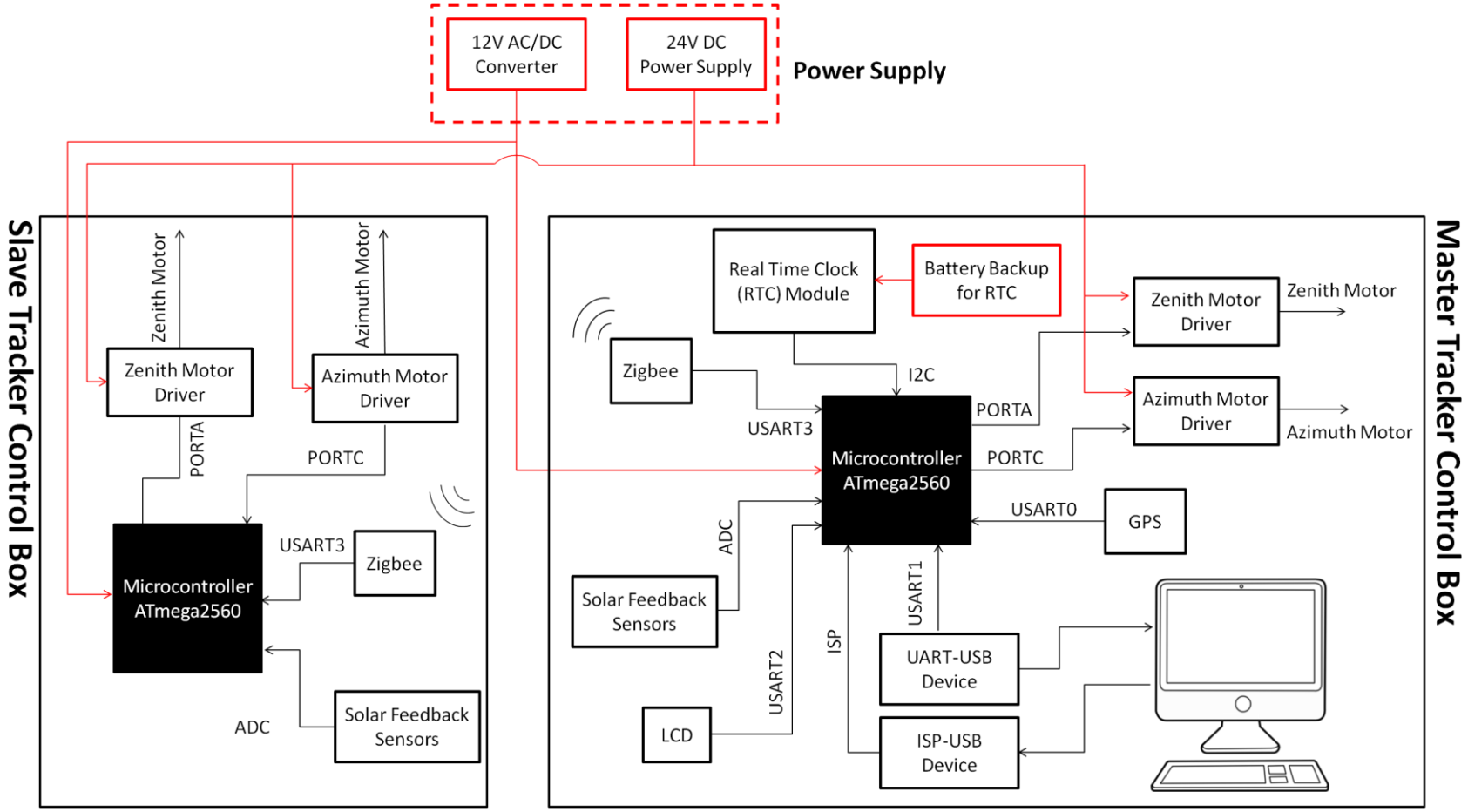


Figure 3.19: Block Diagram of Electrical Circuit of Two Axis Solar Tracking System

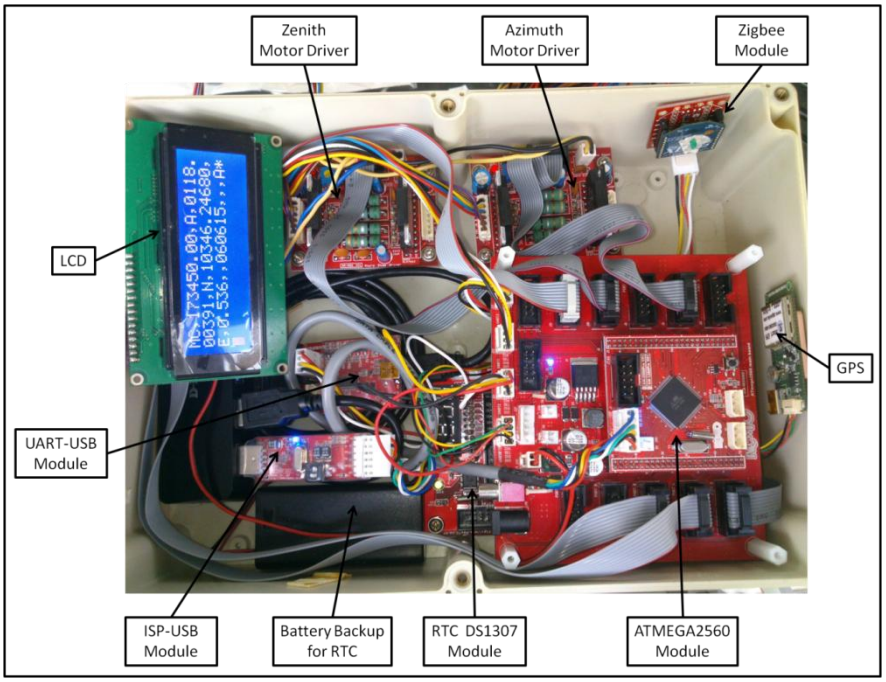


(a)

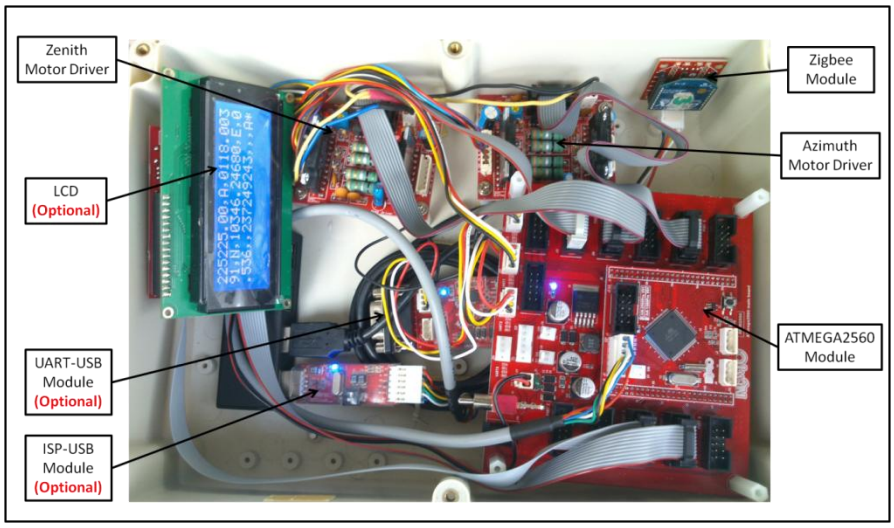


(b)

Figure 3.20: Control Box for (a) Master Tracker (b) Slave Tracker

As a result, a simplified control box does the same tracking job without the need of other electronic modules. The developed control boxes for master and slave trackers are shown in Figure 3.20. Most of the components like LCD, ISP-USB and UART-USB converters are optional and do not require for operation. Only one time use of ISP-USB is required to load the tracking

program in microcontroller. In addition, a small microcontroller like atmega128 can be used for slave trackers. The use of atmega2560 and other optional modules is to have additional feedback regarding system performance, that is developed as a test rig. The developed power supply unit is shown in Figure 3.21, containing 24V DC switching power supply for driving motors and 12V AC/DC converters to power four microcontrollers of each solar tracker.

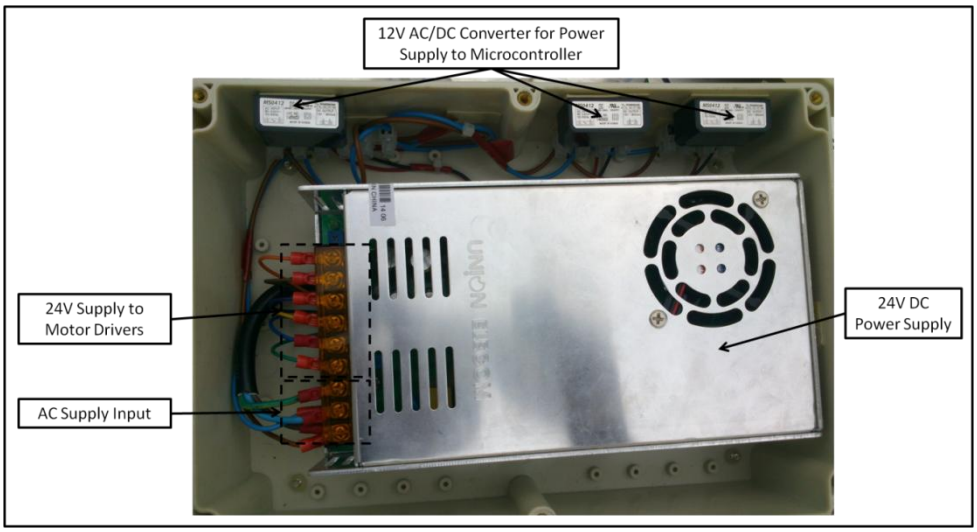


Figure 3.21: The Power Supply Box for Developed CPV System

### 3.4.2 Mechanical Structure and Driving Assembly

The mechanical assembly of solar tracker consists of support structure and driving assemblies. Driving assemblies utilize stepper motor with worm gear and wheel for tracker rotation. The mechanical structure provides rigid support to driving assemblies and provides platform for the installation of CPV modules. Figure 3.22 shows the labelled 3D model of developed two axis solar tracker. The isometric view of tracker is also shown in Figure 3.23. Each of the tracker has two driving assemblies; the lower driving assembly is responsible for azimuth rotation and the upper driving assembly follows zenith

| Sr. No. | Component |
|---|---|
| 1 | CPV Concentrating Assembly |
| 2 | Aluminium Top Mounting Frame |
| 3 | Rotary Shaft |
| 4 | Bearing and Bearing Holder |
| 5 | Shaft Holder |
| 6 | Aluminium Extrusion support for Top Mounting Frame |
| 7 | Stepper Motor (Azimuth) |
| 8 | Bearing Holder |
| 9 | Base Plate |
| 10 | Tracker Base |
| 11 | Thrust Bearing |
| 12 | Worm Wheel (Azimuth) |
| 13 | Bearing and Bearing Holder |
| 14 | Worm Gear |
| 15 | Aluminium extrusions for Tracker Supporting Structure |
| 16 | Stepper Motor (Zenith) |
| 17 | Shaft Coupling |
| 18 | Worm gear |
| 19 | Worm Wheel (Zenith) |

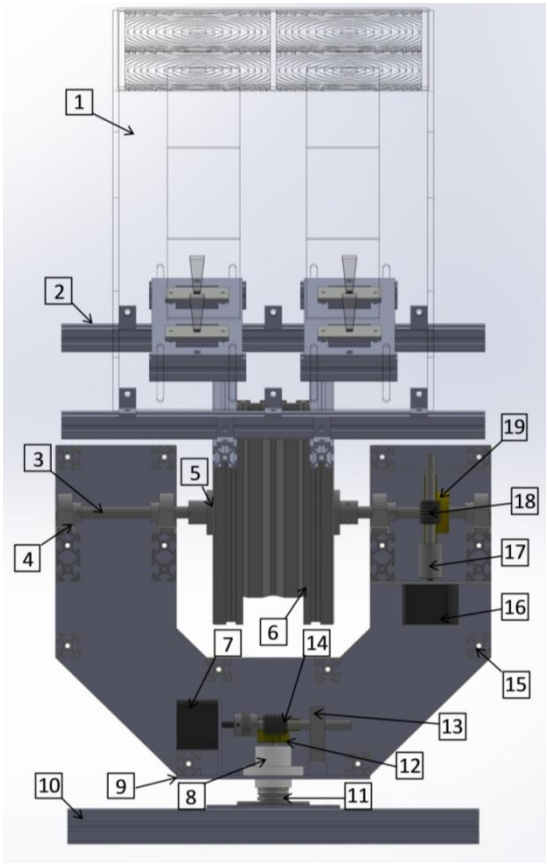


Figure 3.22: Two Axis Solar Tracker Mechanical Components

angle. According to the torque requirements of each of the driving assembly, the gear ratio of 40 and 60 for worm gear and wheel are selected for azimuth and zenith driving assemblies. The higher gear ratio of zenith driving assembly is selected as it has to carry the overall weight of the CPV module. The stepper motor utilized can rotate wit step size of $1.8^{o}$ and the motor drive can further lower this step by maximum 16 times. So, the rotation per step of azimuth and zenith driving assemblies is given by Equations (3.16) and (3.17).

$$Azimuth\ Movement/\ Step = \frac{Motor\ Step}{16 \times Gear\ Ratio} = \frac{1.8}{16 \times 40} = 0.0028125^{o}\ /\ step \quad (3.16)$$

$$Zenith\ Movement/\ Step = \frac{Motor\ Step}{16 \times Gear\ Ratio} = \frac{1.8}{16 \times 60} = 0.001875^{o}\ /\ step \quad (3.17)$$

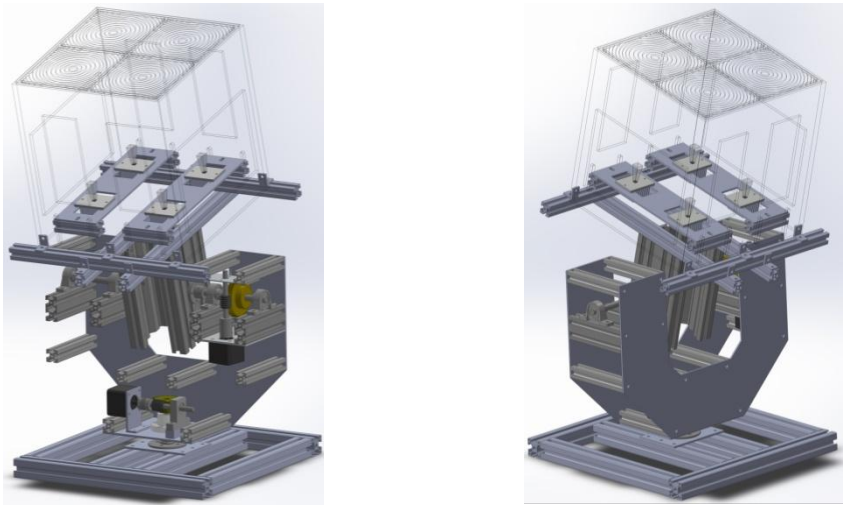

Figure 3.23: Isometric View of Designed Tracker Model

## 3.5 Tracking Algorithm Development

After the development of tracking technique and tracker hardware, the most important part is the development of tracking algorithm, implemented through tracking code. The tracking code was written for AVR microcontroller in C-Programming language and compiled using CodeVisionAVR C Compiler for .hex file. The tracking code is based upon a closed loop hybrid tracking algorithm for which the astronomical technique is executed first, followed by the feedback from the optical method (feedback sensor). The tracking variables associated with hybrid tracking method is shown in Figure 3.24.

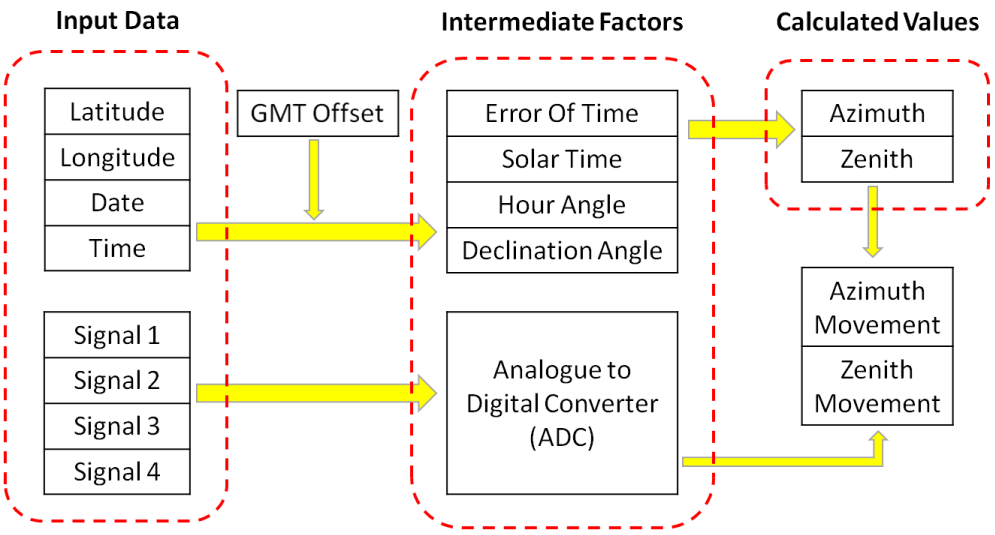


Figure 3.24: Solar Tracking Variables

The input data consists of the GPS and RTC output for astronomical method and the feedback signals from solar feedback sensor. For astronomical tracking, after calculating the intermediate factors, the final azimuth and zenith angles are calculated. However, the feedback signals from photo-sensors are converted to digital values using ADC (Analogue to Digital Converter) feature of microcontroller. So based upon the calculated angles and the feedback signals, the tracker is moved accordingly. For the 10-bit ADC, the conversion formula is given by Equation (3.18), where 1024 is the corresponding digital value for 10-bits ($2^{10}$) and the value 5 represents the reference voltage for which the corresponding digital value is 1024.

$$Digital\,Voltage\,Output = \frac{1024 \times Analogue Voltage input}{5} \qquad (3.18)$$

The tracking algorithm for master and slave trackers are shown in Figures 3.25 and 3.26 respectively, for which the tracking code is developed. The reference planes for tracking algorithm are taken to be the same as the reference planes for astronomical tracking algorithm i.e. tracker must face towards south and

the top mounting frame must be horizontal. For the master tracker, first the GPS data based upon NMEA protocol is received during initialization, as given below:

$GPGGA,020133.440,3723.3040,N,12656.3569,E,1,06,1.2,43.8,M,21.4,M,,0000*6F

$GPGSA,A,3,05,08,10,24,29,21,,,,,,,3.2,1.2,2.9*39

$GPGSV,2,1,06,05,49,079,51,21,30,321,42,08,22,045,35,10,22,093,48*70

$GPGSV,2,2,06,29,21,244,29,24,18,317,43*73

$GPRMC,020133.440,A,3723.3040,N,12656.3569,E,0.000.0,009.7,280410,,,A*61

$GPVTG,009.7,T,M,000.0,N,000.0,K,A*03

The received data is filtered for $GPRMC format and then sorted out to extract latitude, longitude, date and time information. Figure 3.27 shows the breakout of GPS data string in $GPRMC format and its conversion into required information. First column shows the time string, in which first two digits represent hours value, next two digits represent minutes value and the remaining digits represent seconds value. The second and third columns show latitude string and its reference as North, respectively. In latitude string, the first two digits represent the latitude value in degrees (hours) and the remaining digits represent latitude value in minutes, which is needed to be divided by 60 to convert it into degree. The actual converted value of the latitude is given at the bottom of second column. Similar procedure is followed for longitude in fourth and fifth columns. The last column shows the time string, in which the first two digits represent date, the next two digits represent month and the last two digits represent year. The date and time extracted from the GPS data initializes the RTC module.

| $GPRMC,020133.440,A,3723.3040,N,12656.3569,E,0.000.0,009.7,280410,,,A*61 | | | | | | | | | |
|---|---|---|---|---|---|---|---|---|---|
| 020133.440 GMT time | | 3723.3040 Latitude | | N North | 12656.3569 Longitude | | E East | 280410 | |
| 02 | hours | 37 | deg (hours) | Latitude from North | 126 | deg (hours) | Longitude from East | 28 | date |
| 01 | min | 23.304 | min | | 56.3569 | Min | | 04 | month |
| 33.44 | sec | 37+(23.304/60) | deg | | 126+(56.3569/60) | deg | | 10 | year |

Figure 3.27: Breakout of GPS GPRMC Format String

After initialization, using the data received from GPS and RTC, the azimuth and zenith angles are calculated according to solar geometry. The values of calculated angles are then compared with the actual position of the tracker. The actual position of tracker is determined by counting the number of steps of stepper motor or pulse signals released by the microcontroller. The number of pulse signals multiplied with the angular movement per step, gives the actual position of the tracker with respect to reference planes, south for azimuth angle and horizontal plane for zenith angle. The difference between actual position of the tracker and the calculated values of azimuth and zenith angles gives tracking error. If the tracking error is not within the required tracking accuracy limit, $\pm 0.3^{o}$ for current tracking system, it depicts that the sun is not tracked yet and tracker is moved accordingly. The same algorithm is repeated unless the error limit is with required tracking accuracy of $\pm 0.3^{o}$. After completing the astronomical tracking, the feedback signals are obtained from solar feedback sensor via ADC. If any of the photo-sensors gives higher output signal then the tracker is adjusted accordingly to face accurately towards the sun and vice versa. When the sun is accurately tracked, the feedback signals from the solar feedback sensor goes low and the same cycle is repeated continuously.

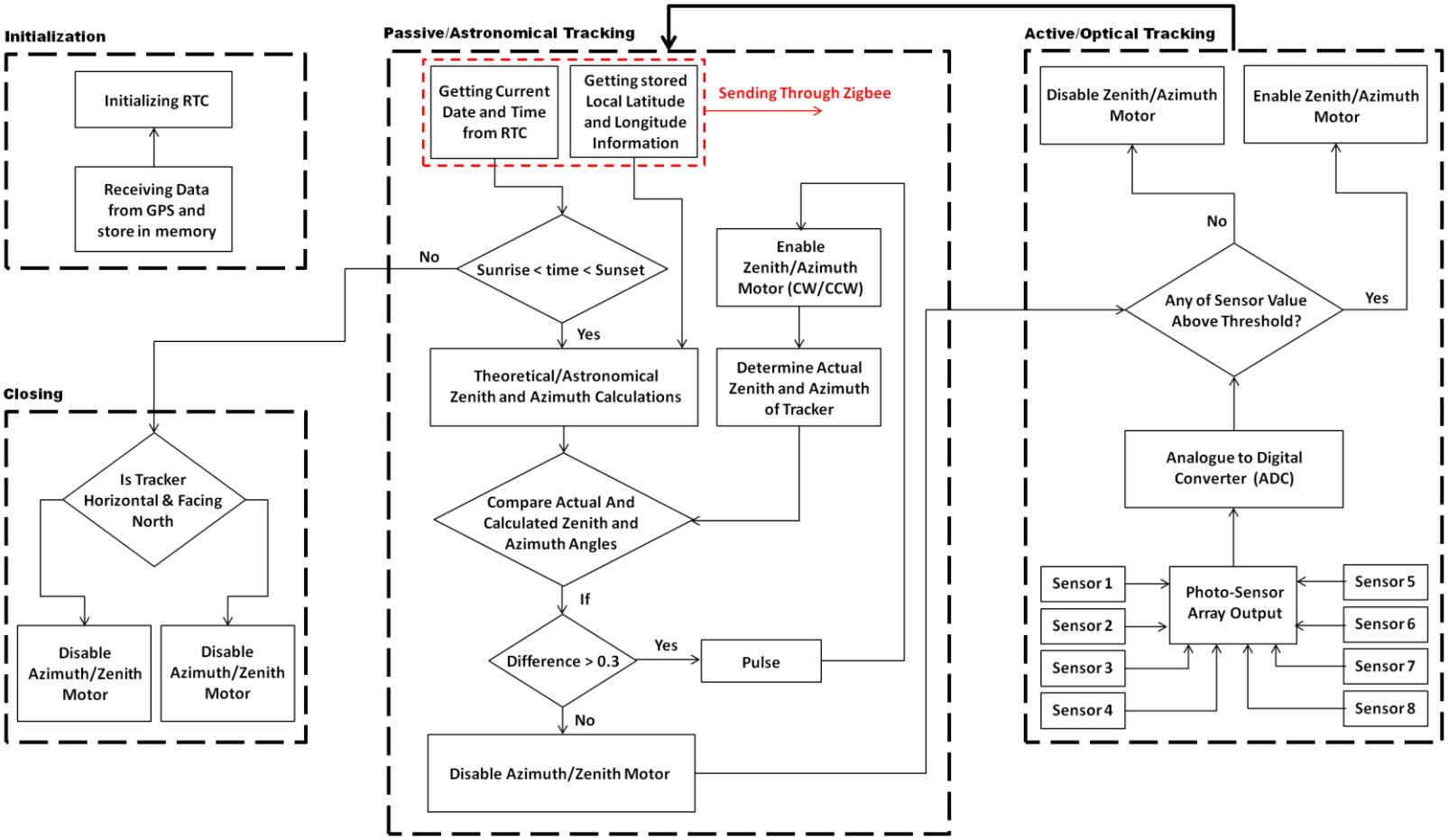


Figure 3.25: Master Tracker Tracking Control Algorithm

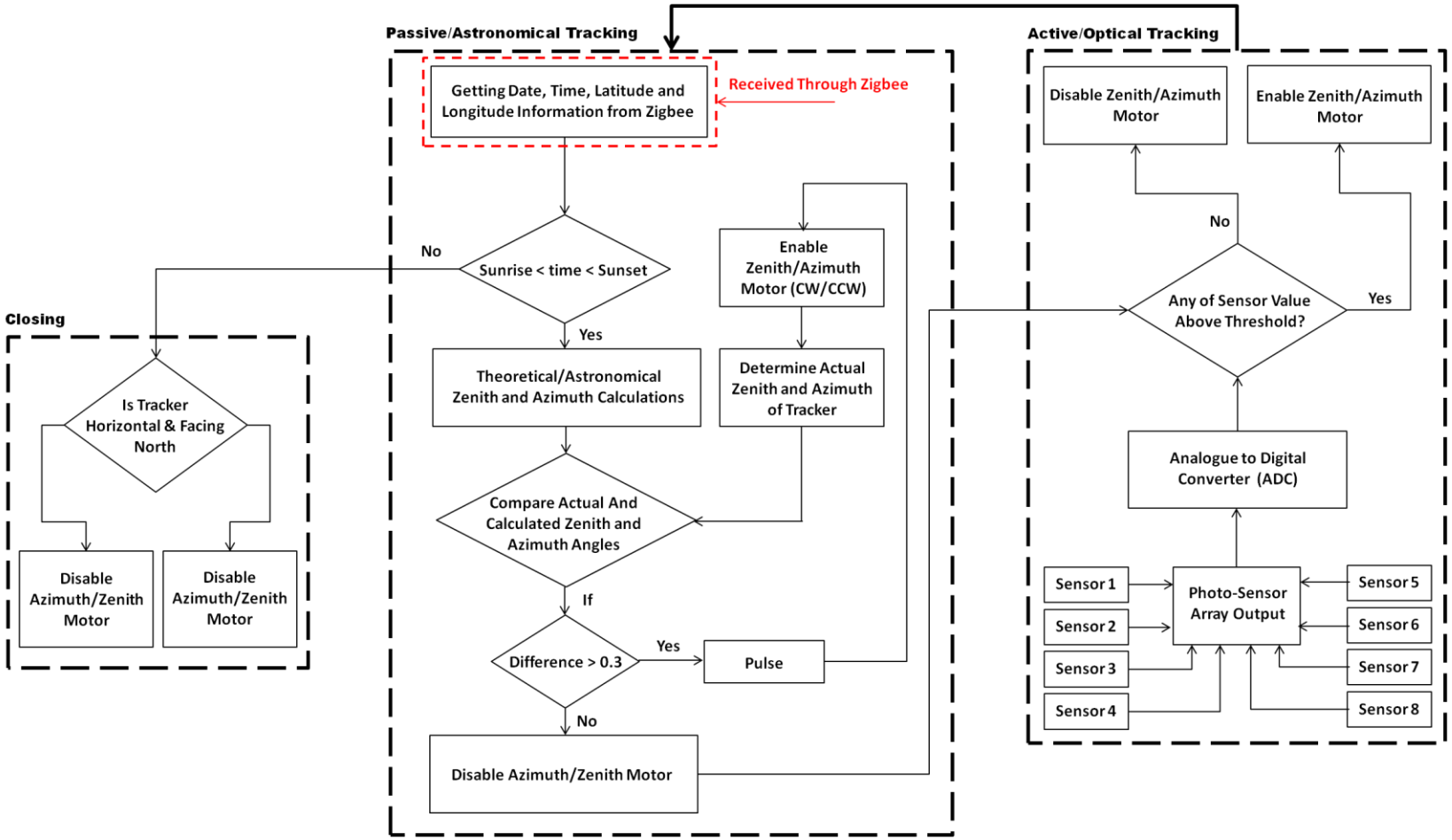


Figure 3.26: Slave Tracker Tracking Control Algorithm

To start and stop the operation of trackers, the sunset and sunrise timings are also calculated continuously. If the sunset timing is reached, the main tracking algorithm is stopped until sunrise and the tracker is rotated to return to its initial reference position. When the sunrise time is reached then the tracker again starts its operation automatically. For master tracker, the latitude, longitude, date and time information is continuously transmitted to slave trackers through ZigBee. The tracking algorithm of slave trackers is similar to the tracking algorithm of master tracker except the initialization, as the tracking information is received from master tracker instead of GPS and RTC.

According to the tracking accuracy, the tracker trajectory during operation is shown in Figure 3.28. In short, the tracking algorithm keeps the tracking error within tracking limit of $\pm 0.3^{o}$. If the tracking goes beyond the limit, it is pulled back within the acceptable range.

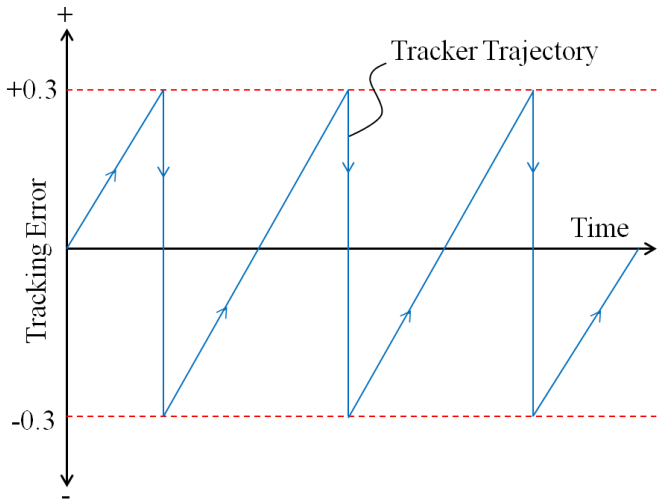


Figure 3.28: Solar Tracker Trajectory During Operation

## 3.6 Tracking Accuracy

In order to verify the accuracy of the developed tracking system, the solar geometry tracking model was compared with the actual solar coordinates first

and then the Colour Tracking Sensor (CTS) camera was utilized to verify the tracking accuracy during operation.

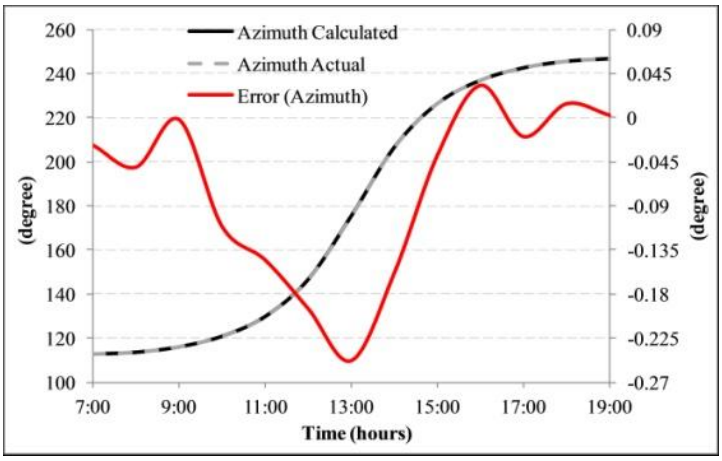


(a)

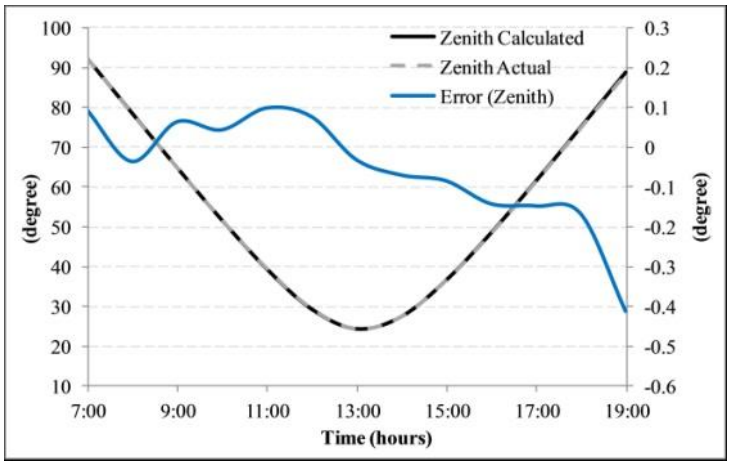


(b)

Figure 3.29: Comparison of Calculated and Actual (a) Azimuth (b) Zenith Angles

The calculated azimuth and zenith angles were compared with the actual values of zenith and azimuth angles obtained from Astronomical Applications Department of the U.S. Naval Observatory for 1st January, 2015 with latitude of 1.299 $^{o}$N and longitude of 103.771 $^{o}$E (for NUS EA-building). The comparison of the tracking coordinates is shown in the Figure 3.29. It can be seen that the lines for calculated and actual azimuth and zenith angles are overlapping. The difference in tracking angles is mostly around 0.1$^{o}$ but not

more than -0.25$^{o}$ and -0.4$^{o}$ for azimuth and zenith angle respectively, just for instance. However, it can be handled through solar feedback sensor.

In order to determine the actual position of the sun and its comparison with the actual tracked position, a colour tracking sensor (CTS) camera was utilized to get solar position using sun images captured during tracker operation. An assembly of CTS camera and BAADER safety film was developed as shown in the Figure 3.30. The CTS camera can detect the position of any colour within its view angle. The BAADER solar safety film was placed in front of the CTS which can block 90-95% of the solar radiations along with the rays from surrounding objects. Therefore, CTS camera only captures the image of sun appearing as the bright spot. Figure 3.31 shows the control software 'CTS Studio' to program the camera and to show the captured image. It can be seen that the captured image contains a bright spot, representing the sun. The solar position through captured image is provided using bright pixel in a 240x180 pixels array. The CTS sensor has a view angle of 90$^{o}$, which shows sensitivity of 0.375$^{o}$/pixel in x-direction and 0.5$^{o}$/pixel in y-direction.

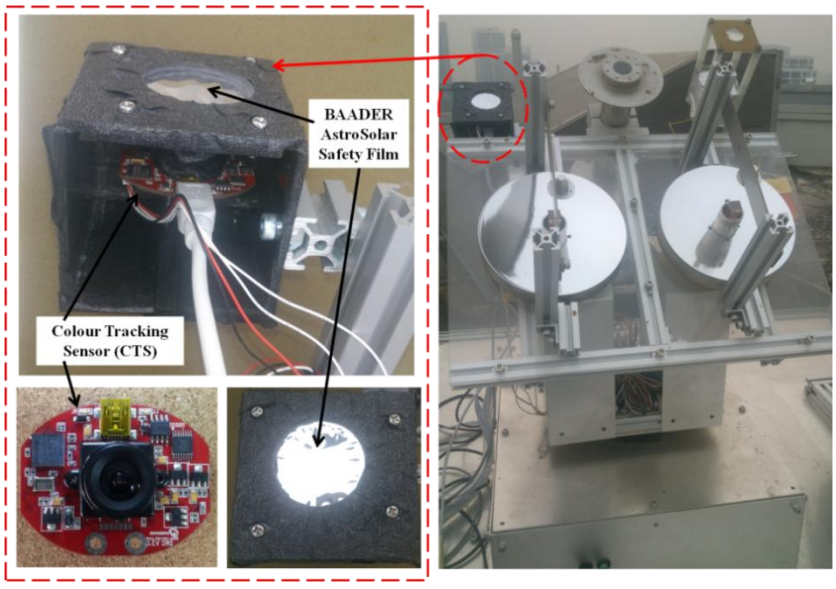


Figure 3.30: Colour Tracking Sensor (CTS) Camera and BAADER Film Assembly to Determine Solar Position

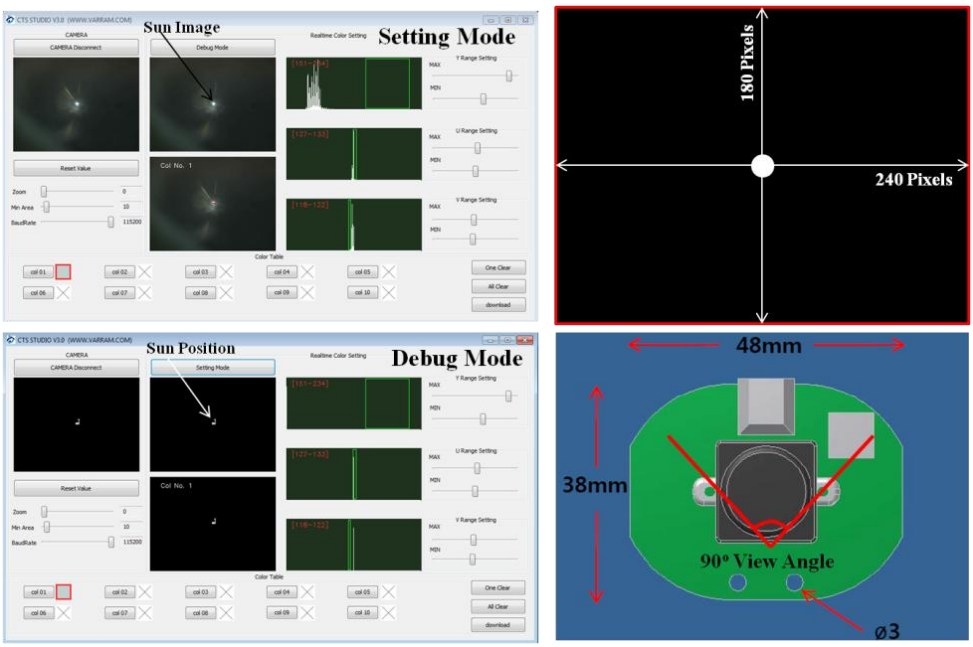


Figure 3.31: CTS Control Software and Determination of Solar Position

The developed CTS sensor was mounted onto developed two axis solar tracker and aligned such that the solar bright spot appear in the centre of the image for perfectly tracked sun, giving coordinates of (120,90) using serial communication through USART port. The CTS sensor is connected to computer using USB connection and through USART port. By taken The coordinates of centre position of sun (120,90) as reference of $0^{o}$ tracking error, the corresponding deviation from reference point is shown in Figure 3.32. It can be seen that the deviation of solar position from reference point is zero during tracker operation except for some point. This does not imply tracking error but rather the limitation of the CTS. with fluctuations during tracking movement but just for instant. It may be due to fluctuations of the sensor during tracker movement, causing confused feedback from CTS. However, most of the time the feedback from CTS shows sun position exactly at zero reference, which verifies the accuracy and stable operation of the developed tracking system.


(a)

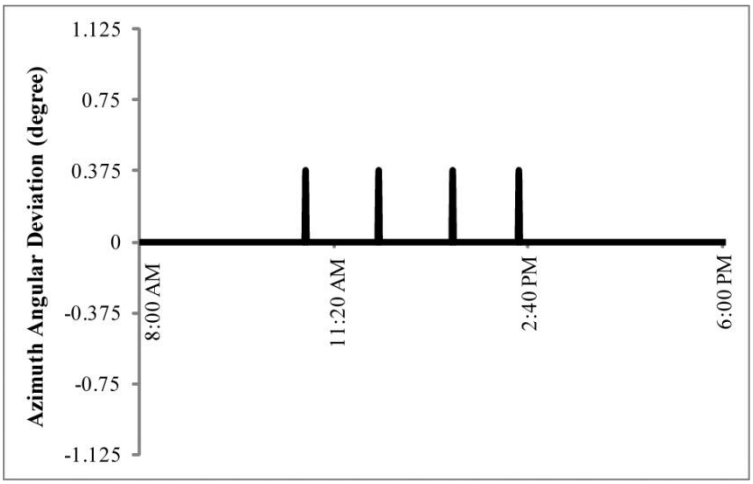


(b)

Figure 3.32: CTS Sensor Measured Angular Deviation for (a) Zenith (b) Azimuth

## 3.7 Summary

In this chapter, the development of an accurate, precise and compact two axis solar tracker with master and slave configuration is proposed and discussed for CPV field operation. The developed tracking system works on a hybrid tracking algorithm with active and passive tracking techniques. The astronomical tracking is based upon the predefined solar geometry. However, for optical tracking, a cheap, accurate and novel solar feedback sensor is

designed, developed and tested with tracking accuracy of up to $0.1^{o}$. For cost effective control of a field of CPV solar trackers, a master and slave technique is proposed, designed and implemented using wireless communication through cheap ZigBee modules. In the proposed master and slave configuration, one tracker acts as master with all required tracking modules and transmits the required tracking information to other slave trackers in the field.

A prototype of the CPV trackers field is developed consisting of four trackers, one master and three slave trackers. The mechanical structure of the trackers is built with aluminium extrusions for rigid and light weight assembly, while the driving assembly is based upon worm gear and worm wheel arrangement. The tracker control box is using microcontroller, GPS, RTC and motor drivers. The driving assemblies have rotation with step size of $0.0028125^{o}$/step for azimuth and $0.001875^{o}$/step for zenith angle. The developed tracker is programmed to operate with tracking accuracy of $0.3^{o}$. In order to verify the accuracy of the tracker, first the solar geometry model was compared with actual solar coordinates obtained from Astronomical Applications Department of the U.S. Naval Observatory. Then the tracker movement was compared with actual solar position recorded using color tracking sensor (CTS).

After the development of tracking system, the design and ray tracing simulation of the concentrating assemblies are discussed in next chapter.

# Chapter 4: Design and Ray Tracing Simulation of Concentrating Assembly for CPV

## 4.1 Introduction

With the development of accurate, precise and compact two-axis solar tracker in the previous chapter, the design and development of CPV concentrating assembly is discussed in this chapter. The design of concentrating assembly is of high importance in the development of concentrated photovoltaic (CPV) system. The concentrating assembly guides and concentrates solar radiations effectively onto small area of multi-junction solar cell (MJC) with uniform ray distribution at minimal loss. The main parameter to evaluate the performance of concentrating assembly is its response to tracking error i.e. minimal ray loss for response of large tracking error. This response against tracking error defines the tracking accuracy requirement; better response can accept low tracking accuracy with less energy consumption by tracker.

The CPV concentrating assembly comprises concentrators as primary optics and a homogeniser as secondary or tertiary optics. Solar concentrators can be of either reflective type reflectors or refractive type lenses. However, each concentrator design has its own significance and limitations. Similarly, homogeniser design can also be reflective and refractive, depending upon the need. In this chapter, different types of the CPV concentrating assemblies are designed and evaluated through ray tracing simulation using TracePro software. For the primary concentrator, parabolic dish and Fresnel lens are considered for current design and analysis. Moreover, for the homogeniser,

dielectric filled compound parabolic concentrator (CPC), tailored glass rod and small conical aluminium reflector are used as homogeniser. In the beginning of this chapter, the design and experimental results of CPV system consisting of mini parabolic dish and CPC is discussed. However, after determining the high optical loss associated with mini dish-CPC concentrating assembly design, it was not considered for further evaluation and performance comparison. The other three different designs were further considered for analysis and comparison.

## 4.2 Mini Dish-CPC Concentrating Assembly

The initial design considered for CPV concentrating assembly was based upon mini parabolic dish as primary reflector and a dielectric filled compound parabolic concentrator (CPC) as homogeniser. A simple schematic of the Mini Dish-CPC concentrating assembly is shown in Figure 4.1. The solar radiations received by the parabolic primary reflector are concentrated at its focal length '$f_{pr}$' where CPC homogeniser is placed. After entering through the CPC homogeniser inlet, solar radiations are directed to a multi-junction solar cell (MJC) placed at outlet of CPC homogeniser, through total internal reflection (TIR). The multi-junction solar cell is attached to a heat sink for heat dissipation, to keep cell temperature within the optimal operational range. Edge rays make rim angle $\theta_r$ at homogeniser inlet. The rim angle is critical for design of concentrating assembly and homogeniser as higher rim angle reduces the overall height of concentrating assembly. However, half of rim angle should always be less than the critical angle of homogeniser glass

material, otherwise the solar radiations will be reflected back from the homogeniser inlet.

It is known that the solar radiation incident on the earth's surface is not exactly parallel to concentrator axis due to solar subtended angle of $0.53^{o}$. It depicts that perfect point focussed concentration of sun light cannot be achieved but instead, the concentration over a small area is achieved. In addition, due to movement of the two-axis solar tracker in steps, the rays hitting the primary reflector cannot be always parallel to axis of concentrating assembly. This causes the focus point of concentrated solar radiation to deviate from the centre of the homogeniser and this deviation depends upon the degree of deviation of incident rays from concentrator axis.

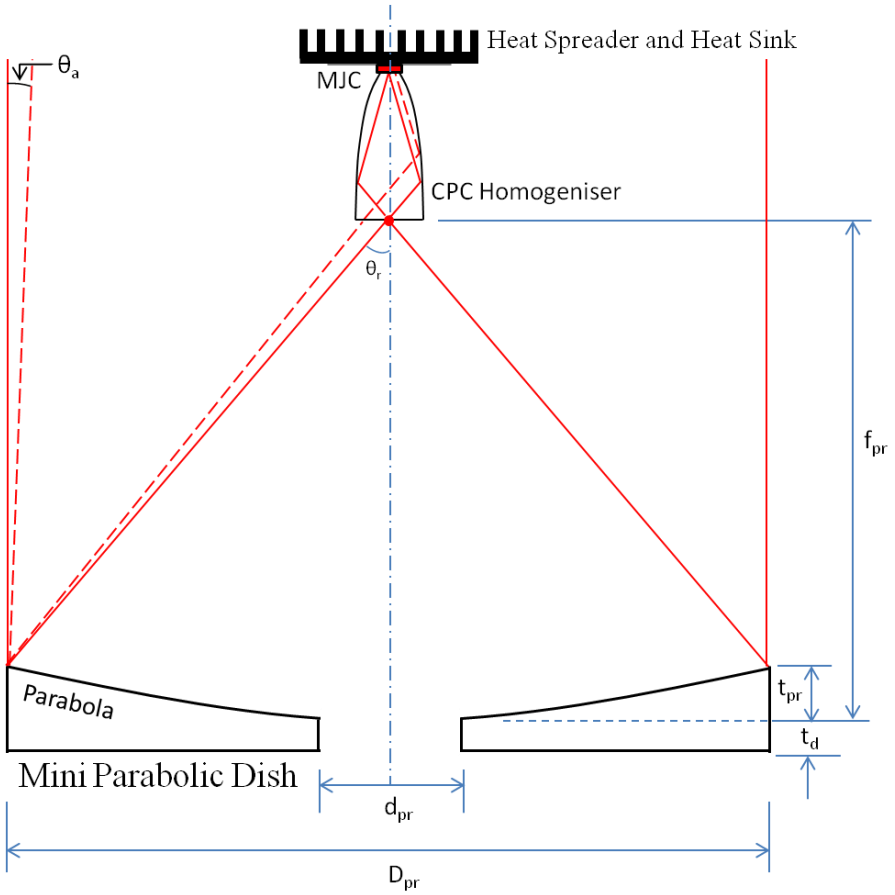


Figure 4.1: Schematic of Mini Dish-CPC Concentrating Assembly

One important parameter in designing the concentrating assembly is the acceptance angle, defined as the maximum angular deviation of the incident rays that can be accepted with minimum losses. The concentrator and homogeniser are designed such that as long as the concentrated rays are falling onto the homogeniser inlet, they are directed towards the MJC. The size of the primary concentrator $D_{pr}$ is selected according to the concentration ratio desired at the solar cell area. The centre hole of dimension $d_{pr}$ is for mounting purpose. The geometric concentration ratio, defined as the ratio of primary concentrator net area to solar cell area, is given by the Equation (4.1).

$$CR_g = \frac{A_{con}}{A_C} \qquad (4.1)$$

Where $A_{con}$ is the net effective area of primary concentrator and $A_C$ is the area of solar cell. For current research work, multi-junction solar cell from Arima Photovoltaic & Co. is used with a cell size of 5.5 mm x 5.5 mm and operating solar concentration of x500. According to the MJC size and centre hole of $d_{pr}$=2.5 cm, the diameter of primary reflector was selected as 15cm with thickness of $t_d$=1cm and concentration ratio of x566. However, the actual concentration at MJC will be less than x500 due to optical losses caused by reflectance and absorbance loss of concentrating assembly. The next section discusses the design of primary parabolic concentrator.

### 4.2.1 Mini Parabolic Dish Design

The profile of the mini parabolic dish is based upon the simple equation of parabola, given by Equation (4.2).

$$y = \frac{x^2}{4 f_{pr}} \qquad (4.2)$$

where x and y represent the coordinates of parabolic profile. The maximum value of x is half of diameter of mini dish (i.e. 15/2 cm) and the value of y value is the depth of parabola, given by the Equation (4.2) for certain focal length. For current study, focal length of 9.75 cm was considered for mini dish. The coordinates of 15cm mini parabolic dish are given in Figure 4.2.

| X (cm) | Y (cm) | X (cm) | Y (cm) |
|---|---|---|---|
| **0** | 0 | **0** | 0 |
| **0.5** | 0.00641 | **-0.5** | 0.00641 |
| **1** | 0.025641 | **-1** | 0.025641 |
| **1.5** | 0.057692 | **-1.5** | 0.057692 |
| **2** | 0.102564 | **-2** | 0.102564 |
| **2.5** | 0.160256 | **-2.5** | 0.160256 |
| **3** | 0.230769 | **-3** | 0.230769 |
| **3.5** | 0.314103 | **-3.5** | 0.314103 |
| **4** | 0.410256 | **-4** | 0.410256 |
| **4.5** | 0.519231 | **-4.5** | 0.519231 |
| **5** | 0.641026 | **-5** | 0.641026 |
| **5.5** | 0.775641 | **-5.5** | 0.775641 |
| **6** | 0.923077 | **-6** | 0.923077 |
| **6.5** | 1.083333 | **-6.5** | 1.083333 |
| **7** | 1.25641 | **-7** | 1.25641 |
| **7.5** | 1.442308 | **-7.5** | 1.442308 |

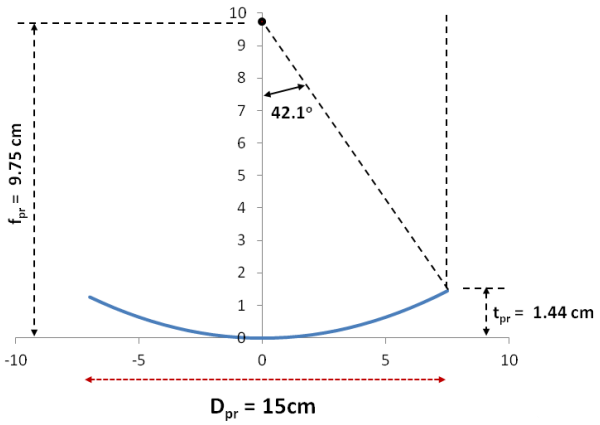


Figure 4.2: Mini Dish Parabolic Concentrator Coordinates

The mini dish offers a rim angle of 42.1°, which is calculated using Equation (4.3) with depth of parabolic profile at $t_{pr}$ = 1.44 cm.

$$Rim\ Angle, \theta_r = \tan^{-1}\left(\frac{D_{pr}/2}{f_{pr}-t_{pr}}\right) = \tan^{-1}\left(\frac{15/2}{9.75-1.44}\right) = 42.1^{o} \qquad (4.3)$$

### 4.2.2 Dielectric Filled Compound Parabolic Concentrator (CPC) Design

The design of compound parabolic concentrator (CPC) **[115]** is based upon combination of two parabolic surfaces. In order to show the characteristics of compound parabolic concentrator, there is a need to express the equation of parabola in polar coordinates Equation (4.4), shown in Figure 4.3.

$$q = \frac{2f_{pr}}{1-\cos\varphi} = \frac{f_{pr}}{\sin^2\frac{\varphi}{2}} \qquad (4.4)$$

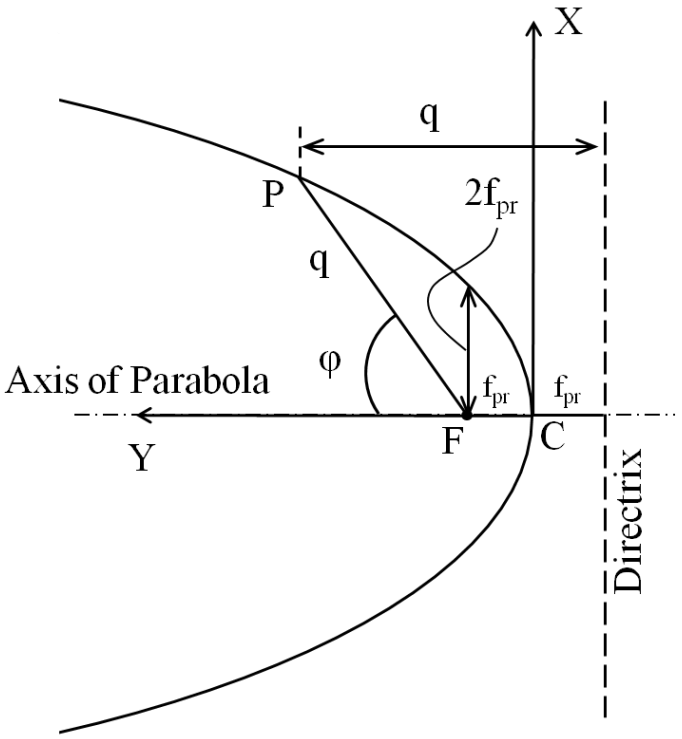


Figure 4.3: Representation of Polar Coordinates of Parabola

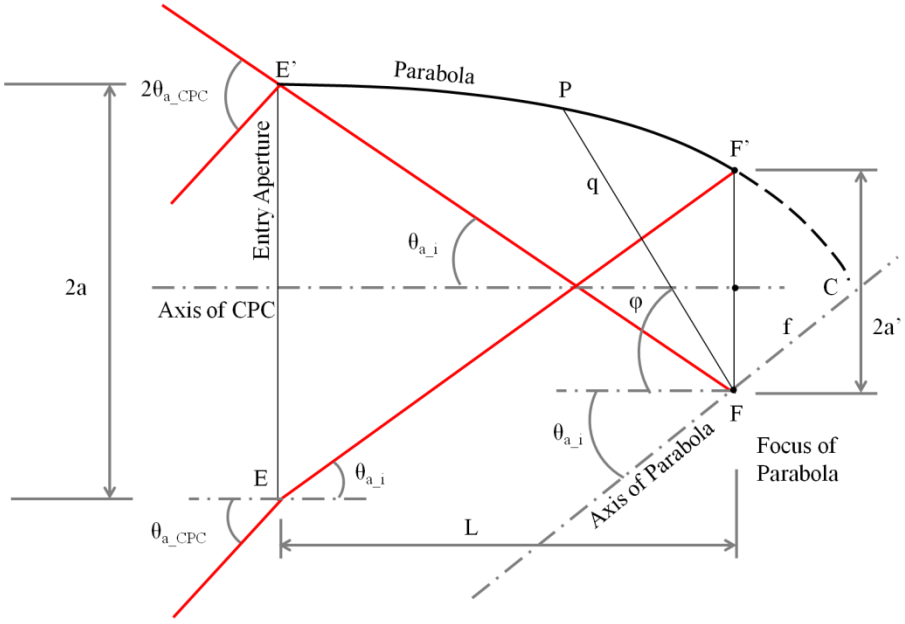


Figure 4.4: Design Schematic of Dielectric Filled Compound Parabolic Concentrator (CPC)

The CPC design is based upon the size of inlet aperture EE' and exit aperture FF', Figure 4.4, whose ratio gives the concentration ratio of CPC. The acceptance angle $\theta_{a\_CPC}$ of CPC, defined as the maximum angle of incident ray

with the axis of CPC which allows the incident ray to hit the exit aperture, is the other parameter describing the design of CPC. However, for the current CPV application, the CPC is used as a glass homogeniser. Due to refraction, the ray entering into the CPC material with maximum angle of $\theta_{a\_CPC}$, bends towards the CPC axis by making angle $\theta_{a\_i}$. Using Snell's law, the angle $\theta_{a\_i}$ can be calculated for acceptance angle $\theta_{a\_CPC}$ through Equation (4.5).

$$\theta_{a\_i} = \sin^{-1}\left(\frac{\sin\theta_{a\_CPC}}{n_{CPC}}\right) \qquad (4.5)$$

Where $n_{CPC}$ is the refractive index of material of CPC at certain design wavelength. Figure 4.4 shows the design of compound parabolic concentrator (CPC). The CPC profile between points E' and F' is a parabola with focus point at F and centre of aperture at point C. The relation between entry and exit aperture is given by Equation (4.6).

$$a + a' = FE'\sin\theta_{a\_i} = a'\frac{(1+\sin\theta_{a\_i})}{\sin\theta_{a\_i}} \qquad (4.6)$$

By simplification,

$$a = \frac{a'}{\sin\theta_{a\_i}} \qquad (4.7)$$

For certain acceptance angle, by fixing the inlet or outlet aperture size, the other dimension can be calculated using Equation (4.7). The overall length of CPC is given by the Equation (4.8).

$$L = FE'\cos\theta_{a\_i} = a'\frac{(1+\sin\theta_{a\_i})}{\tan\theta_{a\_i}\bullet\sin\theta_{a\_i}} = \frac{a+a'}{\tan\theta_{a\_i}} \qquad (4.8)$$

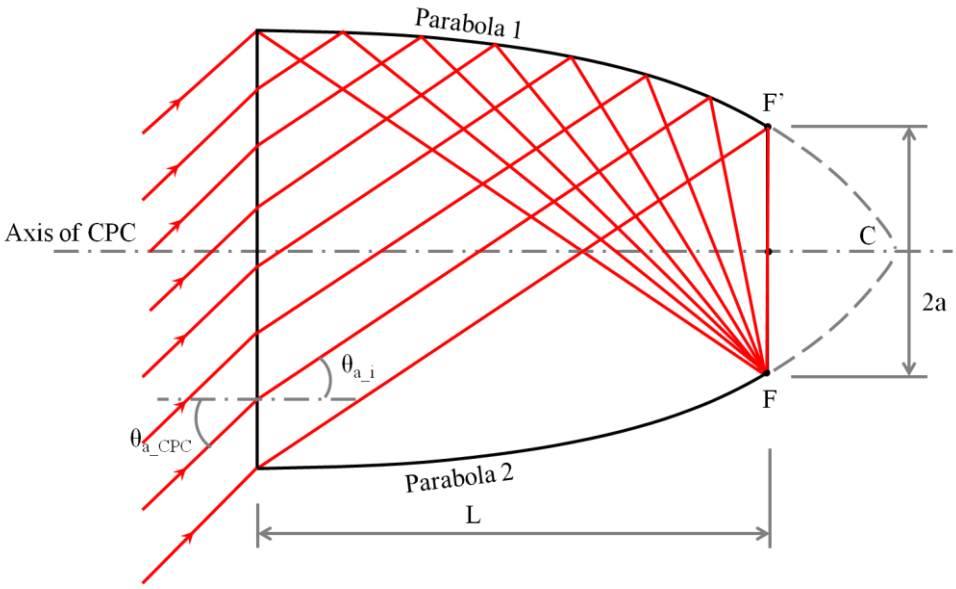


Figure 4.5: Ray Propagation in Dielectric Filled Compound Parabolic Concentrator (CPC)

The schematic of CPC with rays propagation and their interaction with the optical surfaces is shown in Figure 4.5. For parabolic surface 1, the focal point is point F and for parabolic surface 2, point F' which are the two extreme points of exit aperture. So all the edge rays with incident angle of $\theta_{a\_CPC}$, make their way to focal point F, in the case of parabolic surface 1. Similarly, incident rays with angle less than $\theta_{a\_CPC}$, concentrate at different point on exit aperture that causes the light to be uniformly distributed over exit aperture.

In the mini dish-CPC design, the acceptance angle of CPC does not define the acceptance angle of concentrating assembly. However, it define the maximum rim angle of primary concentrator from which it can accept rays. For current study, commercial CPC from Edmund Optics, with acceptance angle of $25^{o}$ and exit aperture size of 2.5 mm was used. The experimental investigation of CPV system based upon mini dish-CPC concentrating assembly is discussed in the next section.

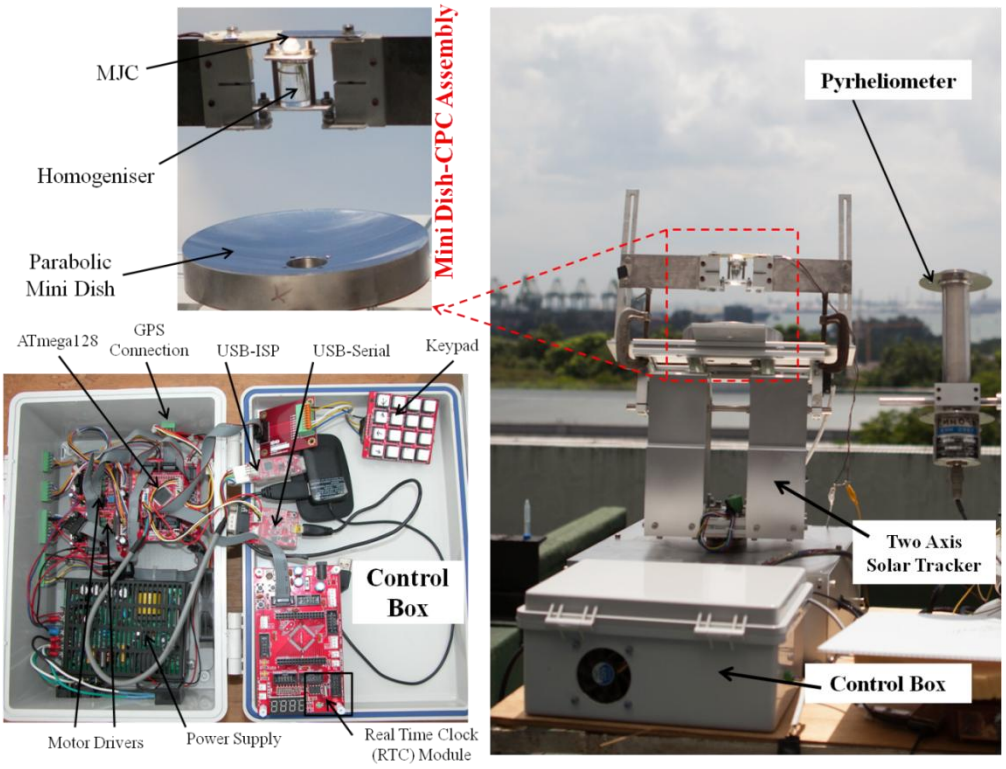


Figure 4.6: Experimental Setup of Mini Dish-CPC CPV System

### 4.2.3 Experimental Performance Investigation of CPV System with Mini Dish-CPC Concentrating Assembly

The experimental setup for CPV system based upon mini dish-CPC concentrating assembly is shown in Figure 4.6. The CPV assembly is mounted onto an aluminium frame of a two axis solar tracker. The Pyrheliometer is used to measure the direct normal irradiance (DNI) received in $W/m^2$, as input to the CPV system. A bright spot of concentrated solar radiations can be seen at cell area. In order to investigate the performance of the CPV system, the performance parameters in form of cell current and voltage at maximum power point were recorded for whole day operation, at an interval of one second. With effective area of mini dish-CPC assembly as 0.007999935 $m^2$, its performance characteristic curves are shown in Figures 4.7 and 4.8.

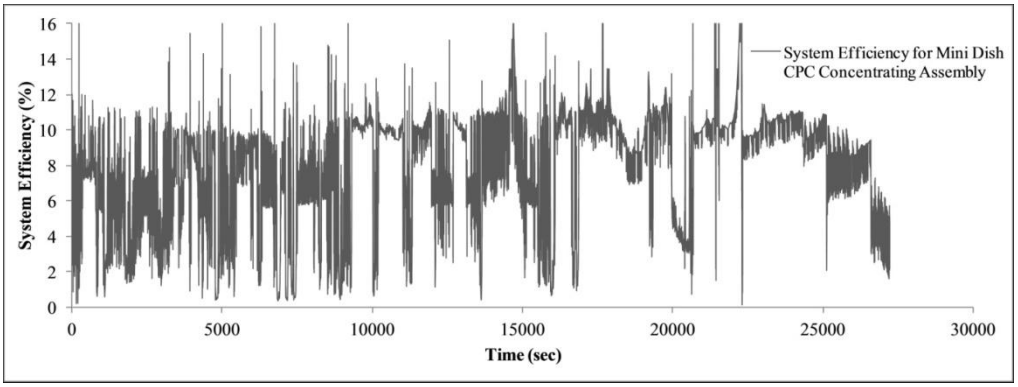


Figure 4.7: System Efficiency Curve for Mini Dish-CPC CPV System

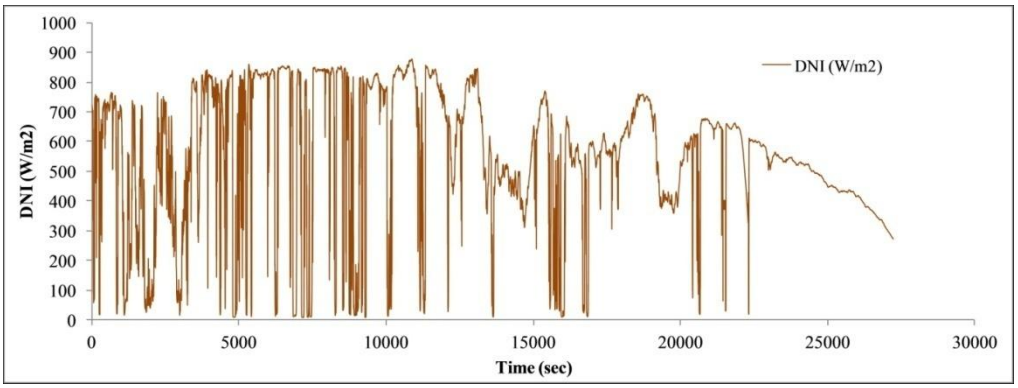


Figure 4.8: DNI Received During Mini Dish-CPC CPV System Operation

Figures 4.7 and 4.8 show the variation of Mini Dish-CPV system against the DNI received, in real field conditions. For higher DNI or concentrations, the efficiency of the CPV system is almost constant. However, at lower DNI or concentrations, efficiency varies in proportional to DNI. The fluctuations in the efficiency curve are due to fluctuations in the DNI availability and due to MPPT searching. It can be seen that maximum system efficiency of mini dish-CPC CPV system obtained is from 12%, which is very low as compared to the conventional solar cells. In order to investigate the causes for low efficiency of CPV system, the ray tracing simulation of mini dish-CPC concentrating was carried out as discussed in the next section.

### 4.2.4 Mini Dish - CPC Assembly Limitations

Despite simple design, there are some limitations and losses associated with the mini dish-CPC concentrating assembly, depicted by the low efficiency. In order to analyze the optical performance of the mini dish-CPC assembly, a ray tracing simulation was conducted using TracePro software. Figure 4.9 shows the developed model of the concentrating assembly in TracePro according to the designed dimensions and spacing. Parabolic dish of 15cm diameter with 9.75 cm focal length and CPC homogeniser of $25^{o}$ acceptance angle were modelled and CPC was placed at the focal length of the mini dish.

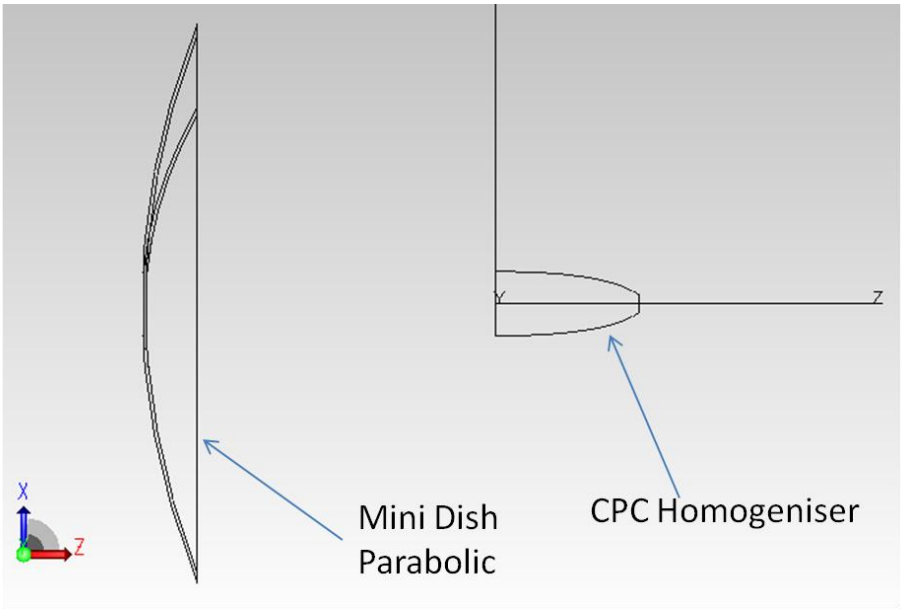


Figure 4.9: Developed Model of Mini Dish-CPC Concentrating Assembly in TracePro

Figure 4.10 shows the ray tracing simulation results of mini dish-CPC assembly. In figure 4.10(b), the expected results can be seen that there is ray leak from the sides of the CPC homogeniser. This is because of the fact that the rim angle for the designed 15cm dish i.e. $42.1^{o}$ is higher than the $25^{o}$ acceptance angle of CPC, causing incident ray to leak from sides of homogeniser instead of outlet aperture. For verification, another simulation

was conducted by considering only that area of dish for which the rim angle is $25^{o}$, as shown in Figure 4.11. It can be seen that all of the incident rays are making it towards outlet aperture of CPC.

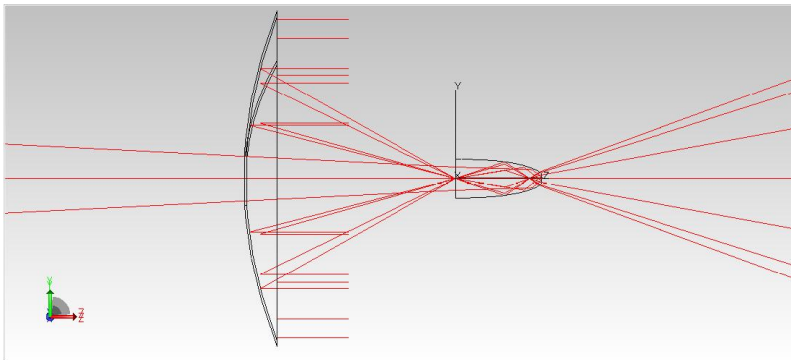

(a)

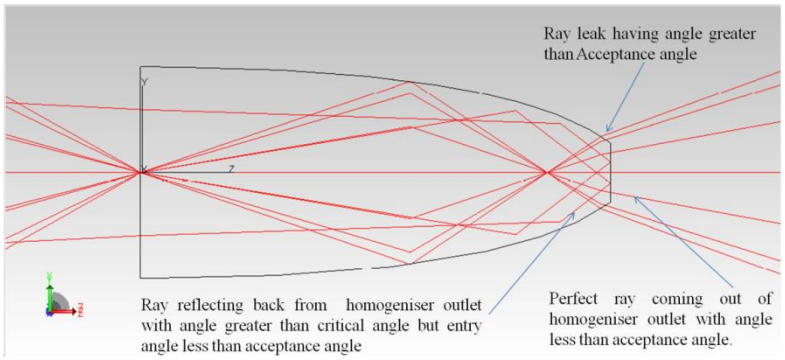


(b)

Figure 4.10: Ray Tracing Simulation of CPV Concentrating Assembly

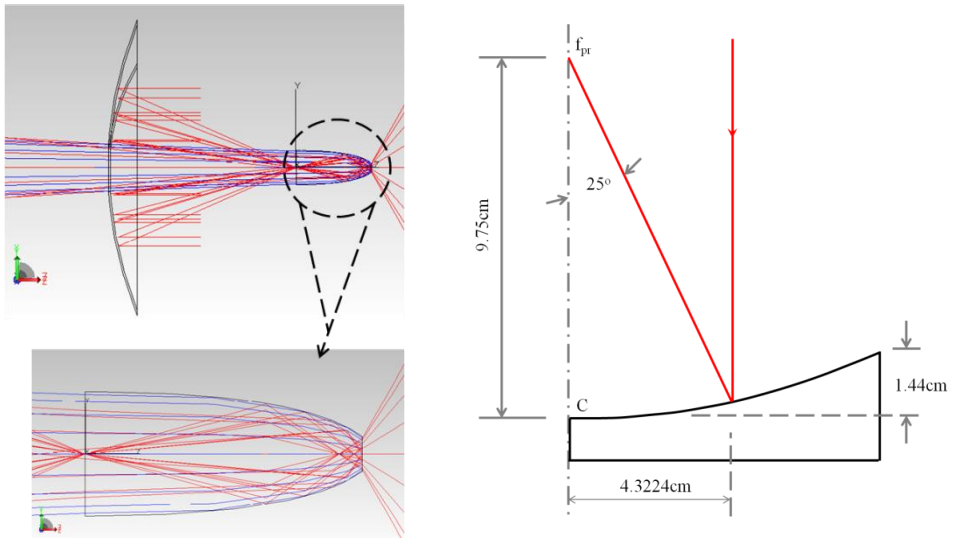


(a) (b)

Figure 4.11: Ray Tracing Simulation of CPV Concentrating Assembly (a) with Angle Less than Acceptance Angle of Homogeniser (b) Effective Radius of Parabolic Dish

The optical loss discussed above is associated with the design limitations. However, there is another inherent optical loss associated with the design of dielectric filled CPC, which occurs even if the incident ray angle is within the acceptance angle of CPC. From Figures 4.10(b) and 4.11(a), it can be seen that some of the rays are reflected back from CPC outlet aperture. This is due to TIR at outlet aperture as the striking ray angle is greater than the critical angle of glass material. The rays hitting near to outlet aperture make angle always greater than the critical angle of CPC material and are reflected back at outlet aperture due to TIR. This rays loss is always associated with dielectric filled CPC design. The effective radius of parabolic dish with rim angle of $25^{o}$ is shown in Figure 4.11(b). In order to have smaller incident ray angle at homogeniser inlet and to avoid TIR at outlet of homogeniser, the concentrating assembly is redesigned in cassegrain arrangement as explained in the next section.

## 4.3 Mini Dish Cassegrain Arrangement Concentrating Assembly Design

A schematic of the mini dish cassegrain arrangement concentrating assembly is shown in Figure 4.12. The cassegrain concentrating assembly is a double-stage concentrator where primary concentrator is a parabolic reflector with focal length $f_{pr}$, while secondary concentrator is a small hyperbolic reflector with two focal points $f1_{hp}$ and $f2_{hp}$. Parallel or beam rays after being reflected from primary reflector try to converge at focal point $f_{pr}$. However, the secondary hyperbolic reflector, placed in the path of converging rays such that focal points of both primary and secondary reflectors $f_{pr}$ and f1 coincides,

further reflects and concentrates rays at its second focal point $f2_{hp}$. At focal point $f2_{hp}$, the glass homogeniser is placed which further guides and uniformly distribute rays over MJC area. The glass homogeniser design is like prism shape long glass rod with square shape inlet and outlet aperture, easy to be installed on square shape MJC. The MJC is then attached to heat spreader and heat sink for heat dissipation.

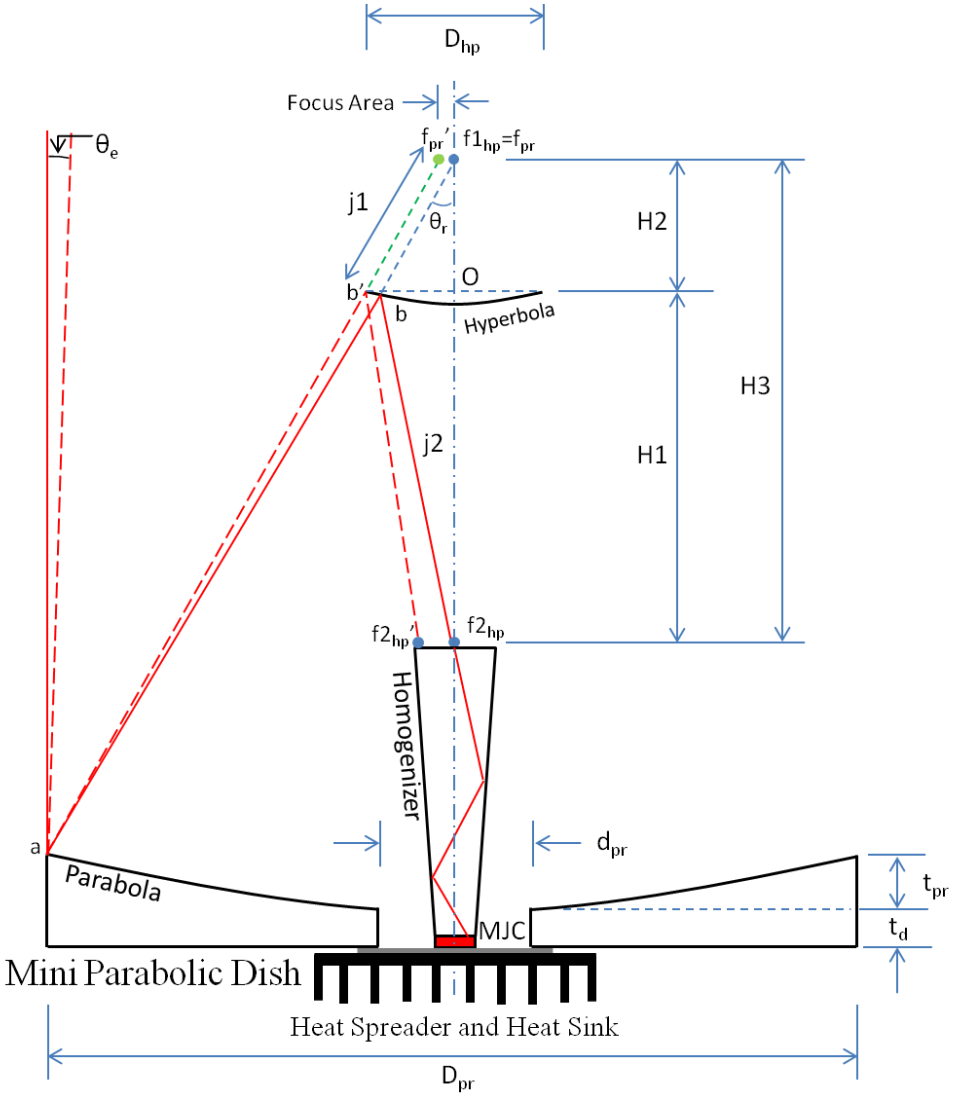


Figure 4.12: Design Schematic of Mini Dish Cassegrain Arrangement Concentrating Assembly

The main advantage of the cassegrain arrangement in comparison with the previous mini dish-CPC concentrating assembly is less incident ray angle at

homogeniser inlet which reduces chance for ray loss at homogeniser outlet due to TIR and it can be designed for any size of primary reflector regardless of rim angle limitation. The size calculation of each component of the cassegrain concentrating assembly, according to space constraints and design requirements are discussed in next sections.

### 4.3.1 Primary Reflector - Mini Parabolic Dish

The mini dish parabolic reflector used in this design as discussed in the previous design, with 15 cm diameter, 9.75 cm focal length $f_{pr}$ and centre hole $d_{pr}$ of size 2.5 cm which provides space for homogeniser mounting.

### 4.3.2 Homogeniser

The TECHSPEC tapered light pipe homogenising rod was used as homogeniser for current concentrating assembly with inlet aperture size of 12 mm x 12 mm, outlet aperture size of 4mm x 4mm and total length of 50 mm.

### 4.3.3 Secondary Reflector - Hyperbolic Dish

The size of the secondary reflector is of great importance, which is designed according to the dimensions of primary reflector and homogeniser. Hyperbolic reflector has two focal points, $f1_{hp}$ and $f2_{hp}$. Focal point $f1_{hp}$ should coincide with the focal point of primary reflector However, the position of its second focal point $f2_{hp}$ is the main design input requirement of hyperbolic reflector. Moreover, size of the reflector should be as small as possible due to the fact that smaller size of secondary reflector results in lower ray angle at homogeniser inlet and less shadow at primary reflector. However, too small reflector can cause difficulty in fabrication and more ray loss can be

experienced with even small error in tracking. The hyperbolic reflector is not only designed for parallel rays but should also accommodate tracking error with rays not parallel to axis of concentrator. For non-parallel rays, focal point of primary reflector shifts from $f_{pr}$ to $f_{pr}$' and focal point $f2_{hp}$ shifts to $f2_{hp}$'. Therefore, to accommodate non-parallel rays, size of secondary reflector Ob' is taken as 3 cm ($D_{hp}$). However, in design calculations, the size of the secondary reflector Ob is taken as 2.5 cm for parallel rays. Moreover, as MJC is planned to be placed at the bottom end of mini parabolic dish, thus if thickness of MJC ($M_t$) is taken as 0.5 mm then the distance between two foci can be found using Equation (4.9) using 50 mm as length of homogeniser L, 9.75 cm focal length $f_{pr}$ of primary reflector and 1cm as thickness of dish $t_d$.

$$H3 = f_{pr} + t_d - L - M_t \qquad (4.9)$$

As the rim angle of primary reflector $\theta_r$ is $42.1^o$, the parameters j1 and H1 can be found using Equations (4.10) and (4.11) respectively.

$$j1 = \left( \frac{Ob/2}{\sin\theta_r} \right) \qquad (4.10)$$

$$H1 = \left( \frac{Ob/2}{\tan\theta_r} \right) \qquad (4.11)$$

So

$$H2 = H3 - H1 \qquad (4.12)$$

By using the Pythagoras theorem, j2 is given by Equation (4.13).

$$j2 = \sqrt{H2^2 + \left( \frac{Ob}{2} \right)^2} \qquad (4.13)$$

Now, the coordinates of hyperbolic reflector can be found using the hyperbolic Equation (4.14).

$$\frac{y^2}{a^2} - \frac{x^2}{b^2} = 1 \qquad (4.14)$$

Where a and b are the constant and can be found by following formula in Equations (4.15) and (4.16) respectively.

$$2a = j2 - j1 \qquad (4.15)$$

$$b = \sqrt{c^2 - a^2} \qquad (4.16)$$

And

$$c = \frac{H3}{2} \qquad (4.17)$$

By simplification of Equation (4.14) we can have:

$$y = \frac{a}{b}\sqrt{b^2 + x^2} \qquad (4.18)$$

| X (mm) | Y (mm) | X (mm) | Y (mm) |
|---|---|---|---|
| **0** | 0 | **0** | 0 |
| **1** | 0.01027 | **-1** | 0.01027 |
| **2** | 0.04105 | **-2** | 0.04105 |
| **3** | 0.09218 | **-3** | 0.09218 |
| **4** | 0.16343 | **-4** | 0.16343 |
| **5** | 0.25449 | **-5** | 0.25449 |
| **6** | 0.36495 | **-6** | 0.36495 |
| **7** | 0.49434 | **-7** | 0.49434 |
| **8** | 0.64213 | **-8** | 0.64213 |
| **9** | 0.80774 | **-9** | 0.80774 |
| **10** | 0.99054 | **-10** | 0.99054 |
| **11** | 1.18988 | **-11** | 1.18988 |
| **12** | 1.40507 | **-12** | 1.40507 |
| **13** | 1.63544 | **-13** | 1.63544 |
| **14** | 1.88027 | **-14** | 1.88027 |
| **15** | 2.13888 | **-15** | 2.13888 |

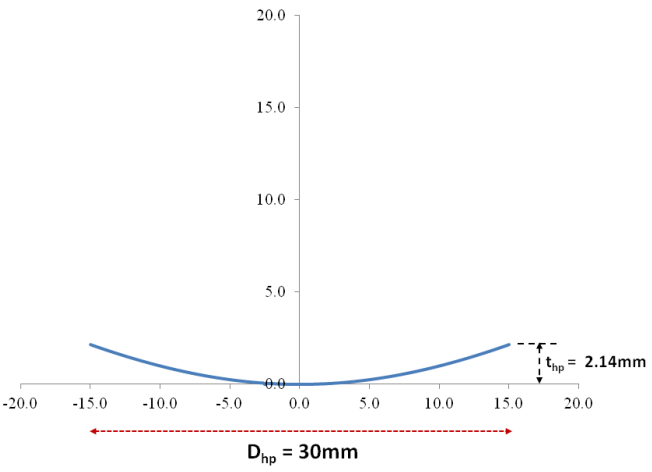


Figure 4.13: Coordinates of Secondary Hyperbolic Reflector

The above equation gives the coordinates of hyperbolic reflector with reference to midpoint of foci $f1_{hp}$ and $f2_{hp}$. In order to have reference point on hyperbolic profile at x=0, there is a need to subtract the value of $(y)_{x=0}$ from Equation (4.18).

$$y = \frac{a}{b}\sqrt{b^2 + x^2} - y_{x=0} \qquad (4.19)$$

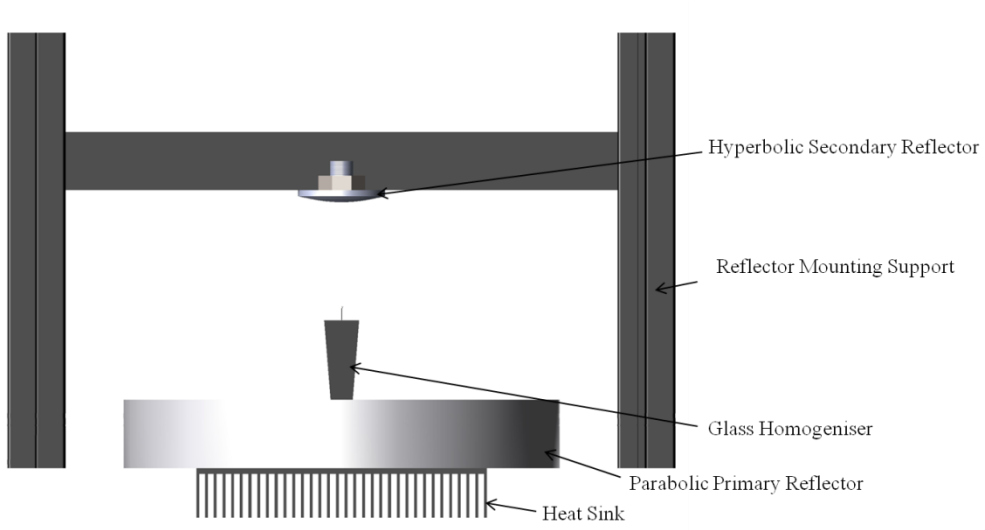


Figure 4.14: Mini Dish Cassegrain Concentrating Assembly Model in TracePro

### 4.3.4 Ray Tracing Simulation of Mini Dish Cassegrain Concentrating Assembly

In order to verify the design and to analyze the performance of the mini dish cassegrain concentrating assembly, the ray tracing simulation was carried out in TracePro software. According to the design parameters, the concentrating assembly was modelled in TracePro. The details of the concentrating assembly model are shown in Figure 4.14. The developed concentrating assembly was simulated for parallel ray grid source. Figure 4.15 shows the ray tracing simulation results for developed concentrating assembly. The rays can be seen

perfectly converging at homogeniser inlet, verifying the design of concentrating assembly.

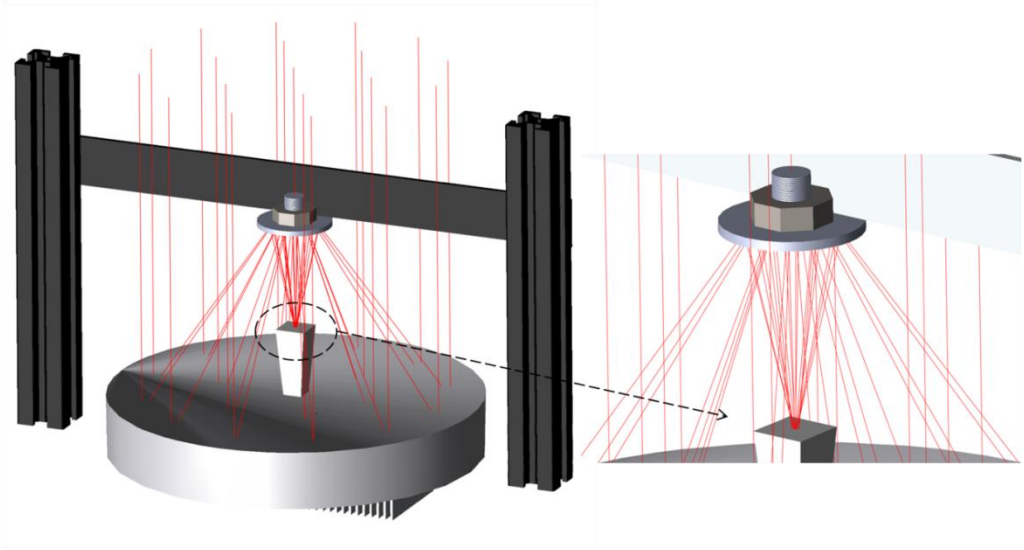

Figure 4.15: Ray Tracing Simulation of Mini Dish Cassegrain Concentrating Assembly

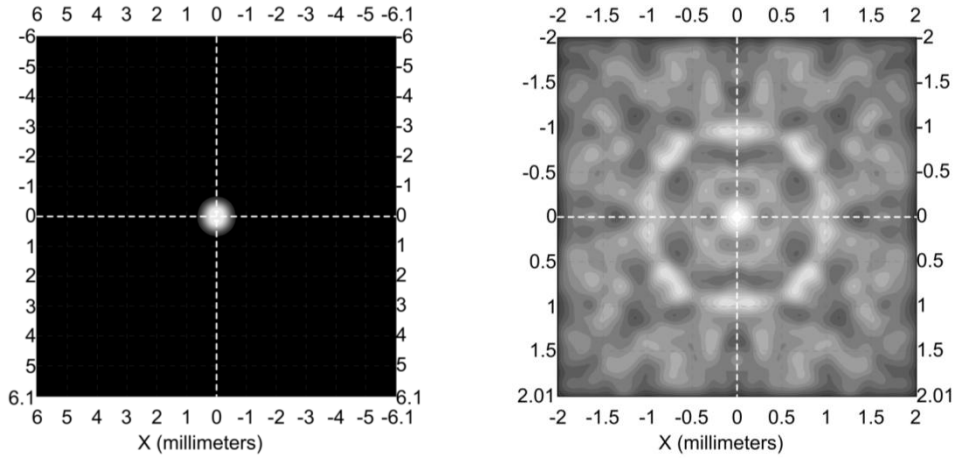


(a) (b)

Figure 4.16: Irradiance Map at (a) Inlet and (b) Outlet of Homogeniser of Mini Dish Concentrating Assembly

The irradiance map at inlet and outlet of homogeniser is shown in Figure 4.16, the concentrated rays at homogeniser inlet are uniformly distributed at homogeniser outlet where the MJC is placed. Uniform distribution of rays at the homogeniser outlet or MJC is an important factor of the concentrating assembly design as it ensures stable and reliable performance of cell.

Moreover, smallest converged rays spot at homogeniser inlet provides more space for the rays to enter homogeniser in case of tracking error, as focus point shifts from centre with tracking error.

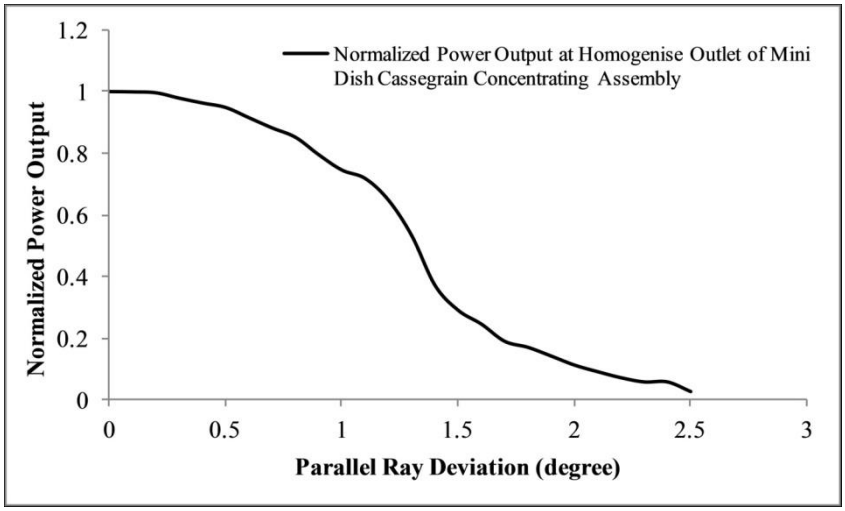


Figure 4.17: Normalized Power Curve for Mini Dish Cassegrain Concentrating Assembly

To analyze the performance of the concentrating assembly for non-parallel rays or tracking error, Figure 4.17 shows the normalized power output or flux at homogeniser outlet of mini dish concentrating assembly. Normalized power output is the ratio of current power output to maximum power output. It can be seen that for $0.3^{o}$ deviation, the normalized power is about 100% and it drops to around 92-93% when the deviation increases to $0.5^{o}$. However, the maximum parallel ray deviation accepted by the mini dish assembly is $2.5^{o}$. It can be seen that the developed design can operate at maximum performance for developed tracking system with tracking accuracy of $0.3^{o}$.

### 4.3.5 Design of Mini Dish CPV System

Based upon the discussed design of mini dish cassegrain concentrating assembly, a prototype of small CPV system based upon two mini dishes is

designed and the developed model is shown in the Figure 4.18. The designed CPV system contains two MJCs with dedicated concentrated assemblies, mounted onto two axis solar tracker. The details of single unit of concentrating assembly with different views are shown in Figure 4.19. In order to reduce the weight of concentrating assembly, extra material from the back side of the parabolic dish is removed, as can be seen from Figures 4.18 and 4.19.

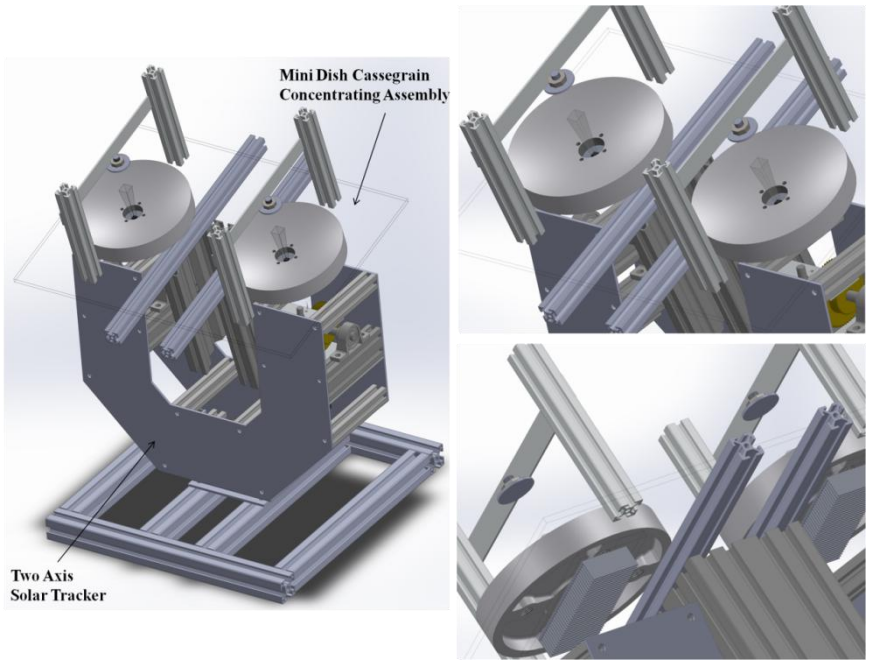


Figure 4.18: Design of Mini Dish CPV System

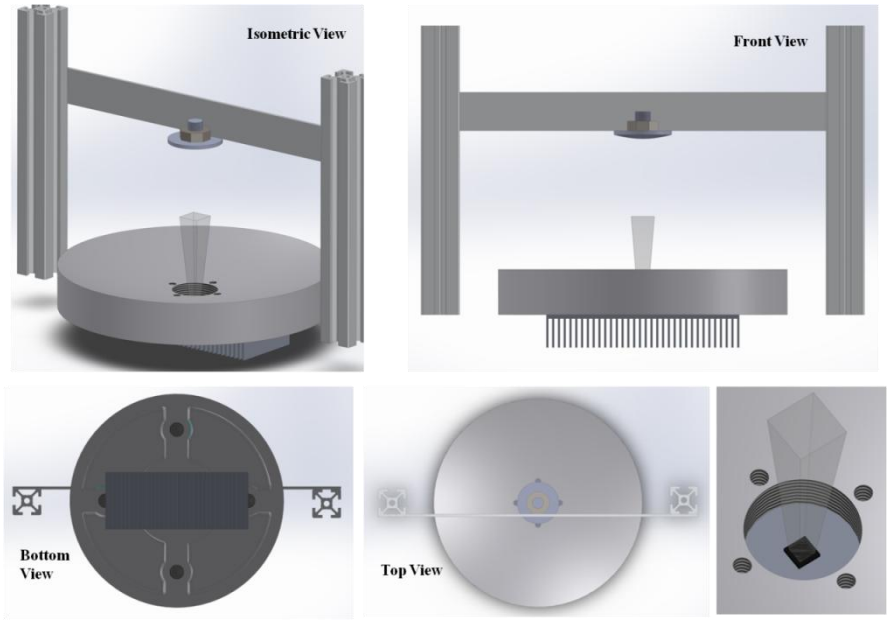


Figure 4.19: Design Model of Mini Dish Cassegrain Concentrating Assembly

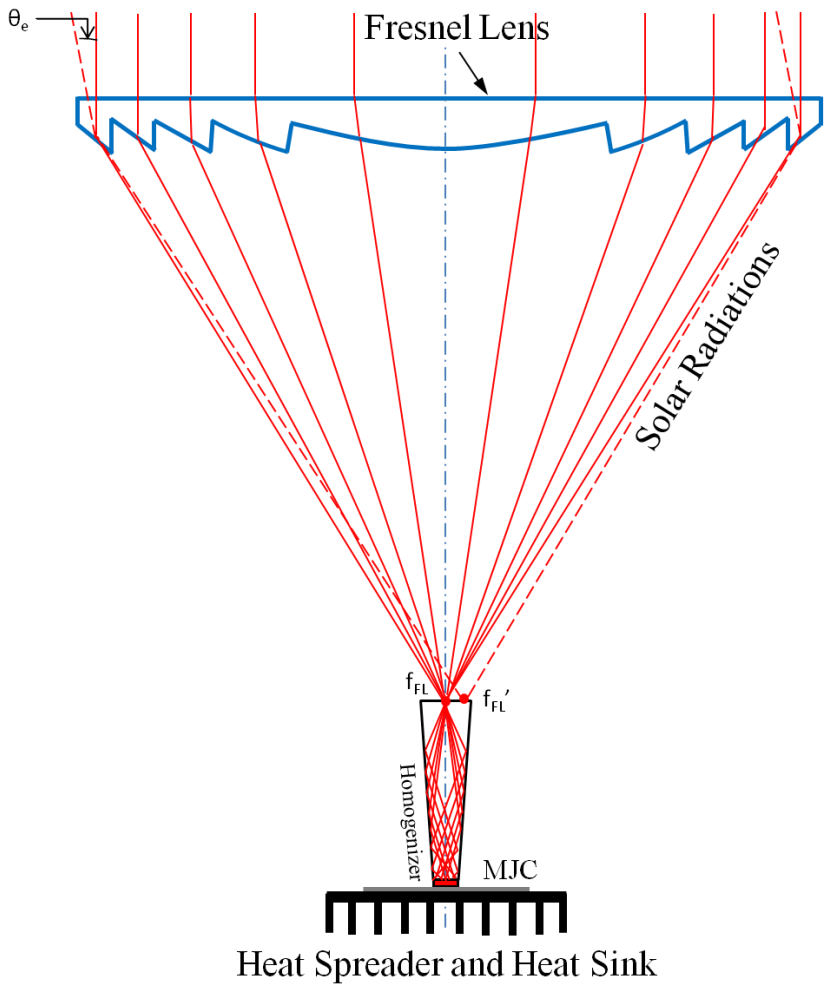


Figure 4.20: Design Schematic of Fresnel Lens-Glass Homogeniser Concentrating Assembly

## 4.4 Fresnel Lens-Glass Homogeniser Concentrating Assembly

In the previous section, the design of mini dish cassegrain arrangement concentrating assembly is discussed and analyzed through ray tracing simulation. The cassegrain arrangement of reflectors provides compact design with overall reduced height of CPV module. However, two stage concentration is sensitive to tracking error which can be seen from the normalized power curve. A single stage refractive concentrating assembly using Fresnel Lens with glass homogeniser, is discussed in this section. A simple schematic of Fresnel Lens-Glass Homogeniser concentrating assembly for CPV system is shown in Figure 4.20. Fresnel lens concentrates solar beam

radiation at its focal point $f_{FL}$ where glass homogeniser is placed, which further guides and uniformly distributes rays onto MJC. Heat Spreader and heat sink are attached to MJC for heat dissipation.

The main advantage of the Fresnel lens over cassegrain arrangement is the simple design with less sensitivity to tracking error due to single stage concentration. However, it has some inherent optical loss at the lens rings. The detailed design for each of the component of Fresnel Lens-Glass Homogeniser concentrating assembly for concentration ratio of x476 is discussed as follows.

### 4.4.1 Glass Homogeniser

For the current design of the Fresnel Lens-Glass Homogeniser concentrating assembly, optical rod is used as homogeniser with 12 mm x 12 mm inlet aperture and 5.5 mm x 5.5 mm outlet aperture, same as size of MJC. The height of the homogeniser is 30 mm.

### 4.4.2 Fresnel Lens Design

Fresnel lens is a form of plano-convex lens with reduced overall height and optical material for almost same performance. The lens surface is based upon aspheric profile as the spherical profile has spherical aberration. The aspheric profile of current Fresnel lens design is optimized from spherical surface. The detailed design of Fresnel lens is shown in Figure 4.21. The general sag equation for lens surface is given by Equation (4.20) **[116]**.

$$Z_L = \frac{C_L {r_L}^2}{1+\sqrt{1-(1+k){C_L}^2{r_L}^2}} + \sum_{i=1} A_i {r_L}^i \qquad (4.20)$$

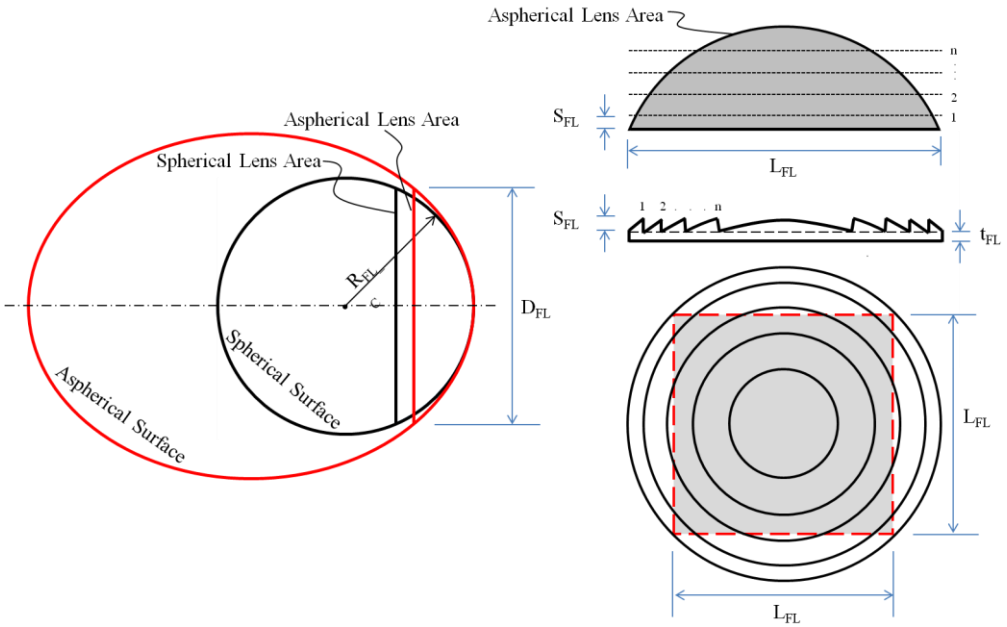


Figure 4.21: Design Schematic for Aspheric Fresnel Lens

Where factor k depends upon the conical surface and for spherical surface k=0. The parameter $C_r$ represents the curvature for corresponding spherical surface, which is reciprocal of radius of curvature.

$$C_L = \frac{1}{R_{FL}} \qquad (4.21)$$

$A_i$ represents the aspheric coefficients corresponding to the aspheric surface. The parameter $r_L$ represents the coordinate of aspheric surface along radial direction. The maximum value of $r_L$ is half of the lens diameter $D_{FL}$. However, in order to have compact design of CPV system, a Fresnel lens of square dimensions is considered with dimension $L_{FL}$ of each side. Hence, the value of $D_{FL}$ is given by Equation (4.22).

$$D_{FL} = \sqrt{{L_{FL}}^2 + {L_{FL}}^2} \qquad (4.22)$$

As the CPV assembly is designed for concentration ratio of x476 with cell size of 5.5 mm x 5.5 mm, then the dimension $L_{FL}$ for each side of square Fresnel

lens can be calculated using Equation (4.1) as 120 mm x 120 mm. Therefore, the diameter of corresponding circular lens is $D_{FL}$=169.7 mm and maximum value of $r_{FL}$ is 84.85 mm.

In order to find the suitable aspheric coefficient, the spherical surface was optimized for aspheric coefficients to have minimum spherical aberration, using optical software TracePro through its 2D interactive optimizer feature. The focal length of 200mm is considered for current Fresnel lens design. The radius of curvature of corresponding spherical surface is given by Equation (4.23).

$$R_{FL} = 1000(n_{FL} - 1) f_{FL} \qquad (4.23)$$

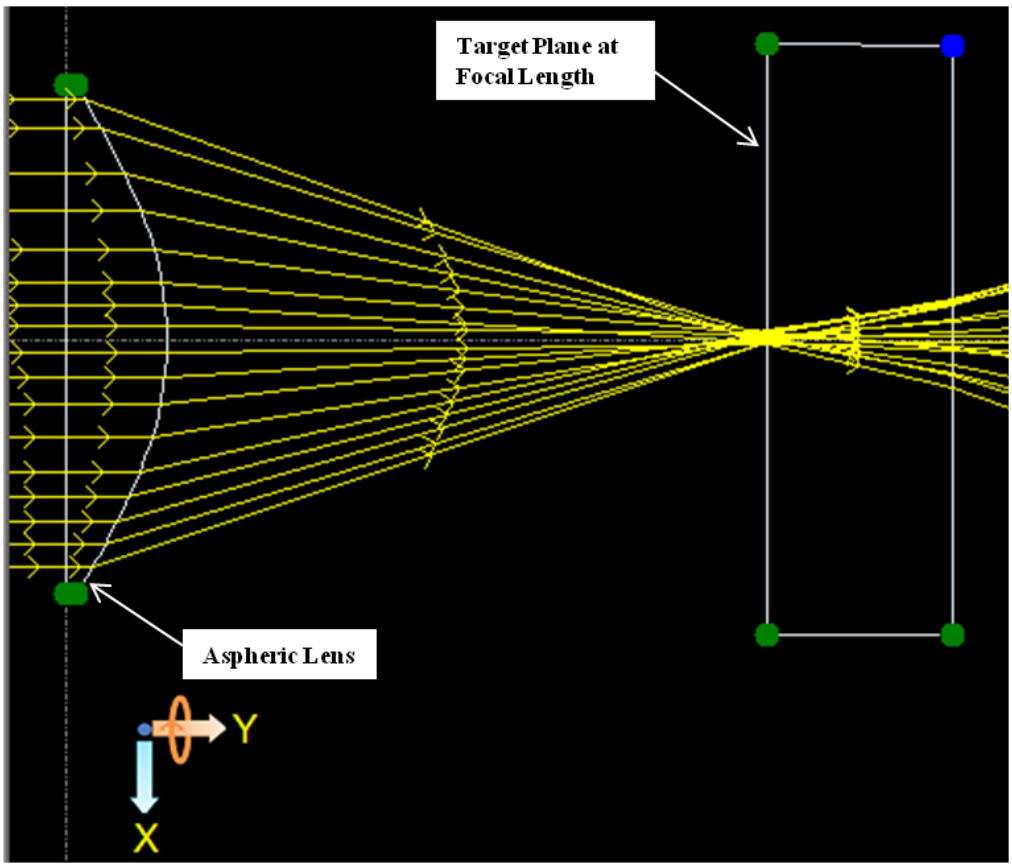


Figure 4.22: Optimized Aspheric Plano-Convex Lens in 2D Interactive Optimizer of TracePro

Where $n_{FL}$ is the refractive index of glass material and $f_{FL}$ is the focal lengthof Fresnel lens in meters i.e. 0.2m. Therefore, by considering the refractive index of 1.5, the radius of curvature is calculated as 100mm. The optimization of lens surface through 2D interactive optimizer of TracePro, is shown in Figure 4.22. The optimized aspheric coefficients are given in Table 4.1. The optimization is carried out by adjusting the aspheric coefficients to have minimum focussed spot size at focal point.

Table 4.1: Aspheric Coefficients of Optimized Aspheric Lens

| Parameter | Value | Parameter | Value |
|---|---|---|---|
| $A_1$ | 0 | $A_6$ | $-2.7\times10^{-6}$ |
| $A_2$ | 0 | $A_7$ | $7.8\times10^{-8}$ |
| $A_3$ | $-8\times10^{-4}$ | $A_8$ | 0 |
| $A_4$ | 0 | $A_9$ | 0 |
| $A_5$ | $-9.3\times10^{-6}$ | $A_{10}$ | 0 |

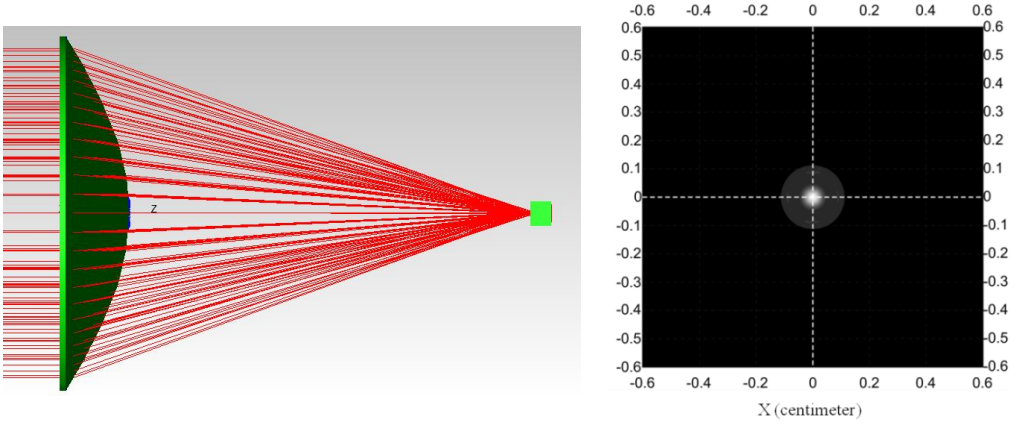


(a) (b)

Figure 4.23: Ray Tracing Simulation of Aspheric Lens (a) Simulation Result (b) Irradiance map

In order to verify the optimized design, the aspheric lens was created in TracePro and the ray tracing simulation was carried out for parallel ray grid. The ray tracing simulation results are shown in Figure 4.23. A perfect

converging of parallel ray at the receiver, placed at focal point can be seen and the size of focussed spot can be verified from irradiance map shown. The designed aspheric lens is converted to a Fresnel lens with a step size of $S_{FL}$=1.8 mm for 17 rings and the lens thickness is taken as $t_{FL}$=3 mm. The ray tracing simulation of designed Fresnel lens concentrating assembly is discussed in next section.

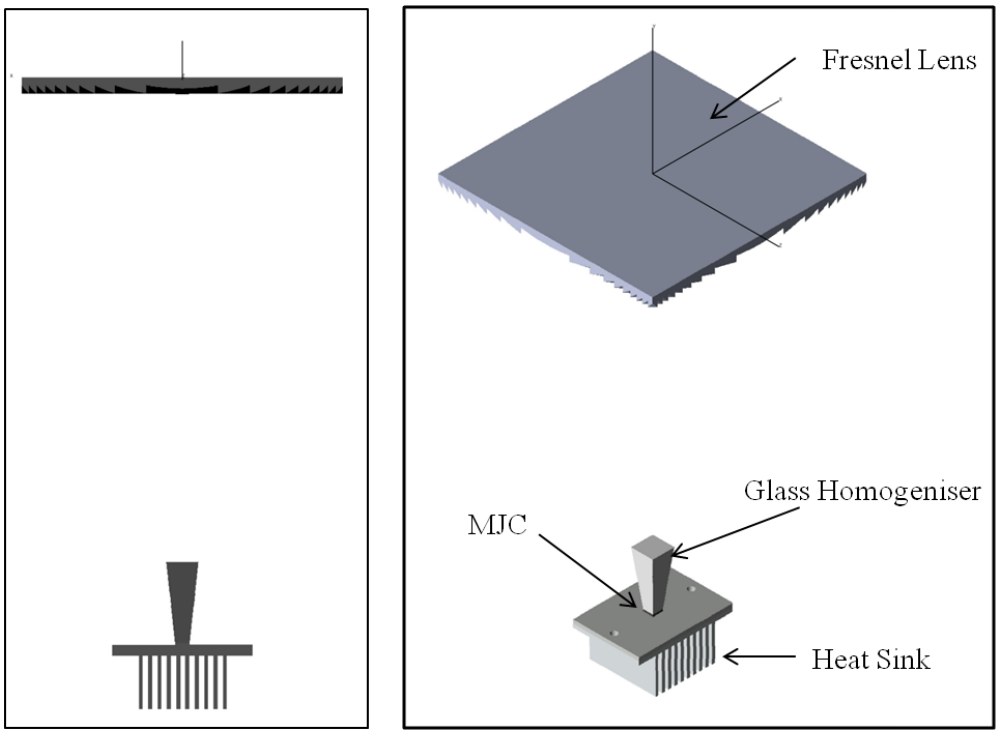


Figure 4.24: Fresnel Lens-Glass Homogeniser Concentrating Assembly Model in TracePro

### 4.4.3 Ray Tracing Simulation of Fresnel Lens-Glass Homogeniser Concentrating Assembly

Figure 4.24 shows the model of Fresnel lens-glass homogeniser concentrating assembly developed in TracePro software for ray tracing simulation. The ray tracing simulation results of the developed concentrating assembly for parallel ray grid are shown in Figure 4.25. A perfect convergence of rays at the centre of homogeniser inlet verifies the design of lens and the concentrating

assembly. The distribution of rays at inlet and outlet of glass homogeniser can be seen through an irradiance map, shown in Figure 4.26, with a perfect bright spot at centre of homogeniser inlet and uniform distribution of rays at homogeniser outlet.

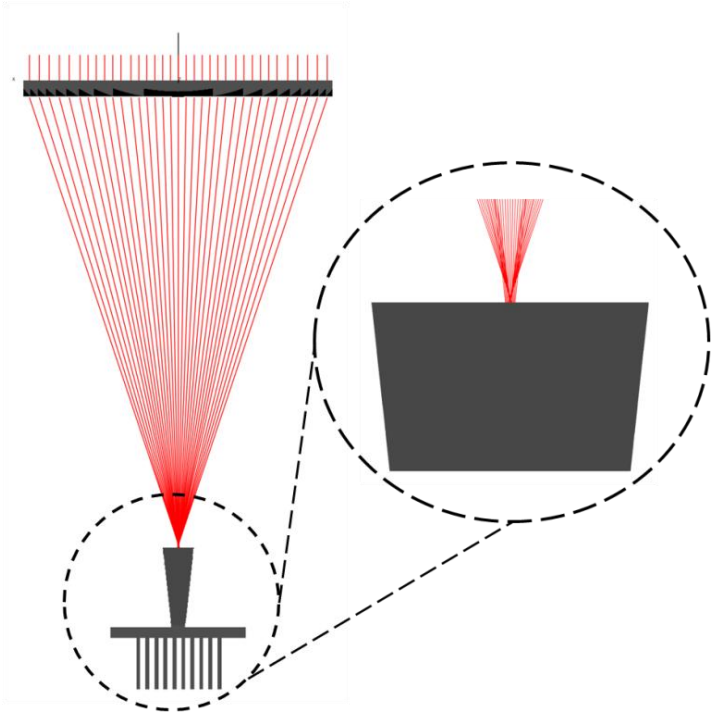

Figure 4.25: Ray Tracing Simulation of Fresnel Lens-Glass Homogeniser Concentrating Assembly

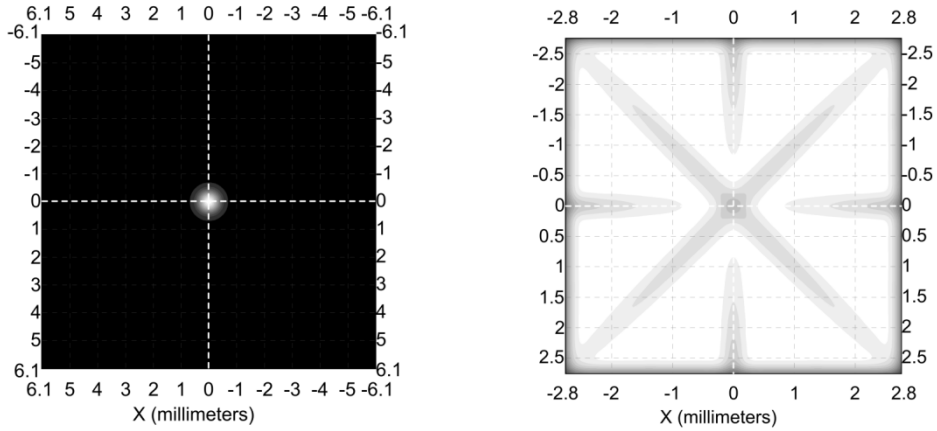


(a) (b)

Figure 4.26: Irradiance Map at (a) Inlet and (b) Outlet of Homogeniser of Fresnel Lens Concentrating Assembly

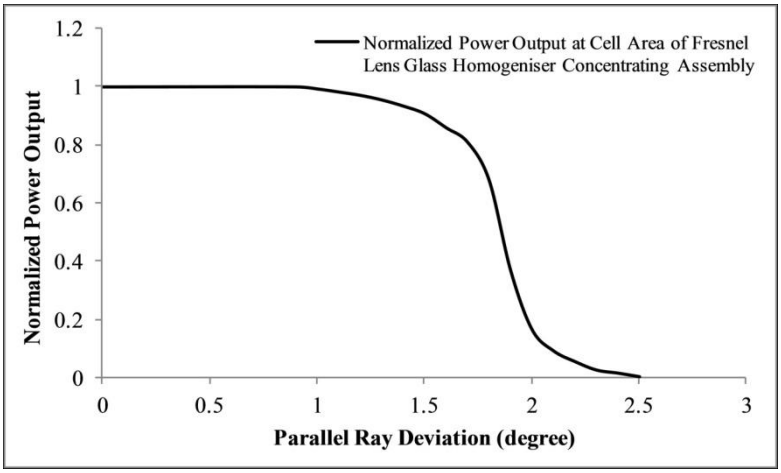


Figure 4.27: Normalized Power Curve for Fresnel Lens-Glass Homogeniser Concentrating Assembly

Figure 4.27 shows the normalized power curve for Fresnel Lens-Glass Homogeniser Concentrating Assembly. It can be seen that the performance of Fresnel lens glass homogeniser concentrating assembly is maximum and remains stable for angular deviation up to $1^o$ and falls to 85% for deviation as high as $1.5^o$. This performance is better and stable than the mini dish concentrating assembly, which is due to less sensitive single stage concentration and smaller height of homogeniser as larger height increases the chances of ray loss at outlet port of homogeniser due to TIR. However, for tracking accuracy of $0.3^o$, both Fresnel lens and mini dish design have almost 100% performance. The maximum angular deviation for Fresnel lens based concentrating assembly is also $2.5^o$.

### 4.4.4 Design of Fresnel Lens-Glass Homogeniser CPV System

Figure 4.28 shows the design of developed prototype of Fresnel Lens-Glass Homogeniser CPV system. The system is based upon a 2x2 array of Fresnel Lens for four MJC submounts housed into a acrylic mounting. The CPV module is mounted onto developed two axis solar tracker. The windows cut in

the acrylic mounting is to reduce the weight of CPV module. The MJC submounts are installed onto an adjustable aluminium housing to adjust the height according to Fresnel Lens focal length. The concentrating assembly for a single Fresnel lens is shown in Figure 4.29.

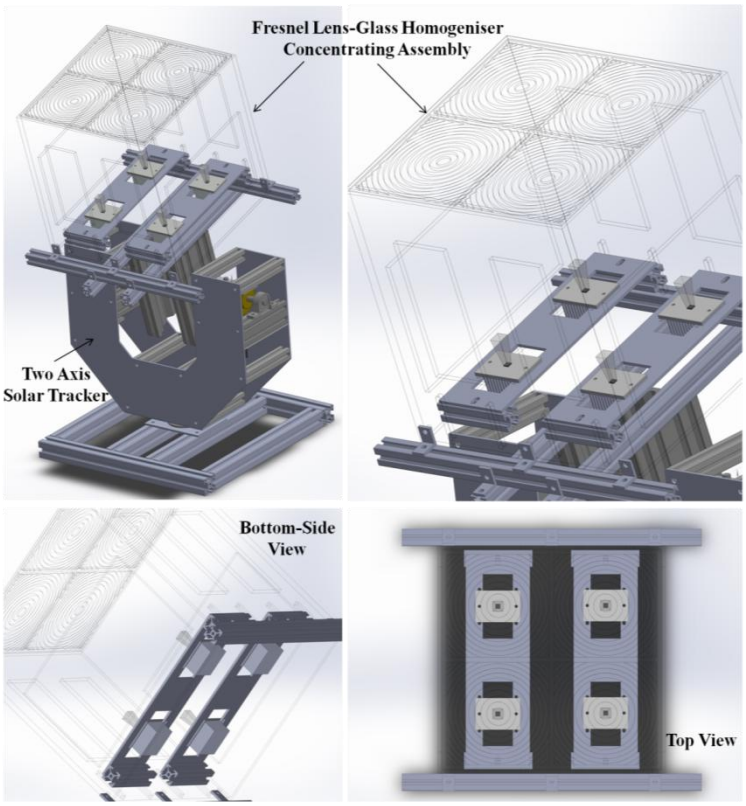


Figure 4.28: Design Model of Fresnel Lens-Glass Homogeniser CPV System

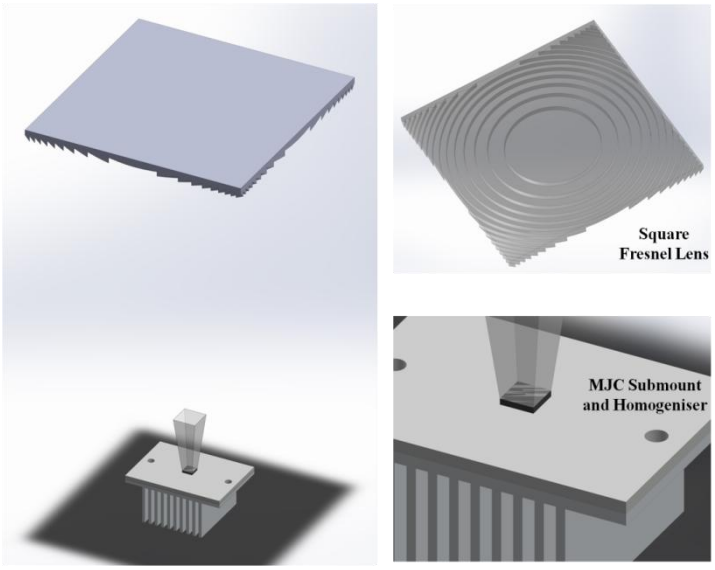


Figure 4.29: Design Model of Fresnel Lens-Glass Homogeniser Concentrating Assembly

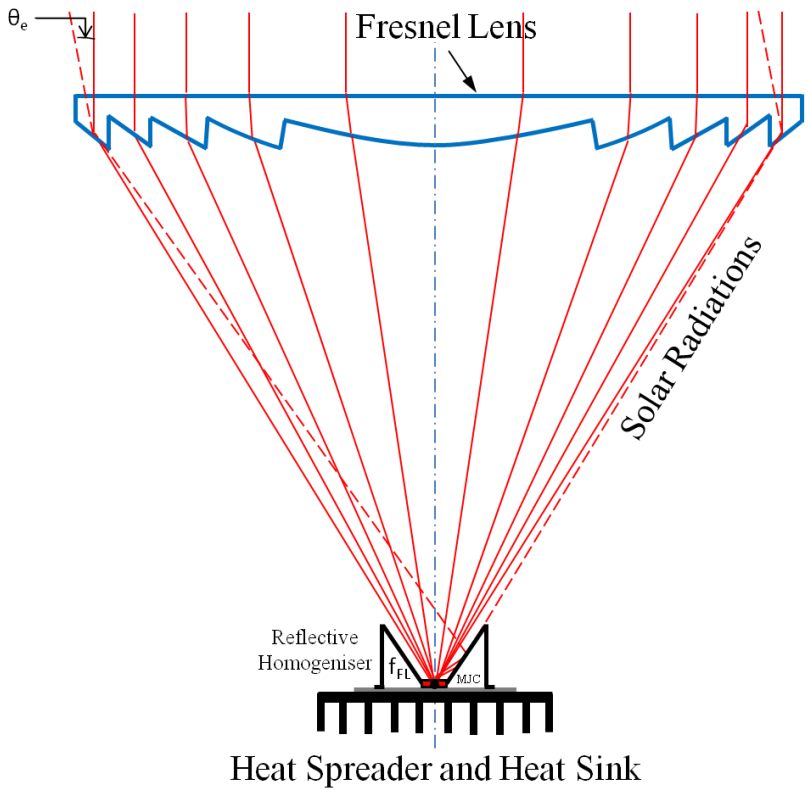


Figure 4.30: Schematic of Fresnel Lens-Reflective Homogeniser Concentrating Assembly

## 4.5 Fresnel Lens-Reflective Homogeniser Concentrating Assembly

The design of the concentrating assembly that is going to be discussed in this section, is similar to the Fresnel Lens design discussed in the previous section. However, instead of glass homogeniser, rays are concentrated directly onto MJC and a reflective homogeniser is used to guide the rays to MJC in case of tracking error. The schematic of Fresnel Lens-Reflective Homogeniser concentrating assembly is shown in Figure 4.30. Fresnel Lens focuses solar radiations directly onto the solar cell area. Therefore, instead of placing MJC directly at focus point, it is place slightly above the focal point to have area focus instead of point focus. The reflective homogeniser is basically a conical reflecting surface surrounding the cell. In case of tracking error or non-parallel

rays, the deviated rays are reflective by the reflective homogeniser onto the cell area. MJC is connected to a heat spreader and a heat sink for heat dissipation.

The size and design of the Fresnel Lens used in the current design is the same as the used one in previous section, 120 mm x 120 mm square shape with focal length of 200 mm. The reflective homogeniser has outlet aperture of 5.5mm x 5.5 mm, same as size of MJC, and inlet aperture of 23 mm x 23 mm. The height of reflective homogeniser is 14.5 mm above the cell thickness. The ray tracing simulation of current concentrating assembly is discussed in next section.

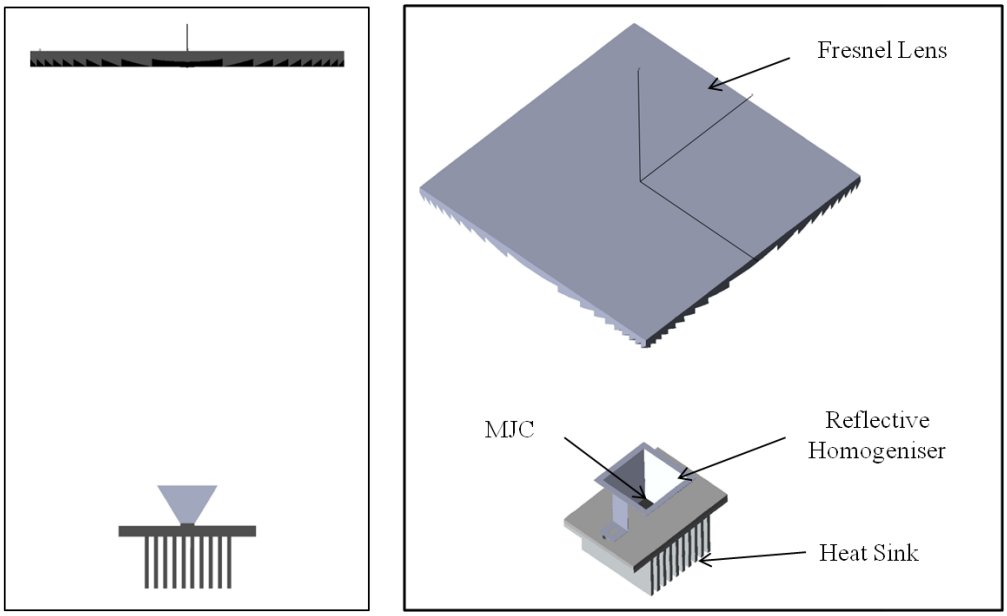


Figure 4.31: Fresnel Lens-Reflective Homogeniser Concentrating Assembly Model in TracePro

### 4.5.1 Ray Tracing Simulation of Fresnel Lens-Reflective Homogeniser Concentrating Assembly

For ray tracing simulation, the model of Fresnel lens-reflective homogeniser concentrating assembly is developed in TracePro software, as shown in Figure

4.31. The optical performance of the system is tested for parallel rays grid. The ray tracing simulation results for the developed concentrating assembly are shown in Figure 4.32. The converged rays at the cell area can be seen in the simulation results. Irradiance map at cell area shows the area concentration for ray distribution. With the angular deviation in the incident rays, in Figure 4.32(b), it can be seen that the rays are hitting the reflective homogeniser which is further reflecting them to the cell area.

The normalized power output curve against the parallel ray deviation is shown in Figure 4.33. It can be seen that the trend of normalized power curves for Fresnel lens-reflective homogeniser concentrating assembly is similar to that for Fresnel lens-glass homogeniser concentrating assembly. The system performance is maximum up to $0.7^{o}$ and a slight step drop is observed after $0.7^{o}$, which is due to some ray loss through reflective homogeniser. After $1.6^{o}$ deviation, the sudden fall in the curve is due to ray loss focussed outside the area of homogeniser. However, the concentrating assembly can respond to maximum of $2.5^{o}$ angular deviation.

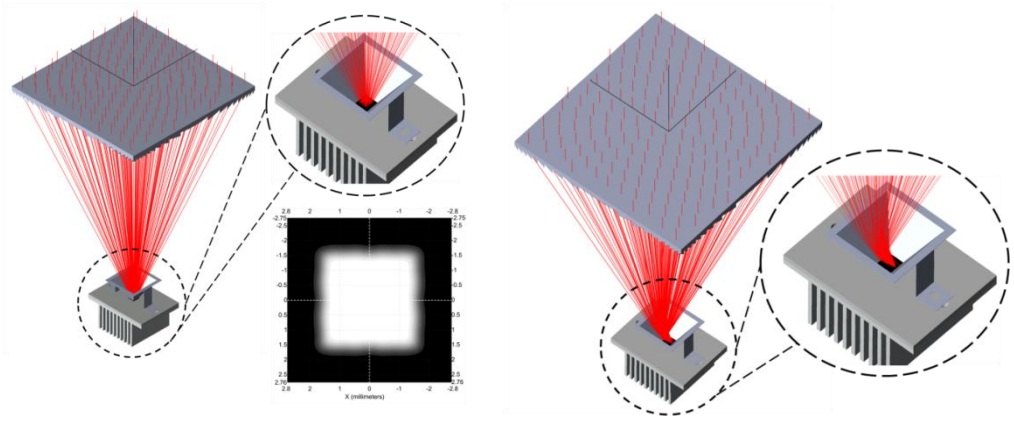

(a) (b)

Figure 4.32: Ray Tracing Simulation of Fresnel Lens-Reflective Homogeniser Concentrating Assembly

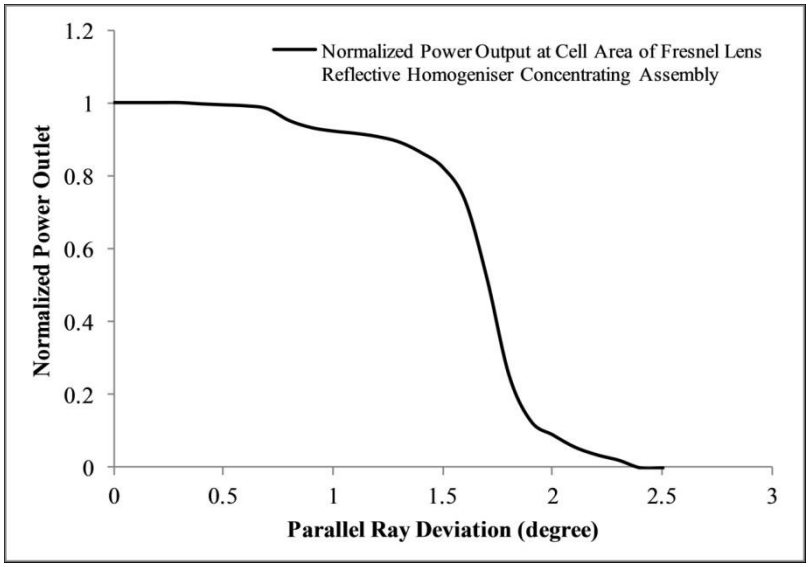


Figure 4.33: Normalized Power Curve for Fresnel Lens-Reflective Homogeniser Concentrating Assembly

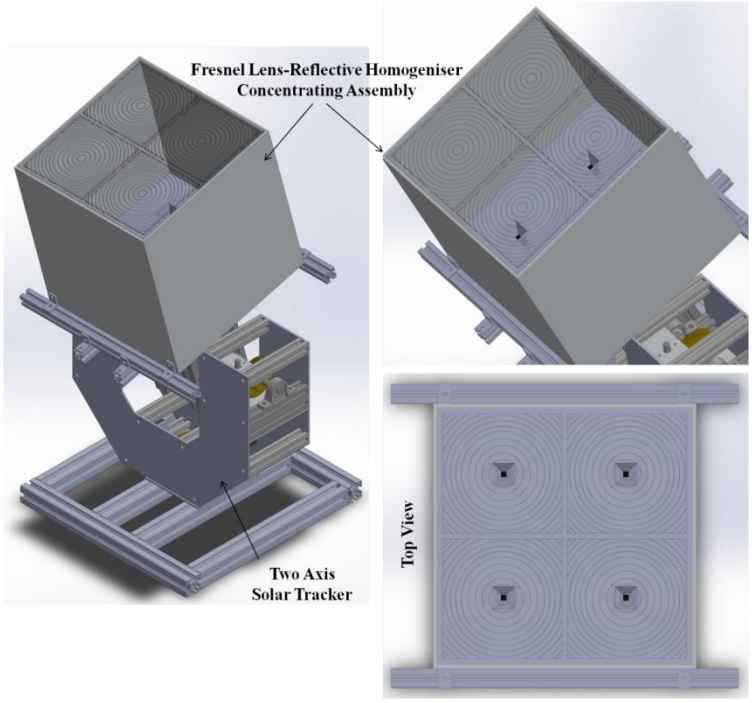


Figure 4.34: Design Model of Fresnel Lens-Reflective Homogeniser CPV System

### 4.5.2 Design of Fresnel Lens-Reflective Homogeniser CPV System

A prototype of CPV system with reflective homogeniser is shown in Figure 4.34. The design is based upon an 2 x 2 array of Fresnel lenses which have size of 120mm x 120mm of each lens. Four MJCs are placed onto an

aluminium base which provides mounting support and acts as heat spreader and heat sink. Reflective homogenisers are then placed on each of MJC submount. This whole assembly is housed into an aluminium frame and mounted onto a developed two axis solar tracker. The arrangement of the single lens MJC assembly is also shown in Figure 4.35.

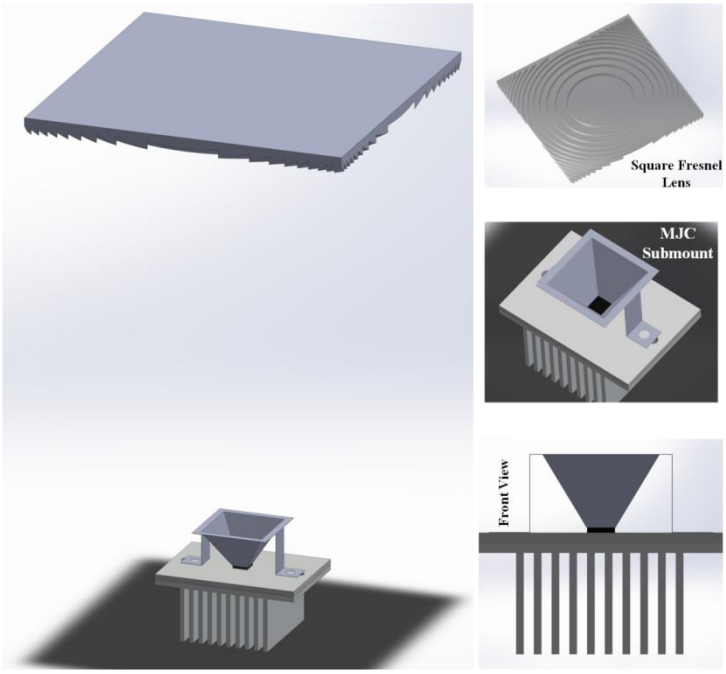


Figure 4.35: Design Model of Fresnel Lens-Reflective Homogeniser Concentrating Assembly

## 4.6 Summary

In this chapter, the different designs of the concentrating assemblies for CPV system are introduced and discussed with their performance analysis using ray tracing simulation. The concentrating assemblies are comprising of reflective concentrator using mini parabolic dish and refractive concentrator using Fresnel lens. The analysis was first carried out on a single stage concentrating assembly with mini parabolic dish as reflective concentrator and compound parabolic concentrator (CPC) as homogeniser. Due to inherent optical loss of concentrating assembly at outlet aperture of homogeniser, the low efficiency

of overall CPV assembly was recorded experimentally. Moreover, due to the limitation of acceptance angle of CPC, the design was unable to utilize the complete area of the mini parabolic dish. Due to optical loss and design limitations, the concentrating assembly was redesigned as double stage concentration using parabolic and hyperbolic reflectors in cassegrain arrangement and tapered glass rod as homogeniser. The mini dish cassegrain design has almost zero design optical loss and acceptance angle of $0.5^{o}$ with about 95% of normalized power output.

Due to high sensitivity and steep normalized power output curve of double stage concentrator design, single stage concentrating assembly using Fresnel lens as refractive concentrator, was designed and analyzed with glass rod and conic reflector as homogenisers. The Fresnel lens design was optimized for aspheric surface coordinates using 2D interactive optimizer of Tracepro, to minimize spherical aberration with focal length of 200 mm. From normalized power output curves, it was found that both Fresnel lens based concentrating assemblies have acceptance angle of $1^{o}$ with 98% stable normalized power output. However, each of the concentrating assembly can accept maximum deviation of $2.5^{o}$.

Based upon the design of concentrating assemblies, the prototype models of CPV system were designed with two mini dishes for cassegrain design CPV and 2x2 array of Fresnel lens for other two CPV system. The experimental performance of developed CPV and CPV-Hydrogen system with development of experimental test rig, are discussed in the next chapter.

# Chapter 5: Experimental Investigation of Concentrated Photovoltaic (CPV) System and CPV-Hydrogen System

## 5.1 Introduction

In the previous chapters, firstly the development of the two axis solar tracking system is discussed with required CPV tracking accuracy. Secondly, the concentrating assemblies with mini parabolic dish and the Fresnel lens were designed and analyzed using ray tracing simulation. Based upon the designed parameters of the concentrating assemblies, the prototypes of the CPV system were then designed and modelled. The main focus of this chapter is to analyze the real field experimental performance of the developed CPV and CPV-Hydrogen systems..

Besides the ray tracing simulation, the experimental investigation of the CPV system is very important as the concentrating assembly of the CPV system is designed for rays parallel to the concentrator axis. However, the solar radiations hitting the surface are not parallel as the sun subtends an angle on the earth because of the finite distance and diameter. Moreover, the material of the concentrator and its surface quality also define performance of the CPV system, which cannot be simulated through the ray tracing simulation. Furthermore, the performance of the multi-junction solar cell also depends upon different parameters like cell temperature and concentration. The temperature of cell and the solar concentration change during the whole day as it depends upon direct normal irradiance (DNI), which doesn't remain constant in actual field conditions. Due to these performance affecting parameters, its

experimental investigation CPV is of prime importance in the system development.

Similarly, as the hydrogen production through electrolysis is claimed to be the suitable option for the energy storage, so the field performance of the CPV system for the production of hydrogen is important to investigate the real potential of the CPV-Hydrogen system. In addition, the performance of the electrolyser depends upon the power supplied by the CPV system, which changes continuously throughout the day. Therefore, the maximum and the average experimental performance of the CPV-Hydrogen system is analyzed which can be expected under different climate conditions

In this chapter, first the design of the test rig developed for control and operation of CPV system is discussed, followed by the fabrication and the real field testing of each of the developed CPV system. The simulated and experimental performances of all the CPV systems are then compared. After performance investigation of the CPV system, the design and development of the CPV-Hydrogen system with the hydrogen compression unit is discussed. Through the CPV-Hydrogen experimentation, the real hydrogen production potential is analyzed under different weather conditions.

## 5.2 CPV Experimental Setup Description

Figure 5.1 shows the design model of the experimental setup, developed to investigate the performance of CPV system. All the four CPV systems are placed together onto a frame built through aluminium extrusion. All the control boxes along with the power supply system and other electronic components are placed in an enclosed compartment at bottom of the frame.

The four CPV trackers are placed onto top aluminium base which is protected through sliding covers. The sliding covers are used to protect the trackers in case of rain and non-operational time.

The covers are mounted onto sliders which moves into guide rails. The design of three CPV systems, Mini Dish Cassegrain CPV, Fresnel Lens-Glass Homogeniser CPV and Fresnel Lens-Reflective Homogeniser CPV, is discussed in the previous chapter. However, the design of fourth CPV system, Multi-Leg Homogeniser CPV is based upon novel design of multi-leg homogenise, which will be discussed and analyzed in chapter 7. In order to record the performance parameters of the CPV, the schematic of the control circuit for developed CPV experimental setup is shown in Figure 5.2. As discussed in previous chapters, one of the tracker acts as master and other three tracker operate as slave trackers.

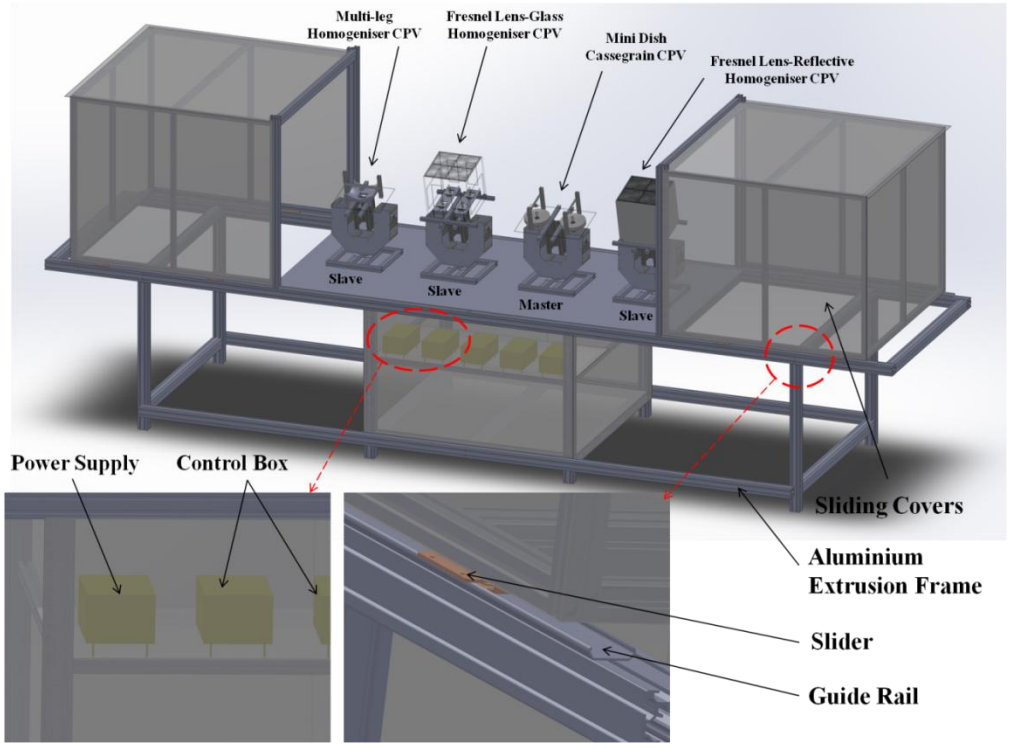


Figure 5.1:Design Model of CPV Systems Experimental Setup

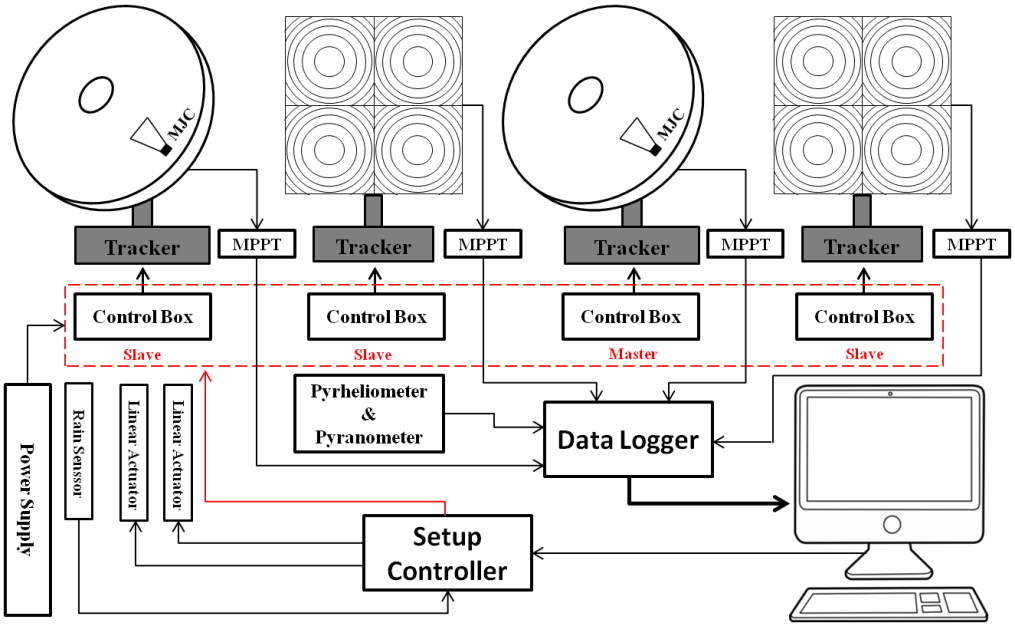


Figure 5.2: Schematic of Control Circuit and System Arrangement for CPV Experimental Setup

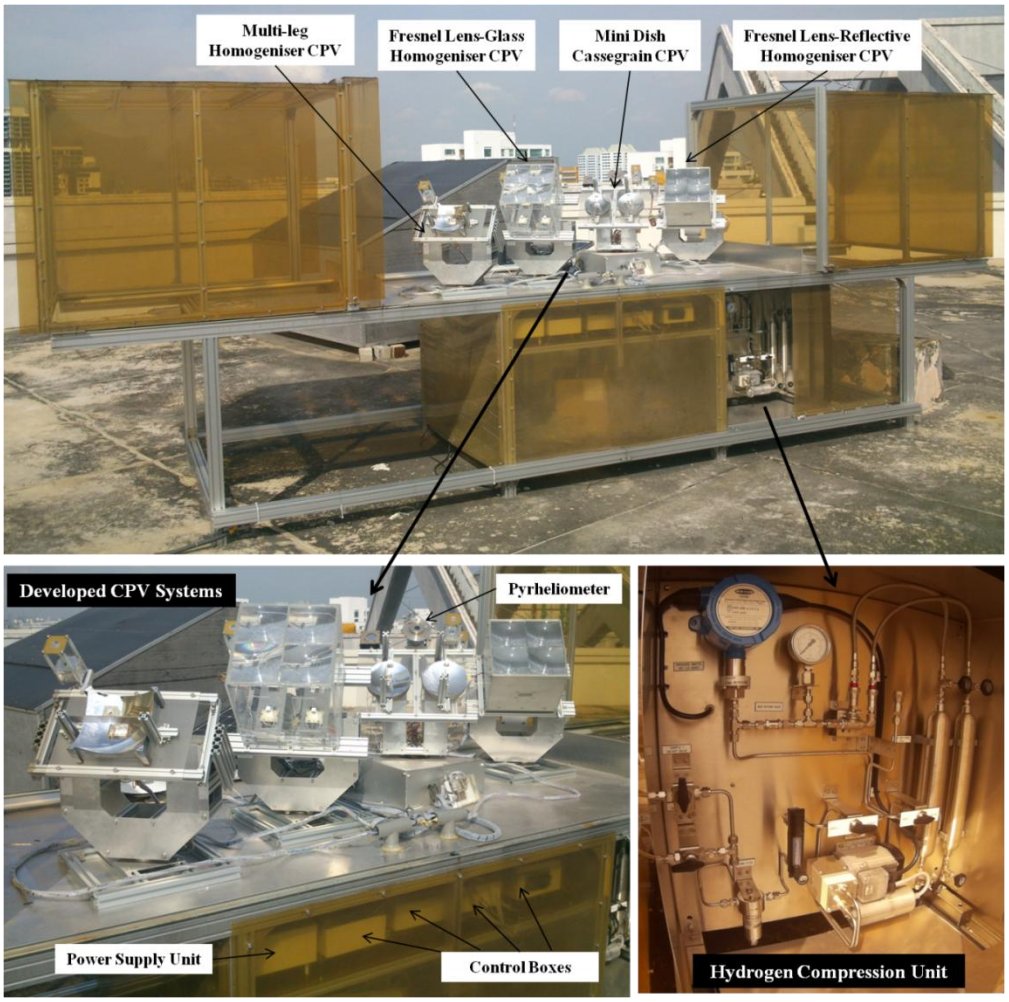


Figure 5.3: Front View of Developed CPV Experimental Setup

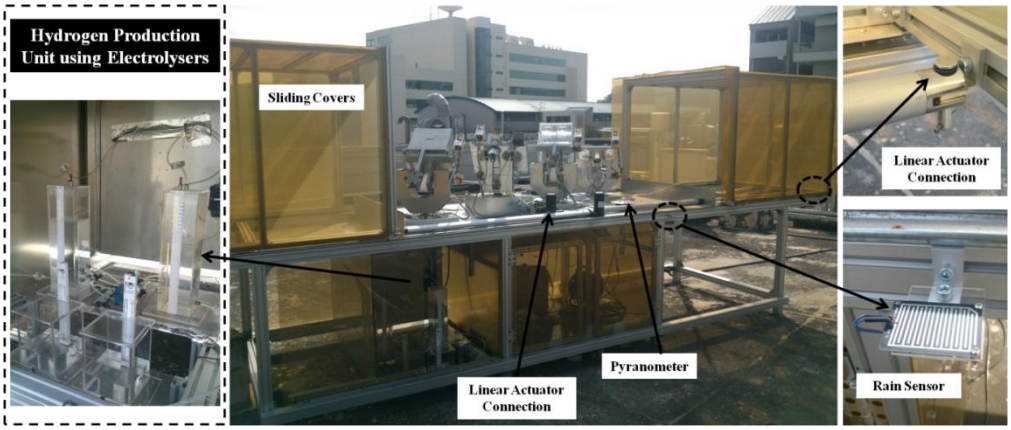


Figure 5.4: Rear View of Developed CPV Experimental Setup

A MPPT is connected to power output of each of the CPV system, which is then connected to a data logging device. In order to measure the solar energy in the form of DNI received by the CPV systems, a Pyrheliometer is utilized and connected to the data logger. Pyranometer is also utilized to measure the DHI. The setup controller is based upon a microcontroller circuit that acts as an communication link between a computer and the trackers. This communication is to control the trackers manually or to stop them in case of closing or initialization of system. The setup controller is also attached to linear actuators, which are attached to the sliding cover to control their opening and closing automatically, in case of rain detected through rain sensor. The developed experimental setup of CPV system is shown in Figures 5.3 and 5.4.

The hydrogen compression system and the electrolyser system shown in Figures 5.3 and 5.4 are used to convert the electricity produced by CPV system into hydrogen and oxygen and compressed into cylinders for energy storage purpose. The design details and performance analysis of hydrogen production and compression system will be discussed in the next section of

this chapter. The Pyrheliometer is installed on the master tracker which needs to track the sun for its operation. The Pyranometer is placed horizontally on top of aluminium base. In order to log and analyze the CPV performance data, a control and analysis program is developed in LabVIEW software.

The LabVIEW program is developed to perform different tasks; it communicates and extracts the CPV performance data from data logger and it also controls the trackers for manual operation with control of linear actuators. Both data logger and setup controller communicate with the LabVIEW through serial communication. The CPV performance data received is based upon the total current and voltage output from the CPV systems. The data is then analyzed to compute the total system power output and system efficiency, which are plotted on real time and saved as a spreadsheet file. The power output $P_{CPV}$ and system efficiency $\eta_{CPV}$ of CPV are computed by Equations (5.1) and (5.2).

$$P_{CPV} = V_{CPV} \times I_{CPV} \qquad (5.1)$$

$$\eta_{CPV} = \frac{P_{CPV}}{DNI \times A_{con}} \qquad (5.2)$$

Where $V_{CPV}$ and $I_{CPV}$ are the total voltage and current output from the CPV system, respectively. The DNI is the beam irradiance received from pyrheliometer and $A_{con}$ is the total effective area of the concentrator. The description and performance analysis of individual systems are discussed in the following sections.

## 5.3 Mini Dish Cassegrain CPV System

Figure 5.5 shows the developed prototype of Mini Dish Cassegrain CPV system according to design as discussed in the previous chapters. The glass

homogeniser is TECHSPEC tapered light pipe made from N-BK7 material. Both primary and secondary concentrators are machined from aluminium block to make them light weight. The reflecting surface of both concentrators is further improved by coating a thin layer of aluminium. The reflecting material and its surface quality actually define the optical efficiency of concentrating assembly, which affect the overall efficiency of CPV system.

The silver material has highest reflectance over the whole solar spectrum and it provides the best option as reflecting surface to achieve higher optical efficiency. After silver, aluminium offers highest reflectance over whole solar spectrum. However, the main difficulty is the oxidation of silver that may lead to surface imperfectness and removal of coating. The reflectance curves for aluminium and silver layers, coated onto glass piece samples, are shown in Figure 5.6. The fluctuating curve of aluminium reflectance, is a result of slightly uneven coating.

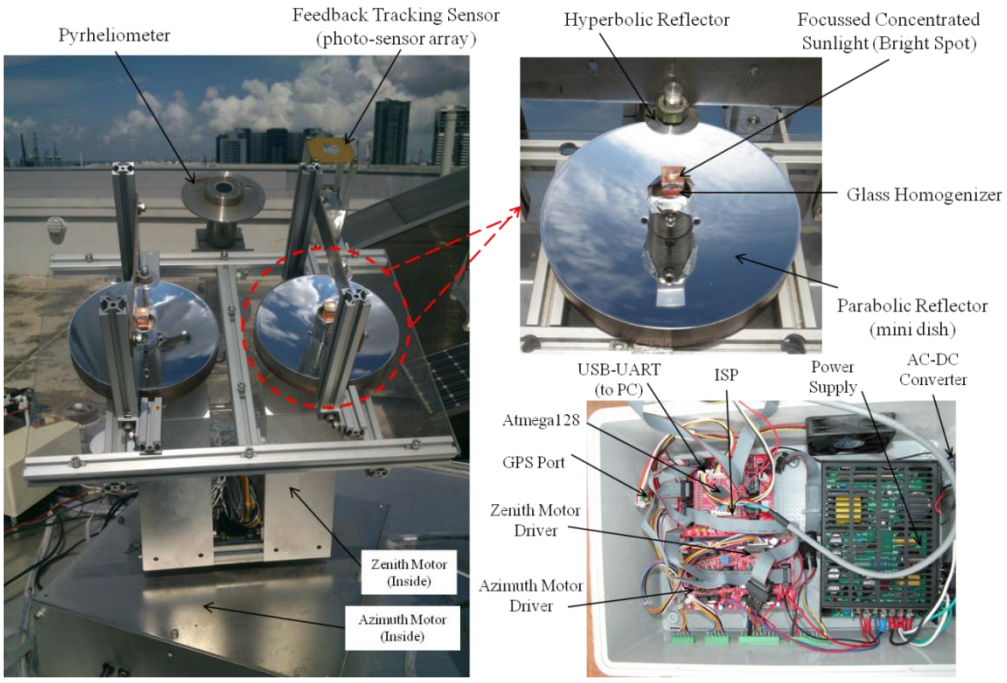


Figure 5.5: Developed CPV System on Mini Dish Cassegrain Design

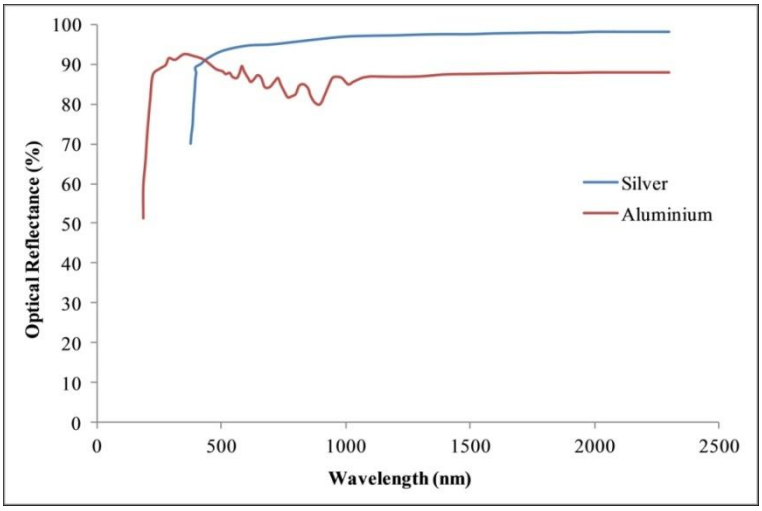


Figure 5.6: Optical Reflectance for Aluminium and Silver

For the current CPV system, the mini parabolic dishes were first tried to be coated with thin layer of silver onto aluminium dish with intermediate layer of chrome for better adhesion. The silver layer was then further coated with $SiO_2$ layer to protect silver from oxidation. The silver coating results are shown in Figure 5.7. The silver coating was first done onto glass piece and it can be seen from sample 1 to 4 that the quality of coating improved with increase in thickness of silver and $SiO_2$ layer. But due to imperfection of machined surface and high humidity, the silver coating on mini parabolic dish still oxidized after two and three days of coating. The silver coating was removed and mini dishes of aluminium were then finally coated with layer of aluminium with intermediate layer of epoxy for better adhesion. A layer of $SiO_2$ was then further applied onto aluminium coating to protect it from oxidation and other environmental effects.

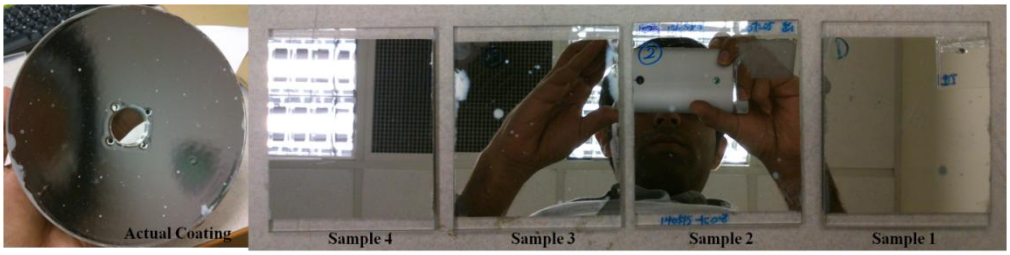


Figure 5.7: Silver Coating Problems on Mini Parabolic Dish

Current CPV system is based upon two parabolic dishes, each with one MJC attached at the end of homogeniser. The perfect bright spot of concentrated rays can be seen at inlet of homogeniser, which verifies the design of concentrating assembly. The MJC is further attached to an aluminium vacuum chamber heat spreader and an aluminium heat sink for heat dissipation, using thermal tape. The MJC cells are connected in series. A temperature sensor is attached at the heat sink to measure the cell back plate temperature, as higher the temperature lowers the efficiency. The performance analysis of mini dish cassegrain CPV system based upon the real field operation, is discussed in the next section.

### 5.3.1 Experimental Investigation of Mini Dish Cassegrain CPV System

Figure 5.8 shows the maximum performance potential of mini dish CPV system in form of system efficiency, in the morning and noon time. It can be seen that the maximum system efficiency of 19% is achieved by mini dish CPV system. The main reason of system performance comparison in the morning and noon time is to see the effect of temperature onto cell performance. The shown temperature profile is for heat sink temperature. It can be seen that the system is operating at efficiency of 19% when temperature is changing from 30-35$^{o}$C and drops to 17.5% when heat sink or back plate temperature is at 45-48$^{o}$C, which is due to high irradiance at noon time, as cell performance is normally rated at higher irradiance but at low temperature. From the results, it can be seen that although the irradiance is higher at noon time but because of increase in temperature, the cell performance decreases.

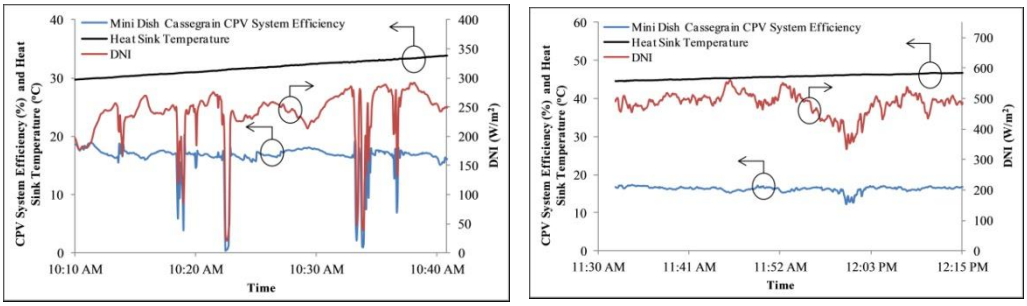


(a) (b)

Figure 5.8: Maximum Performance Potential of Mini Dish Cassegrain CPV System (a) in Morning (b) at Noon

In order to investigate the performance variations of the CPV system, Figure 5.9 shows the performance curves of mini dish cassegrain CPV system for whole day operation. From the results it can be seen that the efficiency of CPV system is higher in morning and afternoon time, while it drops by 3% during noon time. One of the possible reason for this efficiency drop is the higher back plate temperature. On the other hand, after 3:00 pm, it can be seen that the back plate temperature is still as high as in noon time but with comparable higher efficiency. The irradiance at noon time is higher than afternoon and higher irradiance corresponds to higher concentration or radiation flux at solar cell area. This causes higher cell temperature, resulting in lower efficiency than at low irradiance.

It must be noted that the temperature profile shown here represents heat sink temperature, not cell temperature as its difficult to measure cell temperature during operation due to sensor placement limitations. However, it takes time to see the effects of high cell temperature on heat sink temperature, as compared to instantaneous increase in cell temperature due to high flux. Because cell heat is also lost through natural convection near to cell surface and through heat spreader. However, this reason can be justified in form of

increasing back plate temperature after getting maximum irradiance of day, around 1:30 pm. On the other hand, the effect of higher back plate temperature can also be seen as efficiency is 1.5% lower in afternoon time than in morning but at same irradiance.

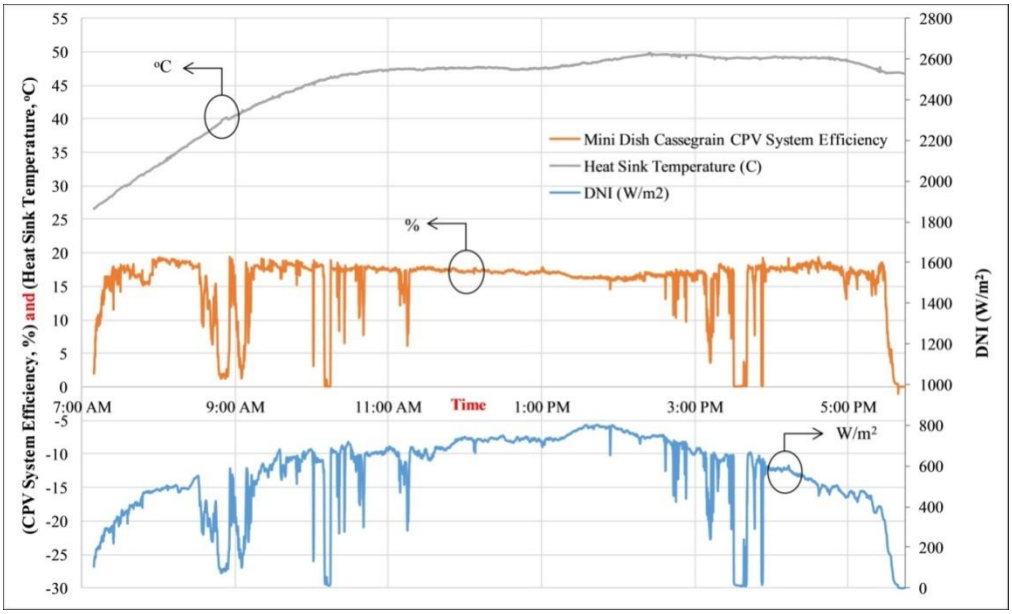


Figure 5.9: Performance Characteristics of Mini Dish Cassegrain CPV for whole Day Operation

Figure 5.10 shows the corresponding total power, voltage and current output of mini dish cassegrain CPV system for same DNI profile as efficiency results shown in figure 5.9. It can be seen that the total output of CPV system is around 4W (per cell 2W) with total voltage of 4.5-4.8V. As MJC cells are connected in series, so the same current is flowing through each cell with maximum value of around 1A. It can be seen that both power and current output are proportional to DNI. However, voltage output decreases with increase in DNI as the maximum power point of cell at higher concentration shifts towards the lower voltage level. For higher concentrations, the fill factor starts to decrease with increase in concentration, causing the maximum power point voltage to decrease because maximum power point current varies in

proportional to concentration, as given in appendix C.2. Another dominant parameter causing decrease in voltage with increase in concentration, is the cell temperature, because maximum power point voltage decreases with increase in temperature, appendix C.2.

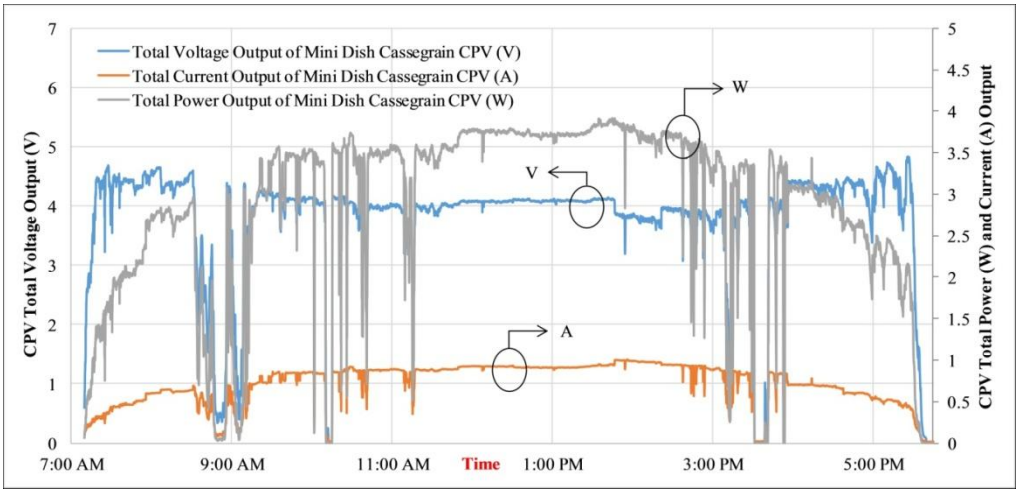


Figure 5.10: Total Voltage, Current and Power output from Mini Dish Cassegrain CPV

The performance curves for the mini dish cassegrain CPV systems are also shown in Figures 5.11 and 5.12 for other two different days testing, to see consistency in the performance. Same consistency of the results can be seen as the efficiency of CPV system is decreasing with increase in temperature and irradiance. It can also be seen the lowest efficiency of the day occur at highest irradiance and highest back plate or heat sink temperature. From Figure 5.11, it can be seen that the overall efficiency of CPV system is higher as compared to performance curve in Figure 5.12. The main reason for this difference is the different peak irradiance in both days. For performance curve in Figure 5.11, maximum irradiance doesn't go above 600 W/m$^2$. However, for other day it is touching about 800 W/m$^2$. It may be noted that the sudden peaks in the performance curve doesn't reveal the actual performance of CPV system due

to calculation confusion due to delay in data logging during transient response of the system.

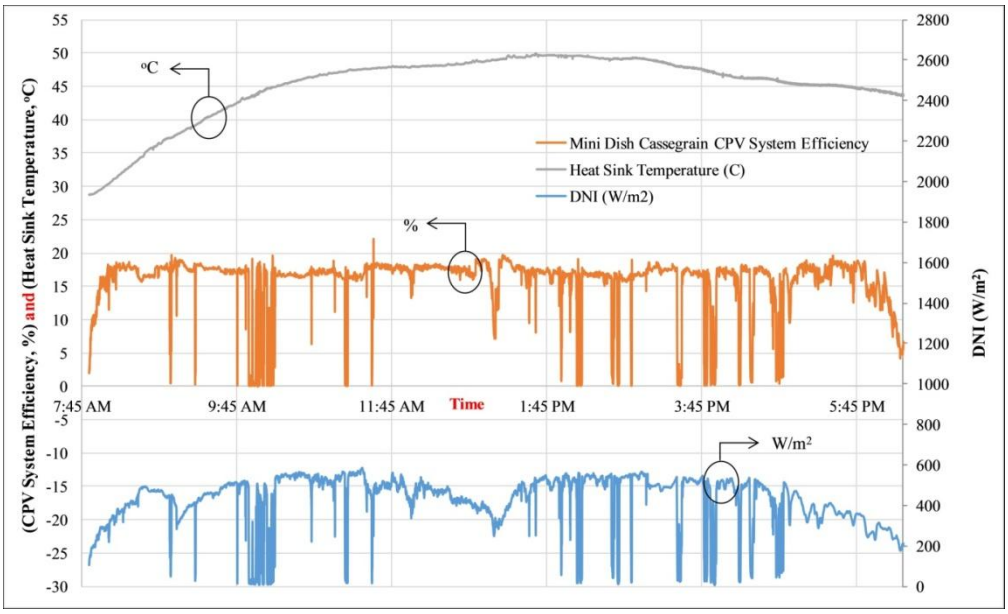


Figure 5.11: System Efficiency against DNI and Heat Sink Temperature for Mini Dish Cassegrain CPV for Experiment Set-2

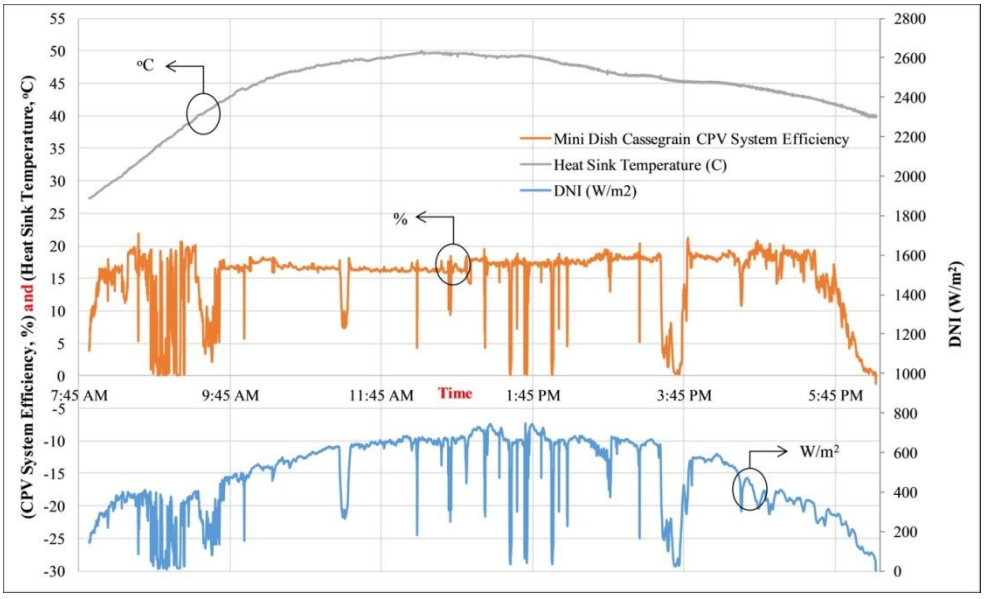


Figure 5.12: System Efficiency against DNI and Heat Sink Temperature for Mini Dish Cassegrain CPV for Experiment Set-3

In the previous chapter, the normalized power output curve of concentrating assembly based upon the ray tracing simulation results was shown. In figure 5.13, the experimental and simulated normalized power output curves are

shown for mini dish cassegrain CPV system. It must be noted that the simulated curve is based upon the total radiation flux output at homogeniser outlet, determined through ray tracing simulation same as discussed in the previous chapter. However, the experimental normalized power output curve is based upon the actual total electrical output of the CPV system as it is the electrical energy not the radiation flux that is of main interest in CPV system.

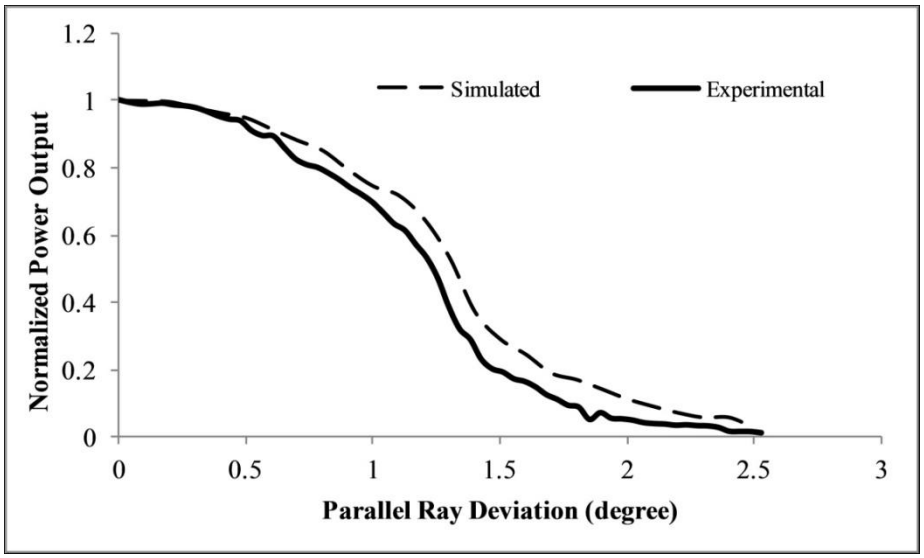


Figure 5.13: Experimental and Simulated Normalized Power Output Curve for Mini Dish Cassegrain CPV

The experimental normalized power curve was obtained at solar noon time around 1:15 pm as sun is at maximum elevation and only azimuth angle is changing. Moreover, irradiance at solar noon is highest and not changing. For experimental normalized curve, a constant load corresponding to maximum power point at start of experiment was attached and the tracker was stopped. The angular deviation was measured by calculating the azimuth angle corresponding to starting and ending time of the experiment. From the normalized power output curves, it can be seen that the trend of experimental and simulated curve is same. But the experimental normalized curve is slightly lower than the simulated curve, at higher angular deviation. This difference is

because of the fact that the experimental normalized power curve is based upon the electrical power output and because of optical loss at higher angular deviations, the maximum power point of CPV system is shifting as constant load is applied across cell output, which causes less power production due to lower operating efficiency. On the other hand, simulated curve is based upon the radiation flux, which is not affected by the load resistance. For $0.3^{o}$ angular deviation, the designed tracking accuracy, the performance of the CPV system is highest and maximum.

## 5.4 Fresnel Lens-Glass Homogeniser CPV System

The fabricated Fresnel Lens-Glass Homogeniser CPV system is shown in Figure 5.14. The developed system consist of a small CPV module with four MJC cells and an 2 x 2 array of Fresnel Lenses, according to design as discussed in the previous Chapter 4. The CPV module is mounted onto aluminium frame of developed two axis solar tracker. The Fresnel lens array is made of PMMA plastic with optical efficiency of 80%. The glass homogeniser is tapered glass rod made of quartz material. The glass homogeniser is attached onto MJC submount with optically graded silicone. Each MJC submount is attached to heat sink with thermal glue for heat dissipation. A thermistor type temperature sensor is attached to heat sink to measure cell back plate temperature. All four MJCs are connected in series and the total power output is connected to MPPT resistor, which is then logged through data logger. A perfect bright spot at centre of homogeniser verifies the design of concentrating assembly. In order to investigate the real field performance of

developed Fresnel Lens-Glass Homogeniser CPV system, the experimental results are discussed in the next section.

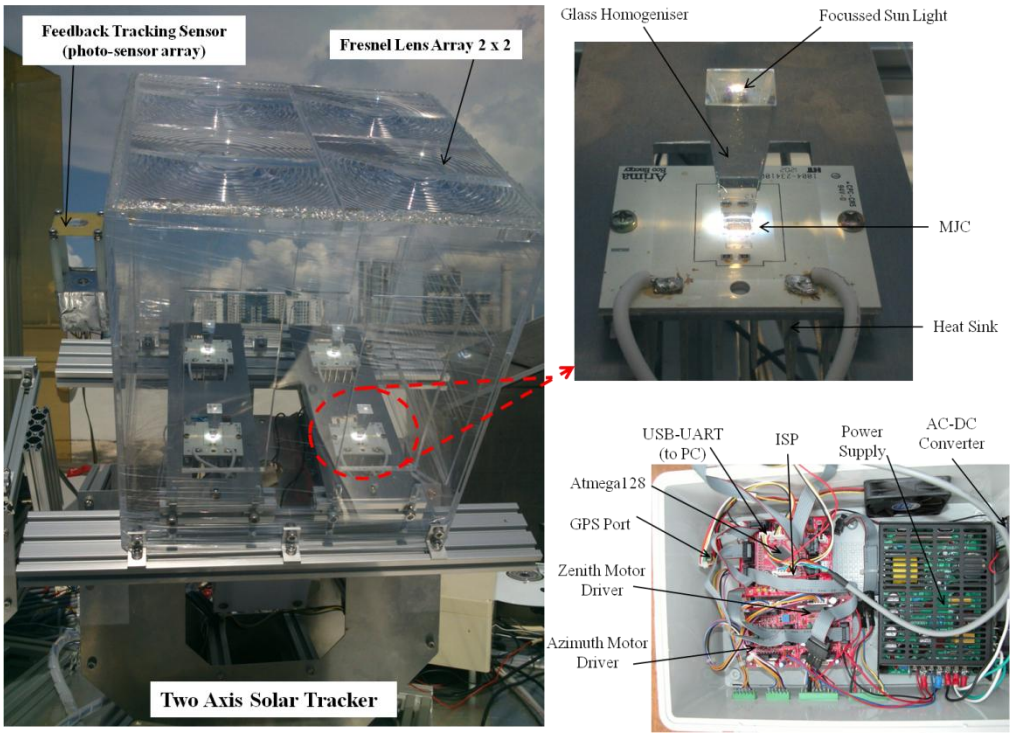


Figure 5.14: Developed CPV System on Fresnel Lens-Glass Homogeniser Design

### 5.4.1 Experimental Investigation of Fresnel Lens-Glass Homogeniser CPV System

Figure 5.15 shows the experimental results of the maximum performance potential of the developed Fresnel Lens-Glass Homogeniser CPV system. Similar to mini dish cassegrain CPV system, the results shown for Fresnel lens are for two different time slots, one for morning and the other for noon time, to see the effect of temperature on the system performance. From experimental results, it can be seen that the maximum efficiency recorded is 28%, which is same as commercial CPV systems and much higher than the mini dish CPV system, with same type of MJC cell. From Figure 5.16(b), it can be seen that the efficiency of system reduces around 3% at higher temperatures during

noon time. The only major reason for lower efficiency of mini dish CPV system is the lower optical efficiency of concentrating assembly, due to surface quality of reflecting surfaces as mini parabolic dishes were coated two time, which resulted in some surface defects. Moreover, the optical reflectance of aluminium varies between around 80-88% and due to two stage concentration, the combine reflectance of two surfaces decreases, causing lower efficiency of mini dish CPV system. Although optical efficiency of Fresnel lens is around 80%, but due to single stage concentration, higher system efficiency is achieved.

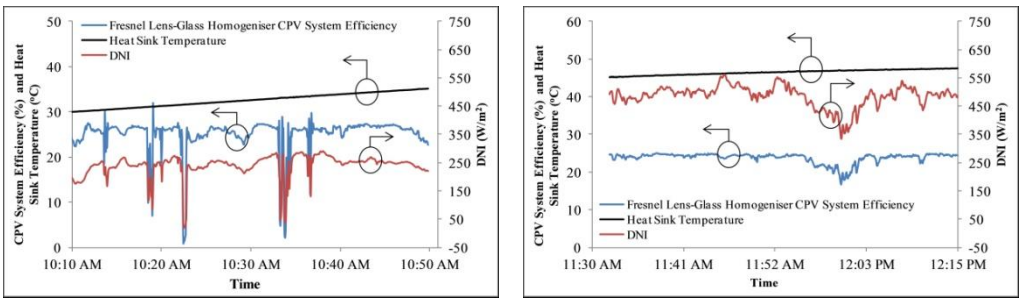


(a) (b)

Figure 5.15: Maximum Performance Potential of Fresnel Lens-Glass Homogeniser CPV System (a) in Morning (b) at Noon

Now, in order to investigate the performance variations of Fresnel Lens-Glass Homogeniser CPV system during whole day operation, the performance curves are shown in Figure 5.16. For comparison, it is worthy to mention here that the performance curves of Fresnel Lens-Glass Homogeniser CPV system presented in Figure 5.16 are recorded for the same day and same time with same DNI profile as that of performance curves of mini dish CPV system, shown in Figure 5.9. A similar trend of results can be seen here as higher system efficiency observed during morning period with lower heat sink temperature. However, efficiency dropped by 3% at solar noon time with highest solar irradiance received and heat sink temperature. The efficiency

curve then increases in the afternoon as irradiance and heat sink temperature start to drop.

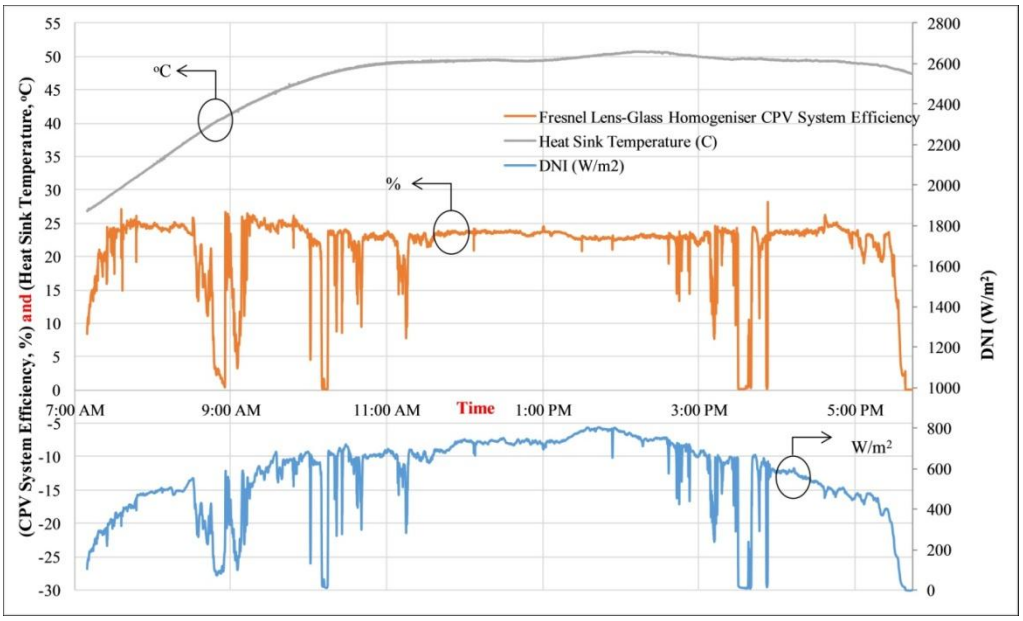


Figure 5.16: Performance Characteristics of Fresnel Lens-Glass Homogeniser CPV for whole Day Operation

Figure 5.17 shows the total power output of Fresnel Lens-Glass Homogeniser CPV system with variation in total voltage and current output of the system for whole day operation. From the results, it can be seen that the total power output of the system is around 10W (per cell 2.5W), which is very high as compared to mini dish CPV system. The first reason is that there are four MJC connected in series in Fresnel Lens-Glass Homogeniser CPV system. The second reason is the higher efficiency of Fresnel Lens-Glass Homogeniser CPV system, causing higher power output per cell. However, similar trend for current and voltage profile can be seen as current is increasing with increase in DNI or power, while voltage output is decreasing due to shifting of maximum power point to low voltage level. The total current output of Fresnel Lens system is higher than that of mini dish system, which is also due to the higher system efficiency and due to series connection, the same current is flowing through each cell.

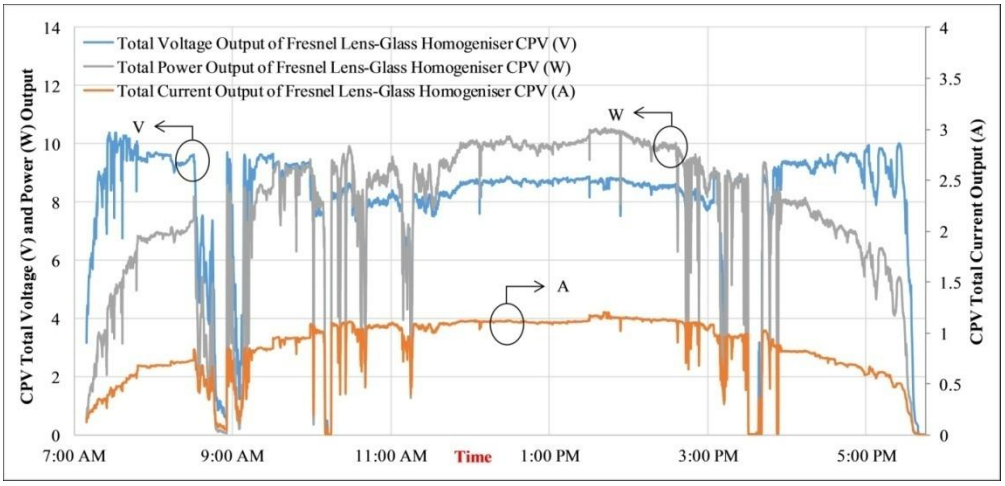


Figure 5.17: Total Voltage, Current and Power output from Fresnel Lens-Glass Homogeniser CPV

In order to see the consistency of the performance of CPV system, the performance curves of other two days testing are shown in Figures 5.18 and 5.19. The operating efficiency of CPV system is almost same as mentioned in maximum performance potential curves, shown in Figure 5.15. Moreover, similar trend of efficiency drop can also be seen due to effects of irradiance and temperature. However, overall higher efficiency is observed for Figure 5.18 than 5.19, which is because of the lower value of peak irradiance during whole day operation.

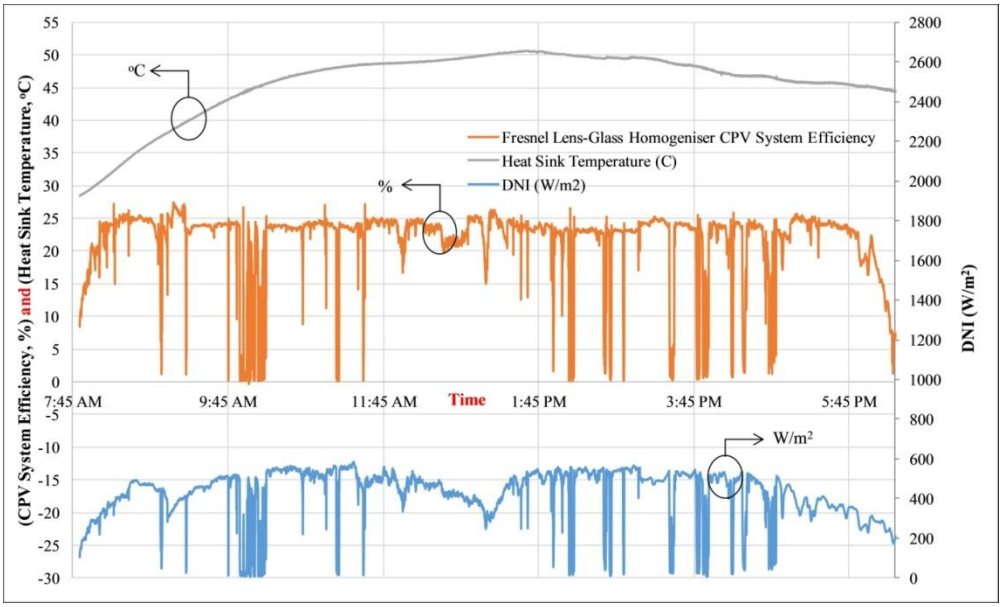


Figure 5.18: System Efficiency against DNI and Heat Sink Temperature for Fresnel Lens-Glass Homogeniser CPV for Experiment Set-2

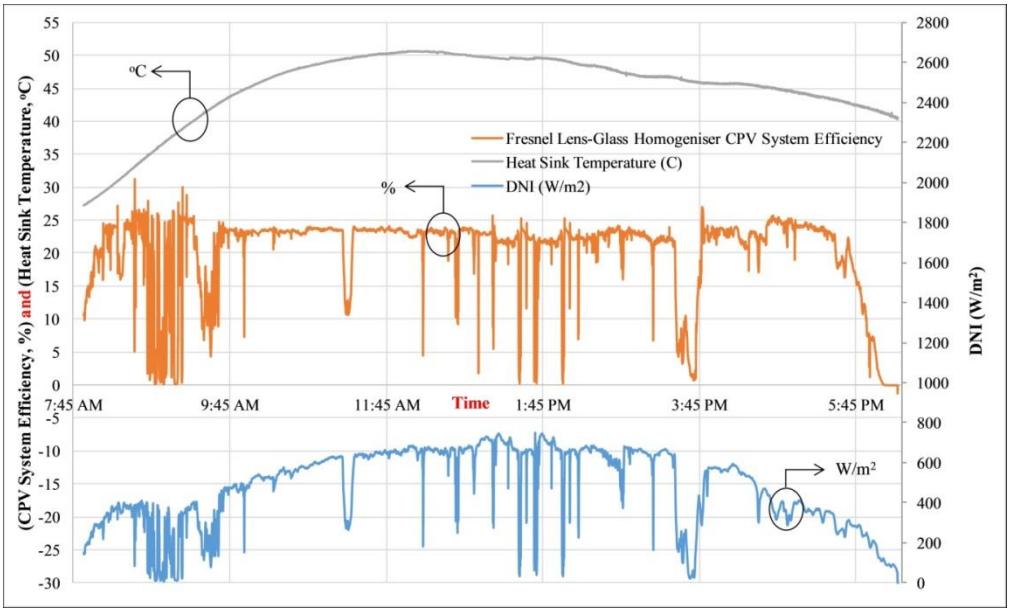


Figure 5.19: System Efficiency against DNI and Heat Sink Temperature for Fresnel Lens-Glass Homogeniser CPV for Experiment Set-3

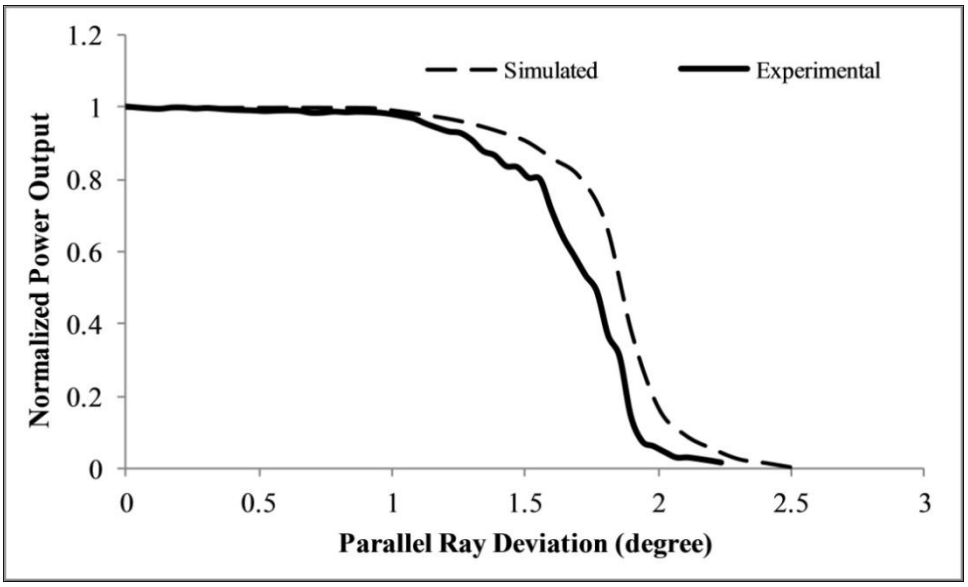


Figure 5.20: Experimental and Simulated Normalized Power Output Curve for Fresnel Lens-Glass Homogeniser CPV

In order to study the acceptance angle of the developed CPV system, Figure 5.20 shows the normalized power output curve obtained through experimental results and compared with the simulated normalized power output. The simulated normalized power curve is based upon the radiations flux output at outlet aperture of homogeniser through ray tracing simulation, as discussed in the previous chapter. The experimental normalized power curve is obtained

from electrical power output with constant load, during solar noon and with clear sky conditions, by following the procedure as mentioned in the previous section for case of mini dish cassegrain CPV system.

The normalized power output curves shows that the CPV system has acceptance angle of around $1^o$ for which the normalized power remain as high as 98%. It can be seen that the trend of experimental normalized curve is same as that of simulated curve. However, as angular deviation increases, the gap between experimental and simulated curves increases. This is because of the shift of maximum power point of cell that resulted in loss in efficiency and power output. As a constant load is connected across the cell during experiment. In addition, as CPV system has higher power output at higher angular deviation, which depicts that it can be operated with low tracking accuracy requirement. However, for the developed tracking system with $0.3^o$ designed tracking accuracy, highest performance of the CPV system can be assured.

## 5.5 Fresnel Lens-Reflective Homogeniser CPV System

The third CPV system developed for performance analysis and comparison of different CPV design, is shown in Figure 5.21, according to the design discussed in previous chapter, in which radiations are directly focussed onto MJC. A reflective type homogeniser is attached at the periphery of the MJC. This reflector does not cover the area of cell but directs the radiation towards cell area through reflection, in case of higher angular deviation. This reflective type homogeniser is made of aluminium without any further coating. Therefore, there is some optical loss due to reflectivity of aluminium is there

when rays hit the reflector. However, in case of glass homogeniser, the optical losses are less, but only due to absorbance of the glass material.

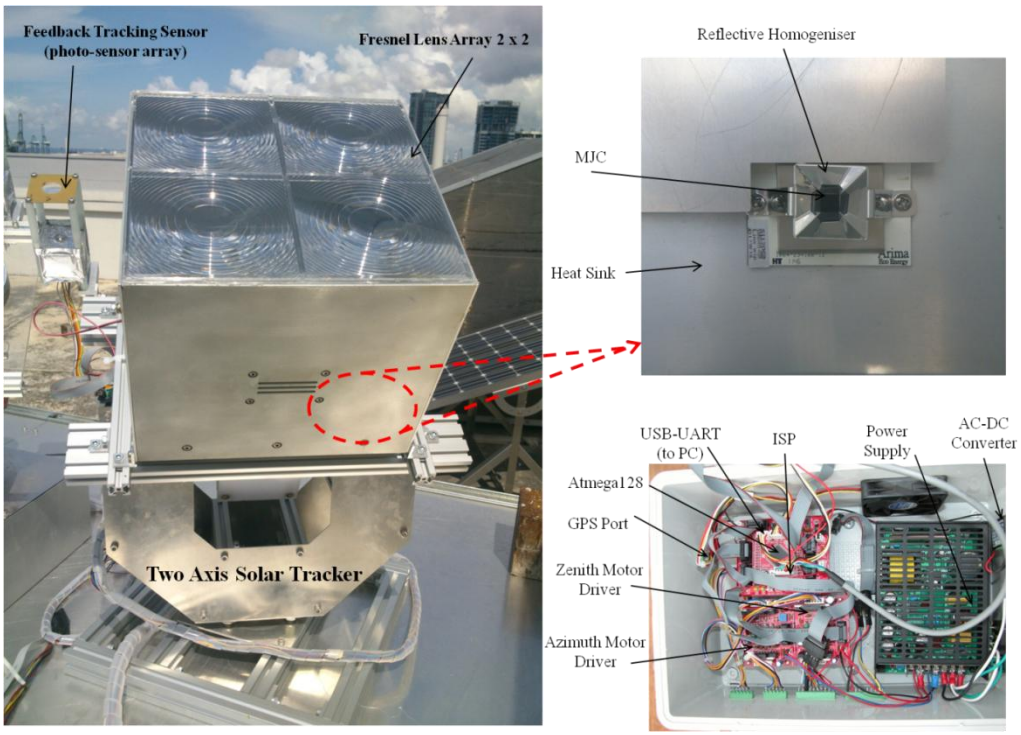


Figure 5.21: Developed CPV System on Fresnel Lens-Reflective Homogeniser Design

The 2x2 array of Fresnel lens is same as used in case of Fresnel lens CPV system with glass homogeniser and made of PMMA plastic. The MJC submounts are screwed to an aluminium base with thermal tape, which not only provide mounting support but also acts as heat sink. A thermistor type temperature sensor is attached with aluminium base plate. The MJC submounts are connected through series electrical connection for higher voltage output. The performance analysis of Fresnel Lens-Reflective Homogeniser CPV system is discussed in next section.

### 5.5.1 Experimental Investigation of Fresnel Lens-Reflective Homogeniser CPV System

In order to investigate the maximum performance potential of current CPV system, the performance curves are shown in Figure 5.22, for morning and

noon time. From the results, it can be seen that the maximum efficiency of the CPV system is recorded as 28%, which is same as Fresnel Lens-Glass Homogeniser CPV system. However, the sudden peaks in the performance curves do not represent the true system performance, rather caused by the data logging delay due to system transient response. The 3% drop in efficiency is observed as heat sink temperature and irradiance goes high during operation at noon time. In order to see the continuous variations in the performance of Fresnel Lens-Reflective Homogeniser CPV system, the performance curves are shown in Figure 5.23, for whole day operation.

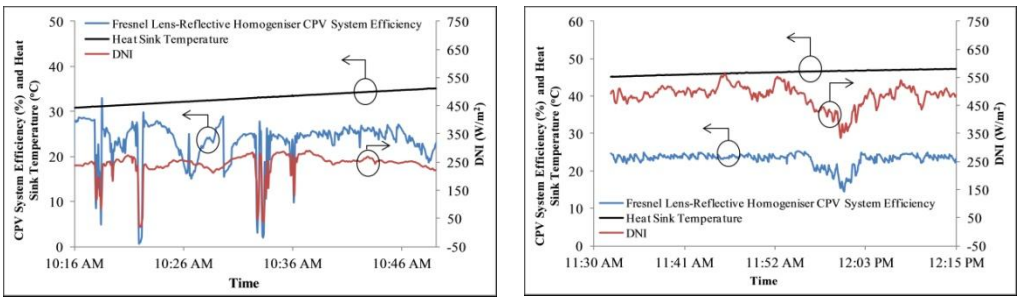


(a) (b)

Figure 5.22: Maximum Performance Potential of Fresnel Lens-Reflective Homogeniser CPV System (a) in Morning (b) at Noon

From Figure 5.23, it can be seen that the CPV system efficiency is almost 25% for whole day operation, same as Fresnel lens CPV system with glass homogeniser. However, some efficiency drop is observed at solar noon time because of the higher DNI that resulted in high cell temperature and the reason for this efficiency drop is already explained in previous sections that higher DNI results in high concentration at cell area, causing increase in cell temperature. For comparison, the performance curve mentioned in Figure 5.23 is for the same DNI profile as that of other two CPV systems.

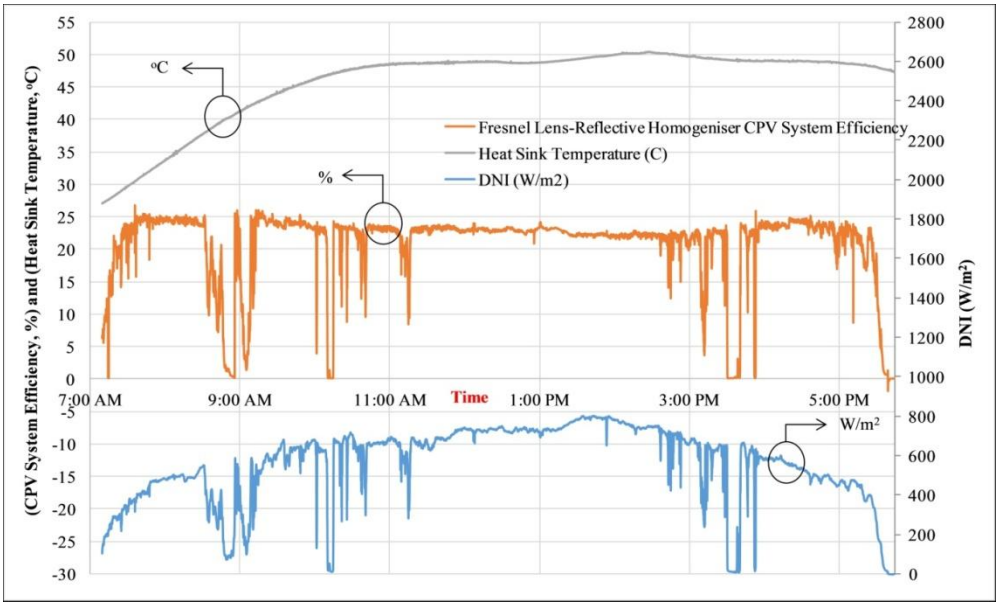


Figure 5.23: Performance Characteristics of Fresnel Lens-Reflective Homogeniser CPV for whole Day Operation

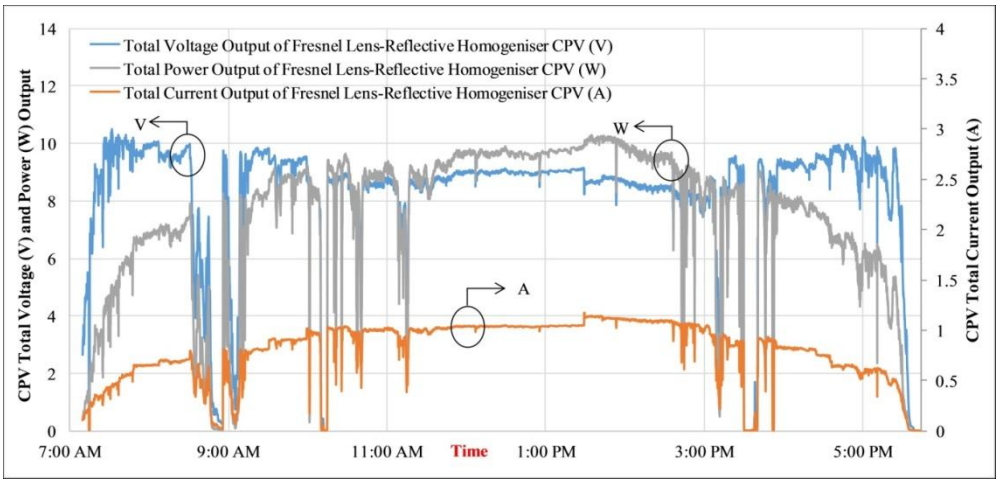


Figure 5.24: Total Voltage, Current and Power output from Fresnel Lens-Reflective Homogeniser CPV

Figure 5.24 shows the total power output, current and voltage of current CPV system. It can be seen that the maximum power output recorded for current CPV system is around 10W, which is same as achieved through Fresnel lens CPV system with glass homogeniser. However, current output is slightly lower and voltage output is slightly higher than the Fresnel lens CPV system with glass homogeniser. However, the overall performance in form of efficiency and power output is almost same, which also implies that the optical loss in glass homogeniser is almost negligible. In order to observe the

consistency of the CPV system performance, the results for other two different days are shown in Figures 5.25 and 5.26. The efficiency of the CPV system is varying around 25% with ±1% change, because of variation in DNI and heat sink temperature. However, overall performance of the system remains as high as reported through maximum potential curves.

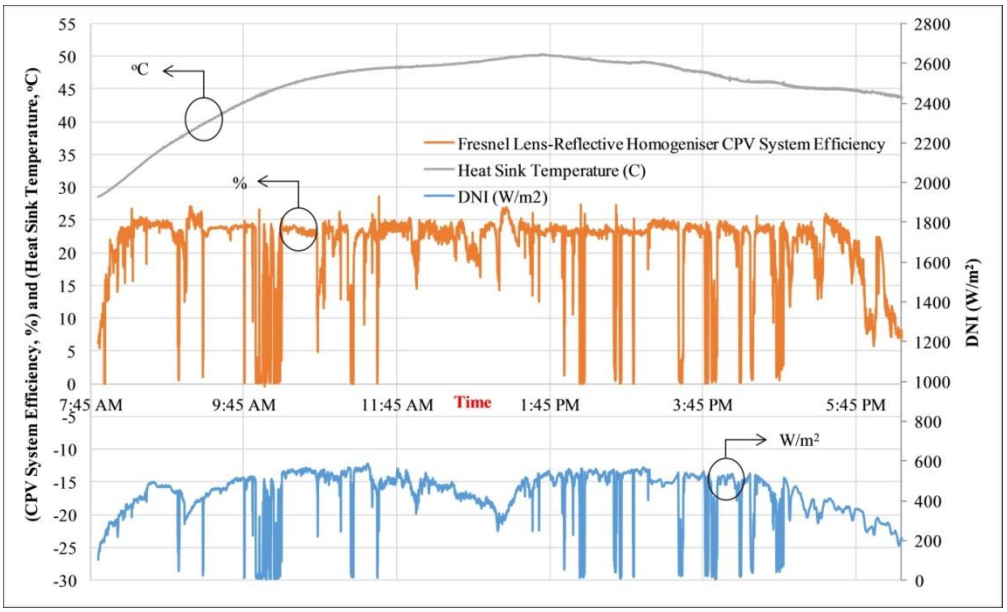


Figure 5.25: System Efficiency against DNI and Heat Sink Temperature for Fresnel Lens-Reflective Homogeniser CPV for Experiment Set-2

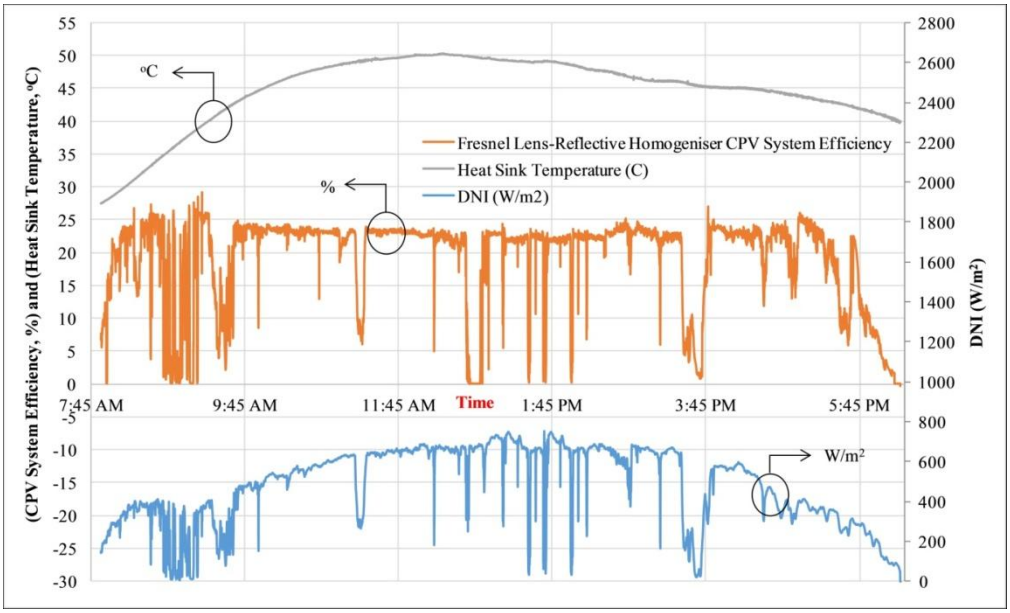


Figure 5.26: System Efficiency against DNI and Heat Sink Temperature for Fresnel Lens-Reflective Homogeniser CPV for Experiment Set-3

Figure 5.27 shows the experimental and simulated normalized power output curves for Fresnel Lens-Reflective Homogeniser CPV system. The experimental curves is based upon electrical power output with constant load, at solar noon time, while the simulated curve is based upon the total flux at cell area. From the normalized power curve, it can be seen that the acceptance angle of current CPV system is around $0.7^{o}$. Even before $0.7^{o}$, a very slight gradual decrease in normalized power can be seen which may be due to uneven distribution of radiation flux over cell area as lens is directly focussing light onto the solar cell. After $0.7^{o}$, a gradual drop in normalized power can be seen, caused by the optical loss due to reflectance of reflective homogeniser. At $0.7^{o}$, same drop in simulated normalized power curve can also be seen, which verifies that the loss is due to interaction of rays with reflective homogeniser. However, gradual drop in experimental normalized power, as compared to simulated curve, is because of reflectivity and surface quality of aluminium reflective homogeniser and due to shift in the maximum power point of the solar cell, which are not considered in the simulation.

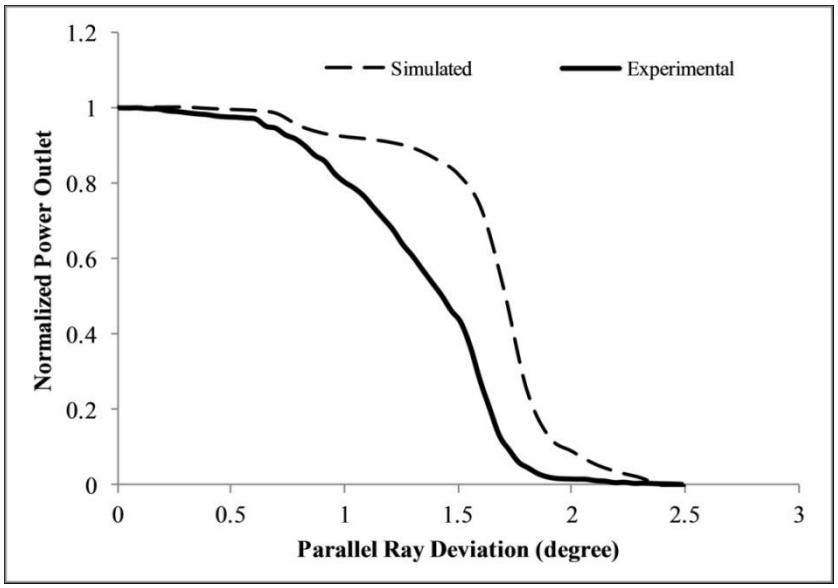


Figure 5.27: Experimental and Simulated Normalized Power Output Curve for Mini Dish Cassegrain CPV

## 5.6 Discussion on Performance Comparison of Developed CPV Systems

Up till now, the performance of each of the CPV systems is investigated separately. However, in this section the performance of all three developed CPV systems is compared and discussed on the same ground. Figure 5.28 shows the experimental and simulated normalized power curve for all three CPV system.

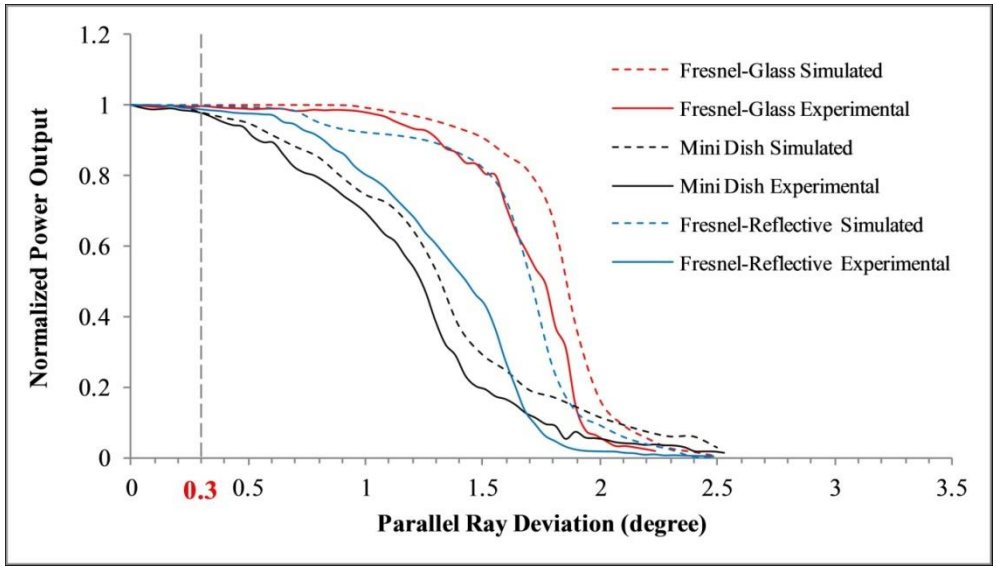


Figure 5.28: Comparison of Experimental and Simulated Normalized Power Output Curve for Developed CPV Systems

At first glance, it can be seen that the Fresnel lens CPV system with glass homogeniser has highest acceptance angle among all three CPV system, followed by the Fresnel lens CPV system with reflective homogeniser and mini dish cassegrain CPV system. The main reason for the lowest acceptance angle of mini dish CPV system is due to double stage concentration with high sensitive to angular deviation. As incident rays are reflected two time, so small deviation in incident rays causes rays to deflect with angle two time higher than the single stage reflector concentration in case of Fresnel Lens CPV

system. From comparison of mini dish CPV system with Fresnel Lens-Glass Homogeniser CPV system, as the inlet aperture of glass homogeniser is same in both system, a small deviation in incident rays causes larger linear deviation of focussed light at homogeniser inlet which causes higher optical loss at higher angular deviation as compared to Fresnel Lens design.

The difference between normalized curve for Fresnel Lens CPV system with glass homogeniser and with reflective homogeniser is because of the fact that in case of glass homogeniser design, the rays are concentrated onto 12 mm x 12 mm area instead of 5.5 mm x5.5 mm cell area, as in reflective homogeniser design. This causes a decrease in simulated normalized power curve after $0.7^{o}$ deviation, which is due to slight loss by reflective homogeniser as compared to glass homogeniser in which light propagates through TIR. However, the experimental normalized curve is of main importance here as the loss due to reflective homogeniser is higher than glass homogeniser, which is loss due to reflectivity of material than TIR. Despite the difference in performance, all three CPV systems have almost 100% normalized power for angular deviation of $0.3^{o}$, which is the accuracy of the developed tracking system. Therefore, the difference in the conversion efficiencies of CPV systems is due to optical efficiency loss due to optical material limitations. Summary of the CPV performance related to all CPV designs, is given in Table 5.1.

Table 5.1: Summary of Performance of Developed CPV systems

| CPV Design | Maximum Efficiency | Maximum Power Output | No. of MJC Used |
|---|---|---|---|
| Mini Dish Cassegrain CPV system | 19% | 4W | 2 |
| Fresnel Lens-Glass Homogeniser CPV System | 28% | 10W | 4 |
| Fresnel Lens-Reflective Homogeniser CPV System | 28% | 10W | 4 |

## 5.7 CPV-Hydrogen System Description

Based upon the experimental investigation of the CPV systems, it was found that the Fresnel Lens CPV system with glass homogeniser showed best performance among all three developed CPV systems. Therefore, in order to analyze the performance of CPV system for production of hydrogen, Fresnel Lens-Glass Homogeniser CPV system was selected to be coupled with the electrolysers to investigate the CPV-Hydrogen system performance. Figure 5.29 shows the schematic of the CPV-Hydrogen system developed for its experimental performance analysis.

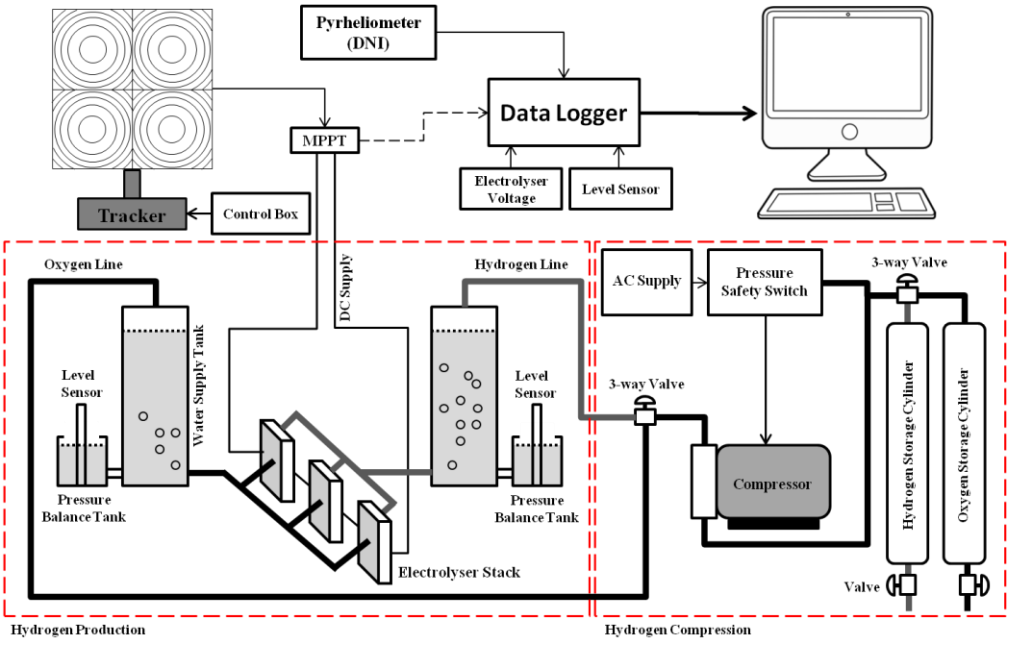


Figure 5.29: Schematic of Control Circuit and System Arrangement for CPV-Hydrogen Experimental Setup

The CPV-Hydrogen system consists of three main sub-systems; one is the Fresnel Lens CPV system with glass homogeniser to convert solar radiations into DC electricity, second is the hydrogen production system that consists of a stack of PEM electrolyser cells connected in series and produces hydrogen and oxygen from electrolysis of distilled water and the last one is the hydrogen

compression system that compresses, delivers and stores the produced hydrogen and oxygen into storage cylinders, for energy storage or other downstream applications like fuel cell etc. The produced hydrogen and oxygen gases are first temporarily stored over water in water supply tanks and then sucked from there through the compressor, to be stored into storage cylinders.

To monitor and record the performance parameter of CPV-Hydrogen system, the output of each of the component is recorded through data logger. The fabricated CPV-Hydrogen system is shown in figures 5.30 and 5.31. However, the details and performance of the CPV system are discussed in the previous section. In the left side of Figure 5.30, the developed hydrogen production system can be seen with the stack of three PEM electrolyser cells connected in series. Each side of electrolyser cell is connected to water supply tanks, which not only supply distilled water to the electrolysers but also provide temporary storage of produced gases over water, to measure the quantity of produced gases.

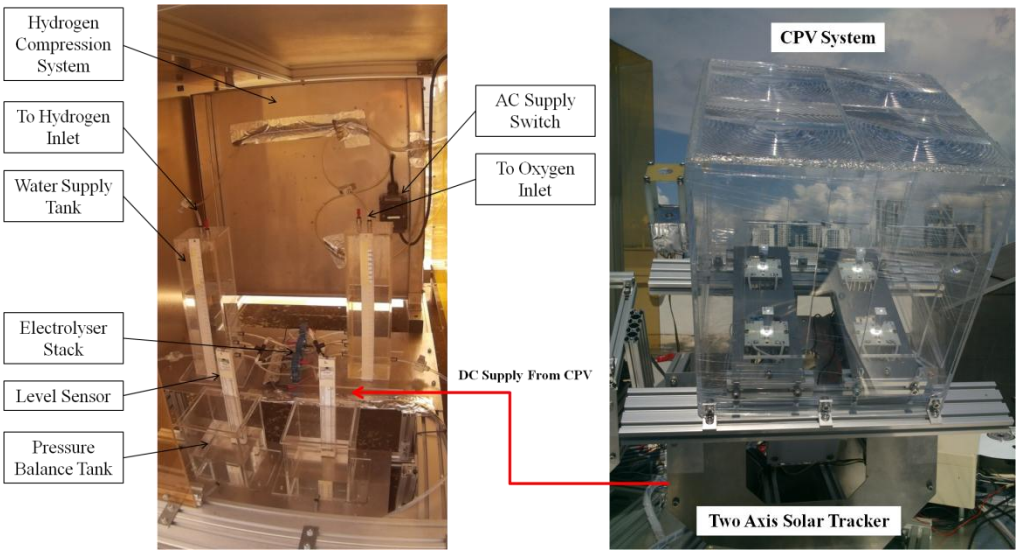


Figure 5.30: CPV-Hydrogen Experimental Setup

The water supply tank, which is closed to atmosphere, is connected to a pressure balance tank, which is open to atmosphere. So the water level in the water supply tank is kept at higher level and the water level in the pressure balance tank is kept at lower level. The gases are stored in water supply tank first and as a result, its water level goes down while the water level in pressure balance tank goes up to keep pressure balance in both tank as atmospheric. A level sensor is dipped into the pressure balance tank to measure the change in water level, which gives the amount of gases produced from electrolysis. The level sensor is a eTape from Milestone Technologies, whose resistance changes is calibrated in terms of water level change and measured through a voltage divider. The output of level sensor is also verified by the manual reading from graduated scale on water supply tank as the volume change in both tanks is same. When water level in the water supply tank goes to lower limit, the produced gases are sucked through the compressor and stored into the storage tanks. The hydrogen compression system is shown in Figure 5.31.


Figure 5.31: Hydrogen Compression System

One common compressor is used for both hydrogen and oxygen compression. However, when one gas is compressed, the flow line of the other gas is closed to avoid mixing. In order to ensure purity of the stored gases, the storage cylinders are first evacuated from any trapped air inside the cylinders. The purity of hydrogen gas is of prime importance in order to be used in downstream applications like fuel cell. Therefore, the purity of hydrogen gas was tested through the gas analyzer and the results before and after the supply of hydrogen gas are shown in Figure 5.32. The results in Figure 5.32(a) are for the case when the inlet port of gas analyser was open to atmosphere. However, in Figure 5.32(b), the results shown are for the case when produced hydrogen was supplied to gas analyser and 99.99% purity of the produced hydrogen was recorded.

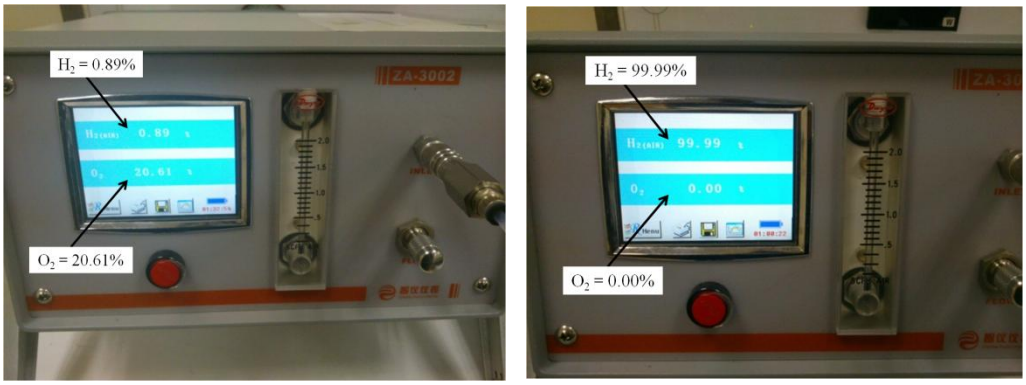


(a) (b)

Figure 5.32: Hydrogen Purity Analyzer (a) Before Hydrogen Supply (b) After Hydrogen Supply

In order to analyze and monitor the real time performance of the CPV-hydrogen system, LabVIEW code was written which was integrated with LabVIEW code written for CPV experimental investigation. The recorded data is analyzed to calculate the performance parameters of CPV-Hydrogen system with real time graphs plotting and the results are also saved in form of spread sheet file. The methodology regarding the calculation of performance

parameters of CPV-Hydrogen system in LabVIEW, is discussed in the next paragraph.

One of the most important performance parameters of CPV-Hydrogen system is amount of hydrogen produced, Equation (5.3), that depends upon the amount of the Faraday efficiency and the amount of current flowing through the electrolyser. With known amount of hydrogen produced at certain current flow, Equation (5.3) can also be used to calculate faraday efficiency of electrolyser. However, for current experimental study, the amount of hydrogen was measured through level sensor.

$$\dot{n}_{E,H2} = \eta_{EF} \frac{N_{EC} I_E}{n_E F} \qquad (5.3)$$

The efficiency of the electrolyser depends upon the amount of hydrogen production for certain amount of power supplied, as given by the Equation (5.4). The amount of hydrogen was measured experimentally and 237200 (J/mol) is the energy corresponding to thermo-neutral voltage of 1.23V. For Faraday efficiency of nearly 100%, the electrolyser efficiency can be taken as the ratio of thermo-neutral voltage and the operating voltage of electrolyser cell.

$$\eta_{EL} = \frac{\dot{n}_{E,H2} \bullet 237200}{I_E \bullet U_E} = \frac{\eta_{EF} \bullet 1.23}{U_E} \qquad (5.4)$$

The overall efficiency of solar to hydrogen conversion can be found through product of CPV efficiency and the electrolyser efficiency, as given by the Equation (5.5).

$$\eta_{CPV\_H2} = \eta_{CPV} \bullet \eta_{EL} \qquad (5.5)$$

From Equation (5.4), it can be seen that the efficiency of the electrolyser depends upon the operating voltage of the electrolyser. So, the electrolyser are designed to operate at lower voltage but with higher current flow, to get high hydrogen production rate. The characteristic curves for the PEM electrolyser are discussed in the next paragraph.

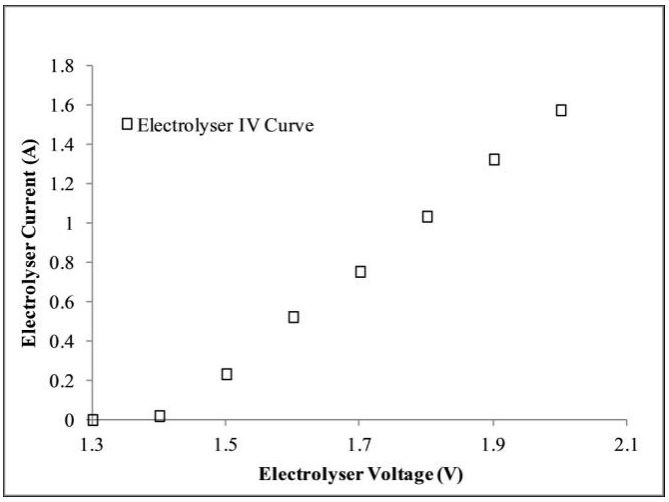


(a)

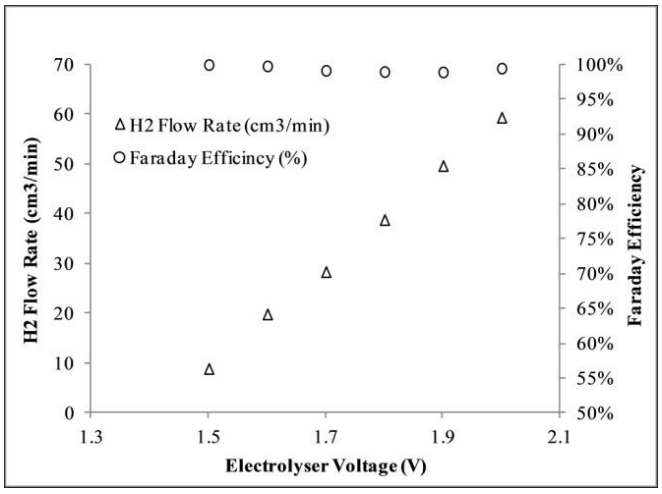


(b)

Figure 5.33: PEM Electrolyser Characteristics (a) IV-Curve (b) Production rate and Faraday Efficiency

For current CPV-Hydrogen system analysis, the utilized mini PEM electrolyser cell is from Horizon company. The performance curves for single cell of PEM electrolyser are shown in Figure 5.33. Figure 5.35(a) shows the

IV curve of the single electrolyser cell. It can be seen that the water splitting starts at about 1.4V and after that, the voltage and current are increasing almost linearly. Figure 5.33 (b) shows the measured Faraday efficiency of the electrolyser corresponding to the electrolyser cell voltage and $H_2$ production flow rate. It can be seen that the Faraday efficiency is almost 100% for complete operating range of electrolyser cell. Therefore, Equation (5.3) can also be used for to calculate the production of the hydrogen as Faraday efficiency is almost 100% for complete operating range of voltage.

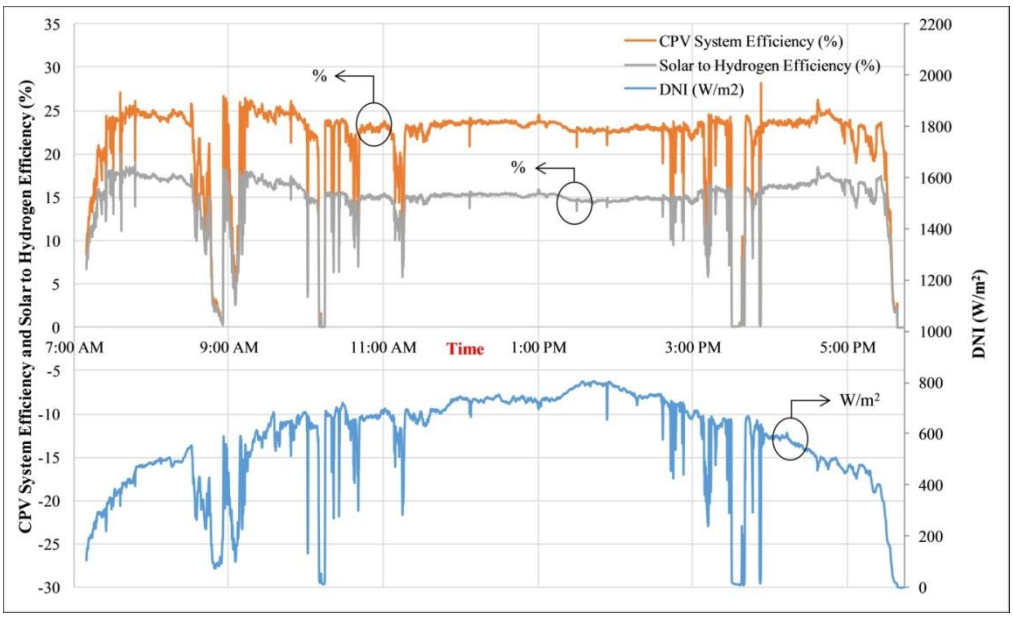


Figure 5.34: Solar to Hydrogen Conversion Efficiency and CPV Efficiency against DNI

## 5.8 Results and Discussion for CPV-Hydrogen System

Figure 5.34 shows the efficiency curves for CPV and CPV-Hydrogen system against the DNI curve, for whole day operation. The efficiency of the CPV system is almost constant with a small variation between 24-26%. However, the solar to hydrogen efficiency is of main importance here. From Figure 5.34, it can be seen that the maximum 18% of solar to hydrogen efficiency is

recorded. However, it drops to 15% with increase in DNI, which is due to drop in the efficiency of electrolyse that can be seen in Figure 5.35. In addition, as CPV-Hydrogen system is capable of converting solar energy to hydrogen with as low as 15% efficiency but still it is at least 3-4 times higher than the conventional stationery PV-Hydrogen systems.

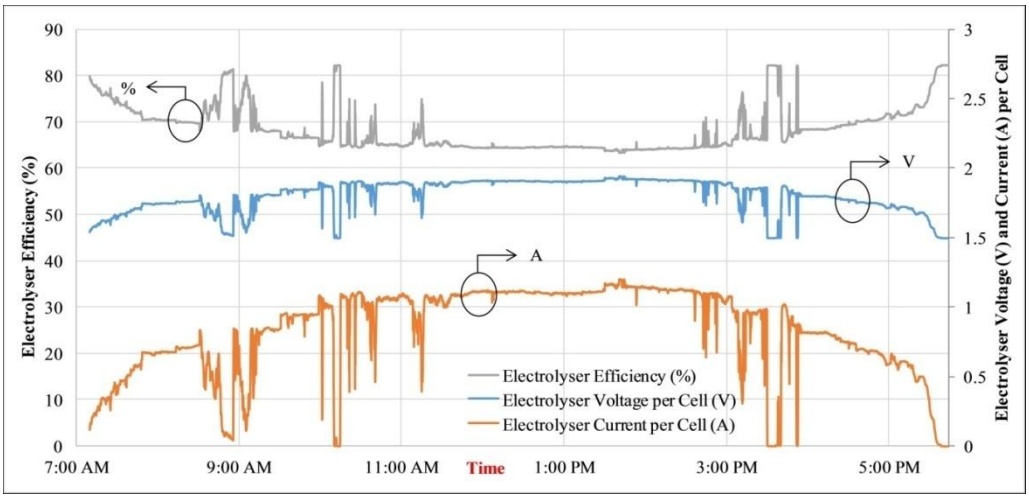


Figure 5.35: Electrolyser Efficiency, Voltage and Current Consumed per Cell of Electrolyser Stack for Whole Day Operation

Figure 5.35 shows the electrolyser efficiency, operating voltage and current consumed per cell of the electrolyser stack, for whole day operation. It can be seen that the voltage and current consumption of the electrolyser are directly proportional to the DNI received. Higher the DNI means higher power output of the CPV system. On the other hand, there is linear relationship between electrolyser voltage and current. So with the increase in the electrolyser current, the operating voltage of electrolyser also increases. It must be noted that only part of the power of CPV is used according to the maximum power capacity of electrolyser stack and the voltage control is managed by MPPT. As the efficiency of electrolyser almost entirely depends upon its operating voltage, given by Equation (5.4), therefore the drop in the electrolyser

efficiency can be seen with increase in the DNI, which causes the drop of solar to hydrogen efficiency. As CPV efficiency is almost constant, therefore, the overall efficiency of solar hydrogen system depends upon the electrolyser efficiency.

For efficient design, the electrolyser must be capable of water splitting with high current density but at lower voltage. As the system efficiency is changing during whole day, therefore, in order to see the overall average performance of the CPV-Hydrogen system, the experiment was repeated for different day and the summary of the results with overall average performance of the CPV-Hydrogen system is given in Table 5.2.

Table 5.2: Daily Average Performance of CPV-Hydrogen System

| Sr. No | Electrolyser Energy Consumed | Solar Energy Received | CPV average efficiency | Electrolyser average Performance | | Solar-Hydrogen average Performance | |
|---|---|---|---|---|---|---|---|
| | kWh/day | kWh/day | %/day | %/day | kWh/kg | %/day | kWh/kg |
| 1 | 0.046 | 0.207 | 22.4 | 67.5 | 48.87 | 15.1 | 217.83 |
| 2 | 0.045 | 0.199 | 22.3 | 66.0 | 49.94 | 14.7 | 223.77 |
| 3 | 0.046 | 0.200 | 23.1 | 67.8 | 48.65 | 15.6 | 210.94 |
| 4 | 0.042 | 0.191 | 22.0 | 67.6 | 48.77 | 14.9 | 221.95 |
| 5 | 0.040 | 0.180 | 22.1 | 68.5 | 48.12 | 15.2 | 217.36 |
| 6 | 0.024 | 0.106 | 22.2 | 70.4 | 46.84 | 15.6 | 211.07 |
| 7 | 0.053 | 0.238 | 22.3 | 66.7 | 49.43 | 14.9 | 221.79 |
| 8 | 0.044 | 0.194 | 22.5 | 66.8 | 49.32 | 15.0 | 219.30 |
| 9 | 0.038 | 0.168 | 22.4 | 66.1 | 49.87 | 14.8 | 222.44 |
| 10 | 0.037 | 0.169 | 22.0 | 68.6 | 48.05 | 15.1 | 218.30 |
| 11 | 0.057 | 0.257 | 22.1 | 65.7 | 50.20 | 14.5 | 227.27 |
| 12 | 0.053 | 0.233 | 22.6 | 66.3 | 49.72 | 15.0 | 219.73 |
| 13 | 0.049 | 0.214 | 22.9 | 66.5 | 49.57 | 15.2 | 216.74 |
| 14 | 0.041 | 0.184 | 22.1 | 68.3 | 48.25 | 15.1 | 218.14 |
| 15 | 0.041 | 0.184 | 22.3 | 68.9 | 47.85 | 15.4 | 214.34 |
| 16 | 0.032 | 0.141 | 22.8 | 70.8 | 46.54 | 16.1 | 204.35 |

From the average performance chart, it can be seen that the overall 15±1% of the solar to hydrogen efficiency is achieved on daily average. The average efficiency gives the real performance insight of the solar energy system as the solar energy keep changing and the average efficiency accounts for all these fluctuations and changes due weather changes or solar intermittency. Moreover, electrolyser can also be seen to be operated with an average efficiency of 66-71%, that actually depends upon the operating voltage of electrolyser or indirectly the peak solar irradiance received for that day. Figure 5.36 shows the daily average electrolyser efficiency against the solar energy received for whole day. It can be seen that with the larger the amount of solar radiation received, the lower is the electrolyser efficiency. But in actual, it is more likely depending upon the DNI received at that particular day, which depicts the operating voltage. The partial cloudy day with longer sun availability may have higher electrolyser efficiency than the clear day with sun availability for very short period. But generally, higher solar energy received is considered as the high DNI received, as the days with higher solar energy at comparatively lower peak DNI are rare.

Figure 5.37 shows the effect of electrolyser efficiency variations on the hydrogen production rating. The results show higher production rating at higher electrolyser efficiency, which depicts low power input is required is needed. The performance parameter kWh/kg of hydrogen production rating is of prime importance for the customers who are interested in hydrogen production as their final product. So, lower kWh/kg factor is favourable for better performance. Here kWh represents the energy consumed by the electrolyser. However, for overall solar to hydrogen conversion performance,

given in Table 5.2, the kWh/kg parameter shows the amount of solar energy received by the concentrator to produce one kilogram of hydrogen.

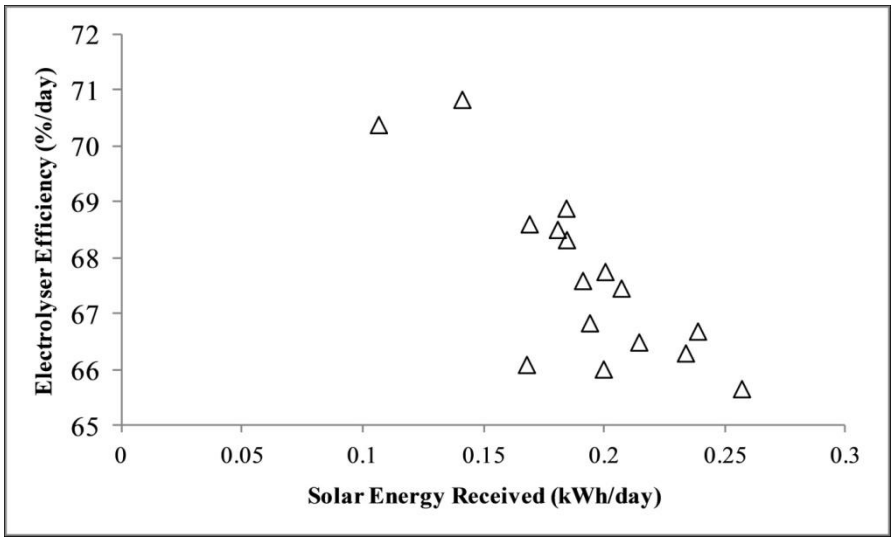


Figure 5.36: Daily Average Electrolyser Efficiency against the Solar Energy Input Received for Whole Day

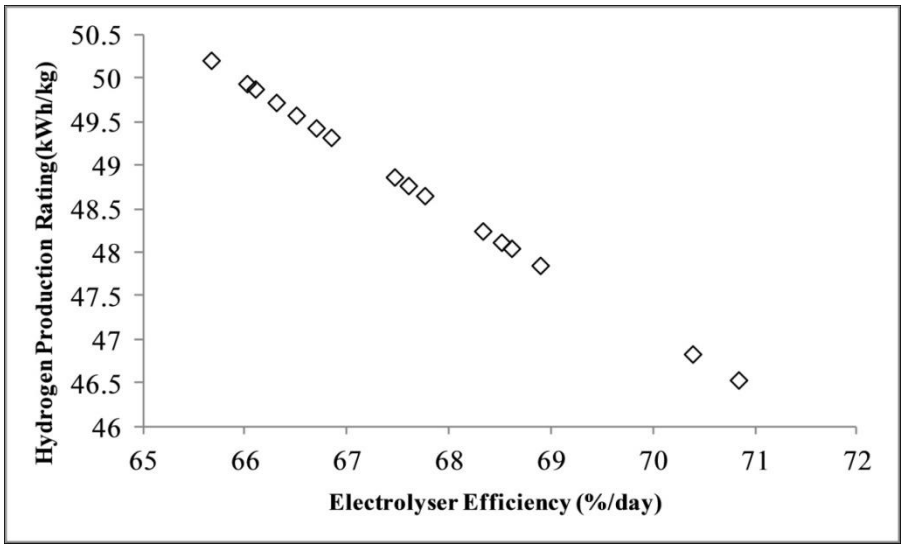


Figure 5.37: The Effect of Variation of Electrolyser Efficiency on Hydrogen Production

## 5.9 Summary

In this chapter, the development of the concentrated photovoltaic (CPV) and CPV-Hydrogen system is discussed, with their performance investigations in the outdoor weather conditions. The operation and control of the developed

experimental setup of CPV and CPV-Hydrogen system through LabVIEW are explained. In the first section of the chapter, the development and the fabrication of all three CPV systems, mini dish cassegrain design, Fresnel lens-glass homogeniser design and Fresnel lens-reflective homogeniser design, are discussed. All three CPV systems are fabricated according to the design criteria discussed in Chapter 4. The mini parabolic and hyperbolic dishes are fabricated using aluminium material, with further optical coating of aluminium to get better surface finish. A 2x2 array of PMMA Fresnel lens, according to optimized design is obtained. All the three fabricated CPV modules are mounted onto developed two axis solar trackers, which are controlled through master slave configuration. The performance of the developed CPV systems is investigated in outdoor weather conditions. The maximum CPV system efficiencies of 17-18% and 27-28% were recorded for mini dish CPV system and both Fresnel lens based CPV systems respectively. From the normalized power curve, the acceptance angles of $0.4^{o}$, $0.7^{o}$ and $1.2^{o}$ were recorded for mini dish CPV, Fresnel lens-reflective homogeniser CPV and Fresnel lens-glass homogeniser CPV, respectively. However, all of the three systems showed highest performance against the developed tracking accuracy of $0.3^{o}$. The lower efficiency for mini dish CPV was due to aluminium coating and double stage reflection, which also caused lower acceptance angle of the concentrating assembly.

Based upon the efficiency and the acceptance angle, the Fresnel lens-glass homogeniser was further considered for performance investigation of CPV-Hydrogen system. The hydrogen production unit was design and developed using PEM electrolysers and feed water tanks. The produced hydrogen was

then compressed and stored into cylinders. The maximum efficiency of solar to hydrogen conversion was recorded as 18%. However, average efficiency of 15% for solar to hydrogen conversion was recorded for whole day operation. Moreover, for series of experiments under different weather conditions, the average performances of 47 kWh/kg and 218 kWh/ kg were measured for electrolyser and overall solar energy to hydrogen conversion, respectively.

In the next chapter the long term performance of the developed CPV systems is investigate using proposed electrical rating methodology.

# Chapter 6: Long Term Electrical Rating of Concentrated Photovoltaic (CPV) Systems

## 6.1 Introduction

Solar energy has the highest energy potential among all the energy resources, to meet the global energy needs **[5]**. In addition, photovoltaic systems offer the direct conversion of solar energy into electricity, providing simple and elegant method of solar energy utilization. Due to diversity of the photovoltaic technology, the existing market is full of different photovoltaic systems ranging from conventional silicon-based stationary photovoltaic (PV) panels to two axis tracked concentrated photovoltaic (CPV) systems. Every photovoltaic system has different performance and working conditions. The performance of the photovoltaic systems is rated through a flash of light of 1000 $W/m^2$ onto the module, with 25$^oC$ cell temperature under standard testing conditions (STC) (IEC 60904-3) or 800 $W/m^2$ with 20$^oC$ ambient temperature and 1m/s flow rate, under standard operating conditions (SOC) or Nominal Operating Cell Temperature (NOCT) (IEC 61215 and IEC 61646) **[117]**. The instantaneous energy conversion efficiency is used as a rating parameter to analyze the performance potential of the photovoltaic system. However, the real field conditions are different than the rated conditions, with temperature much higher than the rated value of 20$^oC$ or 25$^oC$ and cell have to operates for a longer period of time. The intensity of solar radiations is higher only at the noon time, but not necessarily 1000 $W/m^2$. Beside different operating conditions, different photovoltaic technologies also need different working conditions. Although CPV operates at higher efficiency than

conventional PV **[13,118,119]** but it can only accept and convert solar beam radiations into electricity **[120]**. This depicts that conventional PV can still have power production in cloudy conditions but not CPV.

Efficiency of the solar cell varies with temperature and spectrum, affecting the total power output of the system for long term operation than the predicted value **[121]** as ultimately the consumer is interested in the total energy yield of the photovoltaic system. Moreover, dust storms and dust accumulation on the photovoltaic modules reduces the solar irradiance reaching the solar cell, thereby reducing its performance. There are many models developed to estimate the performance of conventional PV systems **[122-124]**. However, because of different operating conditions, PV performance models cannot be used for CPV. Some researchers studied the CPV performance by setting outdoor parameters for laboratory testing **[125]**. Some authors used PV power estimation model but with consideration of yearly average direct normal irradiance and performance ratio **[126]**. However, due to intermittency of solar energy and dynamic nature of meteorological data, DNI data availability and prediction uncertainties varies from region to region. The CPV performance depends upon many factors **[127]** including dust storms **[128]** that increases uncertainties in the estimation or simulation approaches and motivating to propose the long-term electrical rating (LTER) method. The LTER provides energy planners and designers a simple and quick but accurate methodology to determine the size of photovoltaic plant, based upon actual power output of the CPV system from long term field testing data. From LTER, they can understand the real potential and economic viability of a solar photovoltaic plant.

In this chapter, for the first time the long-term electrical rating (LTER) has been introduced. The LTER of two in house built compact concentrated photovoltaic (CPV) systems is reported in tropical weather conditions of Singapore. This is the first ever outdoor field performance data reporting of any CPV system in Singapore, to investigate its power potential as CPV systems are recommended only for desert area because of high DNI availability. The electrical rating in $kWh/m^2$.year, with average system efficiency, is used to investigate the potential of photovoltaic system in real field operating conditions. The electrical rating is the total electrical power output of the system per $m^2$ of the photovoltaic system, normalized for period of one year. All three developed CPV systems, as discussed in the previous chapter with maximum efficiencies of 19% and 28%, are evaluated for long term operation. Experiments were conducted from September, 2014 to August, 2015 and data the regarding electrical power output from CPV systems at the maximum power point and the direct normal irradiance (DNI) received, was recorded at an interval of 1sec. The LTER of the developed CPV systems was compared with the other conventional PV systems installed in Singapore.

## 6.2 Electrical Rating Methodology

Electrical rating is a method, parameter or tool that is proposed to be used to investigate the real field potential of any electrical power producing renewable energy system, utilizing intermittent energy source for its operation like solar energy or wind energy. From the long term power output measurement of the system, electrical rating is represented for particular region in normalized value as $kWh/m^2$.year, in spite of its operating conditions. Instead of using the

performance data from overwhelming catalogue of the photovoltaic manufacturers, the motive of the proposed electrical rating methodology is to provide accurate but simple parameter for consumers and designers to estimate the size of power plant according to the actual power output data at specific location, as the availability of the renewable energy resources varies throughout the year due to their intermittent nature and varies region to region. In addition, the electrical rating provides a common playing field to analyze the real potential and economic viability of any renewable energy system, irrespective of the technology or energy source as the comparison parameter is the electrical energy output.

Moreover, in electrical rating methodology, the focus is on the long term average performance of the system rather than the instantaneous efficiency and rated power. Due to many performance affecting parameters, the CPV instantaneous changes and fluctuates during operation. However, long term average efficiency remains stable and provides a reliable parameter to evaluate the true energy conversion potential of the system. The details of the electrical rating methodology and the system description are are discussed further in this section.

### 6.2.1 CPV System Description under Investigation

The current analysis of the CPV systems is based upon the electrical power output of the module which is measured in terms of the current and voltage through maximum power point tracking, connected at the module output. The performance parameters of the CPV system in form of power output and the DNI input were recorded for whole day operation, from sunrise to sunset, at an

interval of 1sec using Agilent data logger. The DNI was recorded using Pyrheliometer. The description of the CPV system defined in current experimental setup is shown in the Figure 6.1. In order to calculate the total energy yield of the CPV system per day, the power output curve of CPV system was integrated over the whole day period, using OriginPro software. Similarly, the total solar energy input was also calculated by integrating the received DNI over whole day period.

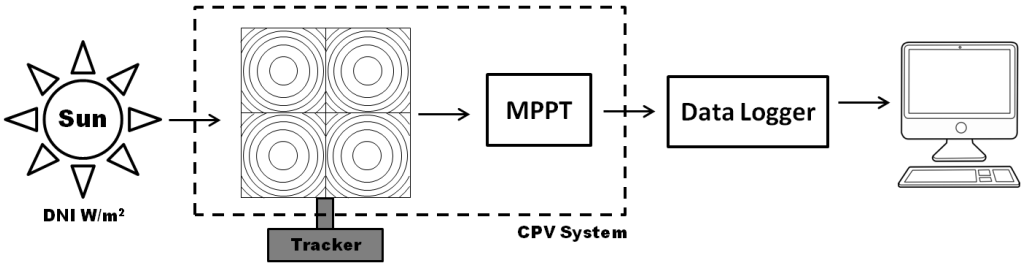


Figure 6.1: Experimental Setup description of CPV System

### 6.2.2 Electrical Rating Parameters

In order to analyze the short term and long term performance of concentrated photovoltaic (CPV) system, Equations (6.1) and (6.2) can be used to calculate the monthly and overall electrical ratings.

$$Monthly\ Electrical\ Rating,\ R_{e,m} = (\sum_{j=1}^{m} E_i).\frac{365}{m} \qquad (\frac{kWh}{m^2.year}) \qquad (6.1)$$

$$Overall\ Electrical\ Rating,\ R_e = (\sum_{j=1}^{q} E_i).\frac{365}{q} \qquad (\frac{kWh}{m^2.year}) \qquad (6.2)$$

The parameter 'm' here represents the maximum number of days in that particular month i.e. 30 or 31 but 28 or 29 for February. The parameter 'q' represents the total number of days for which the experiment was conducted or system performance recorded. The parameter 'E' represents the total daily

energy yield of the CPV system, that can be found using Equation (6.3). Similarly, Equation (6.4) gives the total daily solar energy received by the CPV system.

$$E = \int_1^t \frac{(V_{CPV} . I_{CPV})}{A_{con}} dt = \sum_{i=1}^{t} (\frac{(V_{CPV} . I_{CPV})_i - (V_{CPV} . I_{CPV})_{i-1}}{2 \bullet A_{con}}). S \quad (\frac{kWh}{m^2}) \qquad (6.3)$$

$$D_m = \int_1^t (DNI) dt = \sum_{i=1}^{t} (\frac{(DNI)_i - (DNI)_{i-1}}{2}). S \qquad (\frac{kWh}{m^2}) \qquad (6.4)$$

The parameters $V_{CPV}$ and $I_{CPV}$ represents the CPV total voltage and current recorded at maximum power point and $A_{con}$ is the effective area of the concentrator. The parameter 't' represents the total time in seconds, for the operation of CPV system in that particular day and the measurements are taken at scanning interval of 'S', which is 1sec for current performance analysis. From the daily total energy input and output of the CPV system, Equations (6.5), (6.6) and (6.7) give the daily average, monthly average and overall average DNI efficiency of the system.

$$Daily\ Averge\ DNI\ Efficiency = \frac{E}{D_m} \times 100 \qquad (\%) \qquad (6.5)$$

$$Monthly\ Averge\ DNI\ Efficiency = \frac{\sum_{j=1}^{m} E_i}{\sum_{j=1}^{m} D_m} \times 100 \qquad (\%) \qquad (6.6)$$

$$Overall\ Averge\ DNI\ Efficiency = \frac{\sum_{j=1}^{q} E_i}{\sum_{j=1}^{q} D_m} \times 100 \qquad (\%) \qquad (6.7)$$

As mentioned before, the CPV systems can only accept to solar beam radiations. Therefore, in all the above discussed functions of the average efficiency, the performance of the CPV system is evaluated based upon only DNI as energy input. However, solar energy consists of both beam and diffuse radiations. Therefore, in order to compare the performance of CPV with conventional PV, Equation (6.8) gives the average efficiency of the system based upon the global horizontal irradiance (GHI) as energy input.

$$Overall\ Averge\ GHI\ Efficiency = \frac{\sum_{j=1}^{q} E_i}{\sum_{j=1}^{q} GHI} \times 100 \qquad (\%) \qquad (6.8)$$

In addition, the Equation (6.9) gives the monthly share of beam radiations in total global irradiance received.

$$DNI\ Monthly\ Share = \frac{\sum_{j=1}^{m} D_m}{\sum_{j=1}^{m} GHI} \times 100 \qquad (\%) \qquad (6.9)$$

By using the electrical rating value, the $CO_2$ emissions savings can be calculated for each kWh produced, using the carbon emission factor from International Energy Agency (IEA). It is given by Equation (6.10).

$$CO_2\ Emissions\ Saving = R_e \times 0.635 \qquad (\frac{kg}{m^2.\ year}) \qquad (10)$$

Here the value 0.635 $CO_2$ kg/kWh is provided by the International Energy Agency (IEA) for crude oil **[129]**. For different type of fuels, depending upon their calorific value, carbon emission factor is different and so as the $CO_2$ emission savings.

Table 6.1: Maximum Performance Rating of Multi-Junction Solar Cell and Developed CPVs

| Sr No. | Photovoltaic Technology | Performance | |
|---|---|---|---|
| 1 | Multi-junction Solar Cell | Concentration Ratio = 500 | Efficiency = 39.5% @ 25°C Cell Temperature |
| | | | Efficiency = 35.2% @ 90°C Cell Temperature |
| | | Concentration Ratio = 100 | Efficiency = 38.5% @ 25°C Cell Temperature |
| | | | Efficiency = 33.6% @ 90°C Cell Temperature |
| 2 | Fresnel Lens-Glass Homogeniser CPV System | Geometric Concentration Ratio = 476 | Maximum Module Efficiency = 28% Tested at NUS EA-Building Rooftop |
| 3 | Fresnel Lens-Reflective Homogeniser CPV System | Geometric Concentration Ratio = 476 | Maximum Module Efficiency = 28% Tested at NUS EA-Building Rooftop |
| 4 | Mini Dish Cassegrain CPV System | Geometric Concentration Ratio = 492 | Maximum Module Efficiency = 19% Tested at NUS EA-Building Rooftop |

### 6.2.3 Maximum Performance Characteristics of Systems under Investigation

It is essential to mention here the rated and maximum performance of the CPV, to confirm that the system under comparison have same rated

performance as commercial systems. The maximum performance rating of the MJC cell used, provided by Arima Photovoltaic and Optical Co., and the in house built CPV systems are given in Table 6.1. The installed and tested location of the CPV systems is also mentioned in Table 6.1.

The maximum reported instantaneous efficiencies of the CPV systems are based upon the outdoor field testing of CPV modules at NUS EA-Building of Singapore. The detailed performance graphs are shown in Figures 6.2, 6.3 and 6.4. The performance graphs shows the instantaneous efficiencies with corresponding DNI received with back plate temperatures and at different periods of time. The detailed description and analysis of these results are already discussed in the previous chapter.

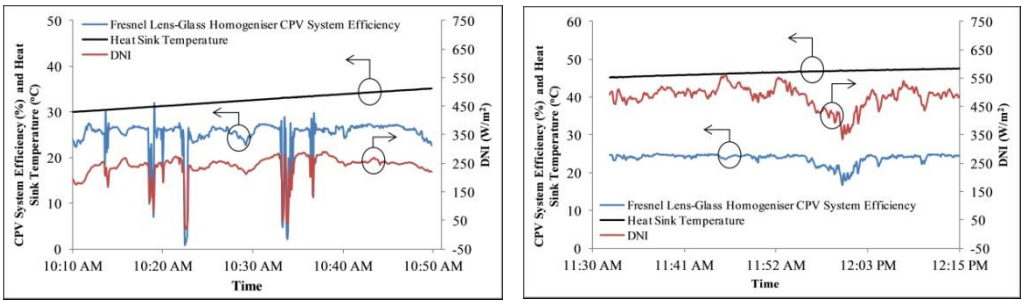


(a) (b)

Figure 6.2: Fresnel Lens-Glass Homogeniser CPV System Performance (a) Test 1 (b) Test 2

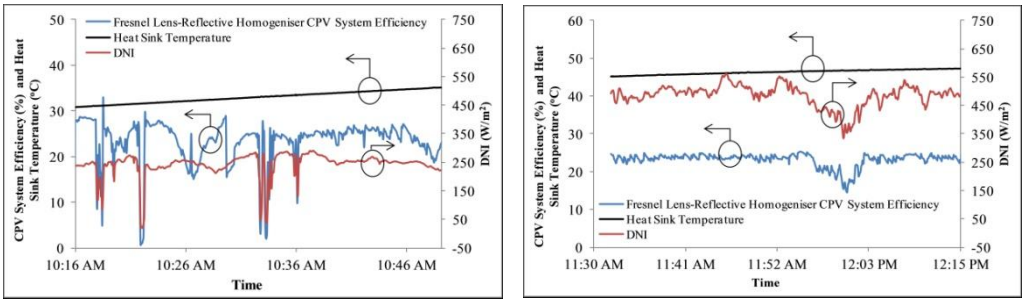


(a) (b)

Figure 6.3: Fresnel Lens-Reflective Homogeniser CPV System Performance (a) Test 1 (b) Test 2

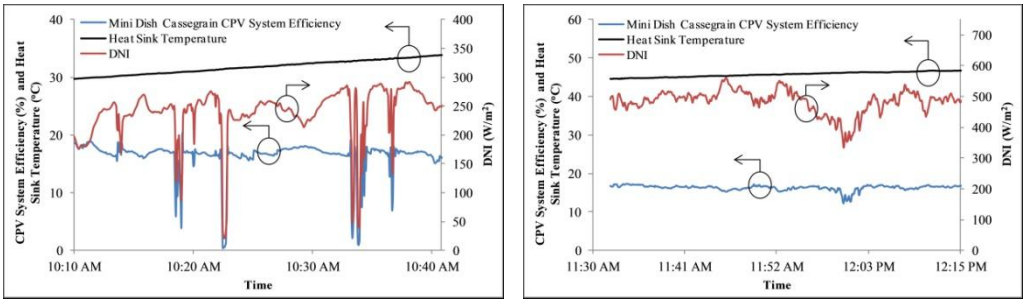


(a) (b)

Figure 6.4: Mini Dish Cassegrain CPV System Performance (a)Test 1(b)Test 2

The testing was performed in the morning and noon time to analyze the effect of temperature and DNI. It is worthy to mention here that the temperature mentioned here is the back plate or heat sink temperature, not the cell temperature which is much higher than the back plate temperature. For both Fresnel lens CPV systems, the maximum instantaneous efficiency is 28%. However, for mini dish cassegrain CPV system, the maximum instantaneous efficiency is 18%, which is due to low reflectance of aluminum coating on reflectors. In addition, all three CPV systems are utilizing same type of MJC cell.

In the next results and discussion section, firstly, the long-term performance of CPV systems is analyzed based upon the monthly and overall electrical rating. Secondly, the LTER of CPV systems is then compared with the LTER and long term average efficiency of the conventional stationary PV systems, installed in Singapore. The maximum rated performances of these conventional PV systems, with their installed locations, are given in Table 6.2 and the system is shown in Figure 6.5. It must be noted that the mentioned performances are under STC conditions.

Table 6.2: Performance Characteristics of Conventional PV systems at CITI (BCA), Singapore

| Sr. No. | Photovoltaic Technology | Performance | Location |
|---|---|---|---|
| 1 | Mono-Crystalline (16.86 $m^2$) | 17.2 % @ STC **[130]** | CITI (BCA), Singapore. |
| 2 | Poly-Crystalline (19.4 $m^2$) | 16.2% @ STC**[131]** | |
| 3 | Thin Film (CIS) (21.27 $m^2$) | 17% @ STC**[132]** | |

Figure 6.5: Conventional Mono-Crystalline, Poly-Crystalline and Thin Film (CIS) PV Systems at CITI (BCA), Singapore **[133]**

## 6.3 Results and Discussion

The monthly average weather data in the form of global irradiance (GHI), direct normal irradiance (DNI), duration of sun availability and the ambient average temperature per day for a period of one year, are shown in Figure 6.6,. The direct normal irradiance data was collected using Pyrheliometer mounted onto two axis solar tracker at NUS EA-Rooftop during one year operation of CPV. The global horizontal irradiance (GHI) data, sunshine duration data and ambient temperature data are average values of the weather data for year 2012,

Table 6.3: Summary of Long Term Weather Data

| Month | Global Horizontal Irradiance | Direct Normal Irradiance | Diffuse Irradiance | DNI Percentage Share | Sunshine Duration | Cloud Cover Delivered | Average Temp. |
|---|---|---|---|---|---|---|---|
| | GHI | $D_m$ | | | E | E | |
| | kWh/m$^2$/day | kWh/m$^2$/day | kWh/m$^2$/day | % | Hours/day | % | $^o$C |
| **September** | 4.63 | 3.46 | 1.17 | 74.66 | 5.72 | 87.96 | 27.97 |
| **October** | 4.75 | 2.84 | 1.90 | 59.91 | 6.07 | 87.39 | 27.95 |
| **November** | 4.10 | 2.18 | 1.92 | 53.22 | 4.78 | 88.68 | 27.24 |
| **December** | 3.78 | 1.08 | 2.70 | 28.54 | 3.61 | 89.23 | 26.73 |
| **January** | 4.71 | 3.42 | 1.28 | 72.72 | 5.77 | 87.67 | 26.64 |
| **February** | 5.12 | 3.71 | 1.42 | 72.34 | 6.60 | 87.66 | 26.97 |
| **March** | 5.28 | 3.18 | 2.10 | 60.17 | 6.58 | 87.57 | 27.74 |
| **April** | 4.53 | 3.15 | 1.37 | 69.64 | 5.58 | 87.96 | 28.01 |
| **May** | 4.27 | 3.78 | 0.49 | 88.57 | 5.60 | 88.08 | 28.32 |
| **June** | 4.40 | 3.70 | 0.70 | 84.12 | 6.15 | 87.61 | 28.90 |
| **July** | 4.31 | 3.38 | 0.93 | 78.36 | 5.80 | 87.92 | 28.07 |
| **August** | 4.34 | 2.63 | 1.71 | 60.61 | 5.57 | 87.92 | 27.87 |

2013 and 2014, which are provide by NEA (National Environment Agency) Singapore **[134]**. From the figure, it can be seen that the longer sunshine is depicting the larger amount of received solar energy. Therefore, for the month of March, the highest solar energy was received with the highest average sunshine duration per day. However, the lowest solar energy was received during November and December with the lowest availability of the sun as the rainy season of Singapore occurs in this time period. A summary of the weather data details is given in the Table 6.3.

Figure 6.7 shows the monthly performance of all three CPV systems based upon the monthly electrical rating, monthly average DNI efficiency with the the percentage share of monthly beam radiations received. From the performance data, it can be seen that the electrical rating depends upon the received DNI. For May and June, it can be seen that the highest values of electrical rating are recorded, 297.6 kWh/$m_2$.year and 296.2 kWh/$m_2$.year for Fresnel Lens-Glass Homogeniser CPV system, 297.2 kWh/$m_2$.year and 278.2 kWh/$m_2$.year for Fresnel Lens-Reflective Homogeniser CPV system and, 235kWh/$m_2$.year and 227.2 kWh/$m_2$.year for the mini dish casssegrain CPV system. It can also be seen that the higher DNI percentage is received for May and June. Although the instantaneous maximum efficiency for both of the Fresnel lens CPV systems is the same, the long term energy yield of the CPV system with reflective homogeniser is found to be always less than the CPV with glass homogeniser. This difference can only be explained from the normalized power output curves discussed in the previous chapter. Although the normalized power curves for both of the Fresnel lens based systems show their maximum performance at defined tracking accuracy, the normalized

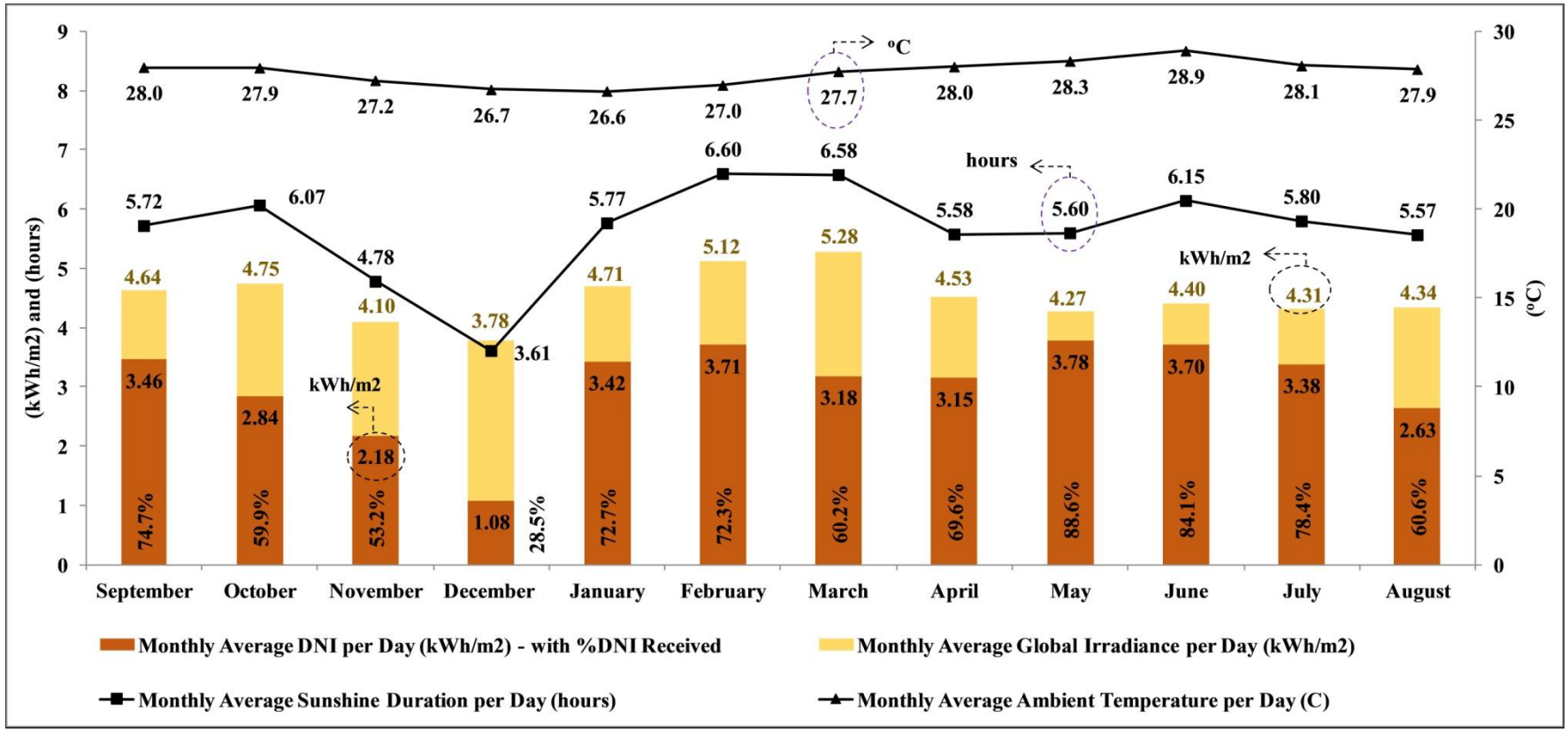


Figure 6.6: Monthly Average Values of Solar Irradiance (Global and DNI) and Sunshine Duration Data per Day

power curve for CPV system with reflective homogeniser is lower than the CPV with glass homogeniser. This is because of the optical loss that occurs when concentrated light reflects through the reflective homogeniser, which is made of aluminum having comparatively low reflectance. In short term performance analysis, this effect of homogeniser is not prominent. However, through long term performance, the true effect of homogeniser design on the system performance can be found. For mini dish CPV system, the reason for low electrical rating is due to comparatively low conversion efficiency.

Beside the best performances, the poor performance of the CPV system was observed in November and December due to low availability of the DNI. Figure 6.7 also shows the average DNI efficiency of each of the CPV system based upon monthly DNI. It can be seen that the average DNI efficiency of Fresnel Lens-Glass homogeniser CPV system is highest i.e. 22% followed by the one with the reflective homogeniser design and the mini dish CPV system with 21.5% and 16% respectively. It can be seen that the average efficiency is lower than the instantaneous rated efficiency, representing the real potential of the system. Furthermore, the average efficiency for each of the CPV system is higher in February. To further explain this trend of higher efficiency, there is need to reconsider Figure 6.6 as the highest sunshine duration and lowest ambient temperature recorded for February.

After discussing the monthly variation of electrical rating of CPV systems, the overall electrical rating for 12-months period of operation is shown in Figure 6.8. For performance comparison purpose, the overall electrical rating of CPV systems is compared with the conventional PV systems installed at CITI (BCA), Singapore. The overall electrical rating recorded for Fresnel lens CPV

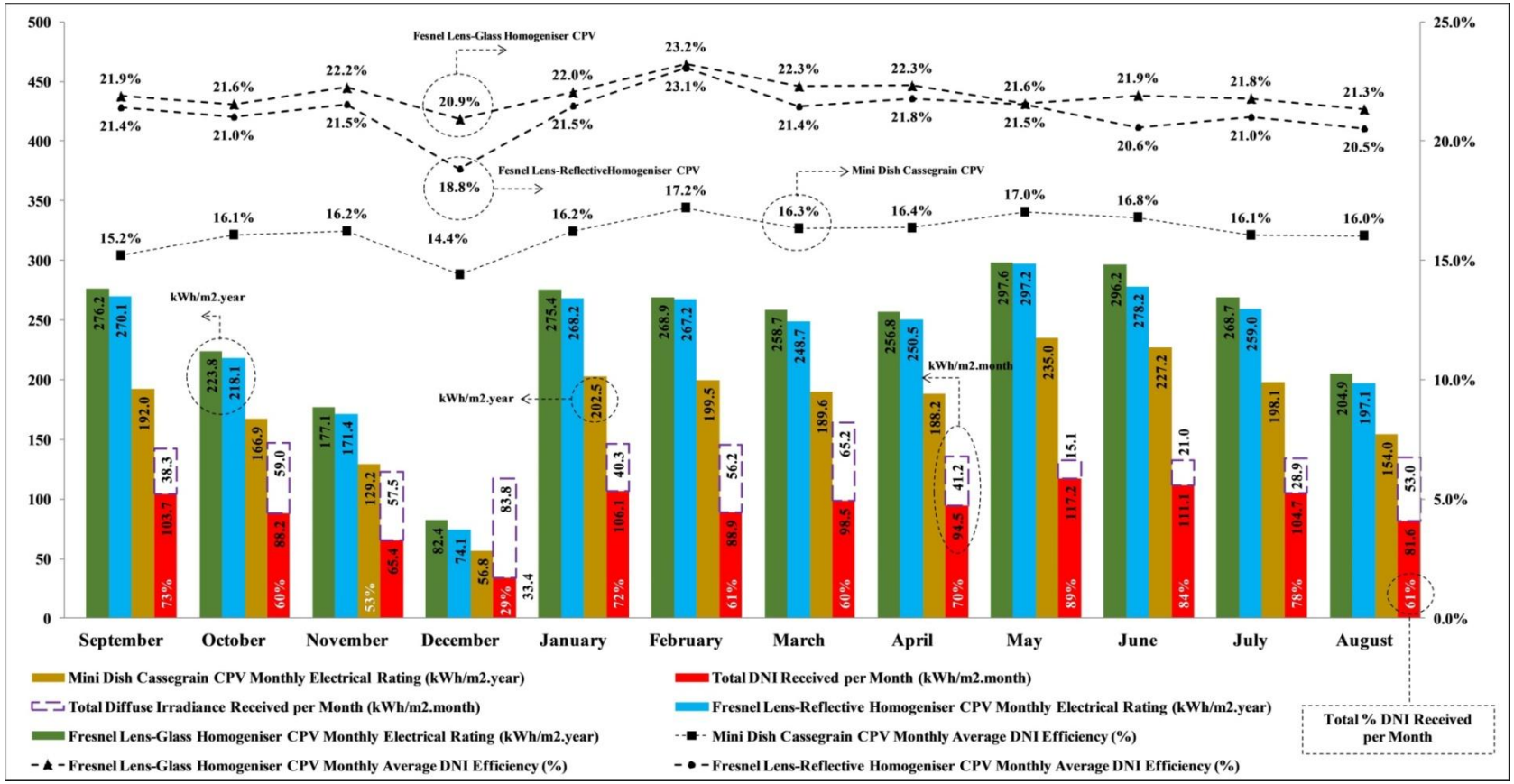


Figure 6.7: Monthly Electrical Rating and Monthly average Efficiency of CPV systems with the DNI Received

systems with glass homogeniser is 240.21 kWh/$m^2$.year, with overall average DNI efficiency of 22%. Similarly, for the Fresnel lens CPV system with reflective homogeniser, the overall electrical rating 232.93 kWh/$m^2$.year is recorded for 21.3% overall average DNI efficiency. However, for the mini dish CPV system, the electrical rating of 178 kWh/$m^2$.year with 16.3% average DNI efficiency was recorded. It can be seen that the electrical ratings of the CPV systems are almost 2-3 fold higher than the conventional stationary PV systems, even in the tropical weather of Singapore, which proves the potential of the CPV system in residential or even tropical regions where the availability of DNI is lower than the recommended desert regions for CPV installations. Due to higher kWh electricity produced, the CPV systems can save the highest amount of $CO_2$ emissions, with the highest value of 152.5 kg of $CO_2$ saved for one $m^2$ of the Fresnel Lens-Glass Homogeniser CPV in a period of one year. So far only DNI has been considered as energy input for the efficiency calculation of CPV system. However, a significant portion of solar energy is also received in the form of diffuse radiations especially in tropical regions like Singapore and CPV systems do not respond to diffuse radiations. The conventional PV systems, on the other hand, can accept both DNI and diffuse radiations for power production. That is why GHI is used for the efficiency calculation of PV systems. In order to analyze all of the photovoltaic systems on the same ground, the overall average efficiency of the all photovoltaic systems is calculated considering GHI input as 1700 kWh/$m^2$.year, which the long term average global solar radiations received by Singapore **[135]**. The overall average GHI efficiency results are shown in Figure 6.9. From the results, it can be seen that the CPV systems are

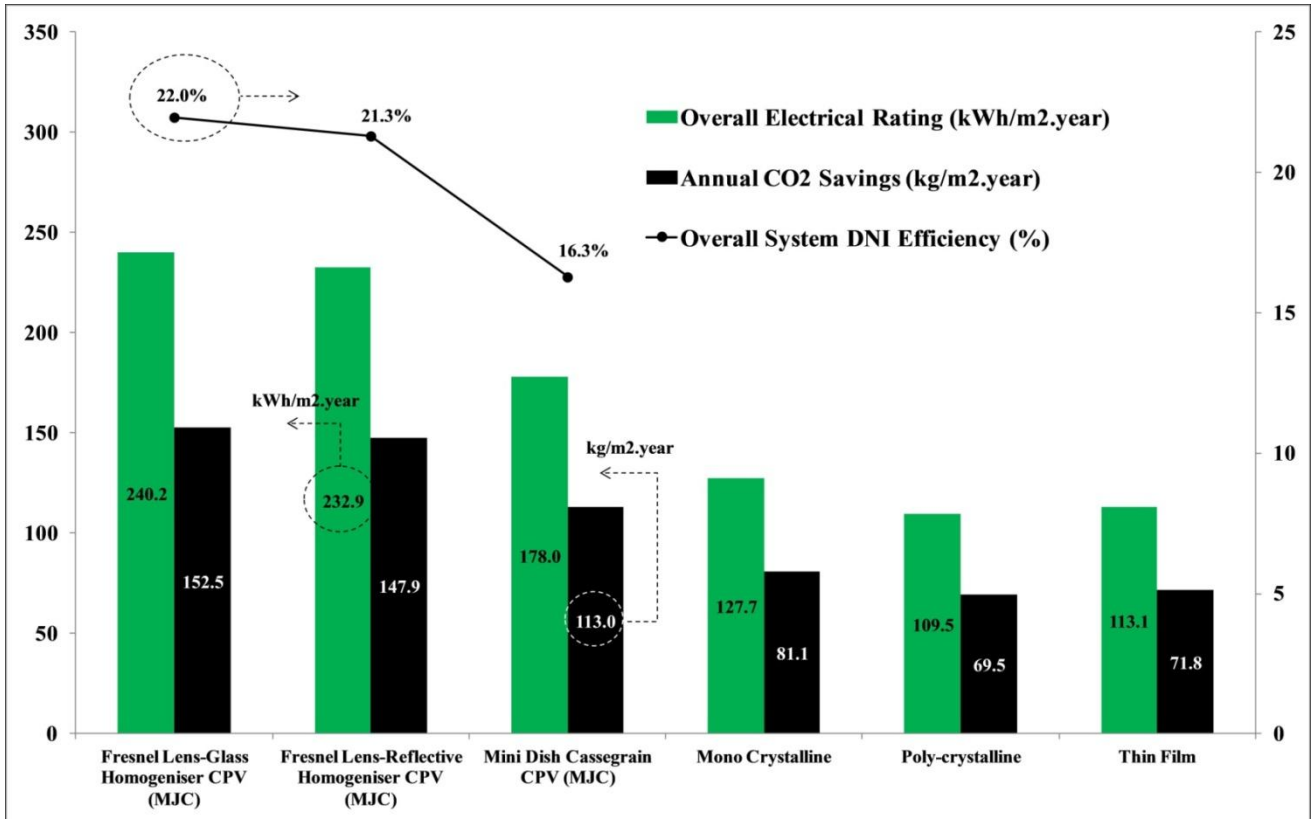


| | | | | | | |
|---|---|---|---|---|---|---|
| Overall Electrical Rating (kWh/m2.year) | 240.21 | 232.93 | 178.00 | 127.7 | 109.5 | 113.1 |
| Annual CO2 Savings (kg/m2.year) | 152.54 | 147.91 | 113.03 | 81.09 | 69.53 | 71.82 |
| Overall System DNI Efficiency (%) | 22.0 | 21.3 | 16.3 | - | - | - |
| | Fresnel-Glass CPV (MJC) | Fresnel-Reflective CPV (MJC) | Mini Dish CPV (MJC) | Mono-Crystalline | Poly-Crystalline | Thin Film (CIS) |

Figure 6.8: CPV Systems and conventional PVs and their $CO_2$ Savings comparison

operating at higher efficiency than the conventional PV, as high as 14% long term efficiency. However, the conventional PV systems showed the maximum of 7.5% long term efficiency. This graph is of great importance when the efficiency of the CPV is needed to be compared with the conventional PV. Due to non-acceptance of diffuse radiations by the CPV systems, the GHI efficiency shows the overall potential of system by considering all forms of solar energy as a input.

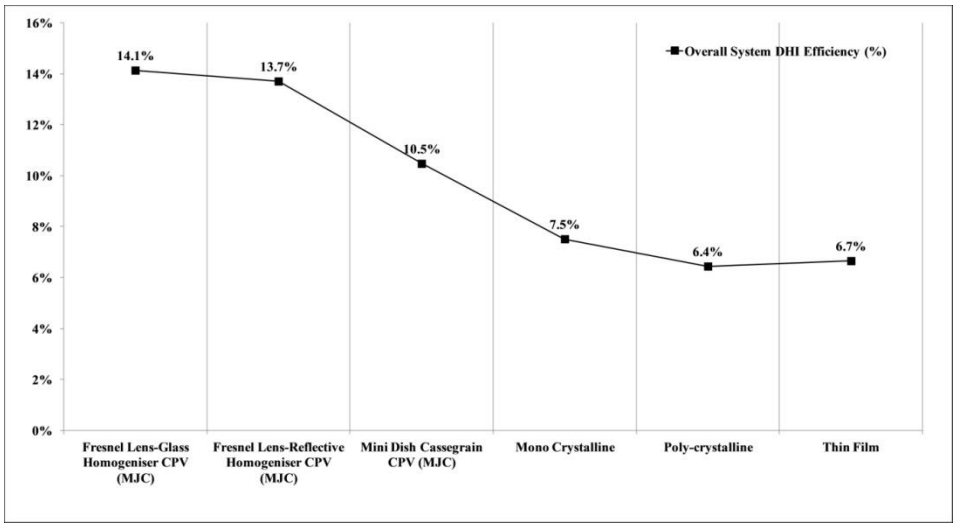


Figure 6.9: Overall Average GHI Efficiency

An overall summary of the monthly and overall performance of each of three CPV system is given in Table 6.4. From the data given, it can be seen that the during one year period of operation, only 66.1% of the total solar energy was received in the form of the beam radiations and the global radiation received is close to average solar energy availability of Singapore as 1700 kWh/$m^2$.year.

From the results, it can be seen that the electrical rating is depending upon the availability of DNI. Therefore, in order to further investigate and quantify their relation, a graph is plotted between total energy output of the system in the form of monthly electrical rating and corresponding monthly solar

Table 6.4: Summary of Long-Term (12 months) Performance Data of CPV Systems

| Month | Solar Input | | | Fresnel Lens-Glass Homogeniser CPV | | Mini Dish CPV | | Fresnel Lens-Reflective Homogeniser CPV | |
|---|---|---|---|---|---|---|---|---|---|
| | GHI | DNI | DNI Share | Total Power Delivered | Average DNI Efficiency | Total Power Delivered | Average DNI Efficiency | Total Power Delivered | Average DNI Efficiency |
| **Sep.2014-Aug.2015** | GHI | $D_m$ | | E | | E | | E | |
| | $kWh/m^2/month$ | $kWh/m^2/month$ | % | $kWh/m^2/month$ | %/month | $kWh/m^2/month$ | %/month | $kWh/m^2/month$ | %/month |
| **September** | 142.04 | 103.75 | 73.0 | 22.70 | 21.89 | 15.78 | 15.2 | 22.20 | 21.4 |
| **October** | 147.20 | 88.19 | 59.9 | 19.00 | 21.6 | 14.17 | 16.1 | 18.52 | 21.0 |
| **November** | 122.97 | 65.44 | 53.2 | 14.55 | 22.2 | 10.62 | 16.2 | 14.09 | 21.5 |
| **December** | 117.21 | 33.45 | 28.5 | 7.00 | 20.9 | 4.82 | 14.4 | 6.30 | 18.8 |
| **January** | 146.37 | 106.10 | 72.5 | 23.39 | 22.0 | 17.20 | 16.2 | 22.78 | 21.5 |
| **February** | 145.17 | 88.83 | 61.3 | 20.63 | 23.2 | 15.30 | 17.2 | 20.50 | 23.0 |
| **March** | 163.73 | 98.52 | 60.2 | 21.97 | 22.3 | 16.10 | 16.3 | 21.12 | 21.4 |
| **April** | 135.77 | 94.55 | 69.6 | 21.10 | 22.3 | 15.47 | 16.4 | 20.59 | 21.8 |
| **May** | 132.31 | 117.19 | 88.6 | 25.28 | 21.6 | 19.96 | 17.0 | 25.24 | 21. |
| **June** | 132.08 | 111.11 | 84.1 | 24.35 | 21.9 | 18.67 | 16.8 | 22.86 | 10.6 |
| **July** | 133.68 | 104.75 | 78.4 | 22.83 | 21.8 | 16.82 | 16.1 | 21.99 | 22.0 |
| **August** | 134.59 | 81.58 | 60.6 | 17.40 | 21.3 | 13.08 | 16.0 | 16.74 | 20.5 |
| **Annual Average** | **1653.12** $kWh/m^2/year$ | **1093.46** $kWh/m^2/year$ | **66.1%** | **240.2** $kWh/m^2/year$ | **22.0%** | **178.0** $kWh/m^2/year$ | **16.3%** | **232.93** $kWh/m^2/year$ | **21.3%** |

availability but normalized to yearly average solar energy input per $m^2$, as shown in the Figure 6.10. For the CPV system, the power output is plotted against the DNI and for the conventional photovoltaic systems i.e. mono crystalline, poly-crystalline and thin film, the electrical rating is plotted for DNI that is 66.1% of the long term GHI i.e. 1700 $kWh/m^2$.year as the performance of stationary PV depends upon the GHI. The plotted data is fitted through linear regression. It can be seen that the electrical rating and the direct normal irradiance (DNI) availability are directly proportional to each other with $R^2$ value of 0.996, 0.9921 and 0.990 for both Fresnel lens based glass and reflective homogeniser CPVs and the mini dish CPV system, respectively. However, the main point of interest is that the electrical rating and DNI are proportional to each other through the long term average efficiency. It can be seen that the slope of the regressed line is the same as the long term DNI efficiency of the CPV or PV systems i.e. 22%, 21.3% and 16.3% for CPVs against DNI and 7.5%, 6.4% and 6.7% for conventional PVs against GHI.

This electrical rating graph has the main importance from the design point of view of photovoltaic plant. From this graph, it can be seen that if the total average annual DNI availability is known then by knowing the average efficiency of the CPV system, not maximum or rated efficiency, a quick estimate of the total power output of the CPV system can be made at a particular region. Although the study is based upon the tropical region, however, if the higher total DNI availability for desert regions like Gulf countries, is known then the higher electrical rating can be achieved and estimated from electrical rating graph, if the average efficiency of the CPV system is known.

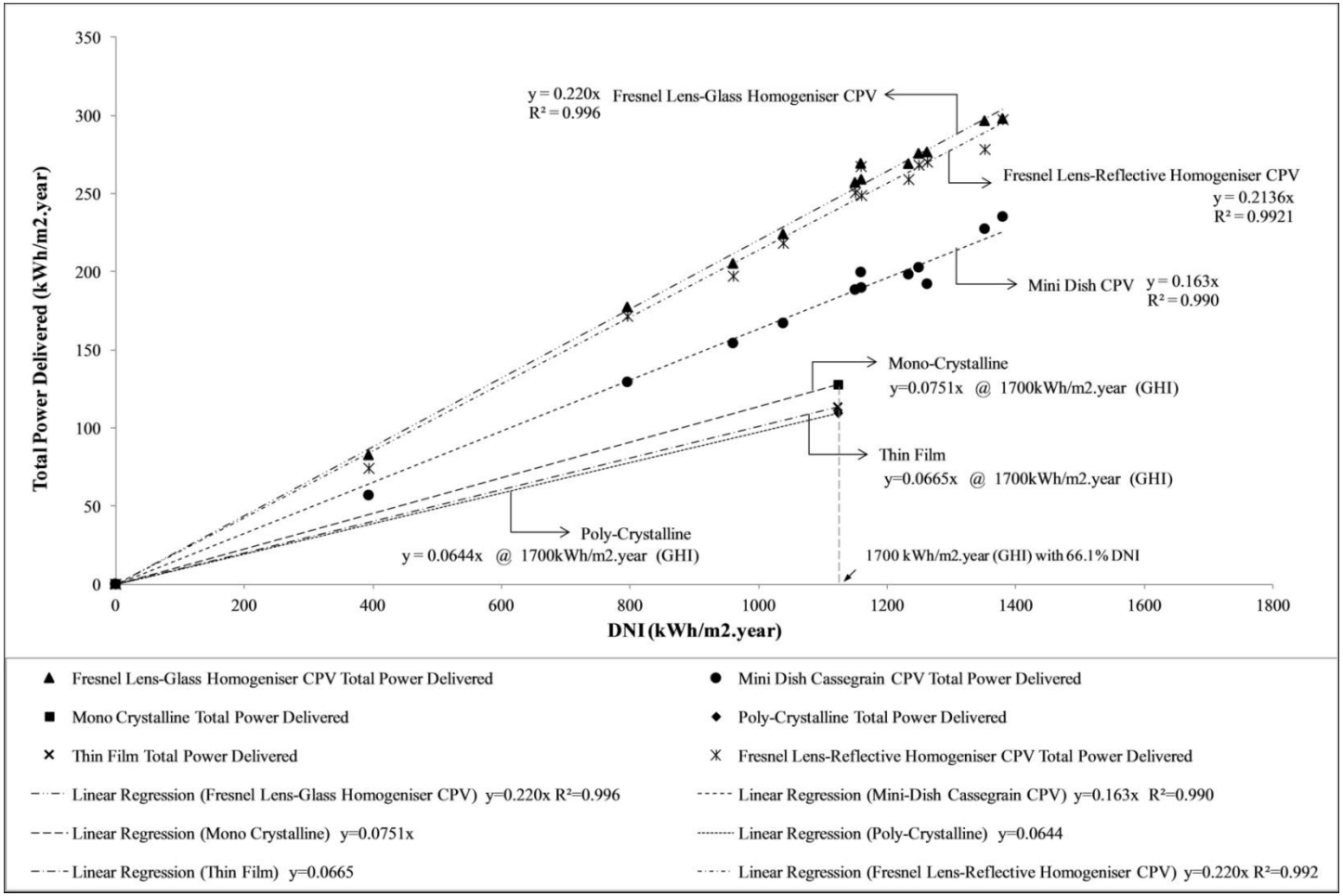


Figure 6.10: Total Power Delivered by assorted PV Systems against DNI and Global Irradiance

## 6.4 Summary

Due to many factors affecting the performance of the photovoltaic system, a simple and accurate electrical rating methodology is proposed to analyze the field performance of any photovoltaic system. The conventional rating methods for photovoltaic system performance analysis employ a certain constant factor under laboratory conditions. Moreover, the solar cell temperature is kept either at $25^{o}$C according to the standard rating procedures. However, the real field conditions change continuously, especially solar irradiance along with variations in cloud cover and ambient temperature. Another important factor is the dust covering that reduces the system performance significantly. Even all the models developed to simulate the performance of the photovoltaic systems, are unable to cover all the performance which in actual cannot be predicted accurately. Despite operating conditions, the working conditions of CPVs are different from PVs. The consumers are ultimately interested in the total electricity yield by the system. Therefore, an electrical rating methodology provides the actual performance data of the photovoltaic systems to designers and consumer to accurately predict the size of a photovoltaic plant, under climate conditions of a particular region.

The performance of the developed CPV systems: Fresnel lens-Glass Homogeniser, Fresnel lens-Reflective Homogeniser and mini dish cassegrain, was evaluated for long term operation of one year (12-months). The performance parameters of the CPV systems in terms of the voltage and current output at maximum power point were recorded to measure the system power output. By integrating the power output curve over whole day period,

the daily electric energy yield was calculated and by summing up daily energy yield for each of months, the overall average efficiency and the monthly/overall electrical ratings of all three systems were obtained. Electrical ratings of 240.21 kWh/$m^2$.year, 232.93 kWh/$m^2$.year and 178.00 kWh/$m^2$.year were recorded with the overall average efficiency of 22.0%, 21.3% and 16.3% for the Fresnel lens CPV system with glass homogeniser, reflective homogeniser and the mini dish cassegrain CPV system respectively. The recorded electrical ratings are 2-3 folds higher than the conventional PV systems installed in Singapore. Moreover, the electrical rating chart shows the proportional relation of electrical against received DNI. From the electrical rating chart, the total power output of the CPV system can be accurately predicted if the average efficiency of the system and the annual DNI availability is known.

In the next chapter, the design, development and testing of novel multi-leg homogeniser concentrating assembly is discussed for CPV applications.

# Chapter 7: Development of a Multi-leg Homogeniser Concentrating Assembly for Concentrated Photovoltaic (CPV) System

## 7.1 Introduction

Among all the photovoltaic technologies, concentrated photovoltaic (CPV) system offers the highest efficiency for solar energy to electricity conversion, as highly efficient multi-junction solar cells (MJC) are utilized. Because of high production cost of the MJC, it is not cost effective to build them in panels like conventional silicon based stationary PV modules. Therefore, in CPV system, low cost solar concentrators are used to concentrate sun rays onto a small area of MJC and as a result, reducing the use of expensive solar cell material by replacing it with cheap solar concentrators. In the conventional design of the CPV concentrating assembly, as discussed in the previous chapters, a single concentrator is used to concentrate solar radiation onto a single solar cell. In this chapter, a novel design of the CPV concentrating assembly is proposed which can concentrate solar radiation onto four MJCs using a single set of concentrators. The main motive for the development of this novel concentrating assembly design is to further reduce the cost of CPV system by reducing the number of concentrators needed for same capacity of system. As the concept of concentrated photovoltaic makes the use of multi-junction solar cells cost effective by replacing expensive solar cell material with the low cost solar concentrators, this novel concept of concentrating

assembly design will further reduce the cost of CPV system by reducing the number of concentrators needed for the same power capacity.

Figure 7.1 shows the simple schematic of the novel concentrating assembly for CPV to concentrate and distribute solar radiations onto four MJCs by using multi-leg homogeniser and single set of concentrators. This proposed multi-leg homogeniser concentrating assembly (MHCA) design consists of two reflecting concentrators in cassegrain arrangement and a multi-leg homogeniser. The parallel rays are reflected and concentrated by the primary and secondary concentrators onto multi-leg homogeniser. The purpose of the homogeniser here is to divide the received solar radiation into four parts and to further guide, distribute and concentrate them onto four MJCs placed at the four outlets of the homogeniser. In this chapter, first the design and the size calculations are discussed for reflectors and multi-leg homogeniser. Then based upon the design model, the prototype of the CPV system based upon multi-leg homogeniser concentrating assembly (MHCA) is developed and evaluated through experimentation and ray tracing simulation.

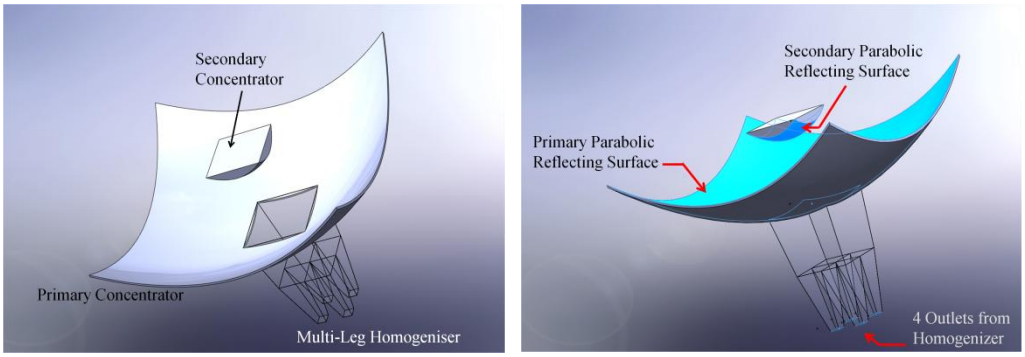


(a) (b)

Figure 7.1: Schematic of Multi-leg Concentrating Assembly for CPV

## 7.2 Design of Multi-leg Homogeniser Concentrating Assembly

The design schematic of the CPV concentrating assembly based upon multi-leg homogeniser is shown in Figure 7.2. Unlike the conventional design of the mini dish cassegrain concentrating assembly, as discussed in the previous chapters, the current design is based upon the two parabolic reflectors and as a result, area concentration is achieved instead of point concentration. Both of the reflectors of concentrating assembly are arranged such that the foci of both of the reflectors, primary and secondary, coincide with each other. The parallel rays, after being reflected by the primary parabolic reflector, are concentrated at its focal point. The secondary parabolic reflector is placed in the way of the converging rays such that its focal point coincides with the focal point of primary reflector. The converging solar radiations after being reflected by the secondary reflector, become parallel again as both of the reflectors have parabolic curvature, and the radiations then enter the multi-leg homogeniser.

In order to design the concentrating assembly, the targeted ray path is designed such that the edge ray of primary reflector at point 'a' must hit secondary reflector surface at point 'b', which is at the same level as point 'b' and focal points. The parallel incident ray, after being reflected from point 'b', becomes parallel again and after entering into the multi-leg homogeniser, it is reflected at point 'c' due to total internal reflection, towards the outlet aperture of homogeniser. The point 'c' is at the junction of top and bottom tapered portion of the homogeniser. So the slope and the height of the bottom tapered portion is designed such that the ray after being reflected from point 'c', hits the point 'e' which is at the extreme edge of homogeniser outlet aperture and

hits the MJC which is placed there. As the edge ray leaves from point 'e' of the homogeniser outlet, the subsequent rays are then assured to be uniformly distributed over the entire area of the solar cell, as shown in the Figure 7.3. To keep the cell temperature within the optimum operating limit, all four MJCs are attached to heat spreader and heat sink. As the parallel incident rays also become parallel after the secondary reflector, the concentrated rays at the inlet aperture of multi-leg homogeniser then take the shape of primary reflect. However, the size of the secondary reflector determines the size of the concentrated rays area.

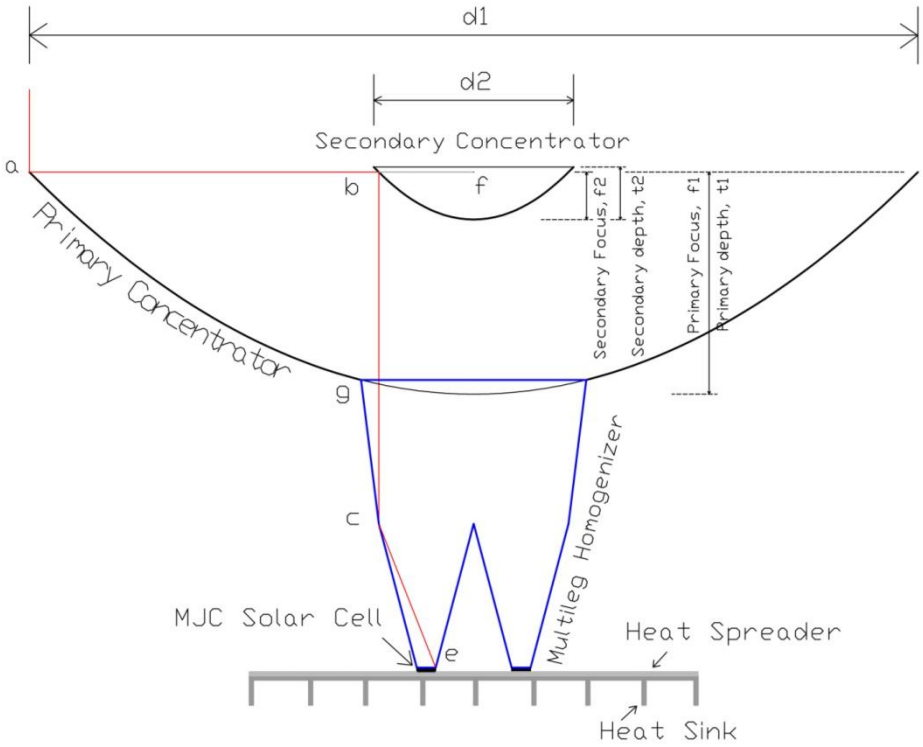


Figure 7.2: Design of Multi-Leg Homogeniser Concentrating Assembly

The design procedure for MHCA is divided into three steps. The first step is related to the size calculations and the design of primary concentrator. The second step is the design of the multi-leg homogeniser, followed by the third step related to the design and size calculations of the secondary concentrator, as the size of secondary concentrator depends upon the size of inlet aperture of

multi-leg homogeniser. A detailed procedure of design and development of prototype of MHCA for a certain concentration ratio is explained below.

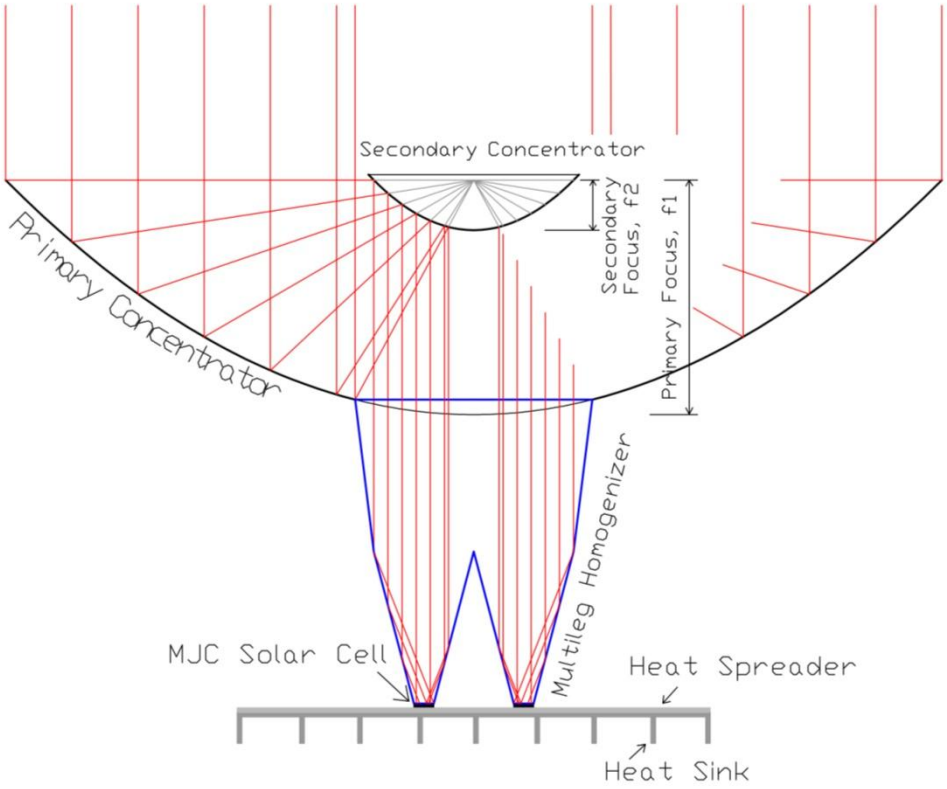


Figure 7.3: Distribution of Rays in Multi-Leg Homogeniser Concentrating Assembly

Table 7.1: Design parameters for Primary Reflector

| Sr. No. | Parameter | Symbol | Units | Value |
|---|---|---|---|---|
| 1 | Geometric Concentration Ratio | $CR_g$ | - | 165 |
| 2 | Area of MJC | $A_C$ | $m^2$ | 0.00003025 (5.5mm x 5.5mm) |
| 3 | Area of Centre Square Hole | $A_{HO}$ | $m^2$ | 0.0025 (50mm x 50mm) |

The design parameters related to the size calculation of primary reflector/concentrator are given in Table 7.1. The geometric concentration ratio of x165 is selected for the design of current MHCA. The geometric concentration ratio is the ratio of the effective concentrating area and the area of multi-junction solar cell (MJC). The size of MJC is 5.5 mm x 5.5 mm,

provided by Arima Photovoltaic and Optical Co., as explained in the previous chapters. The system can be designed for higher concentration ratio. However, lower concentration ratio is only selected for prototype purpose as higher concentration ratio needs bigger reflector area that can make system expensive at testing stage. In order to provide the space for mounting of multi-leg homogeniser, a 50 mm x 50 mm square hole is cut in the centre of the primary reflector, as shown in the Figure 7.4. Therefore, the net effective area of concentrating assembly and the total area of primary reflector are given by Equations (7.1) and (7.2), respectively.

$$\text{Effective Area of Concentrating Assembly, } A_{con} = CR_g \times A_C \times 4 \qquad (7.1)$$

$$\text{Area of Primary Concentrator } = d_1^2 = A_{con} + A_{HO} \qquad (7.2)$$

The parameter $d_1$ gives one of the dimensions of the primary reflector as its shape is assumed to be square. The square shape of primary reflector is helpful to obtain the compact arrangement of concentrators in a CPV module. The value '4' in Equation (7.1) represents the total number of MJCs accommodated by the MHCA. Therefore, with the concentration ratio of 165, the size of the primary reflector given by Equation (7.1) is 150 mm x 150 mm. It must be noted here that the primary reflector is basically a square cut part of the circular parabolic reflector, as shown in Figure 7.4. The diameter of the corresponding circular primary reflector is equal to the diagonal of the square reflector. However, the effective area of the primary reflector is shown by the white shaded area in Figure 7.4. Equation (7.3) gives the diameter of the corresponding circular diameter.

$$D_1 = \sqrt{d_1^2 + d_1^2} = \sqrt{2d_1^2} \qquad (7.3)$$

In order to design a compact and small system, the overall height of the concentrating assembly or primary reflector is kept minimum. The minimum effective height of the primary reflector can be achieved when the height or depth 't' of the reflector is the same as that of its focal length $f_1$. Therefore, by using the equation of parabola, the focal length of the primary reflector is given by the Equation (7.4).

$$f_1 = \frac{(D_1/2)^2}{4t_1} = \frac{D_1^{\,2}}{16 f_1} \qquad (f_1 = t_1)$$

$$f_1^{\,2} = \frac{D_1^{\,2}}{16} \qquad (7.4)$$

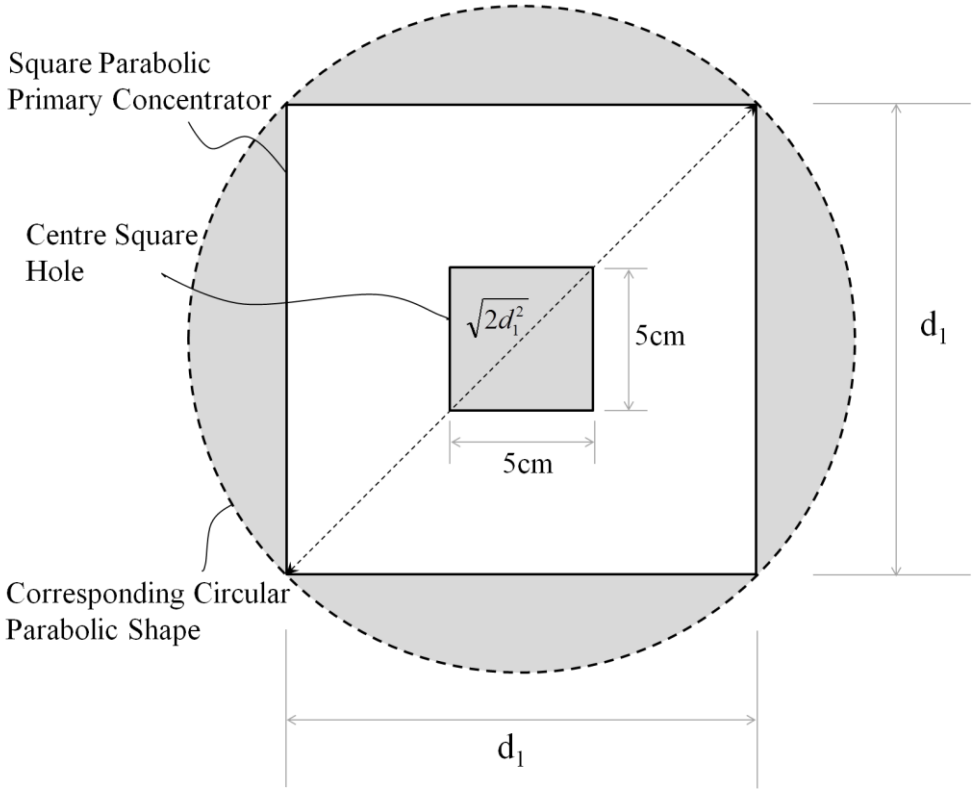


Figure 7.4: Schematic for Size Calculations for Primary Reflector

From Equation (7.3), the value of the $D_1$ is calculated as 21.2132 cm, with value of $d_1$ as 15 cm. Therefore, by using Equation (7.4), the focal length of

the primary reflector $f_1$ can be calculated as 5.3033 cm. For the development and fabrication of the primary reflector, the coordinates of the parabolic curvature are given by Equation (7.5) and are shown in Figure 7.5.

$$x^2 = 4fy \qquad (7.5)$$

| x(cm) | y(cm) | x(cm) | y(cm) |
|---|---|---|---|
| 10.6066 | 5.3033 | -10.6066 | 5.3033 |
| 10.5 | 5.1972 | -10.5 | 5.1972 |
| 10 | 4.7140 | -10 | 4.7140 |
| 9.5 | 4.2544 | -9.5 | 4.2544 |
| 9 | 3.8184 | -9 | 3.8184 |
| 8.5 | 3.4059 | -8.5 | 3.4059 |
| 8 | 3.0170 | -8 | 3.0170 |
| 7.5 | 2.6517 | -7.5 | 2.6517 |
| 7 | 2.3099 | -7 | 2.3099 |
| 6.5 | 1.9917 | -6.5 | 1.9917 |
| 6 | 1.6971 | -6 | 1.6971 |
| 5.5 | 1.4260 | -5.5 | 1.4260 |
| 5 | 1.1785 | -5 | 1.1785 |
| 4.5 | 0.9546 | -4.5 | 0.9546 |
| 4 | 0.7542 | -4 | 0.7542 |
| 3.5 | 0.5775 | -3.5 | 0.5775 |
| 3 | 0.4243 | -3 | 0.4243 |
| 2.5 | 0.2946 | -2.5 | 0.2946 |
| 2 | 0.1886 | -2 | 0.1886 |
| 1.5 | 0.1061 | -1.5 | 0.1061 |
| 1 | 0.0471 | -1 | 0.0471 |
| 0.5 | 0.0118 | -0.5 | 0.0118 |
| 0 | | | 0 |

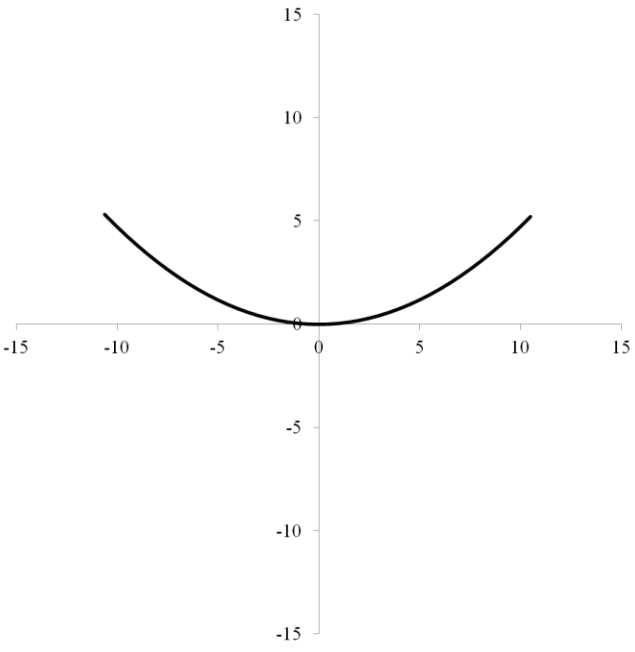


Figure 7.5: Coordinates of the Primary Reflector

After the design of primary reflector, the second step is to design the multi-leg homogniser. The homogeniser design is based upon the assembly of four similar units to make a single piece of homogeniser. In the design of homogeniser, first the design of single unit of homogeniser is explained, followed by the assembly of the complete unit of multi-leg homogeniser. The simple design schematic of the multi-leg homogeniser is shown in Figure 7.6, showing the 2D-view of the homogeniser with only two outlet aperture shown as the design of the homogeniser is symmetrical. The design of the homogeniser is divided into two portion: the lower tapered portion that is below line 'eb' and the upper tapered portion that is above line 'eb'. The lower

tapered portion, as explained before, is designed such that when the incident rays are parallel to the concentrator axis, they are uniformly distributed over the cell area with edge ray leaving homogeniser outlet at point 'c'. However, the upper tapered portion is designed to handle the tracking error when the rays are not parallel to the concentrator axis. Here, the design of lower tapered portion is discussed first for the case of parallel incident rays.

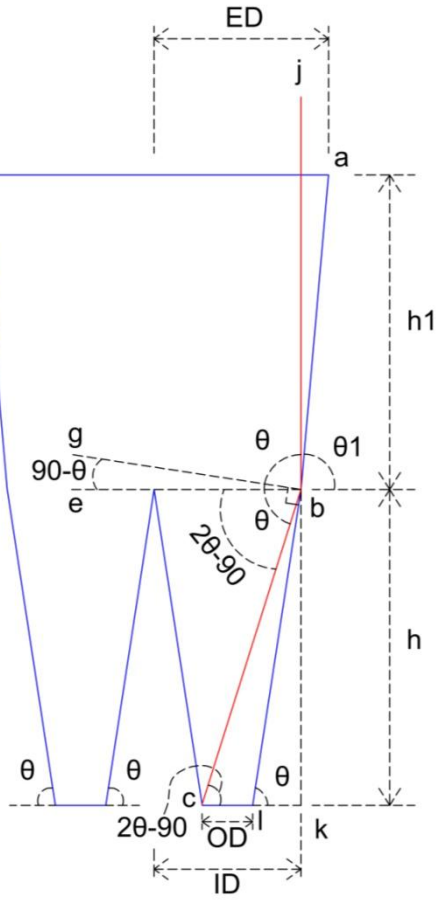


Figure 7.6: Schematic of Multi-leg Homogeniser Design

As shown in Figure 7.6, the parallel edge ray 'j' received from the secondary reflector, is reflected from the point 'b' of homogeniser. The angle 'θ' or slope of the line 'bl' is of great importance here as it should be selected such that the edge ray 'j' must leave the homogeniser at point 'c'. The representation and the dependence of angles, shown in Figure 7.6, are based upon the trigonometric

laws. The line 'bg' is perpendicular to lower tapered side 'bl' and the edge ray 'j', after being reflected by the side 'bl', according to optics law, makes angle 'θ' with perpendicular 'bg'. Therefore, if right angle triangle Δckb is considered, the height 'h' of the lower tapered portion is given by Equation (7.6).

$$h = \left[ OD + \left( \frac{ID - OD}{2} \right) \right] . \tan(2\theta - 90) \qquad (7.6)$$

It can be seen that there are two unknowns 'h' and 'θ' in Equation (7.6). Therefore, another Equation (7.7) is obtained from the right angle triangle Δblk.

$$h = \left( \frac{ID - OD}{2} \right) . \tan\theta \qquad (7.7)$$

By comparing Equations (7.6) and (7.7), the slope 'θ' of lower tapered portion of homogeniser is given by Equation (7.8).

$$\left[ OD + \left( \frac{ID - OD}{2} \right) \right] . \tan(2\theta - 90) = \left( \frac{ID - OD}{2} \right) . \tan\theta \qquad (7.8)$$

The size of the outlet aperture of homogeniser 'OD' is 5.5mm, same as the size of MJC. The value of 'ID' is taken as the 16 mm. The value of 'ID' is assumed according to the convenience of fabrication but not very small and not very large as it will cast shadow on the reflector. Later, it will be shown that the value of 'ID' also affects the size of the secondary reflector. Therefore, by solving Equation (7.8) with hit and trial for the given values of 'ID' and 'OD', the value of slope 'θ' is calculated as $81.33^{o}$. The height 'h' of the lower tapered portion can now be calculated using Equation (7.7) as 34.43 mm.

The lower tapered portion of the homogeniser is designed to accommodate the parallel rays. Now, the upper tapered portion of the homogeniser is needed to be designed to accommodate the non-parallel rays. The aim of the design of the upper taper portion is to accommodate rays with tracking error up to $1^o$. From the graphical method, it is found that with small deviation in the incident ray, it experiences an increase of $1^o$ angle after being reflected by the primary reflector. Moreover, there is a further increase of $2^o$ angle after being reflected by the secondary reflector. Therefore, with the incident ray having a tracking error or angular deviation of $1^o$ from the axis of concentrator, the angle of ray entering the homogeniser has an angle of $4^o$, as graphically shown in Figure 7.7. Half of the size of multi-leg homogeniser inlet aperture was found to be as 19 mm, by using the graphical method, to accommodate the tracking error of $1^o$. Therefore, the rays with angular deviation less than $1^o$, are directed towards the outlet aperture of homogeniser by the upper tapered portion.

After the design of the multi-leg homogeniser, the third and final step in design of MHCA is the design and size calculation for the secondary reflector. As explained before, the size of the secondary reflector is based upon the inlet size 'ID' of the lower tapered portion of homogeniser. Therefore, the focal point for secondary reflector can also be found using Equation (7.4) but the value of '$D_1$' is replaced with 'ID' as the depth or height of the secondary reflector is also assumed to be the same as its focal length due to primary reflector design constraint. Similarly, the coordinates of the parabolic curvature of the secondary reflector can also be found using Equation (7.5). The maximum value of 'x' is taken as 19mm, half of the size of inlet aperture of multi-leg homogeniser. It should be noted that the foci of both of the

reflectors must coincide with each other in order to get parallel rays and these parallel rays must hit the lower taper portion of the homogeniser for which 'ID=16mm'. This is the reason that, to calculate the focal point of secondary reflector, $D_1$=16mm is used with depth of the reflector taken equal to its focal length. Meanwhile, the half of the overall dimension of the secondary reflector is 19mm, the same as the half of the inlet aperture of homogeniser to accommodate tracking error.

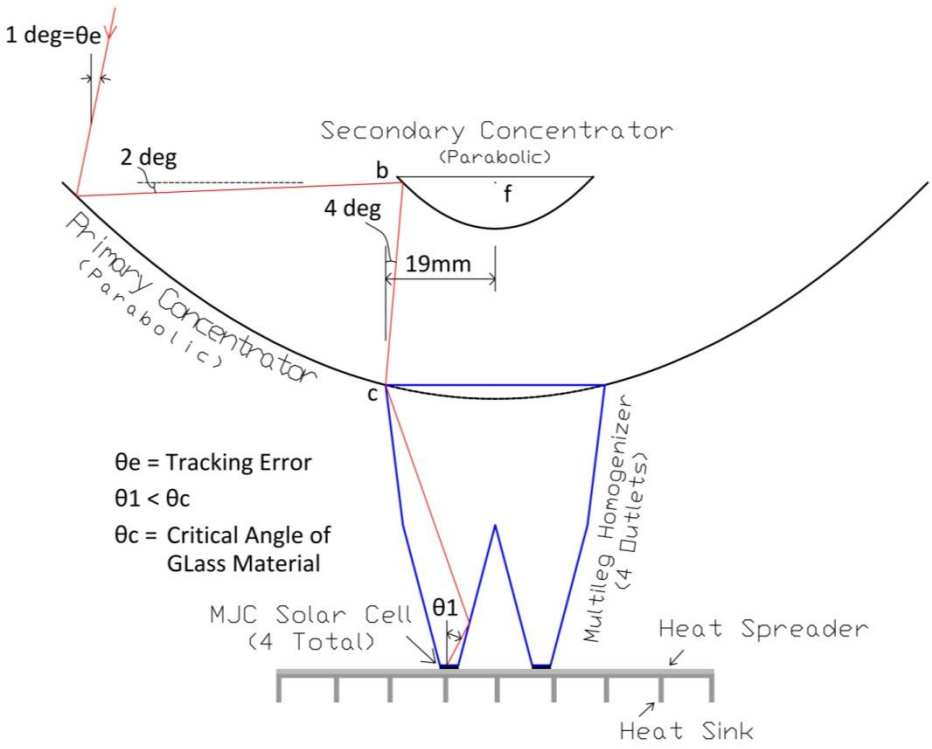


Figure 7.7: Acceptance Angle Calculation through Schematic of Multi-Leg Homogeniser Concentrating Assembly

The 3D design model of the developed prototype of CPV system with multi-leg homogeniser concentrating assembly, mounted onto two axis solar tracker, is shown in Figure 7.8. The multi-leg homogeniser is placed in the centre hole of primary reflector, with four MJCs at its outlet. The secondary reflector is mounted in the centre of the primary reflector with the help of aluminium extrusions.

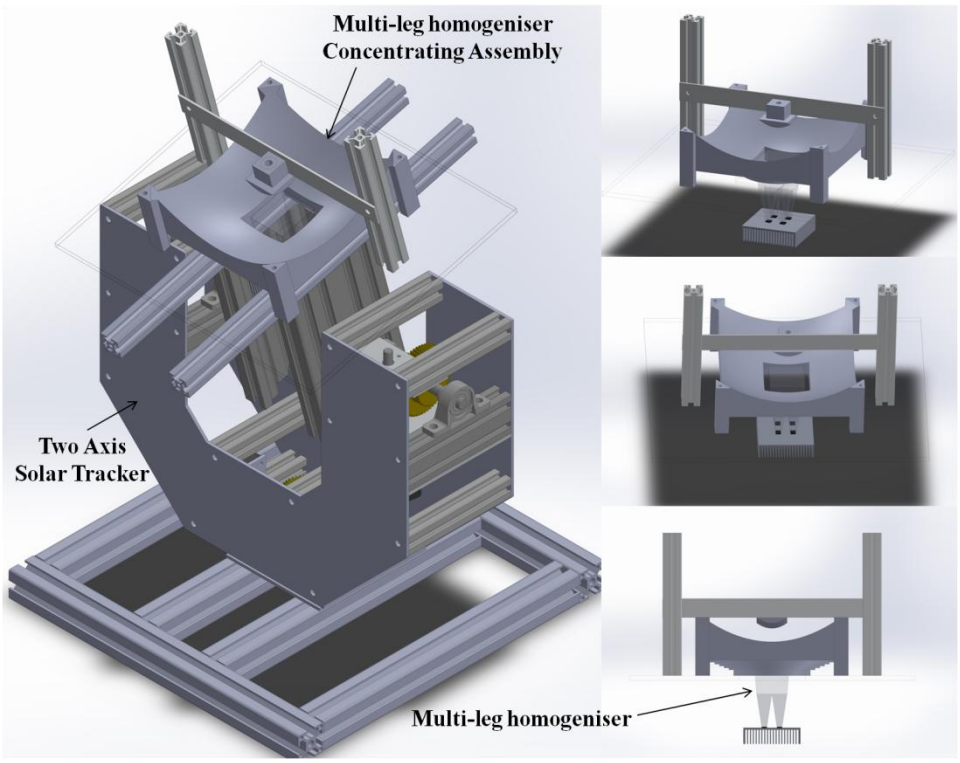


Figure 7.8: Design Model of Multi-leg Homogeniser Concentrating Assembly

## 7.3 Development of Experimental Setup of Multi-leg Homogeniser CPV System

In order to investigate the real field performance of the designed novel multi-leg homogeniser concentrating assembly (MHCA), the prototype of the CPV system is developed based upon the designed 3D model, as shown in Figure 7.8. To verify the design of the multi-leg homogeniser concentrating assembly (MHCA), the developed CPV prototype for concentration ratio of 165 is shown in the Figure 7.9. The details of the two axis solar tracker and the control box have been explained in Chapter 3. The developed concentrating assembly is mounted onto the aluminium frame of the solar tracker. Both primary and secondary reflector are fabricated from aluminium block with a further coating of aluminium to make the surface quality better. Just like mini dish cassegrain CPV system, the primary and secondary concentrators of

current concentrating assembly were coated with a layer of silver and $SiO_2$. However, the oxidation and peeling of the coating layers were observed. The oxidation of the silver coating and the surface quality are shown in the figure 7.10. Both of the reflectors were then recoated with a layer of aluminium and $SiO_2$.

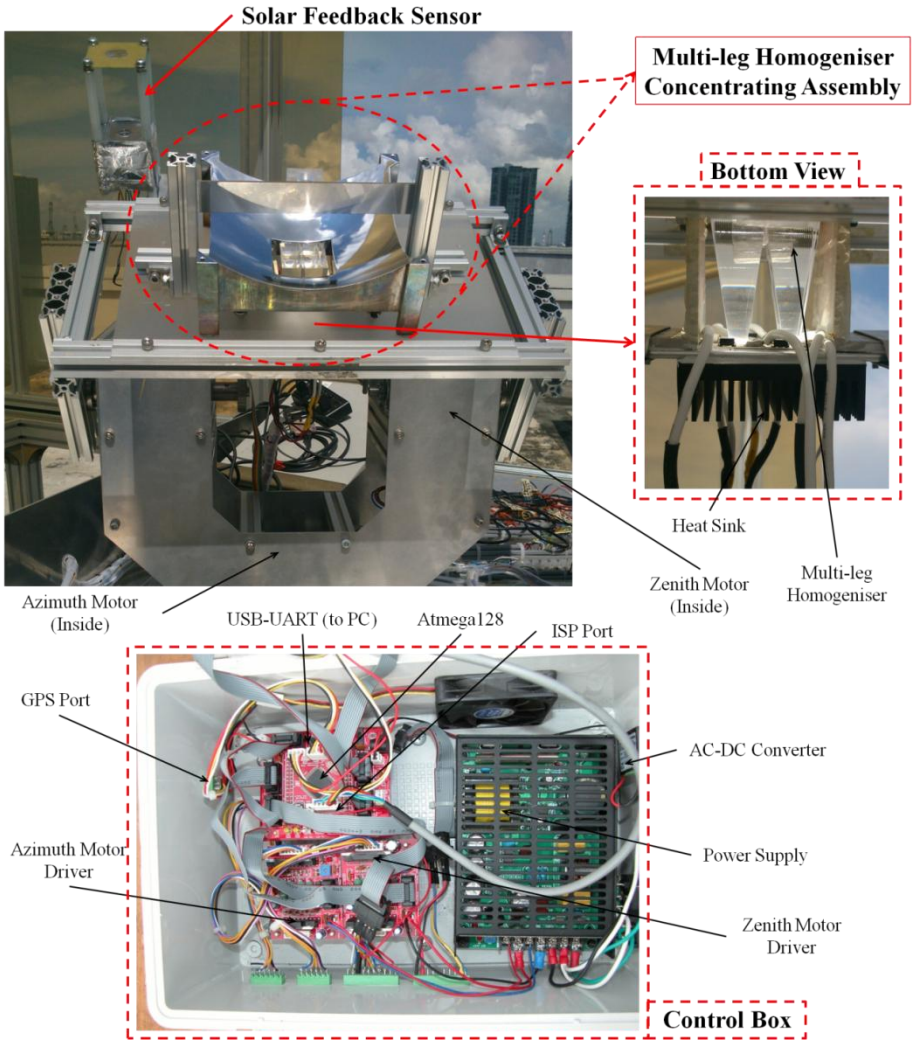


Figure 7.9: Experimental Setup of Multi-leg Homogeniser CPV System


Figure 7.10: Oxidation of Silver Coating

The details of the fabricated multi-leg homogeniser concentrating assembly (MHCA) is shown in Figure 7.11. The secondary reflector is mounted in the centre of primary reflector through mounting plates and aluminium extrusions. However, the mounting height was adjusted such that the foci of both reflectors coincide with each other . All of the four MJCs were connected in series electrical connection, placed side by side to each other. The distance between two MJCs was kept the same as the distance between two outlet apertures of the homogeniser. The output of the CPV system was supplied to MPPT and then to data logger for performance parameters measurements. The homogeniser was then placed on the top of the MJC assembly with mechanical mounting. The MJCs were attached to heat spreader and heat sink through thermal tape, for heat dissipation. In order to measure the back plate or heat sink temperature of the CPV assembly, a thermistor type temperature sensor was attached to the heat sink. The multi-leg homogeniser is made of four similar single pieces of glass rod, according to the design explained in the previous section. The development of the multi-leg homogeniser is shown in the Figure 7.12.

The designed multi-leg homogeniser can be made as a single unit using glass moulding as glass machining techniques have limitations. However, for prototype purpose, the glass moulding is not the option due to high cost of mould. Therefore, the homogeniser was fabricated first in four separated pieces, which were then joined together as one unit. UV cured optical glue was used to join all the four pieces. The blue light shown is the UV light to cure the glue. In addition, N-BK7 glass material was used for the fabrication of current homogenise.

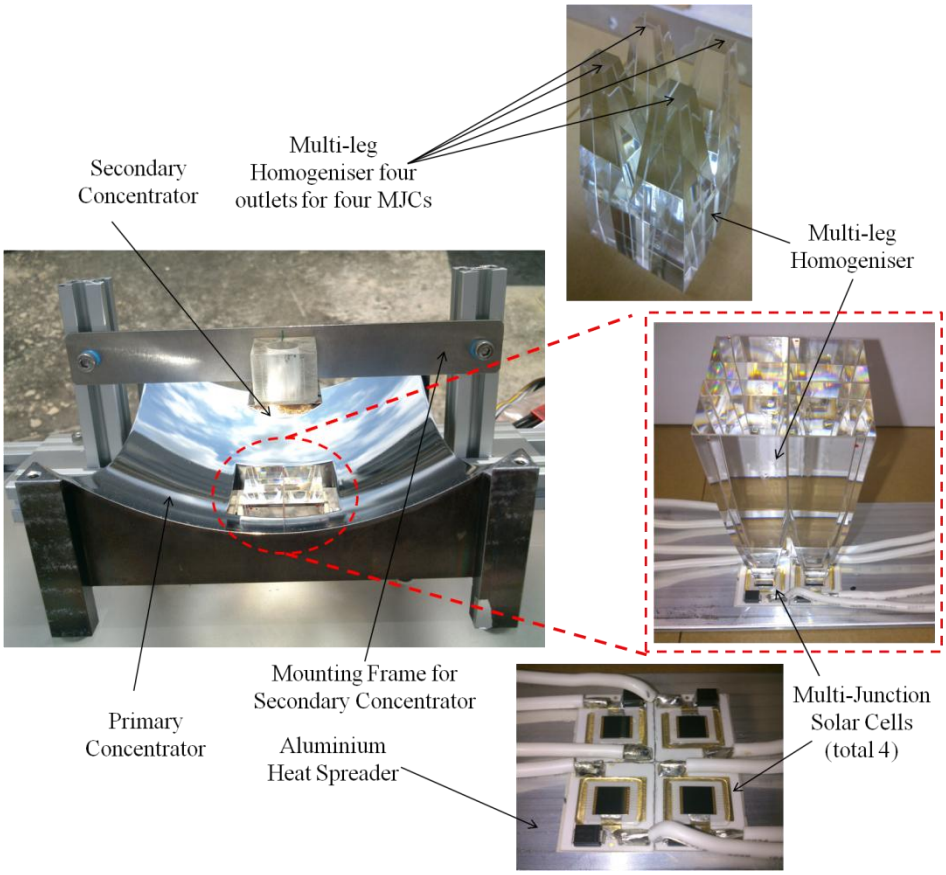


Figure 7.11: Development of Multi-leg Homogeniser Concentrating Assembly

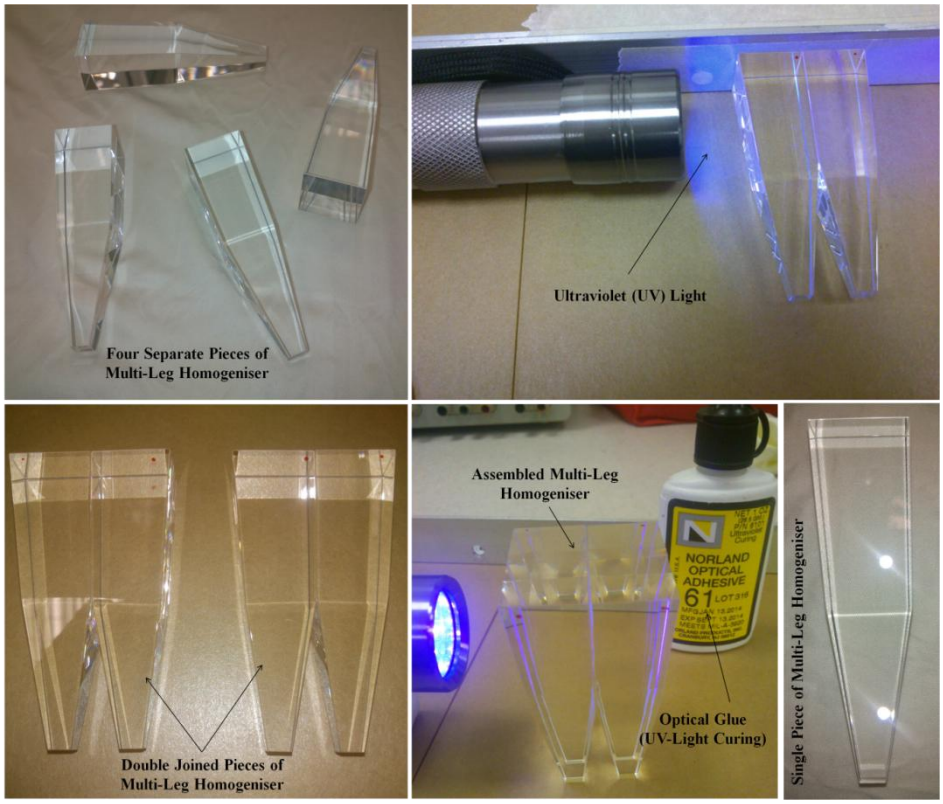


Figure 7.12: Development of Multi-Leg Homogeniser

In order to calculate the system efficiency, same performance equations were used related to CPV experimentation, as discussed in Chapter 5. The CPV system considered here is based upon CPV module and MPPT. The system parameters were calculated and recorded on a spread sheet file using the same developed LabVIEW program.

## 7.4 Results and Discussion

The performance of the developed multi-leg concentrating assembly (MHCA) was first evaluated using ray tracing simulation to verify the design and uniformity of ray distribution at the outlet apertures of multi-leg homogeniser. The model of the multi-leg homogeniser concentrating assembly was developed in TracePro for ray tracing simulation, as shown in Figure 7.13. In order to simulate the concentrating assembly, a square grid source was used as the primary reflector is also in square shape. The ray tracing simulation of the concentrating assembly was first carried out for parallel rays and secondly for the rays with solar subtended angle. The ray tracing simulation results of the multi-leg homogeniser concentrating assembly for parallel rays are shown in Figure 7.14, with the irradiance maps to show the distribution of rays at the four outlets of the homogeniser. As can be seen from the simulation results, the parallel rays after being reflected by the secondary reflector, become parallel again which are then separated and concentrated onto four MJCs. According to the design, it can also be seen that all of the parallel rays are hitting at the lower taper portion of the homogeniser. In addition, rays can also be seen equally and uniformly distributed at the four outlets of the homogeniser.

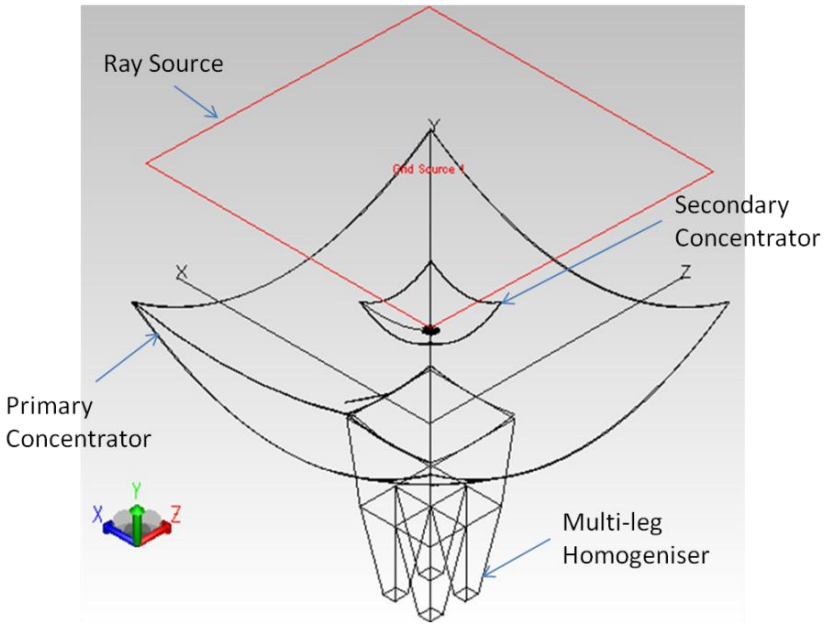


Figure 7.13: TracePro Model of Multi-leg Homogeniser Concentrating Assembly

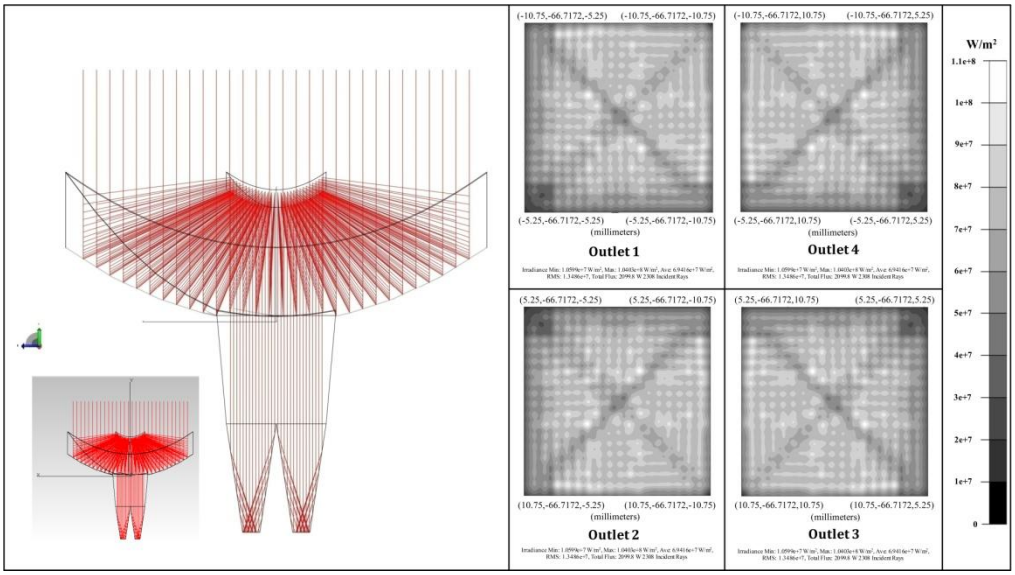


Figure 7.14: Ray Tracing Simulation of Multi-leg Homogeniser Concentrating Assembly with Parallel Rays

In Figure 7.15, the ray tracing simulation of the concentrating assembly is shown with the incident rays having solar subtended angle. In actual field operation, the solar radiation are not parallel due to finite distance of sun from the earth, and the rays subtend a certain angle with axis of the concentrator. From the simulation results, it can be seen that the rays are still perfectly

distributed among all the four outlets of homogeniser and uniformly concentrated over the outlet apertures of the homogeniser. However, it can be seen that the rays, after being reflected by the secondary reflector, hit the upper taper portion of the homogeniser, which is designed to accommodate the tracking error or non-parallel rays. The rays with the subtended solar angle are non-parallel to the concentrator axis and that is why they are hitting the upper taper portion of the homogeniser, which further guides them towards the outlet of homogeniser.

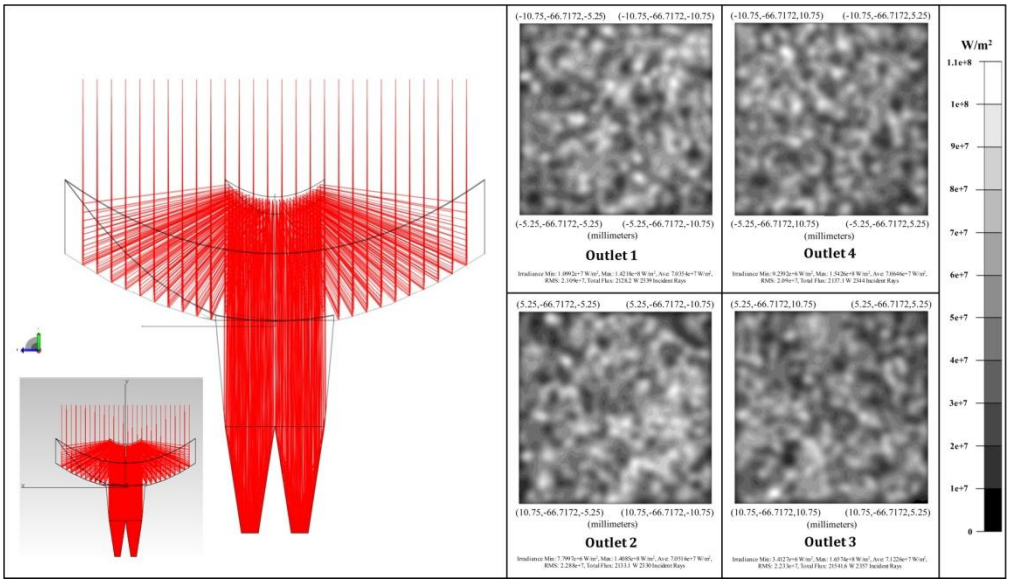


Figure 7.15: Ray Tracing Simulation of Multi-leg Homogeniser Concentrating Assembly with Solar Ray Angle

To analyze the real outdoor field performance of the developed multi-leg homogeniser CPV system, the experiment was conducted under the tropical weather of Singapore at rooftop of NUS EA-building. The system was operated for whole day and the performance parameters of the CPV system were recorded at an interval of one second. The CPV system efficiency variation against the received DNI for whole day operation, is shown in Figure 7.16. From the experimental results, it can be seen that the maximum

efficiency of 15% is achieved by the developed multi-leg homogeniser CPV system. But the average efficiency is around 14% during operation. This CPV efficiency is slightly lower than the mini dish cassegrain CPV system, while having the same reflective coating. The main reason of lower efficiency is due to lower concentration ratio, as the multi-junction solar cell operates at comparatively lower efficiency at lower concentration. It must be noted that the MHCA has concentration ratio of x165, while for mini dish cassegrain CPV system, it is x496.

The total power output of the CPV system, with total voltage output, is shown in Figure 7.17. It can be seen that the power output is proportional to the DNI received; it increases with increase in the DNI and vice versa. However, with the increase in power, the total voltage output decrease as at higher DNI, the maximum power point voltage reduces. The maximum power output achieved from the system is around 2W. As the MJCs are connected in series, the same amount of current flows through each of the solar cell. From the ray tracing simulation result, the equal and uniform distribution of the concentrated rays have already been seen at the outlet of the homogeniser. However, in order to verify the distribution of power and voltage among four MJCs during whole day operation, the power and voltage output curves of each of the four MJCs are shown in Figures 7.18 and 7.19.

It can be seen that both the voltage and power output of each of the MJC are almost equal for whole day operation. This gives the experimental verification of the equal distribution of the solar energy among the four MJCs using single set of concentrators, which was the main motive for development of current multi-leg homogeniser concentrating assembly (MHCA).

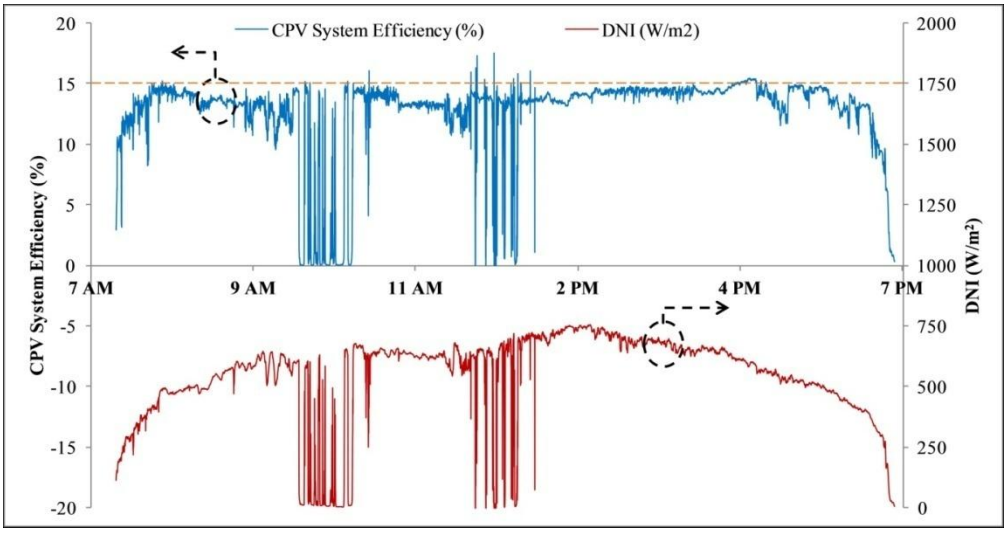


Figure 7.16: Efficiency Curve for Multi-leg Homogeniser CPV System

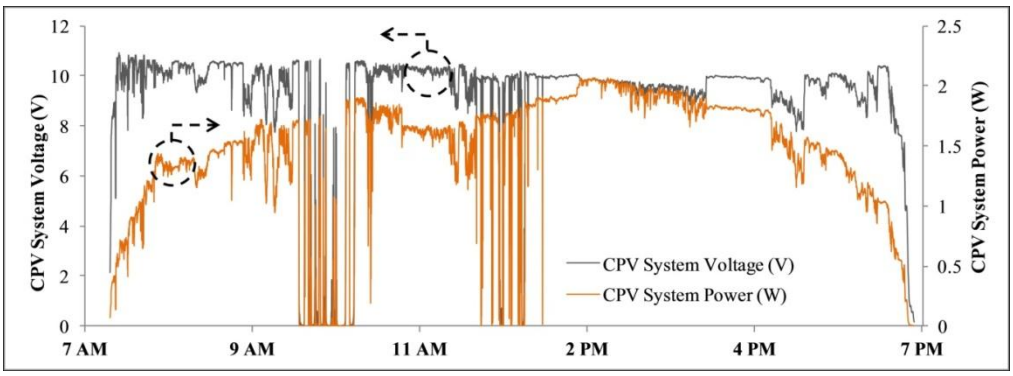


Figure 7.17: Power and Voltage Curve for Multi-leg Homogeniser CPV System

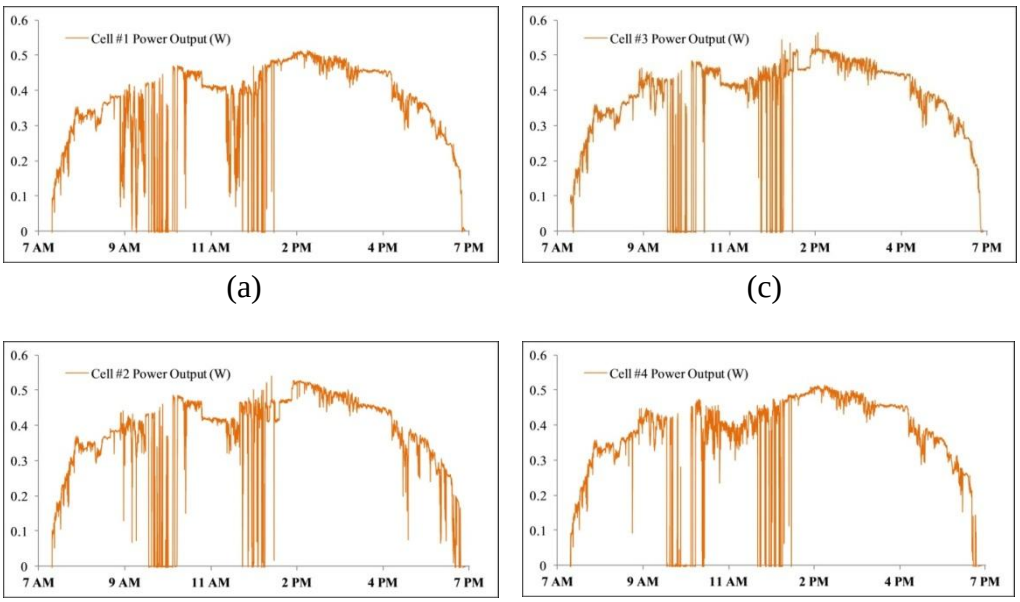


Figure 7.18: Power Output for Each Individual Cell of Multi-leg Homogeniser CPV System

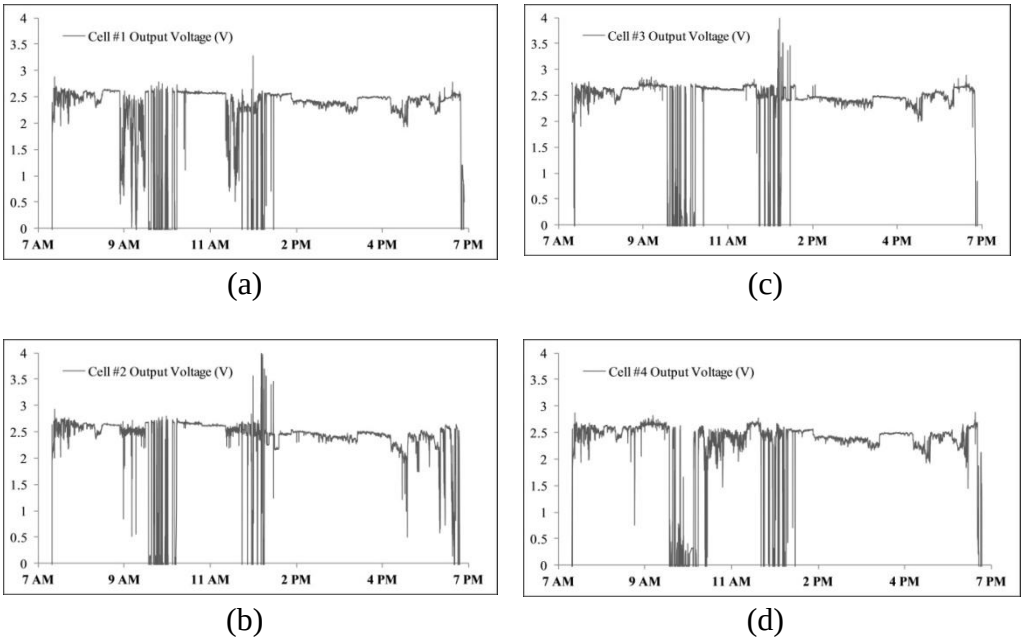


Figure 7.19: Voltage Output for Each Individual Cell of Multi-leg Homogeniser CPV System

The performance of the developed CPV system is investigated through simulation either for parallel rays or for rays with solar subtended angle and experimentally where the tracking accuracy is only $0.3^{o}$. However, another important aspect of the concentrating assembly is its acceptance angle. As explained before, the acceptance angle is represented by the normalized power output curve. It also helps to decide the tracking accuracy suitable for that particular concentrating assembly. The simulated and experimental normalized power output curves for the multi-leg homogeniser CPV system, against the angular deviation with constant output load, are shown in Figure 7.20. It can be seen that there is a good agreement of simulated and experimental normalized power curves until point 'A', i.e. at $1.4^{o}$ tracking error. However, almost 100% of the maximum power is achieved within tracking error of $1^{o}$. Beyond angular deviation of $1^{o}$, both simulated and experimental curves start to drop, indicating ray loss. However, there is a sudden drop in the experimental curve as compared to the simulated curve. After point 'A', the

experimental curves propagate in steps, while there is a gradual drop in the simulated curve.

In order to investigate the varying trends of the simulated and experimental normalized power curves, the irradiance map at all the four outlet apertures of the homgeniser, against the specific mentioned points are shown in Figure 7.21. The irradiance maps are obtained from ray tracing simulation of the developed MHCA. Before discussion, it is worth mentioning here that the simulated curve is based upon the total flux at outlet apertures of the homogeniser. However, the experimental curve is based upon the actual electrical power output of the CPV system at constant output load. From the irradiance maps at point 'A' in Figure 7.21(A), it can be seen that the Cell 3 and Cell 4 are under shadow. The solar cell under shadow operates with lower performance. This justifies the sudden drop of the experimental curves after point 'A' as Cell 3 and cell 4 come under shadow. And when the angular deviation goes beyond point 'A', they pulls down the overall power output of the system as all four MJCs are connected in series.

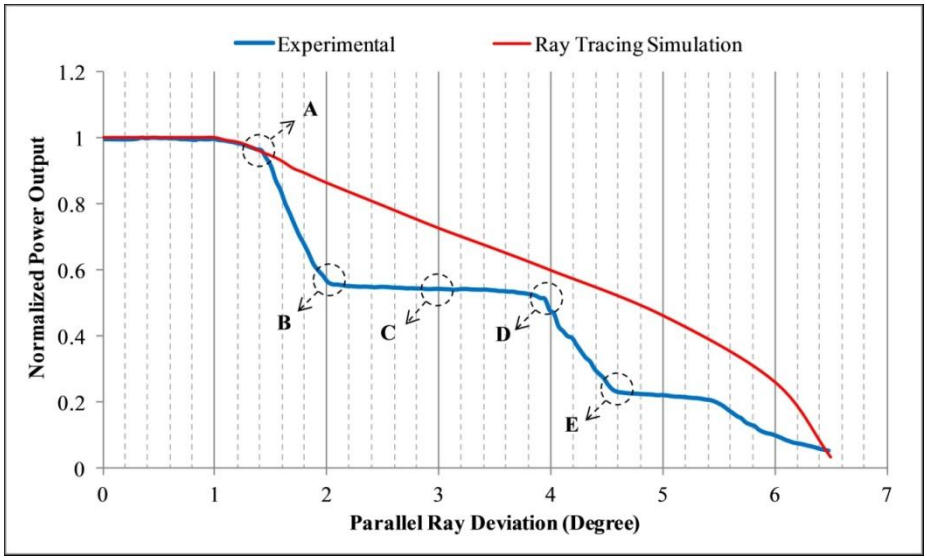


Figure 7.20: Normalized Power Output Curves for Multi-leg Homogeniser CPV System

Furthermore, it can also be seen that the normalized power output moves steadily at 52%, through points B,C and D. From the irradiance maps, it can be seen that at all these point, Cell 3 and Cell 4 are under complete shadow, which means that only two cells are operating at these points. However, it does not mean that the total radiation flux is also reduced to 50%, which can be seen from the simulated curve. The main reason for lower electrical power output is due to shift of maximum power point and pulling effect from cells under shadow. The experimental curve again starts to drop after point "D" as now Cell 1 and Cell 2 are coming under shadow, shown in Figures 7.21(D) and 7.21(E).

The performance data of the developed CPV system in terms of daily power output, daily solar input and overall daily DNI efficiency, is shown in Table 7.2. The electrical rating is based upon daily power output projected for one year. The data shown here is based upon the system operation under different weather conditions, i.e. clear sky and cloudy conditions. As concluded in the previous chapter, the average efficiency is more effective to analyze the true system performance than the instantaneous system efficiency as it changes continuously throughout the day. It can be seen that the average efficiency of the developed CPV system is varying at around 11%. But the overall average efficiency of 10.57% is recorded for the set of experiments mentioned in Table 7.2, although the instantaneous efficiency is around 15%. In order to estimate the system performance for high and low DNI regions and for systems with different average efficiencies, a graph is plotted between daily electrical rating and yearly DNI received, as shown in Figure 7.22.

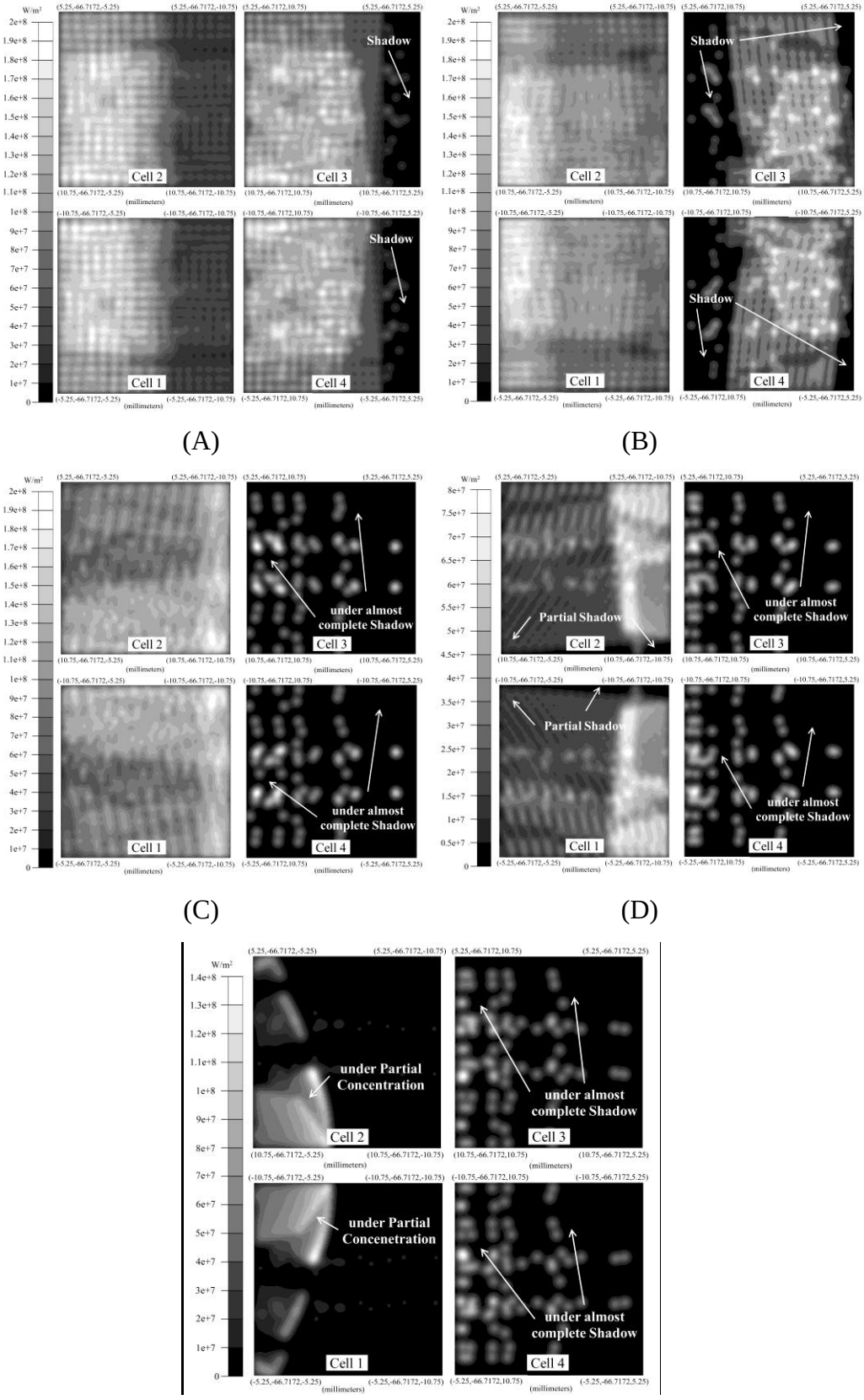


Figure 7.21: Simulated Irradiance Map at Each Cell Outlet of Multi-leg Homogeniser at Different Parallel Ray Deviation Angles

Table 7.2: Daily Performance Data for Developed CPV System

| Sr. No. | Total DNI ($kJ/m^2$/day) | Total DNI ($kWh/m^2$.year) | MJC Output (kJ/day) | Electrical Rating ($kWh/m^2$.year) | Average Daily Efficiency (%) |
|---|---|---|---|---|---|
| 1 | 14371.65 | 1457.13 | 9.83 | 44.28 | 3.04 |
| 2 | 6034.80 | 611.86 | 13.83 | 62.32 | 10.19 |
| 3 | 6719.27 | 681.26 | 15.42 | 69.48 | 10.20 |
| 4 | 21502.40 | 2180.10 | 52.31 | 235.70 | 10.81 |
| 5 | 10419.86 | 1056.46 | 24.32 | 109.60 | 10.37 |
| 6 | 19429.16 | 1969.90 | 46.22 | 208.26 | 10.57 |
| 7 | 18858.67 | 1912.06 | 45.26 | 203.96 | 10.67 |
| 8 | 11587.55 | 1174.85 | 27.30 | 123.03 | 10.47 |
| 9 | 1795.16 | 182.01 | 3.53 | 15.89 | 8.73 |
| 10 | 24338.01 | 2467.60 | 60.50 | 272.61 | 11.05 |
| 11 | 19509.75 | 1978.07 | 48.55 | 218.78 | 11.06 |
| 12 | 25356.25 | 2570.84 | 63.09 | 284.27 | 11.06 |
| 13 | 23470.92 | 2379.69 | 59.05 | 266.08 | 11.18 |
| 14 | 21201.88 | 2149.64 | 51.78 | 233.32 | 10.85 |
| 15 | 19751.69 | 2002.60 | 49.50 | 223.04 | 11.14 |
| 16 | 19725.04 | 1999.90 | 50.03 | 225.44 | 11.27 |
| 17 | 20113.67 | 2039.30 | 52.27 | 235.55 | 11.55 |
| 18 | 16361.74 | 1658.90 | 42.12 | 189.80 | 11.44 |
| **Overall Average Efficiency** | | | | | **10.57** |

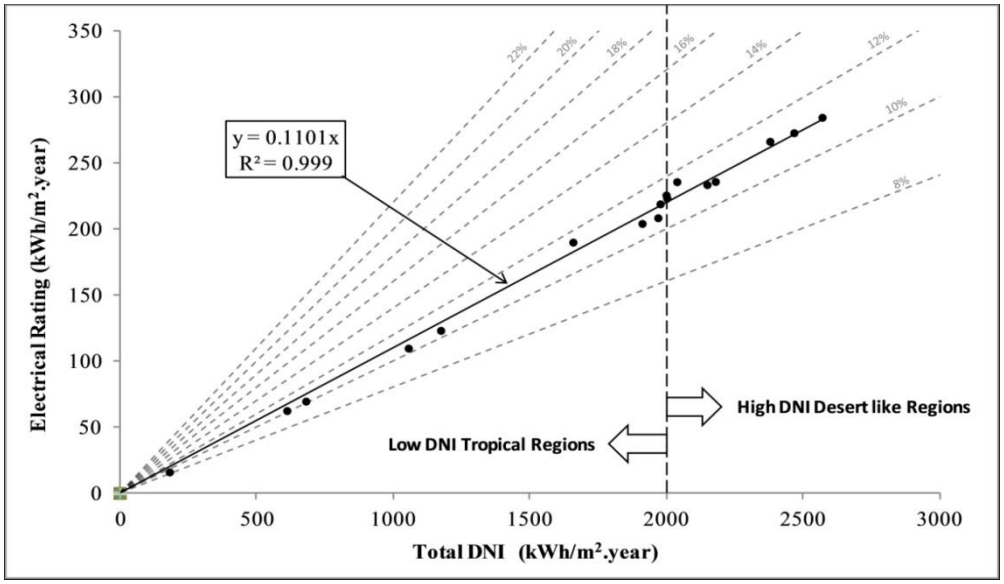


Figure 7.22: Electrical Rating of Developed CPV System against Total Available DNI

This graph is similar to the electrical rating graph discussed in the previous chapter. It can be seen that the experimental data is regressed with average efficiency of 11.01%. However, high efficiency systems can be designed with higher concentration ratio and optical efficiency. By knowing the corresponding average efficiency curve, the output of the developed system can be truly estimated in low or high DNI regions if annual average received DNI is known.

## 7.5 Summary

In this chapter, a novel multi-leg homogeniser concentrating assembly (MHCA) is proposed, designed and developed for CPV applications. As compared to the conventional CPV concentrating assembly design that uses single concentrator for single MJC, the proposed design is able to use single set of concentrators to concentrate solar radiations onto four MJCs. As a result, this can further help to lower the cost of the CPV system with less number of concentrators

The design of the MHCA is discussed based upon three steps. First step is the design of primary reflector according to the required concentration ratio of x165 and with the parabolic reflecting curvature. The primary concentrator is designed in square shape for compact system design with lowest effective focal length. After the design of primary concentrator, the second step is the design of the multi-leg homogeniser. The design of homogeniser is based upon the design of one single piece, then joined together as complete unit of multi-leg homogeniser. The homogeniser design has two tapered portions. The lower tapered portion handles the parallel rays and guides them according to the

design; while the upper tapered portion is designed to handle the tracking error or non-parallel rays. Based upon the inlet aperture size of the multi-leg homogeniser, the size of the secondary reflector was selected and designed with parabolic reflecting surface using same design equations as that of the primary reflector. However, the foci of both of the reflectors must coincide with each other to get the parallel concentrated rays.

Based upon the designed MHCA, a CPV prototype was fabricated to investigate its performance in real field. Both reflectors were made and coated with aluminium. All the four pieces of multi-leg homogeniser were joined together as a complete unit, using UV cured optical glue. The system performance was first investigated using ray tracing simulation in TracePro. The rays were observed to be distributed uniformly and equally at outlet apertures of the homogeniser. To verify the design and simulation results, the system was experimentally investigated for whole day operation. Maximum efficiency of 15% was recorded with average daily efficiency of 11%. Equal power output of all four MJCs was recorded for whole day operation. From the normalized power output graph, the concentrating assembly was found to have an acceptance angle of $1^{o}$.

The multi-leg homogeniser CPV system is designed and investigated through simulation and experimentation. The proposed system is believed not to only simplify the system assembly, but also to lower the overall cost of the system as less number of concentrators are needed for same capacity of the system. In the next chapter, the methodology regarding the standalone operation of CPV-Hydrogen system will be discussed.

# Chapter 8: Design Optimization and Energy Management of Concentrated Photovoltaic (CPV-Hydrogen) System using micro Genetic Algorithm for Standalone Operation

## 8.1 Introduction

In the previous chapter, the performance of the CPV system is analyzed for the production of the hydrogen along with the significance of hydrogen as energy storage. The main need of the energy storage system is due to the intermittent nature of the solar energy caused by the cloud cover in the day time and its unavailability during the night time. In Chapter 5, only the potential of hydrogen production using CPV system is investigated. However, for operation of any solar energy system, energy storage as energy backup is compulsory for the steady uninterrupted power supply or for off-grid operation. Excess energy produced at the time of the low energy demand is stored and then supplied back when the produced power by the solar energy system is not enough to meet the energy demand. For this purpose, there is a need for the system design to be optimized such that the system has enough capacity to produce enough stored energy for continuous power supply to the load at lowest overall cost (investment and operational) of system. This requires a design modeling and optimization of energy system with respect to size of system, its control strategies and economics. In literature, there are many optimization techniques developed for the standalone operation of PV, using hydrogen production as energy storage. However, for the standalone

operation of the concentrated photovoltaic (CPV) system, the most efficient system among all the photovoltaic technologies, there is no optimization algorithm or tool and energy management technique discussed in the literature.

There are some commercial tools also developed for the design optimization and the simulation of the renewable energy systems. One of the most popular commercial tools is HOMER (Hybrid Optimization of Multiple Energy Resources), which is developed by the NREL (National Renewable Energy Laboratory) USA, for design, simulation and optimization of the renewable energy system and hybridization with other power production or energy storage systems. Similarly, another commercial tool iHOGA (improved Hybrid Optimization by Genetic Algorithms) is developed by the University of Zaragoza, which also provides the different algorithm and design strategies related to the design and optimization of the renewable energy systems. Both of these commercial tools, HOMER and iHOGA, only consider conventional photovoltaic (PV) systems for the optimization and simulation analysis **[136,137]**. However, none of these tools considers CPV for system analysis. Another tool TRNSYS is developed only for the simulation of renewable energy systems, but without optimization. By combining TRNSYS with HYDROGEMS libraries, developed at IFE, the renewable energy systems alone or hybrid systems can be optimized but still the analysis is limited to the PV system only. There are many other commercial tools developed like HYBRIDS2, SOLSIM, RAPSIM, ARES and SOMES. However, all of these tools can only be used to simulate renewable energy system without optimization and even for simulation, only PV system can be analyzed,

without CPV consideration **[138]**. A summary of the commercial renewable energy analysis tools is shown in table 8.1.

Table 8.1: Comparison Summary of Renewable Energy System Simulation and Optimization

| | Optimization | Simulation | Hydrogen Energy Storage | Analyze CPV? |
|---|---|---|---|---|
| HOMER[136] | x | x | x | No |
| iHOGA[137] | x | x | x | No |
| TRNSYS + HYDROGEMS[138] | x | x | x | No |
| HYBRIDS2[138] | | x | x | No |
| SOLSIM[138] | | x | | No |
| INSEL[138] | | x | | No |
| ARES[138] | | x | | No |
| SOMES[138] | | x | | No |
| RAPSIM[138] | | x | | No |

Because of the highest solar energy conversion efficiency, the concentrated photovoltaic (CPV) system is of the main interest for the future research. On the other hand, it can be seen that there is no optimization and design algorithm discussed in the literature and all commercial tools are also lacking for CPV system consideration for design and optimization analysis. The main aim of this chapter is to develop the design model and optimization algorithm with the control strategies for the standalone operation of the CPV system with the hydrogen production as energy storage. For the developed technique, the multi-variable design and multi-objective optimization strategy is proposed with the techno-economic analysis of the overall CPV-hydrogen system. The CPV-Hydrogen system is optimized with regards to its size for zero PSFT (power supply failure time) and optimum state of the energy storage with

minimum overall system annual cost. As discussed in chapter 6, most of the CPV performance prediction models are not reliable to be used for performance prediction considering all details of the system. Therefore, a CPV performance model is also proposed based upon the CPV system basic parameters and cell characteristics using the actual weather data and then the results are verified with the electrical rating discussed in the previous paper. Besides optimized design, the chapter also discusses the simulated long term performance of the individual system of the CPV-Hydrogen, using the weather data of the Singapore.

## 8.2 CPV-Hydrogen System Description

The schematic of the proposed CPV-Hydrogen system considered for the optimization of the standalone operation simulation is shown in the Figure 8.1. The concentrated photovoltaic (CPV) system is consisting of the CPV modules utilizing multi-junction solar cells (MJCs). The CPV modules are installed onto the two axis solar trackers, which are one of the main component of the CPV system as the concentrators need to face towards the sun all the time. For the analysis, the CPV module of any type can be considered; It can be either Fresnel lens based refractive type CPV module or Mini Dish based Casegrain reflector type CPV module. The performance model of the CPV system only considers the solar concentration at the cell area, regardless of the type of the concentrator. The output of each of the CPV system is connected to a MPPT (maximum power point tracking) device to ensure the CPV operation at maximum power or efficiency point . The DC output power of each of the CPV system is fed into the main DC line at a

certain voltage through DC/DC converter. All of the other components of the CPV-Hydrogen system, either power producing or power consuming, are connected to this main DC line, directly or directly for power exchange.

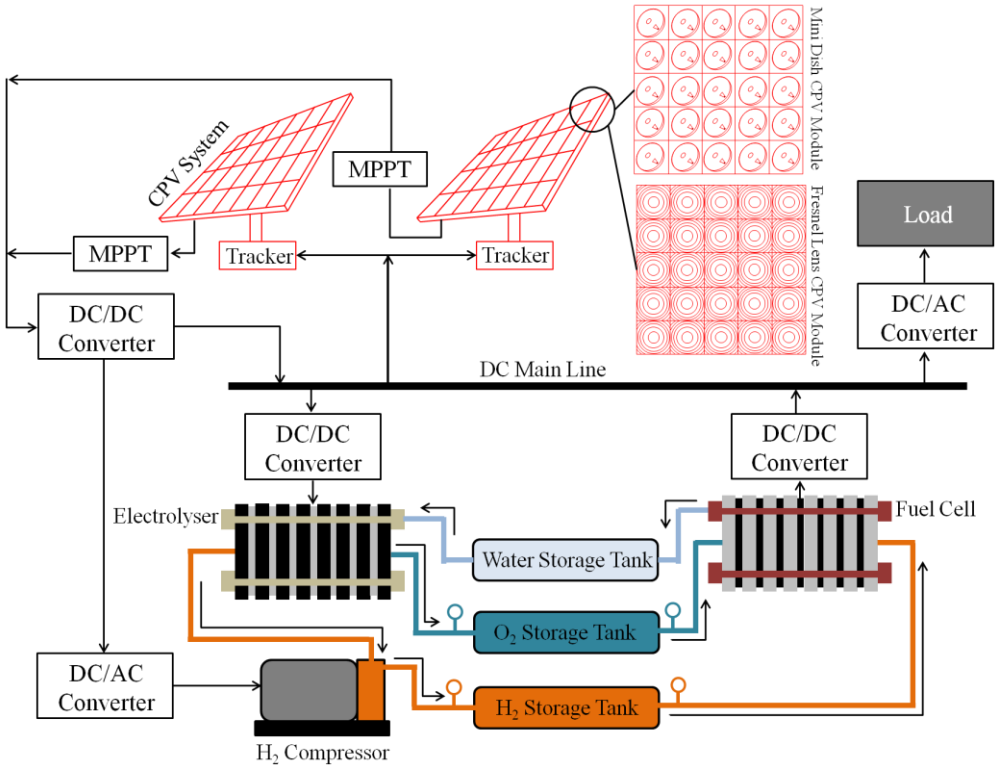


Figure 8.1: Schematic of CPV-Hydrogen System for Standalone Operation

The power required for the operation of the two axis solar trackers is also supplied from the main DC line. The primary objective of the current CPV-Hydrogen system optimization is to have uninterrupted electric (AC) power supply to the consumer load. This load is also connected to the main DC line through AC/DC converter. The power to the solar trackers and consumer load, is supplied at first priority. Then the excess power produced by the CPV systems is supplied to the electrolyser for the production of the hydrogen and oxygen for energy storage purpose. The produced hydrogen is further compressed through mechanical compressor and stored into the storage tanks. The compressor is also powered from the CPV systems via the main DC line

through AC/DC converter. If the supplied power from the CPV is not enough to meet the consumer load requirements, the power deficit is covered through the stored energy, i.e. by the power supplied from the fuel cell that utilizes the hydrogen and oxygen gases.

## 8.3 Development of Performance Model for CPV-Hydrogen System

The performance model developed for the optimization of CPV-Hydrogen system, is based upon the performance model of each of the subsystems. All of the individual components of the CPV-Hydrogen system are linked with each other according to the energy management flow chart, as shown in Figure 8.2. The input for the current system simulation and the optimization is the weather data that is taken in the form of the direct normal irradiance (DNI). The main reason for the consideration of only DNI data is because of the fact that, unlike the conventional stationary PV systems, the CPV system can only accept the beam components of solar radiations. The DNI input is used to calculate the concentration at cell area. Therefore, by knowing the size of the concentrator, optical efficiency of concentrating assembly, performance characteristics of the MJC and total number of the CPV systems, the total power output of the CPV system can be determined at certain DNI input.

Hourly electric load profile is another input parameter to the current system simulation, according to which the system will be optimized. The power requirement of the solar trackers and the hydrogen compressor is the other timely system load that is also considered with the total electrical load requirements. If the power supplied by the CPV systems is in excess, it is

supplied to the electrolyser, and the electrolyser model is then used to calculate the production of hydrogen and oxygen. Similarly, in case of the power deficit, the fuel cell model is used to calculate the consumption of hydrogen and oxygen according to the power deficit. The water tank is connected in loop to both the electrolyser and the fuel cell as the water consumed by the electrolyser is replenished by the water production from the fuel cell.

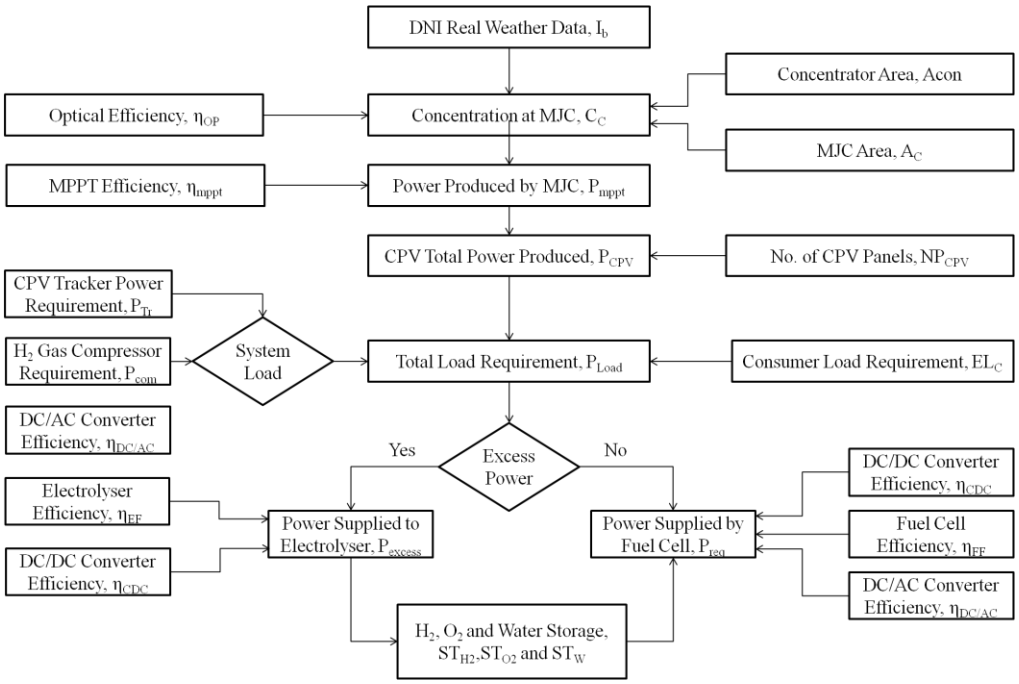


Figure 8.2: Energy Management Flow Chart for Proposed CPV-Hydrogen System

### 8.3.1 Direct Normal Irradiance (DNI) Weather Data

As mentioned before, the DNI is used as the input weather data for current simulation and optimization, and it is based upon the real solar beam radiation data collected at the rooftop of EA-Building of National University of Singapore for one year period from September 2014 to August 2015. The data was collected using Eppley Pyrheliometer mounted onto two axis solar tracker

and at an interval of one second. The summary of the weather data in the form of the beam solar energy is shown in the figure 8.3. Other weather parameters like the ambient temperature and the global radiations are obtained from the National Environment Agency (NEA) Singapore **[134]**. The summary of these parameters, along with the monthly percentage of beam radiations received, is also shown in Figure 8.3. The shown data is the same as used for the electrical rating analysis.

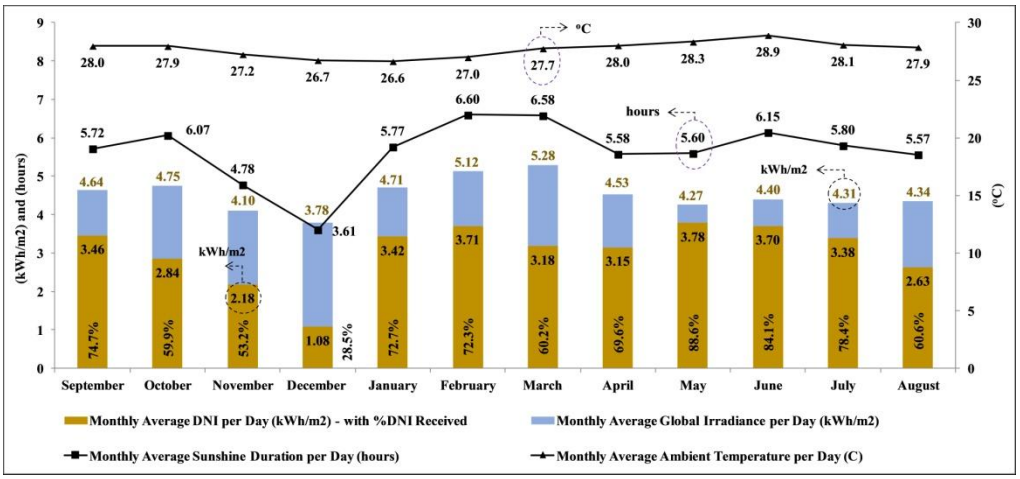


Figure 8.3: Summary of Monthly Solar Energy Received by Singapore

### 8.3.2 Electrical Load Profile

The consumer electrical load profile for which the CPV-Hydrogen system is optimized for standalone operation is shown in Figure 8.4. This electrical load profile is obtained from Energy Market Authority (EMA) Singapore **[139]**, at an interval of 30 minutes. The electrical load profile provided by the EMA is basically for whole country, in megawatt units. However, for current simulation, a part of the total electrical load is considered with the same trend of the electrical profile, extracted for 2nd February, 2015. However, the units are taken in watts with the same numerical value, instead of megawatt.

Furthermore, the electrical load profile is considered to be same throughout the yearly operation as the hourly change in the load is minimum.

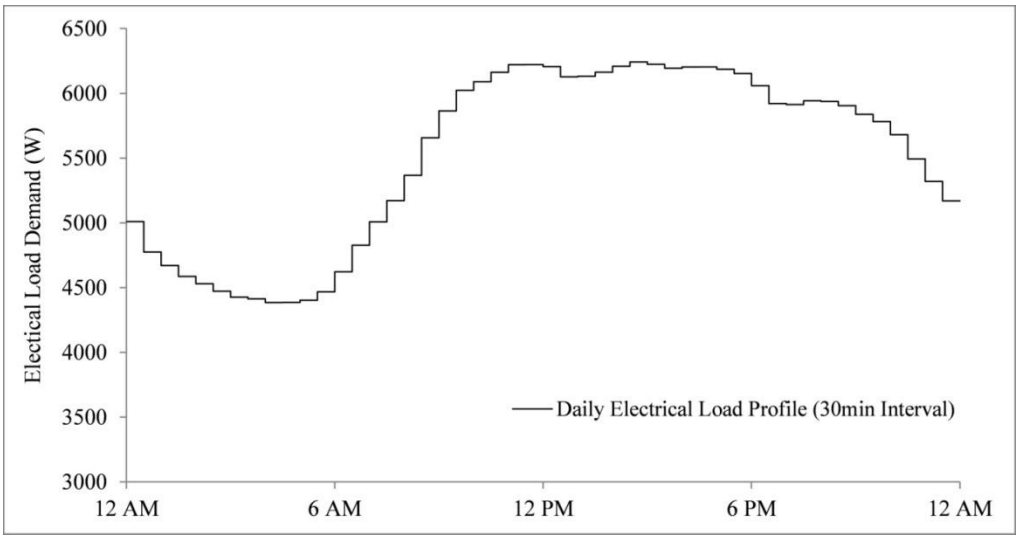


Figure 8.4: Part of Electrical Load Profile of Singapore with 30 minutes internal

### 8.3.3 Concentrated Photovoltaic (CPV) System

The concentrated photovoltaic (CPV) model considered in this paper is based upon the multi-junction solar cell (MJC) characteristics and Equation (8.1) gives the power output of MJC **[140]**.

$$P_C = I_C V_C = V_C \left[ I_o \left\{ \exp\left( \frac{qV_C}{nkT_C} \right) - 1 \right\} - I_{SC} \right] \qquad (8.1)$$

The solar cell current "$I_C$" in the above equation is given by the simple diode model for the solar cell but operating under concentration **[141]**. The constant parameter related to Equation (8.1) are given in Table 8.2.

Table 8.2: Parameters for Diode model for Solar Cell Under Concentration

| Symbol | Parameter Description | Value |
|---|---|---|
| **q** | Elementary charge [Coulomb] | $1.6021765 \times 10^{-19}$ |
| **k** | Boltzman's Constant | $1.3806488 \times 10^{-23}$ |
| **n** | Diode ideality factor for concentrated solar cell | 2 |

From the definition of open circuit voltage $V=V_{OC}$ and I=0, the diode saturation current factor "$I_o$" can be found using Equation (8.2).

$$I_o = \frac{I_{SC}}{\left[\exp\left(\frac{qV_{OC}}{nkT_C}\right)-1\right]} \qquad (8.2)$$

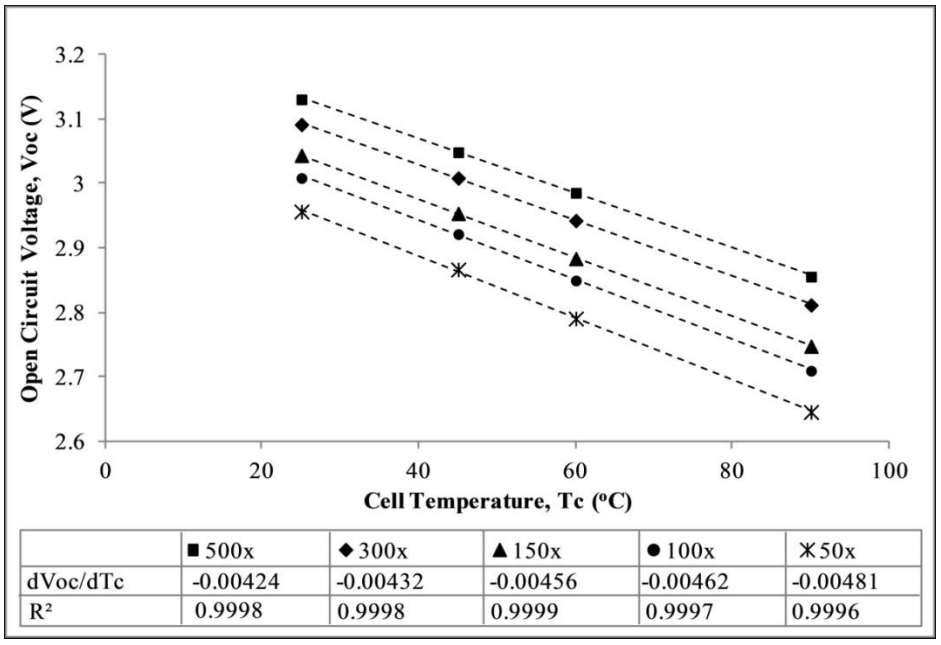


| | ■ 500x | ◆ 300x | ▲ 150x | ● 100x | ✳ 50x |
|---|---|---|---|---|---|
| dVoc/dTc | -0.00424 | -0.00432 | -0.00456 | -0.00462 | -0.00481 |
| $R^2$ | 0.9998 | 0.9998 | 0.9999 | 0.9997 | 0.9996 |

Figure 8.5: Variation of Cell Open Circuit Voltage ($V_{OC}$) with Concentration and Temperature

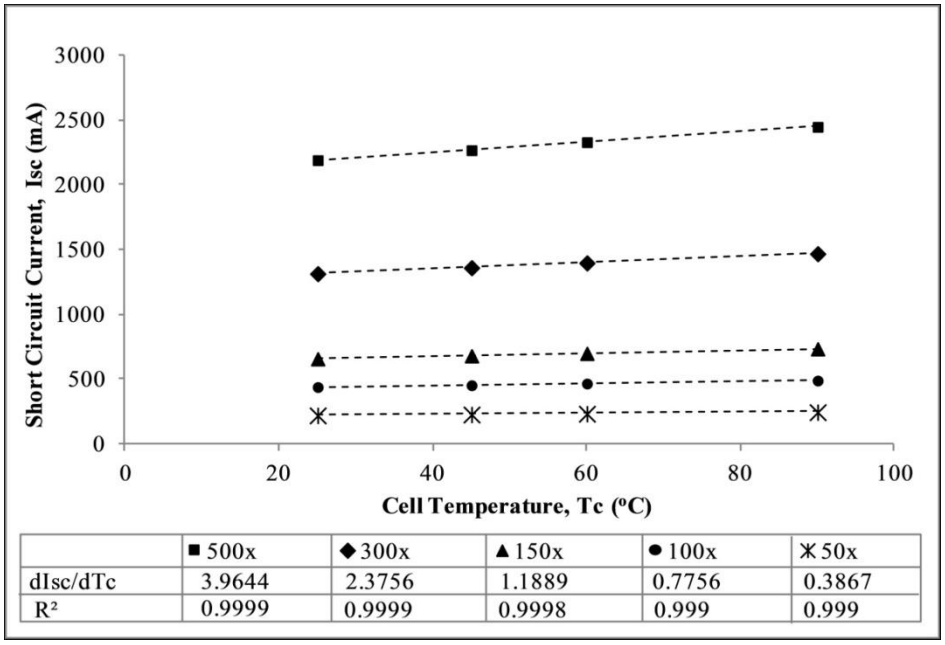


| | ■ 500x | ◆ 300x | ▲ 150x | ● 100x | ✳ 50x |
|---|---|---|---|---|---|
| dIsc/dTc | 3.9644 | 2.3756 | 1.1889 | 0.7756 | 0.3867 |
| $R^2$ | 0.9999 | 0.9999 | 0.9998 | 0.999 | 0.999 |

Figure 8.6: Variation of Cell Short Circuit Current ($I_{SC}$) with Concentration and Temperature

The two most important parameters affecting the performance of MJC are solar concentration at the cell area and the temperature of the cell. Therefore, in order to accurately predict the performance of MJC, the temperature and concentration characteristics of the InGaP/InGaAs/Ge MJC are employed by Arima Photovoltaic and Optical Corporation. The characteristic curves for the MJC under consideration, are shown in Figures 8.5 to 8.8. From the data, it can be seen that the trend of $V_{OC}$ variation is logarithmic against the concentration. However, short circuit current "$I_{SC}$" is directly proportional to the concentration at the cell area. Therefore, if the variation trend of the parameters is known at 25°C with the temperature coefficients at different solar concentration, then the parameters $V_{OC}$ and $I_{SC}$ can be found at any temperature and concentration using Equations (8.3) and (8.4).

$$V_{OC}(T_C, C_C) = \left[V_{OC}(at\ 25^o C)\right]_C + (T_C - 25)\left[\frac{dV_{OC}}{dT_C}\right]_C \qquad (8.3)$$

$$I_{SC}(T_C, C_C) = \left[I_{SC}(at\ 25^o C)\right]_C + (T_C - 25)\left[\frac{dI_{SC}}{dT_C}\right]_C \qquad (8.4)$$

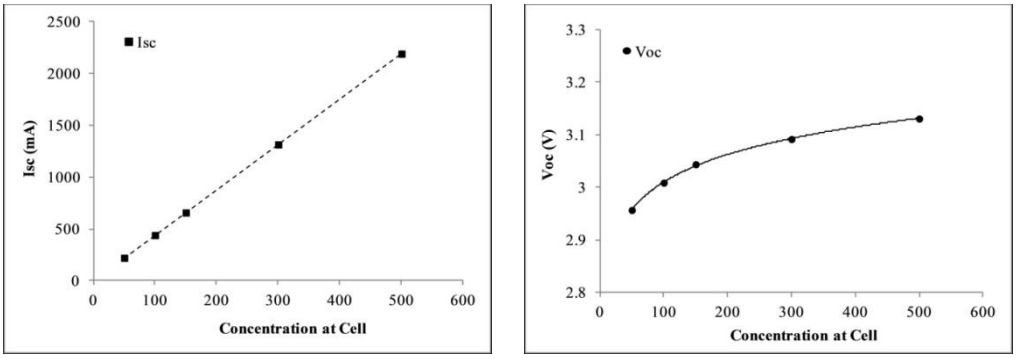


(a) (b)

Figure 8.7: Multi-junction Cell (a) Short Circuit Current (b) Open Circuit Voltage Versus Concentration at 25°C

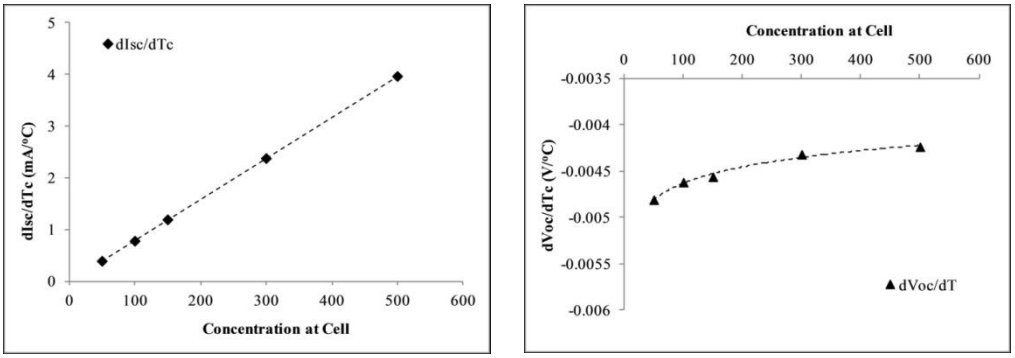


(a) (b)

Figure 8.8: Temperature Coefficients of Multi-junction Cell (MJC) against Concentration (a) Short Circuit Current (b) Open Circuit Voltage

The cell temperature for the current analysis is assumed to be 40$^{o}$C higher than the ambient temperature data, obtained from the weather department, as the temperature of the solar cell can be approximated 10$^{o}$C above the back plate temperature **[142]** and the temperature of the back plate is assumed to 20-30$^{o}$C higher than the ambient temperature. By using the concentrator area, optical efficiency of concentrating assembly and the direct normal irradiance (DNI), the solar concentration at the cell area is given by Equation (8.5).

$$C_C = DNI \times \frac{A_{con}}{A_C} \times \eta_{OP} \qquad (8.5)$$

For the efficient operation of the solar cell, there is a need to operate it at its maximum power point. The model for maximum power point tracking device can be obtained by taking the first derivative of the MJC power function and equating it to zero, as given by Equation (8.6).

$$\frac{dP_C}{dV_C} = 0 \qquad (8.6)$$

$$\frac{d}{dV_C}\left[V_C I_o \left\{\exp\left(\frac{qV_C}{nkT_C}\right) - 1\right\} - V_C I_{SC}\right] = 0 \qquad (8.7)$$

By taking the derivative and simplifying the expression, the MJC cell voltage, cell current and the cell power at the maximum power point can be found from Equations (8.8), (8.9) and (8.10).

$$V_{mppt} = V_{OC} - \frac{nkT_C}{q} \ln\left[1 + \frac{qV_{mppt}}{nkT_C}\right] \tag{8.8}$$

$$\mathrm{I}_{\mathrm{mppt}} = \mathrm{I}_{\mathrm{o}}\left\{\exp\left(\frac{qV_{mppt}}{nkT_C}\right) - 1\right\} - I_{SC} \tag{8.9}$$

$$P_{mppt} = \eta_{mppt} \times I_{mppt} \times V_{mppt} \tag{8.10}$$

Therefore, by using the power and the efficiency functions, the total power output of the CPV system can be found by using Equation (8.11).

$$P_{CPV} = \eta_{DC/AC} \times \eta_{CDC} \times \eta_{Tr} \times P_{mppt} \times N_{CM} \times NP_{CPV} \tag{8.11}$$

Where $N_{CM}$ represents the maximum number of the cell in a single CPV panel, which are considered as 25 for the current CPV system with a 5x5 array of the concentrators as the CPV panels are available in various sizes of concentrators like 4x4, 4x5 and 6x6 **[143,144]**. The values of the constant parameters appearing in Equation (8.11), are given in Table 8.3. The power requirement of two axis solar trackers is only considered during diurnal period, from sunrise to sunset, and the sunrise and sunset timings can be found using the solar geometry described in **[112]**. Regarding the optical efficiency of the concentrating assembly, most of the available CPV panels offer module efficiency of 29-30% while equipped with 40-41% efficient MJCs, which gives an optical efficiency of about 72-73% [**144]**. On the other side, for PMMA based Fresnel lens concentrators, the material transmittance varies

from 90-50% over the whole solar spectrum with an average of 80% transmittance efficiency. Moreover, about 92% is the reflective efficiency of the incident radiations at the inlet of the lens aperture **[145]**. Further 1% optical loss can be assumed to be at homogeniser due to material absorbance and the surface reflectance.

The comparison of the developed MJC model with the experimentally measured MJC efficiency, is shown in Figure 8.9.

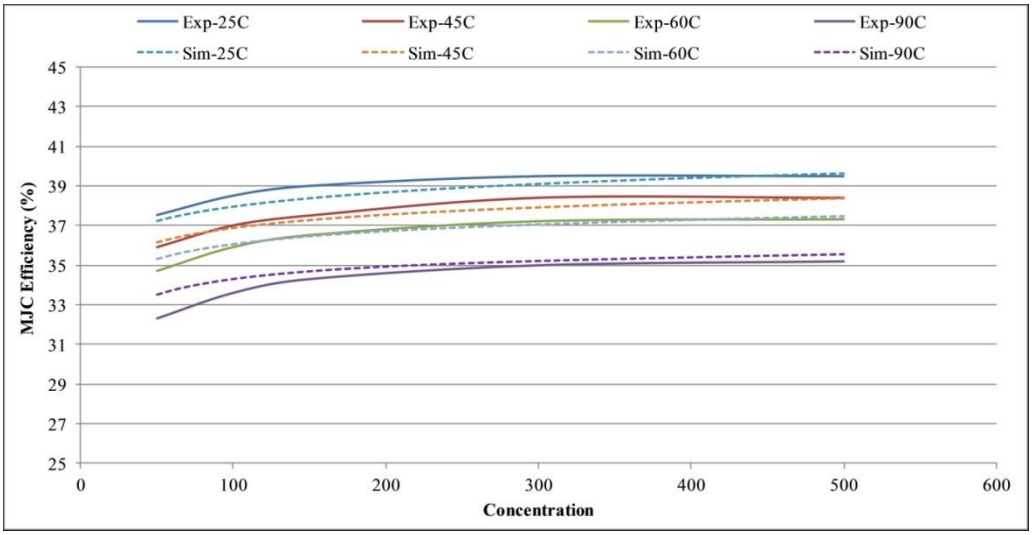


Figure 8.9: MJC efficiency Experimentally Measure and Simulated

Table 8.3: Parameters for Concentrated Photovoltaic (CPV) System

| Symbol | Value | Symbol | Value |
|---|---|---|---|
| $\eta_{mppt}$ [146] | 85% | $\eta_{Tr}$ [151] | 95% |
| $\eta_{DC/AC}$ [147,148] | 90% | $\eta_{OP}$ [145] | 72.5% |
| $\eta_{CDC}$ [149,150] | 95% | $N_{CM}$ | 25 |

### 8.3.4 Electrolyser

For the current system analysis, the alkaline electrolyser was considered for which the cell characteristics are provided by **[152]**. For the single cell of alkaline electrolyser, the IV characteristics can be found by using Equation

(8.12). The electrolyser is assumed to be operated at steady thermal condition, at a temperature of 80°C. The constant parameters related to Equation (8.12) are provided in Table 8.3.

$$U_E = U_{rev} + \frac{r_1 + r_2 T_E}{A_E} I_E + (S_1 + S_2 T_E + S_3 T_E^{\ 2}) \log\left( \frac{t_1 + \frac{t_2}{T_E} + \frac{t_3}{T_E^{\ 2}}}{A_E} I_E + 1 \right) \quad (8.12)$$

Table 8.4: Performance Parameters for Electrolyser Model

| Symbol (Units) | Values | Symbol (Units) | Values |
|---|---|---|---|
| $U_{rev}$ (V) | 1.229 | $A_E$ ($m^2$) | 0.25 |
| $r_1$ ($\Omega m^2$) | $7.331 \times 10^{-5}$ | $S_3$ ($V\ ^oC^{-2}$) | $-1.606 \times 10^{-5}$ |
| $r_2$ ($\Omega m^2\ ^oC^{-1}$) | $-1.107 \times 10^{-7}$ | $t_1$ ($m^2\ A^{-1}$) | $1.599 \times 10^{-2}$ |
| $S_1$ (V) | $1.586 \times 10^{-1}$ | $t_2$ ($m^2\ A^{-1}\ ^oC^{-1}$) | -1.302 |
| $S_2$ ($V\ ^oC^{-1}$) | $1.378 \times 10^{-3}$ | $t_3$ ($m^2\ A^{-1}\ ^oC^{-2}$) | $4.213 \times 10^{2}$ |

The amount of the hydrogen and oxygen produced by the electrolyser is based upon the amount of current flowing through the electrolyser cell and the Faraday efficiency. As the water molecule contains two atoms of hydrogen and one atom of oxygen, so the hydrogen production rate is double than the oxygen production rate. The hydrogen and the oxygen production can be calculated by using Equations (8.13) and (8.14) and their constant parameters are given in Table 8.5.

$$\dot{n}_{E,H2} = \eta_{EF} \frac{N_{EC} I_E}{n_E F} = 2 \dot{n}_{E,O2} \quad (8.13)$$

$$\eta_{EF} = a_1 . \exp\left( \frac{a_2 + a_3 T_E + a_4 T_E^{\ 2}}{\frac{I_E}{A_E}} + \frac{a_5 + a_6 T_E + a_7 T_E^{\ 2}}{\left(\frac{I_E}{A_E}\right)^2} \right) \quad (8.14)$$

Table 8.5: Parameters for Faraday Efficiency of Electrolyser

| Symbol (Units) | Values | Symbol (Units) | Values |
|---|---|---|---|
| a1 | 0.995 | a5 ($m^4$/A) | 1502.7083 |
| a2 ($m^2$/A) | -9.5788 | a6 ($m^4$/ A.$^o$C) | -70.8005 |
| a3 ($m^2$/A.$^o$C) | -0.0555 | a7 | 0 |
| a4 | 0 | $n_E$ | 2 |
| F (As/mol) | 96,485 | - | - |

The size of electrolyser is the main design parameter in current CPV-Hydrogen system optimization, that is needed to be determined in terms of the total number of electrolyser cells. The required number of the electrolyser cells can be calculated using Equation (8.15). The size of the electrolyser or the number of required electrolyser cells depend upon the maximum excess power available, that is the difference between maximum CPV power produced and the minimum load requirement. For currently considered alkaline electrolyser cells, the maximum cell voltage is 1.8V and the maximum current drawn is 750A. Moreover, the maximum rated power of the MJC is 5W, which is the rated power that most of the commercial MJC offers. It is assumed that the electrolyser cells are connected in series such that the same amount of current flows through each of the cell, given by the equation (8.16).

$$N_{EC} = \frac{(P_{MJC,\max} \times N_{CM} \times NP_{CPV}) - L_{\min}}{V_{EC,\max} \times I_{EC,\max}} \qquad (8.15)$$

$$I_E = \frac{\eta_{CDC} \times P_{excess}}{N_{EC} \times U_E} \qquad (8.16)$$

The $P_{excess}$ is the excess power supplied to electrolyser after fulfilling the total load requirements, the consumer electric load and the system load (CPV tracker and hydrogen compressor power requirements).

### 8.3.5 Fuel Cell

The PEM (Proton Exchange Membrane) fuel cell considered for the current system analysis is discussed in **[152]**. The fuel cell consumes the hydrogen and the oxygen for power production and like the electrolyser, the consumption of hydrogen is double than the oxygen. The rate of the hydrogen and the oxygen consumption depends upon the current supplied by the fuel cell and its faraday efficiency. For current fuel cell system, the faraday efficiency is assumed to be 0.7. The rate of the hydrogen and oxygen production can be found by using Equation (8.17)

$$\dot{n}_{F,H2} = \eta_{FF} \frac{N_{FC} I_F}{n_E F} = 2\dot{n}_{F,O2} \qquad (8.17)$$

Equation (8.18) gives the IV characteristics of the single cell of PEM fuel cell. The constant parameters for Equation (8.18) are given in Table 8.6. The active area per single cell of PEM fuel cell is taken as $A_F = 300\ cm^2$.

$$U_F = U_o - b\log\left(\frac{I_F}{A_F}\right) - R\left(\frac{I_F}{A_F}\right) \qquad (8.18)$$

Table 8.6: Performance Parameters for Fuel Cell Model

| $T_F = 70\ ^oC$ | | $T_F = 35\ ^oC$ | |
|---|---|---|---|
| Symbol (Units) | Values | Symbol (Units) | Values |
| $U_o$ (mV) | 1065 | $U_o$ (mV) | 1049 |
| b (mV/dec) | 80 | b (mV/dec) | 108 |
| R (Ω/cm) | 0.438 | R (Ω/cm) | 0.412 |

Similar to the design of electrolyser, the size of the fuel cell, in terms of the number of cells connected in series, is the main design parameter that is

needed to be optimized for the current system analysis. The number of the required cells depends upon the maximum load requirement of the system that is the consumer electric load during the system operation. For PEM fuel cell under consideration, the maximum power produced by single cell is 114.6W. Therefore, the total number of cells required to fulfill maximum power deficit requirements are given by equation (5.19).

$$N_{FC} = \frac{L_{\max}}{\eta_{CDC} \times \eta_{DC/AC} \times P_{FC,\max}} \qquad (5.19)$$

The current flow provided by the fuel cell depends upon the power deficiency, $P_{req}$ the power that CPV system is unable to provide to the consumer load and given by equation (5.20).

$$I_F = \frac{P_{req}}{\eta_{CDC} \times \eta_{DC/AC} \times N_{FC} \times U_F} \qquad (8.20)$$

### 8.3.6 Hydrogen Compressor

The excess electrical energy produced by the CPV system is stored in the form of the hydrogen and oxygen, by using electrolyser. The produced hydrogen is compressed and stored in storage cylinders as the mechanical compression provides a reliable and suitable solution. However, the oxygen is stored at its produced pressure without any compression. The power consumed by the mechanical compressor depends upon the inlet pressure and the pressure at compressor outlet i.e. storage tank pressure. The power consumed by the compressor can be computed using the equation (8.21) **[153]**.

$$P_{com} = \left( \dot{n}_{E,H2} \times \frac{M_{H2}}{1000} \right) \times CP_H \times \frac{T_{com}}{\eta_{DC/AC} \times \eta_{com}} \left\{ \left( \frac{P_{ta}}{P_E} \right)^{\left( \frac{r-1}{r} \right)} - 1 \right\} \qquad (8.21)$$

The details of the parameters appearing in the equation (8.21) are provided in Table 8.6. The flow rate of the hydrogen through the compressor is the same as the rate of hydrogen production from electrolyser. In addition, the compressor operating temperature "$T_{com}$" and the electrolyser operating temperature "$T_E$" are assumed to be the same because the gas being compressed is coming directly from the electrolyser. The parameters "$P_E$" and "$P_{ta}$" are the operating pressure of the electrolyser and pressure of the hydrogen storage tank, which are pressures at the compressor inlet and outlet respectively.

Table 8.7: Parameters for Faraday Efficiency of Electrolyser

| Symbol (Units) | Values | Symbol (Units) | Values |
|---|---|---|---|
| $M_{H2}$ (g/mol) | 2.0159 | $\eta_{DC/AC}$ (%) | 90 |
| $CP_H$ (J/kg.K) | 14304 | $\eta_{com}$ (%)[153] | 70 |
| $T_{com}$ (K) | 306 | r | 1.4 |

### 8.3.7 Hydrogen Storage Tank

For storage of hydrogen in the storage tanks, the model is developed using the ideal gas equation based upon the compressibility factor and is given by Equation (8.22).

$$P_{ta} = \frac{n_{ta} R T_{ta}}{V_{ta}} \times Z_H \qquad (8.22)$$

The pressure in the storage tank is directly proportional to the amount of the gas stored in the tank. The compressibility factor considered for the hydrogen "$Z_H$", is based upon the real gas pressure data at the constant tank volume of 3.34 $m^3$ and at the constant temperature of 33$^oC$ **[154]**. Figure 8.8 shows the

variation of the compressibility factor of hydrogen against the total number of moles of gas in the storage tank. From the curve fitting, the compressibility factor against the number of moles of hydrogen is given by Equation (8.23).

$$Z_H = 3.5012 \times 10^{-11} n_H^{\ 2} + 4.3154 \times 10^{-5} n_H + 1 \qquad (8.23)$$

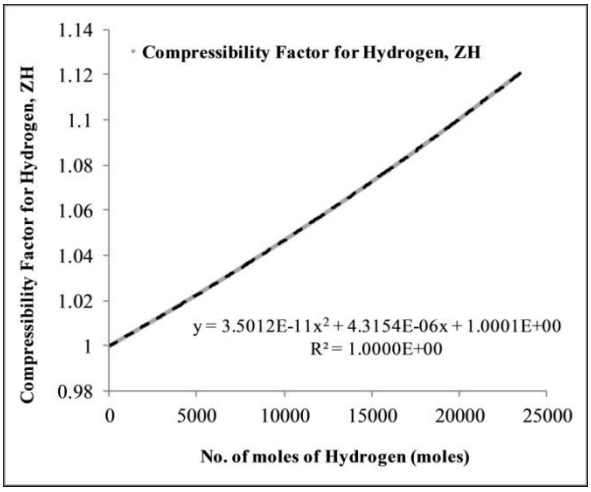


Figure 8.10: Compressibility Factor for Hydrogen Storage

By substituting the hydrogen compressibility factor "$Z_H$" into Equation (8.21), the pressure of hydrogen storage tank against the number of moles of hydrogen is given by Equation (8.24).

$$P_H = 2.666 \times 10^{-8} n_H^{\ 3} + 0.0032872 n_H^{\ 2} + 761.7476 n_H \qquad (8.24)$$

## 8.4 Objective Function and Optimization Criteria

The main objective of the current system optimization is to find out the optimum size and configuration of each of the components of the proposed CPV-Hydrogen system such that there is zero power supply failure time (PSFT) at minimum total cost of the overall system. The Power Supply Failure Time (PSFT) is a time factor in seconds or hours for which the current system configuration is failed to fulfill the total load requirements, including both

system and consumer load. The PSFT factor is calculated during the system simulation by summing up the time during power supply failure. This criteria of zero PSFT factor has been given the first priority in the optimization algorithm and in order to proceed to the second criteria, this criteria has to be completed. The PSFT factor can be calculated using Equation (8.25).

$$PSFT = \sum_{year} t_{PF} = 0 \qquad (8.25)$$

Where $t_{PF}$ is the time, taken in seconds or hours, when the storage is not enough to meet the load requirements.

Furthermore, it is also assumed that at the start of the simulation the storage tanks are already filled with certain amount of the storage mediums. In addition, the system is also assumed to operate in cyclic manner, according to the system performance of the first year. Therefore, after each of the simulation cycle, the state of the storage must be in a certain range of the initial state of storage i.e. before start of the simulation. The second objective function considered for current system optimization is given by Equation (8.26).

$$L1 < ST_{H2(f)} - ST_{H2(i)} < L2 \qquad (8.26)$$

During the simulation, only the state of the hydrogen tank is verified as the state of storage tanks of the other storage mediums is linked with the hydrogen storage tank. Based upon the second optimization criteria given by Equation (8.26), the difference between the state of storage tanks before and after the simulation cycle must be within certain limit range. This criteria must be

fulfilled for cyclic operation of the system, to ensure that the storage is enough for next year operation. The parameters L1 and L2 represents the upper and lower limit of the storage difference and $ST_{H2(f)}$ and $ST_{O2(i)}$ represents the state of the storage of hydrogen tanks before and after the simulation cycle respectively. Therefore, for the current CPV-Hydrogen system optimization, the values of the L1 and L2 parameters are taken as -10 and 35 respectively. The lower limit of -10 is selected to be minimum because it is expected for the state of storage tanks to restore to their initial state. This limit is necessary as in the multi-objective optimization, it is difficult to restore to exactly the same value. However, for upper limit a higher value of 35 is selected with the intention to have extra storage in order to uncertain weather changes that may occur in the coming years of system performance as the storage of 30-35 kg is enough to handle 10-12 days of cloudy weather, which can be seen in the results section.

The third and the most important optimization criteria is related to the economic analysis of proposed CPV-Hydrogen system, in terms of the minimum overall cost of the system. Equation (8.27) gives the overall system cost function considering the investment cost, yearly operation and maintenance cost and replacement cost if any. For the overall system cost, the lifetime period of the whole CPV-Hydrogen system is taken as 20 years, which is mostly taken for lifetime of most of the PV systems design **[25]**. So the cost of the individual components with their operational and maintenance (O&M) cost and replacement cost with replacement period, are given in Table 8.8 **[155-157]**.

$$C_{AT} = C_{CPV} + C_{EL} + C_{FC} + C_{STH2} + C_{STO2} + C_{com} \quad (8.27)$$

$$C_{CPV} = (NP_{CPV} \times N_{CM} \times P_{MJC,\max}) \times [CC_{CPV} + (OMC_{CPV} \times CRF)] \quad (8.28)$$

$$C_{EL} = (N_{EC} \times P_{EL,\max}) \times [CC_{EL} + (RC_{EL} \times SPPW) + (OMC_{EL} \times CRF)] \quad (8.29)$$

$$C_{FC} = (N_{FC} \times P_{FC,\max}) \times [CC_{FC} + (RC_{FC} \times SPPW) + (OMC_{FC} \times CRF)] \quad (8.30)$$

$$C_{STH2} = STM_{H2} \times [CC_{STH2} + (OMC_{STH2} \times CRF)] \quad (8.31)$$

$$C_{STO2} = STM_{O2} \times [CC_{STO2} + (OMC_{STO2} \times CRF)] \quad (8.32)$$

$$C_{com} = P_{com} \times [CC_{com} + (OMC_{com} \times CRF)] \quad (8.33)$$

Table 8.8: Cost Parameters for Individual Components of CPV-Hydrogen System

| Component | CC | OMC | RC | Replacement Period |
|---|---|---|---|---|
| Concentrated Photovoltaic (CPV) | 2.62 \$/$W_P$ | 2.125% of CC | N.A. | N.A. |
| Electrolyser | 3.774 \$/W | 2% of CC | 0.777 \$/W | 10 years[158] |
| Fuel Cell | 2.997 \$/W | 2% of CC | 0.888 \$/W | 10 years[159] |
| Hydrogen Storage | 666 \$/kg | 2% of CC | N.A. | N.A. |
| Oxygen Storage | 44.4 \$/kg | 2% of CC | N.A. | N.A. |
| Hydrogen Compressor | 3000 \$/kW | 20% of CC | N.A. | N.A. |

Equations (8.34) and (8.35) give the capital recovery factor (CRF) and the single payment present worth (SPPW) factor used for calculation of yearly O&M cost and one time replacement cost. For economic analysis, the interest rate is taken as 6% **[160]**.

$$CRF = \left[ \frac{i \times (1+i)^{w}}{(1+i)^{w} - 1} \right] \qquad (8.34)$$

$$SPPW = \frac{1}{(1+i)^{y}} \qquad (8.35)$$

It should be noted that the cost for the water storage is not considered in the overall cost function of the system due to negligible effect as compared to the other parameters cost. Moreover, the cost related to the two axis solar tracker and voltage converters i.e. DC/DC and DC/AC is assumed to be included in the cost of their respective individual components.

## 8.5 Optimization Method and the Implementation of micro Genetic Algorithm

The multi-objective optimization requires some searching algorithm to find the optimal solution of the given problem. For that purpose, it is necessary to select a reliable optimization algorithm which is simple to implement and takes less computational power and time. There are many algorithms developed in the literature with the performance comparison, regarding the multi-objective optimization. The genetic algorithm (GA) is proved to be the simple but reliable optimization algorithm, which can even effectively handle non-linear and mixed integer problems of complex engineering systems. The GA methodology is based upon the concept of nature evolution **[161,162]**. However, there are many other optimization algorithms developed which are claimed to be as effective as GA, like particle swarm optimization (PSO) technique which is appearing to be the competitor of GA by offering the same optimal solution. Currently, there is no benchmark regarding the performance

comparison and limitations of the PSO against the GA as the searching criteria for both of the algorithms is different **[163,164]**. There are some of the studies claiming to find as efficient solution from PSO as GA but with faster convergence towards the optimal solution **[165,166]**. On the other hand, a lot of studies show that the better performance of the PSO is only under certain conditions and for certain kind of problems **[167-169]**. It is also studied that actually PSO takes overall more time than the GA for the total number of generations, due to time of the particle communication after each generation **[170]**. Some studies also showed clearly the better performance of GA over PSO **[171]**. Therefore, the GA is proved to be the most reliable optimization technique implemented in various case studies. However, this simple and conventional GA requires more convergence time and the computational power than the modified GA versions like micro-GA and NSGA-II **[172]**. The micro-GA works on the same methodology as of the simple GA, but with relatively very small population size **[173-175]**. While the NSGA-II also follows the same methodology of GA but with difference selection criteria for the individuals **[176,177]** and with relatively large population size than the micro-GA **[178]**. Both micro-GA and NSGA-II are popular for the multi-objective optimization problems **[179]** but in many case, the micro-GA has shown the better performance than NSGA-II **[178]** especially in terms of the computational time which is 8-12 times faster than the NSGA-II and with better optimal solution and Pareto front **[180]**.

Therefore, after developing the overall performance model of the CPV-Hydrogen system, the optimization model is developed based upon micro Genetic Algorithm (micro-GA) due to its less computational power

requirements and convergence time. The micro-GA optimizes the CPV-Hydrogen system according to the objective function discussed in the previous section and the developed optimization strategy as shown in Figure 8.11. The working of micro-GA algorithm is the same as simple GA but with small population and re-initialization. During the micro-convergence of the micro-population, based upon the fitness value, the most fit or best set of the individuals goes to the next population, while the remaining individuals go through tournament selection, uniform crossover and the mutation. After the micro-convergence, the algorithm and the population is reinitialized with the elitism, by carrying forward the best individual and the rest of the individuals of the population are selected randomly.

The FORTRAN is used to develop the system optimization model and the developed model is based upon two sections. One section is based upon the system optimization model according to the modeling equations of the individual systems discussed in the previous sections and according to the energy management flow chart shown in Figure 8.2. The second section of the developed FORTRAN code is based upon the optimization strategy utilizing micro-GA that optimizes the system in a certain sequence of objective functions. During the simulation, at any stage if any of the objective function does not follow the defined criteria then the simulation loop is terminated and new simulation cycle is started with new micro GA generations and optimization parameters, which helps to reduce the computational time. For current optimization problem in order to obtain high accuracy of the results, the simulation is based upon an interval of one second as the weather data of DNI is available in this interval of one second. However, to reduce the

computational time, the simulation can be based upon the hourly or daily average data for estimation of the system design. For accurate results, the interval of one second or one minute is recommended for simulation and optimization of the system.

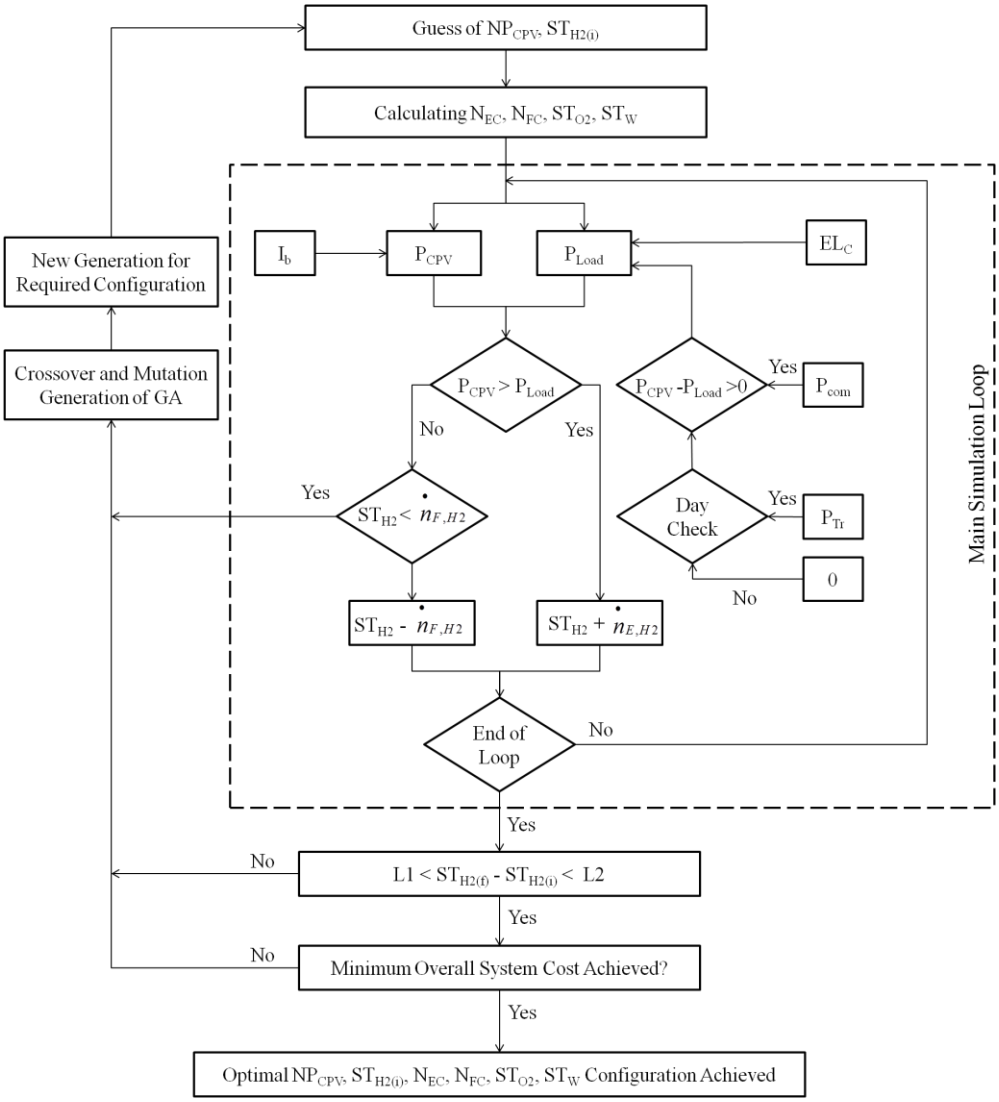


Figure 8.11: Proposed Optimization Strategy for CPV-Hydrogen System for Stand Alone Operation

The main parameters considered to optimize in the current study, are the number of CPV panels "$NP_{CPV}$" and the initial state of the hydrogen storage tank "$ST_{H2(i)}$". The other design parameters, number of the electrolyser cells ($N_{EC}$), number of the fuel cell cells ($N_{FC}$), oxygen initial storage ($ST_{O2}$) and

the water initial storage, are directly or indirectly linked to $NP_{CPV}$ and $ST_{H2(i)}$ as per the developed performance model. The optimization was carried out with maximum 300 generations of micro-GA and with population size of 5. The optimized parameters, optimization results, analysis and the verification are discussed in the next section.

## 8.6 Results and Discussion

Figure 8.12 shows the optimization curves for the overall CPV-Hydrogen system cost, with the PSFT factor curve and the hydrogen storage round difference curve which defines the second objective function of optimization i.e. the difference in the states of the hydrogen storage tanks ($ST_{H2(f)}$ - $ST_{O2(i)}$) before and after the simulation, . It can be seen that the PSFT factor is zero for all the selected optimized configurations and the hydrogen storage round difference curve is also within the required limit of -10 to 35. The limit range for the hydrogen storage round difference is represented by the dotted lines on the graph at -10 and 35 values. In addition, it can be seen that the curve for overall system cost is decreasing in steps according to the change in the optimization parameters and almost after 51-52 generations, it stabilizes at the minimum cost which gives the best optimized configuration of CPV-Hydrogen system. Figure 8.13 shows the breakup for the overall cost of the CPV-Hydrogen system. From the results, it can be seen that the electrolyser and the CPV system are the most expensive components in the CPV-Hydrogen system, responsible for 86% of total system cost. However, electrolyser is the most expensive among all the components, contributing 51% of the overall cost of the system. The main reason for the high cost of the

electrolyser is because of its larger size which is associated with the size of the CPV system. Moreover, due to the involvement of the replacement cost of the electrolyser, its becomes most costly component in the whole system.

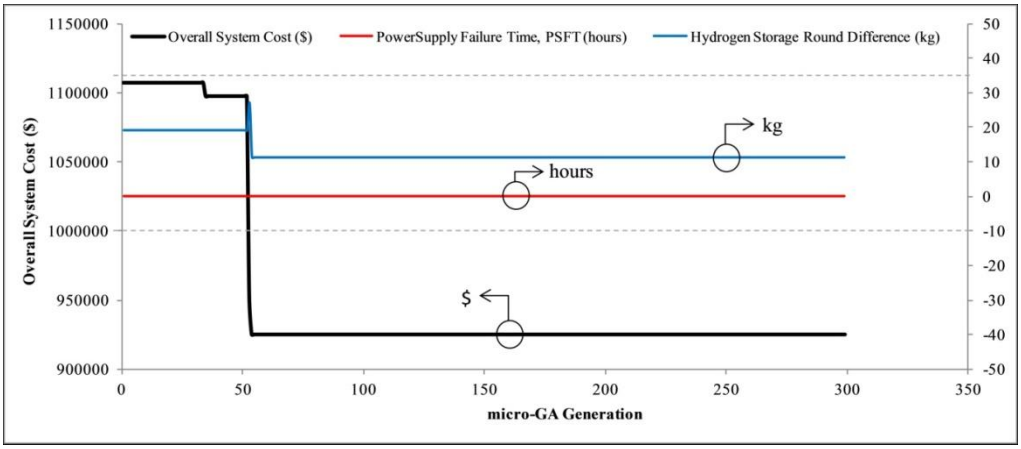


Figure 8.12: Optimization Curve against micro Genetic Algorithm (micro-GA) Generations

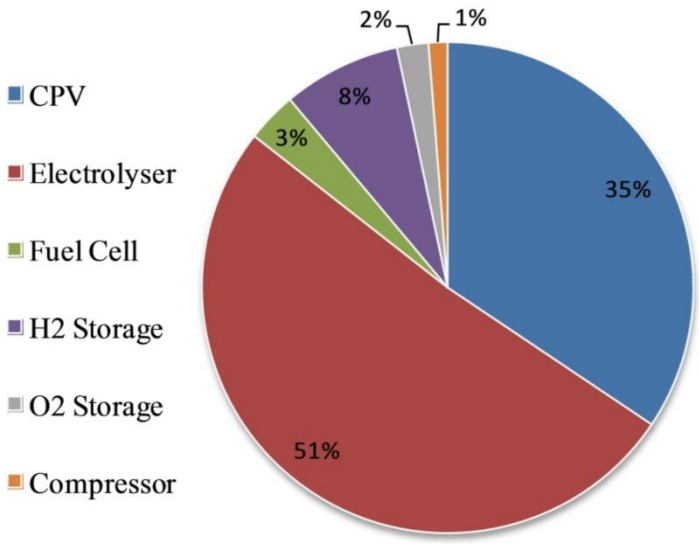


Figure 8.13: Cost Breakup for Optimized CPV-Hydrogen System

As explained before, the system is assumed to have the same yearly cyclic performance during its lifetime, therefore another important parameter of interest is the state of the storage media in the storage tank during 12-months operation from September, 2014 to August 2015. The states of the hydrogen and oxygen storage tanks for the corresponding months, are shown in Figure

8.14. It can be seen that the trend of variation of state of the storage tanks is the same over the whole period of operation as when hydrogen is consumed or produced, at the same time oxygen is also consumed or produced. Moreover, from the state graph it can be seen that at the end of the one year cycle of operation, the state of storage tanks is restored to its initial state i.e. before start of the operation.

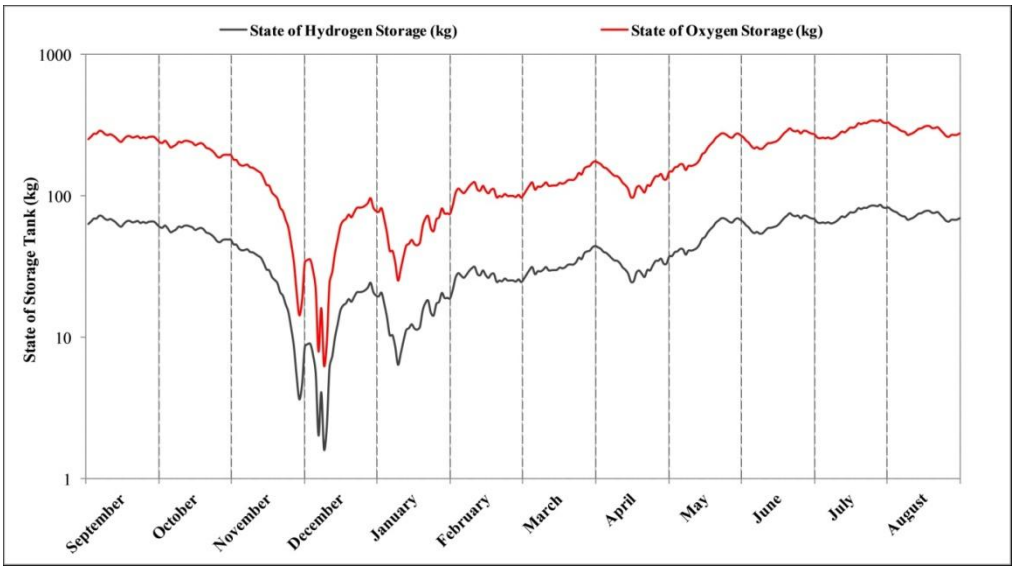


Figure 8.14: The State of Hydrogen and Oxygen Storage Tanks over Period of Operation

During months of November and December, the lowest state of the storage tanks can be seen due to lowest availability of the total DNI. This trend can be verified through Figure 8.15, that shows the percentage share of the load covered through fuel cell operation on the monthly basic, for the diurnal period only and for the full day operation. From the figure, it can also be seen that for the months with low total DNI availability, the total load is almost fully covered by the fuel cell, resulting in the lowering of the states of the hydrogen and oxygen tanks.

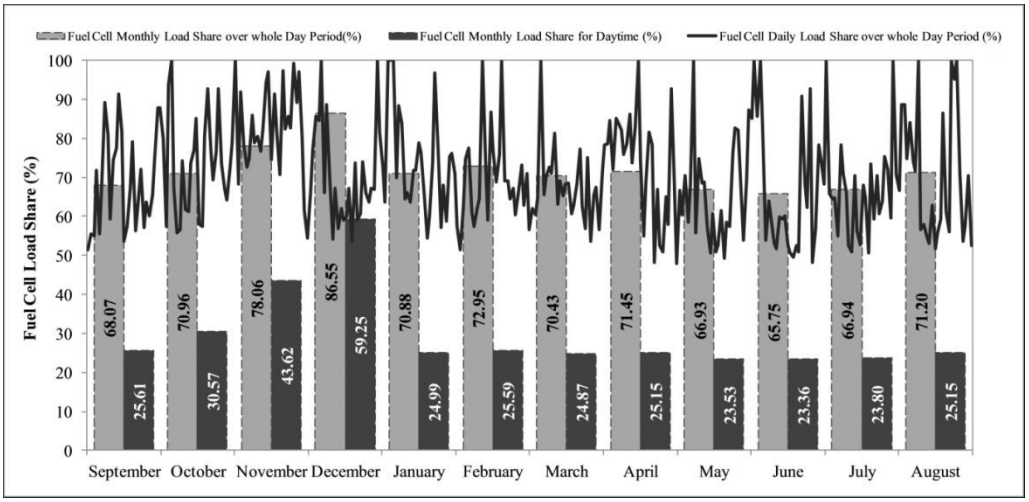


Figure 8.15: Percentage Share of Load Contributed by Fuel Cell on Monthly and Daily Basis

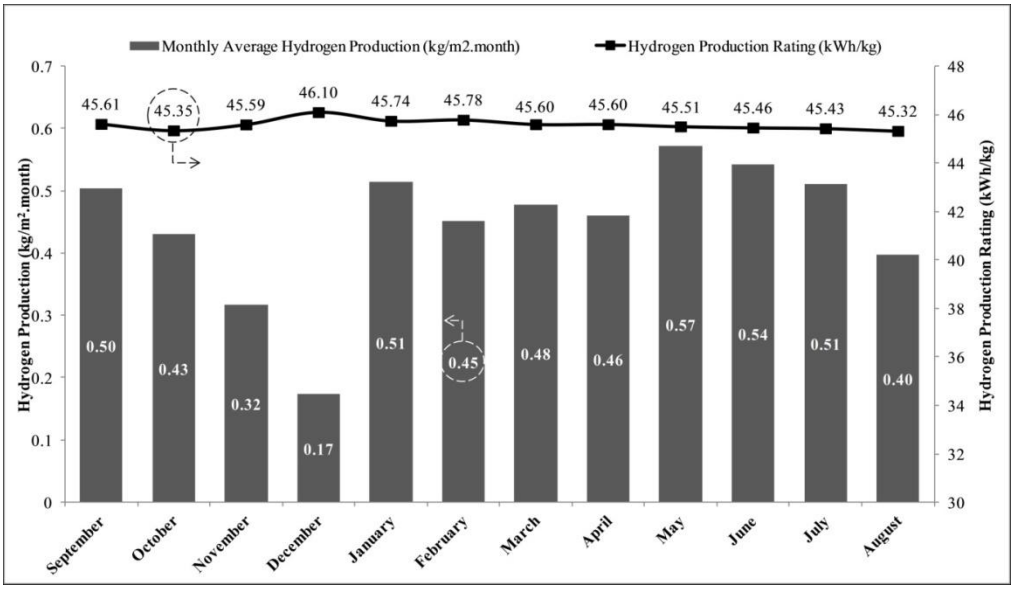


Figure 8.16: Monthly Total Hydrogen Production with Corresponding Production Rating

In order to analyze the performance of the electrolyser operation, total monthly hydrogen production per $m^2$ area of the CPV and the production rating for corresponding months are given in Figure 8.16. it can be seen that the hydrogen production is proportional to the availability of the total DNI for that particular month. Higher the DNI means excess power produced by the CPV system as the total load profile is assumed to be the same for each day. On the other hand, the hydrogen production rating, given in the form of the

kWh of the CPV energy consumed for one kg production of the hydrogen, is almost constant for the whole period of operation except for the month of December, for which the excess power available is far less as compared to the other months.

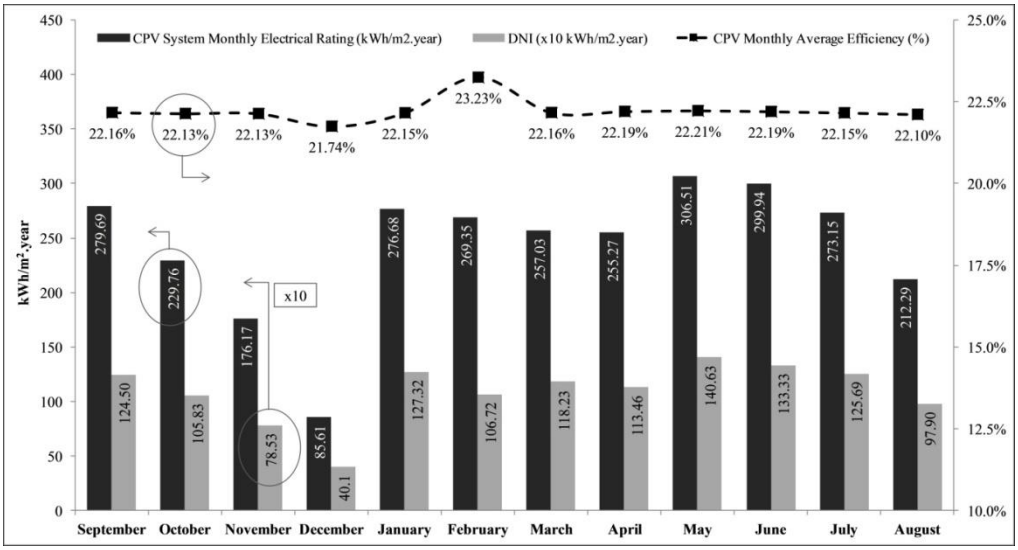


Figure 8.17: Simulated Performance of CPV System in form of Monthly Electrical Rating

The simulated performance of the CPV system in the form of the electrical rating (kWh/$m^2$.year) for different month of operation is also shown in Figure 8.17. The weather used for the current system simulation and optimization is the real weather data collected during the long term performance testing of the CPV system. The simulated electrical rating trend seems to be the same as discussed in the previous chapter of long term performance testing of the CPV system. In order to compare the actual and the simulated monthly electrical rating, both parameters are shown together in Figure 8.18. It can be seen that the simulated electrical rating is almost equal to experimentally measured electrical rating. The slight difference in the simulated and experimental values is due to fluctuations of the power or the measured data, experienced during the experiment. This verifies the proposed CPV model, which can also

be used to estimate the performance of CPV system is any region, according to the meteorological data of that region.

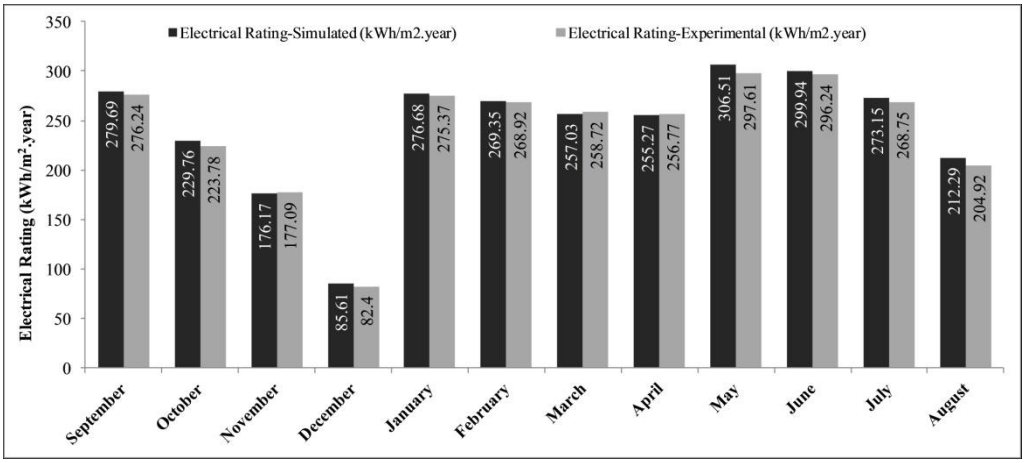


Figure 8.18: Comparison of Simulated and Experimental Electrical Rating

The design summary regarding the optimization of the proposed CPV-Hydrogen system for standalone operation is shown in Table 8.9. The maximum rated power or capacity of each of the component of the proposed CPV-Hydrogen system is given in Table 8.9 as the total number of the CPV panels, CPV rated power, electrolyser rated power, fuel cell rated power and the maximum storage capacity of the hydrogen, oxygen and the water. For the storage of hydrogen, the multiple interconnected storage cylinders are considered with single cylinder capacity of 3.34 $m^3$ and 47 kg or 200 bar. For the storage of oxygen and water, single cylinder storage is assumed at their production pressure. The rated power of the hydrogen compressor is 1.17 kW according to the pressure ratio of 200:7 and considering the maximum flow rate of hydrogen through the compressor, that is equal to the maximum hydrogen production rate of the electrolyser.

The presented design model for the standalone operation of CPV-Hydrogen system is based upon the defined energy management strategy, optimization

criteria and the objective functions. In addition, it should also be noted that the daily electrical load profile is assumed to be constant throughout the period of operation, for current study. However, seasonal electrical load profile can be considered if the changes in the load requirements are significant. Furthermore, the PSFT factor is considered to be zero as one of the optimization criteria. However, if higher value of PSFT is considered, in case of any other power backup source, then the number of the CPV panels and electrolyser size with overall system cost, can be reduced. In addition, the oxygen storage for the current study is considered to be without compression. The main reason for this consideration is that the oxygen can be easily obtained from atmosphere in case of shortage; however, it is not applicable to the hydrogen.

## 8.7 Summary

In this chapter, the energy management and the optimization technique for standalone operation of the CPV-Hydrogen system is proposed, developed and verified. The multi-objective and muti-variable design and techno-economic optimization of the CPV-Hydrogen system is successfully conducted using micro-GA. The performance model of CPV-Hydrogen system is developed by considering the performance model of each of the individual components of the system, which are linked together through the proposed energy management technique. The developed CPV performance mode is based upon the characteristic model of the MJC and by knowing the concentrator area and the optical efficiency of the concentrating assembly, the total power output of the CPV system can be easily calculated according to the total number of the

Table 8.9: Optimization Summary for Proposed CPV-Hydrogen System

| Parameter Description | Units | Value |
|---|---|---|
| CPV System | | |
| No. of CPV Modules | | 782 |
| Rated Power of CPV System | kW | 97.75 |
| Total Energy Delivered by CPV System | MWh | 62.17 |
| Total power consumed for Tracking | MWh | 3.11 |
| Electrolyser | | |
| Electrolyser rated power | kW | 94 |
| No. of electrolyser cells Connected in series | | 70 |
| Total Energy Consumed by Electrolyser | MWh | 35.94 |
| Operating Hours of Electrolyser | Hours | 1888.4 |
| Total Hydrogen Production | kg | 788.78 |
| Total Oxygen Production | kg | 3130.18 |
| Total Water consumption | kg | 3524.48 |
| Fuel Cell | | |
| Fuel Cell rated power | kW | 7.33 |
| No. of cells of Fuel Cell connected in series | | 64 |
| Total Energy Produced by Fuel Cell | MWh | 29.93 |
| Operating Hours of Fuel Cell | Hours | 5733.6 |
| Total Hydrogen Consumption | kg | 777.44 |
| Total Oxygen Consumption | kg | 3085.19 |
| Total Water Production | kg | 3473.83 |
| Energy Storage | | |
| Hydrogen Storage Maximum | kg | 88 |
| Oxygen Storage Maximum | kg | 349 |
| Hydrogen Storage Maximum Pressure | bar | 200 |
| Volume of Single Hydrogen Cylinder | $m^3$ | 3.34 |
| Capacity of Single Hydrogen Cylinder | kg | 47 |
| Oxygen Storage Maximum Pressure | bar | 7 |
| No. of Hydrogen Storage Cylinders | - | 2 |
| Maximum Water Storage Tank | kg | 539 |
| Hydrogen Compressor | | |
| Hydrogen Compressor Rated Power | kW | 1.17 |
| Total Energy Consumed by Hydrogen Compressor | MWh | 2.21 |

MJCs in the system. The alkaline electrolyser model and the PEM fuel cell model are also based upon the single cell characteristics. Their rated power depends upon the maximum excess power available and the maximum load requirements, respectively. For the storage purpose, only hydrogen compression is considered, while oxygen and water are stored at their own production pressure i.e. without any compression. For the overall system optimization, three objective functions are defined; zero PSFT factor, the minimum overall cost of the system and the enough energy storage available at the start and end of the simulation cycle.

Simulation and optimization code is developed in FORTRAN using micro-GA algorithm and the system is optimized according to developed optimization strategy. The parameters considered to be optimized are the number of the CPV panels and the initial storage of hydrogen. The optimized design is verified against all the defined objective functions. Such an approach can be optimally configured in any region or weather condition with high or low solar irradiance. Moreover, the proposed methodology can be integrated with the commercially available tools of renewable energy systems simulation, to enhance their capability to consider CPV for their analysis.

# Chapter 9: Conclusion

In this thesis, a theoretical and experimental study of the concentrated photovoltaic (CPV) system has been extensively conducted for four configurations of CPV, employing a compact yet cost effective system design and with the hydrogen production as energy storage. The major findings of the current work following the order of presentation in the thesis are:

1. The developed, compact hybrid tracking system incorporated with low cost tracking sensor and controls providing the sophisticated an accurate solar tacking methodology at a fraction of the cost of commercially available solar trackers. The wireless controlled architecture of the tracker design enables field communication from a master CPV to the arrays of slave-CPV units that can be located on rooftop of buildings.
2. The ray tracing simulation and field experimentation show that the single stage concentrator, namely the Fresnel lens based system, provides suitable CPV design with minimum sensitivity of tracking error, and when hybridized with glass homogeniser, it shows overall highest long term rating or efficiency.
3. In addition, the novel multi-leg homogeniser concentrator requires less number of concentrators needed for same capacity of the CPV system and as a result, the overall cost of the CPV system and the assembly efforts will reduce.
4. The study demonstrated that long-term electrical rating methodology gives the reliable performance data because it captures the efficiencies of concentrator, MJC cell, the tracking algorithm as well as the

meteorological irradiance input and the maintenance level. It provides the real production output of a photovoltaic system for designers and consumers for actual sizing of the photovoltaic plants. Of all the CPV systems tested, the Fresnel CPV system has a LTER of 240.21 kWh/$m^2$.year at 22.0% overall efficiency, which is 2 to 3 folds higher than the conventional silicon based PV systems in the same period of measurement.

5. In the hybrid CPV-Hydrogen system, the long term rating yields an efficiency of 15% with a specific hydrogen production of 215-220 kWh/kg which is of interest for designers of hydrogen plant. However, for steady power production and standalone but cost effective operation of the CPV system, the performance model with optimization strategy and energy management technique have been developed, considering hydrogen as energy storage. The proposed model can be used by the designers to simulate and analyze the long term performance of CPV or CPV-Hydrogen system. In addition, the performance model can be easily integrated with the commercial optimization and simulation tools to enhance their capability to consider CPV for system analysis.
6. Such a compact CPV system has been proven to be suitable at the rooftop of one or more residential or commercial buildings, for reliable long-term operation of CPV system. By adopting the concept of mini-CPVs, the lower cost fabrication techniques can be exploited for mass production of key components of CPV such as small concentrators, homogenisers and the tracker gearbox and motors.

For future work, the LTER of the CPV system should be recorded for desert regions in order to develop a CPV performance database for different climate conditions. A cost-effective system for dust control has to be developed cost effectively for the mini-CPVs. A prototype of multi-leg homogeniser CPV system with high concentration ratio, is also recommended to be fabricated and tested. In addition, the standalone operation of CPV-Hydrogen system can be verified experimentally using proposed methodology and this methodology or performance model can also be integrated into commercial software like TRNSYS etc.

# References

**[1]** BP Energy Outlook 2035, January 2014.

**[2]** International Energy Agency, World Energy Outlook 2013.

**[3]** U.S. Energy Information Administration / Annual Energy Review 2011. Energy Consumption by Sector.

**[4]** International Energy Agency, Redrawing the Energy-Climate Map, World Energy Outlook Special Report, 10 June 2013.

**[5]** IPCC, Renewable Energy Sources and Climate Change Mitigation. Special Report of the Intergovernmental Panel on Climate Change. 2012.

**[6]** Dincer I, Joshi AS. Solar Based Hydrogen Production Systems, Springer, 2013.

**[7]** Sun Y, Wang Y, Zhu L, Yin B, Xiang H, Huang Q. Direct liquid-immersion cooling of concentrator silicon solar cells in a linear concentrating photovoltaic receiver. *Energy* 2014, **65**, 264-271.

**[8]** Chantana J, Ueno S, Ota Y, Nishioka K, Minemoto T. Uniqueness verification of direct solar spectral index for estimating outdoor performance of concentrator photovoltaic systems. Renewable Energy 2015, 75, 762-766.

**[9]** García-Domingo B, Piliougine M, Elizondo D, Aguilera J. CPV module electric characterisation by artificial neural networks. Renewable Energy 2015, 78, 173-181.

**[10]** Fraunhofer Institute for Solar Energy Systems, ISE. PHOTOVOLTAIC REPORT. https://www.ise.fraunhofer.de/de/downloads/pdf-files/aktuelles/photovoltaics-report-in-englischer-sprache.pdf. 17 November, 2015.

**[11]** Ispy Publishing, PV and Solar Market Intelligence Report, Report - 1, 2013.

**[12]** Schlumberger SBC Energy Institute, http://www.sbc.slb.com/SBCInstitute/Publications/SolarPhotovoltaic.aspx. Date Retrieved: 23-03-2014.

**[13]** Green MA, Emery K, Hishikawa Y, Warta W, Dunlop ED. Solar cell efficiency tables (Version 45). *Progress in photovoltaics: research and applications* 2015, **23(1)**, 1-9.

**[14]** Yastrebova NV. High-efficiency multi-junction solar cells: Current status and future potential. Centre for Research in Photonics, University of Ottawa, April 2007.

**[15]** National Renewable Energy Laboratory (NREL). http://www.nrel.gov/ncpv/images/efficiency_chart.jpg. Date retrieved: 17-11-2015.

**[16]** Cherucheril G, March S, Verma A. Multijunction Solar Cells. Department of Electrical Engineering. Iowa State University. 2011.

**[17]** Mathur SS, Negi BS, Kandpal TC. Geometrical designs and performance analysis of a linear Fresnel reflector solar concentrator

with a flat horizontal absorber. *International journal of energy research* 1990, **14(1)**, 107-124.

**[18]** Siaw FL, Chong KK, Wong CW. A comprehensive study of dense-array concentrator photovoltaic system using non-imaging planar concentrator. *Renewable Energy* 2014, **62**, 542-555.

**[19]** International Energy Agency (IEA). Trends 2015 in Photovoltaic Applications, Survey Report of Selected IEA Countries between 1992 and 2014. Report IEA-PVPS T1-27:2015.

**[20]** Cavallo AJ. Energy storage technologies for utility scale intermittent renewable energy systems. *Journal of solar energy engineering* 2001, **123(4)**, 387-389.

**[21]** Cook TR, Dogutan DK, Reece SY, Surendranath Y, Teets TS, Nocera DG. Solar energy supply and storage for the legacy and nonlegacy worlds. *Chemical reviews* 2010, **110(11)**, 6474-6502.

**[22]** Darras C, Sailler S, Thibault C, Muselli M, Poggi P, Hoguet JC, ... Fontès G. Sizing of photovoltaic system coupled with hydrogen/oxygen storage based on the ORIENTE model. *International Journal of Hydrogen Energy* 2010, **35(8)**, 3322-3332.

**[23]** Lund PD. Optimization of stand-alone photovoltaic systems with hydrogen storage for total energy self-sufficiency. *International journal of hydrogen energy* 1991, **16(11)**, 735-740.

**[24]** Zhou K, Ferreira JA, De Haan SWH. Optimal energy management strategy and system sizing method for stand-alone photovoltaic-

hydrogen systems. *International journal of hydrogen energy* 2008, **33(2)**, 477-489.

**[25]** Khan MJ, Iqbal MT. Pre-feasibility study of stand-alone hybrid energy systems for applications in Newfoundland. *Renewable energy* 2005, **30(6)**, 835-854.

**[26]** Agbossou, K., Kolhe, M., Hamelin, J., & Bose, T. K. (2004). Performance of a stand-alone renewable energy system based on energy storage as hydrogen. *Energy Conversion, IEEE Transactions on*, **19(3)**, 633-640.

**[27]** U.S. Census Bureau, Total Midyear Population for the World: 1950-2050, http://www.census.gov/population/international/data/idb/worldpoptotal.php. Date Retrieved: 24-03-2014.

**[28]** Worldometer, http://www.worldometers.info/world-population/. Date Retrieved, 24-03-2014.

**[29]** World Energy Council, World Energy Resources - 2013 Survey, 2013.

**[30]** Masjuki HH, Mahlia TMI, Choudhury IA, Saidur R. Potential CO2 reduction by fuel substitution to generate electricity in Malaysia. *Energy Conversion and Management* 2002, **43**, 763–770.

**[31]** Ong HC, Mahlia TMI, Masjuki HH. A review on energy scenario and sustainable energy in Malaysia. *Renewable and Sustainable Energy Reviews* 2011, **15**, 639–647.

**[32]** Carbon Dioxide Information Analysis Center, CDIAC. http://cdiac.ornl.gov/trends/emis/glo_2010.html. Date retrieved: 14-11-2015.

**[33]** NASA, Global Climate Change. http://climate.nasa.gov/400ppmquotes/. Date retrieved: 14-11-2015.

**[34]** International Energy Agency, Solar Energy Perspectives, Renewable Energy Technologies, 2011.

**[35]** Myers DR. The Solar Resource. Solar Hydrogen Generation - Towards a Renewable Energy Future. Springer. 2008.

**[36]** NREL. http://rredc.nrel.gov/solar/spectra/am1.5/. Date Retrieved: 14-11-2015.

**[37]** Duffie JA, Beckman WA. Solar Engineering of Thermal Process, 3rd ed. John Wiley & Sons, Inc. Hoboken, New Jersey. 2005.

**[38]** Thekaekara MP. Solar irradiance: total and spectral and its possible variation. Applied Optics, Vol. 15, No. 4, April 1976.

**[39]** Lewis NS. Toward cost-effective solar energy use. *Science* 2007, **315(5813)**, 798-801.

**[40]** Shockley W, Queisser HJ. Detailed balance limit of efficiency of p–n junction solar cells. *Journal of Applied Physics* 1961, **32(3)**, 510–519.

**[41]** Razykov TM, Ferekides CS, Morel D, Stefanakos E, Ullal HS, Upadhyaya HM. Solar photovoltaic electricity: Current status and future prospects. *Solar Energy* 2011, **85**, 1580–1608.

**[42]** NREL, National Center for Photovoltaic. Research Cell Efficiency Records. http://www.nrel.gov/ncpv/. Date Retrieved: 25-11-2015.

**[43]** Mendelsohn M, Lowder T, Canavan B. Utility-Scale Concentrating Solar Power and Photovoltaics Projects: A Technology and Market Overview. NREL/TP-6A20-51137. April 2012.

**[44]** Garboushian V, Roubideaux D, Yoon S. Integrated high-concentration PV Near-term alternative for low-cost large-scale solar electric power. *Solar Energy Materials and Solar Cells* 1997, **47**, 315 323.

**[45]** Moana L. CPV systems – solar, not cost per view. http://lamoana.hubpages.com/hub/CPV-systems-solar-not-cost-per-view#. Date Retrieved: 30-04-2014.

**[46]** Photovoltaic Efficiency: Concentrated Solar Power. http://www.teachengineering.org/collection/cub_/lessons/cub_pveff/Attachments/cub_pveff_lesson04_fundamentalsarticle_v2_dwc.pdf. Date Retrieved: 27-04-2014.

**[47]** Chroma Energy Pvt. Ltd. http://www.chromaenergy.in/enr/index.php?option=com_content&view=article&id=80&Itemid=101. Date Retrieved: 30-04-2014.

**[48]** InterPV. http://www.interpv.net/tech/tech_view.asp?idx=109&part_code=010030012. Date Retrieved: 22-05-2014.

**[49]** GPIII Solar. http://www.gpiiisolar.com/gps600. Date Retrieved: 30-04-2014.

**[50]** Burgess EL, Pritchard DA. *Proc 13th Photovoltaic Specialists Conference (IEEE New York)* 1978, 1121.

**[51]** Sala G, Araújo GL, Luque A, Ruiz J, Coello MA, Lorenzo E, Chenlo F, Sanz J, Alonso A. *Proc ISES International Solar Energy Society Silver Jubilee Congress (Pergamon, New York)* 1979, 1737.

**[52]** Claverie M, Dupas A, Esteve A. (CNRS, France). *Proc 3rd E.C. Photovoltaic Solar Energy Conference (Reidel, Dordrecht)* 1980, 381.

**[53]** Giuffrida M, Tornielli GP, Pidatella S, Repetto A, Bellafronte E, Zani PE. *Proc. 3rd E.C. Photovoltaic Solar Energy Conference (Reidel, Dordrecht)* 1980, 391.

**[54]** Salim A, Eugenio N. *Solar Cells* 1990, **29**,1.

**[55]** Luque A, Miñano JC, Davies PA, Terrón MJ, Tobías I, Sala G, Alonso J. *Proc IEEE PV Specialists Conference (IEEE New York)* 1991, 99.

**[56]** O'Neil Ml, McDanal A, Walters R, J. Perry. *Proc 22nd Photovoltaic Specialists Conference (IEEE, New York)* 1991, 523.

**[57]** Garboushian V, Roubideaux D, Yoon S. *Proc 25th Photovoltaic Specialists Conference (IEEE, New York) 1996*, 1373

**[58]** Bett AW, Burger B, Dimroth F, Siefer G, Lerchenmüller H. High concentration PV using III-V solar cells. *Proc 2006 IEEE 4th World Conference Photovoltaic Energy Conversion.*

**[59]** Tsadka S, Segev R, Migalovich P, Levin O, Tarazi E, Whelan R. Solar electricity generation system. US Patent application publication; 2009. p. US2009/0065045.

**[60]** Singh P, Liburdy JA. A solar concentrator design for uniform flux on a flat receiver. Energy Conversion and Management 1993, **34**, 533‑543.

**[61]** Clemens DD. Photovoltaic concentrator system. US Patent 5,660,644, 1997.

**[62]** Walter L, John L. Multiple reflector concentrator solar electric power system. US Patent 5,374,317, 1994.

**[63]** Chong KK, Siaw FL, Wong CW, Wong GS. Design and construction of nonimaging planar concentrator for concentrator photovoltaic system. Renewable Energy 2009, **34**, 1364‑1370.

**[64]** Chong KK, Wong CW, Siaw FL, Yew TK. Optical characterization of nonimaging planar concentrator for the application in concentrator photovoltaic system. Journal of Solar Energy Engineering 2010, **132(1)**, 011011.

**[65]** Ittner III WB. An array of directable mirrors as a photovoltaic solar concentrator. Solar Energy 1980, **24**, 221‑234.

**[66]** Akiba S, Michael E, Amnon Y. Hybrid concentrated photovoltaic and thermal power conversion at different spectral bands. Solar Energy 2004, **76**, 591‑601.

**[67]** Diaz V, Alvarez LL, Alonso J, Luque A, Mateos C. *Proc European PV Solar Conference (WIP, Munich)* 2004, 2086.

**[68]** Bett AW, Dimroth F, Gluntz SW et al. *Proc 19th European PV Solar Conference (WIP, Munich)* 2004, 2488.

**[69]** Roland W, Alexander R. Concentrating photovoltaic system using a Fresnel lens and non-imaging secondary optics. US Patent application publication, 2008, p.US2008/0245401.

**[70]** Chen Leon LC. Stationary photovoltaic array module design for solar electric power generation systems. US Patent 6,653,551, 2003.

**[71]** Chen Leon LC. Photovoltaic array module design for solar electric power generator systems. US Patent 6,717,045, 2004.

**[72]** Andreev VM, Grilikhes VA, Khvostikov VP, Khvostikova OA, Rumyantsev VD, Sadchikov NA, Shvarts MZ. Concentrator PV modules and solar cells for TPV systems. *Solar energy materials and solar cells* 2004, **84(1)**, 3-17.

**[73]** David FK, Patrick MY. Concentrating solar collector with solid optical element. US Patent application publication, 2006, p. US2006/0231133.

**[74]** Horne S, Conley G, Gordon J, Fork D, Meada P, Schrader E, Zimmermann T. A solid 500 sun compound concentrator PV design. *In Photovoltaic Energy Conversion, Conference Record of the 2006 IEEE 4th World Conference on* 2006, **1**, 694-697.

**[75]** Garboushian V, Stone KW, Slade A. The Amonix High-Concentration Photovoltaic System. *Concentrator Photovoltaics* 2007, **130**, 253.

**[76]** David FK, Stephen HJ. Laminated solar concentrating photovoltaic device. US Patent application publication, 2007, p. US2007/0256726.

**[77]** McConnell R. A Solar Concentrator Pathway to Low-Cost Electrolytic Hydrogen. In *Solar Hydrogen Generation*. Springer New York. 2008, (pp. 65-86).

**[78]** Luque-Heredia I, Moreno JM, Magalhaes PH, Cervantes R, Quemere G, Laurent O. 11 Inspira's CPV Sun Tracking. *Concentrator Photovoltaics* 2007, **130**, 232-251.

**[79]** Luque-Heredia I, Cervantes R, Quemere G. A sun tracking error monitor for photovoltaic concentrators. *In Photovoltaic Energy Conversion, Conference Record of the 2006 IEEE 4th World Conference on* 2006, **1**, 706-709.

**[80]** Xu G, Zhong Z, Wang B, Guo R, Tian Y. Design of PSD based solar direction sensor. *In Sixth International Symposium on Precision Mechanical Measurements, International Society for Optics and Photonics* 2013, 89162-89162.

**[81]** Vosen SR Keller JO. Hybrid energy storage for stand-alone electric power systems: optimization of system performance and cost through control strategies. *Int. J. Hydrogen Energy* 1999, **24**, 1139–1156.

**[82]** Agbossou K, Chahine R, Hamelin J, Laurencelle F, Anouar A, St-Arnaud JM, Bose TK. Renewable energy system based on hydrogen for remote applications. *J. Power Sources* 2001, **96**, 168–172.

**[83]** Galli S, Stefanoni M, Havre K, Borg P, Brocke W, Mergel J. SAPHYS: a JOULE-II E.C. project for solar hydrogen. *In 11th World Hydrogen Energy Conf., Stuttgart, Germany,* June 1996.

**[84]** Barton JP, Infield DG. Energy storage and its use with intermittent renewable energy. *Energy Conversion, IEEE Transactions on* 2004, **19(2)**, 441-448.

**[85]** Turner JA. Sustainable hydrogen production. *Science* 2004, **305(5686)**, 972-974.

**[86]** J.W. Sheffield and Ç. Sheffield (eds.). *Assessment of Hydrogen Energy for Sustainable Development,* 135–146.

**[87]** Santhanam KSV, Miri MJ, Bailey AV, Takacs GA. *Introduction to hydrogen technology*. John Wiley. 2009.

**[88]** Barbir F. PEM electrolysis for production of hydrogen from renewable energy sources. *Solar energy* 2005, **78(5)**, 661-669.

**[89]** Zoulias E, Varkaraki E, Lymberopoulos N, Christodoulou CN, Karagiorgis GN. A Review on Water Electrolysis. Center for Renewable Energy Sources and Saving.

**[90]** Harrison KW, Remick R, Martin GD. Hydrogen Production: Fundamentals and Case Study Summaries. *18th World Hydrogen Energy Conference. NREL/CP-550-47302,* January 2010.

**[91]** Harrison K, Levene JI. Electrolysis of Water. *Solar Hydrogen Generation - Toward a Renewable Energy Future*. Springer. 2008.

**[92]** Durbin DJ, Malardier-Jugroot C. Review of hydrogen storage techniques for on board vehicle applications. *International Journal of Hydrogen Energy* 2013, **38(34)**, 14595-14617.

**[93]** Jorgensen SW. Hydrogen storage tanks for vehicles: Recent progress and current status. *Current Opinion in Solid State and Materials Science* 2011, **15 (2)**, 39–4.

**[94]** Satyapal S, Petrovic J, Read C, Thomas G, Ordaz G. The U.S. Department of energy's national hydrogen storage project: progress towards meeting hydrogen-powered vehicle requirements. Catalysis Today 2007, **120(3-4)**, 246-256.

**[95]** Hua TQ, Ahluwalia RK, Peng J-K, Kromer M, Lasher S, McKenney K, et al. Technical assessment of compressed hydrogen storage tank systems for automotive applications. *International Journal of Hydrogen Energy* 2011, **36(4)**, 3037-3049.

**[96]** Wolf J. Liquid-hydrogen technology for vehicles. *MRS Bulletin* 2002, 684-687.

**[97]** Weinberger B, Lamari FD. High pressure cryo-storage of hydrogen by adsorption at 77 K and up to 50 MPa. *International Journal of Hydrogen Energy* 2009, **34**, 3058-3064.

**[98]** Mori D, Haraikawa N, Kobayashi N, Kubo H, Toh K, Tsuzuki M, et.al. High-pressure metal hydride tank for fuel cell vehicles. *In MRS Proceedings* 2005, **884**, 6-4).

**[99]** Umegaki T, Yan JM, Zhang XB, Shioyama H, Kuriyama N, Xu Q. Boron- and nitrogen-based chemical hydrogen storage materials. *International Journal of Hydrogen Energy* 2009, **34(5)**, 2303-2311.

**[100]** Sakintuna B, Lamari-Darkrim F, & Hirscher, M. Metal hydride materials for solid hydrogen storage: a review. *International Journal of Hydrogen Energy* 2007, ***32*(9)**, 1121-1140.

**[101]** Darras C, Sailler S, Thibault C, Muselli M, Poggi P, Hoguet JC, ... Fontès G. Sizing of photovoltaic system coupled with hydrogen/oxygen storage based on the ORIENTE model. *International Journal of Hydrogen Energy* 2010, **35(8)**, 3322-3332.

**[102]** Lund PD. Optimization of stand-alone photovoltaic systems with hydrogen storage for total energy self-sufficiency. *International journal of hydrogen energy* 1991, **16(11)**, 735-740.

**[103]** Zhou K, Ferreira JA, De Haan SWH. Optimal energy management strategy and system sizing method for stand-alone photovoltaic-hydrogen systems. *International journal of hydrogen energy* 2008, **33(2)**, 477-489.

**[104]** Dufo-López R, Bernal-Agustín JL, Contreras J. Optimization of control strategies for stand-alone renewable energy systems with hydrogen storage. *Renewable energy* 2007, **32(7)**, 1102-1126.

**[105]** Nelson DB, Nehrir MH, Wang C. Unit sizing and cost analysis of stand-alone hybrid wind/PV/fuel cell power generation systems. *Renewable energy* 2006, **31(10)**, 1641-1656.

**[106]** Kolhe M, Agbossou K, Hamelin J, Bose TK. Analytical model for predicting the performance of photovoltaic array coupled with a wind turbine in a stand-alone renewable energy system based on hydrogen. *Renewable Energy* 2003, **28(5)**, 727-742.

**[107]** Castañeda M, Cano A, Jurado F, Sánchez H, Fernández LM. Sizing optimization, dynamic modeling and energy management strategies of a stand-alone PV/hydrogen/battery-based hybrid system. *International Journal of Hydrogen Energy* 2013, **38(10)**, 3830-3845.

**[108]** Santarelli M, Pellegrino D. Mathematical optimization of a RES-H 2 plant using a black box algorithm. *Renewable Energy* 2005, **30(4)**, 493-510.

**[109]** Shiroudi A, Taklimi SRH, Mousavifar SA, Taghipour P. Stand-alone PV-hydrogen energy system in Taleghan-Iran using HOMER software: optimization and techno-economic analysis. *Environment, development and sustainability* 2013, **15(5)**, 1389-1402.

**[110]** Karakoulidis K, Mavridis K, Bandekas DV, Adoniadis P, Potolias C, Vordos N. Techno-economic analysis of a stand-alone hybrid

photovoltaic-diesel–battery-fuel cell power system. *Renewable Energy* 2011, **36(8)**, 2238-2244.

**[111]** Rehman S, Alam MM, Meyer JP, Al-Hadhrami LM. Feasibility study of a wind–pv–diesel hybrid power system for a village. *Renewable Energy* 2012, **38(1)**, 258-268.

**[112]** Oh SJ, Lee YJ, Chen K, Kim YM, Lim SH, Chun W. Development of an embedded solar tracker for the enhancement of solar energy utilization. *International Journal of Energy Research* 2012, **36(2)**, 249-258.

**[113]** Aviation Formulary V1.44 by ED Willams. http://williams.best.vwh.net/sunrise_sunset_algorithm.htm, Date retrieved:26-11-2015.

**[114]** Farahani S. *ZigBee wireless networks and transceivers*. newnes, 2011.

**[115]** Winston R, Miñano JC, Benitez PG. *Nonimaging optics*. Academic Press. 2005.

**[116]** Malacara-Hernández D, Malacara-Hernández Z. *Handbook of optical design*. CRC Press, 2013.

**[117]** Arndt R, Puto IR. Basic Understanding of IEC Standard Testing for Photovoltaic Panels. TUV SUD America Inc. http://www.tuvamerica.com/services/photovoltaics/articlebasicunderstandingpv.pdf. Date Retrieved: 21-10-2015.

**[118]** Renzi M, Egidi L, Comodi G. Performance analysis of two 3.5 kWp CPV systems under real operating conditions. *Applied Energy* 2015, **160**, 687-696.

**[119]** Pérez-Higueras P, Muñoz E, Almonacid G, Vidal PG. High Concentrator PhotoVoltaics efficiencies: present status and forecast. *Renewable & Sustainable Energy Reviews* 2011, **15**, 1810–18155.

**[120]** Fernández EF, Pérez-Higueras P, Garcia Loureiro AJ, Vidal PG. Outdoor evaluation of concentrator photovoltaic systems modules from different manufacturers: First results and steps. *Progress in Photovoltaics: Research and Applications* 2013, **21**, 693–701.

**[121]** De Soto W, Klein SA, Beckman WA. Improvement and validation of a model for photovoltaic array performance. *Solar energy* 2006, **80(1)**, 78-88.

**[122]** Akinyele DO, Rayudu RK, Nair NKC. Development of photovoltaic power plant for remote residential applications: The socio-technical and economic perspectives. *Applied Energy* 2015, **155**, 131-149.

**[123]** Chin VJ, Salam Z, Ishaque K. Cell modelling and model parameters estimation techniques for photovoltaic simulator application: A review. *Applied Energy* 2015, **154**, 500-519.

**[124]** Caamaño E, Lorenzo E, Zilles R. Quality control of wide collections of PV modules: lessons learned from the IES experience. *Progress in Photovoltaics: Research and Applications* 1999, **7**, 137–149.

**[125]** García-Domingo B, Aguilera J, de la Casa J, Fuentes M. Modelling the influence of atmospheric conditions on the outdoor real performance of a CPV (Concentrated Photovoltaic) module. *Energy* 2014, **70**, 239–50.

**[126]** Talavera DL, Pérez-Higueras P, Ruíz-Arias JA, Fernández EF. Levelised cost of electricity in high concentrated photovoltaic grid connected systems: Spatial analysis of Spain. *Applied Energy* 2015, **151**, 49-59.

**[127]** Eccher M, Salemi A, Turrini S, Brusa RS. Measurements of power transfer efficiency in CPV cell-array models using individual DC–DC converters. *Applied Energy* 2015, **142**, 396-406.

**[128]** Said, S. A. M. (1990). Effects of dust accumulation on performances of thermal and photovoltaic flat-plate collectors. *Applied Energy*, **37(1)**, 73-84.

**[129]** International Energy Agency, $CO_2$ Emissions from Fuel Combustion Highlights, 2013.

**[130]** Yingli Green Energy Holding Co. Ltd., PANDA 60 CELL SERIES 2, www.yinglisolar.com

**[131]** Yingli Green Energy Holding Co. Ltd., YGE 48 Cell 40mm SERIES, www.yinglisolar.com

**[132]** MiaSolé Hi-Tech Corp., FLEX–02N SERIES CIGS MODULE, www. miasole.com

**[133]** Burhan M, Oh SJ, Shahzad MW, Ng KC. Electrical Rating of Concentrated Photovoltaic (CPV) Systems for Long Term Performance. *The 6th International Symposium on Physics of Fluids (ISPF6)* 2015, Xining, China.

**[134]** National Environment Agency (NEA) Singapore, www.nea.gov.sg

**[135]** Shahzad MW, Thu K, Park YC, Chun W, Ng KC. Solar Thermal Rating: A methodology for evaluating the long term performance of renewable energy systems. *International Meeting on Advanced Thermofluids* 2013.

**[136]** HOMER (Hybrid Optimization of Multiple Energy Resources). Available from: http://www.homerenergy.com/software.html

**[137]** iHOGA (Improved Hybrid Optimization by Genetic Algorithms). Available from: http://personal.unizar.es/rdufo/index.php?option=com_content&view=article&id=2&Itemid=104&lang=en

**[138]** Bernal-Agustin JL, Dufo-Lopez R. Simulation and optimization of stand-alone hybrid renewable energy systems. Renewable and Sustainable Energy Reviews 2009, **13**, 2111-2118.

**[139]** Energy Market Authority (EMA) Singapore, http://www.ema.gov.sg

**[140]** Nishioka K, Takamoto T, Agui T, Kaneiwa M, Uraoka Y, Fuyuki T. Annual output extimation of concentrator photovoltaic systems using high-efficiency InGaP/InGaAs/Ge triple-junction solar cells based on

experimental solar cell's characteristics and field-test meteorological data, *Solar Energy Materials & Solar Cells* 2006, **90**, 57-67.

**[141]** Cotal H, Sherif R. Temperature Dependence of the IV Parameters from Triple Junction GaInP/InGaAs/Ge Concentrator Solar Cells, *IEEE 4th World Conference on Photovoltaic Energy Conversion* 2006, **1**, 845-848.

**[142]** Calderón M, Calderón AJ, Ramiro A, González JGI, González, I. Analysis of the performance of the photovoltaic array through the exergy efficiency. *International Conference on Renewable Energy and Power Quality* 2011, 13-15.

**[143]** Horne S, McDonald M, Hartsoch N, Desy K. (2009). Reflective optics CPV panels enabling large scale, reliable generation of solar energy cost competitive with fossil fuels.

**[144]** ArzonSolar. http://www.arzonsolar.com/wp-content/uploads/2015/02/uModule-Datasheet.pdf. Date retrieved: 16-11-2015.

**[145]** 3M, Renewable Energy Division. Factors Influencing the Optical Efficiency of Fresnel Lens Concentrators. http://www.lapptannehill.com/wp-content/uploads/2014/02/3M-Factors.pdf. Date retrieved: 16-11-2015.

**[146]** Pan CT, Juan YL. A novel sensorless MPPT controller for a high-efficiency microscale wind power generation system. *Energy Conversion, IEEE Transactions on* 2010, **25(1)**, 207-216.

**[147]** Chiu HJ, Lin LW. A high-efficiency soft-switched AC/DC converter with current-doubler synchronous rectification. *Industrial Electronics, IEEE Transactions on* 2005, **52(3)**, 709-718.

**[148]** Ki SK, Lu DDC. Implementation of an efficient transformerless single-stage single-switch AC/DC converter. *Industrial Electronics, IEEE Transactions on* 2010, **57(12)**, 4095-4105.

**[149]** Wang K, Lin CY, Zhu L, Qu D, Lee FC, Lai JS. Bi-directional DC to DC converters for fuel cell systems. *In Power Electronics in Transportation* 1998, 47-51.

**[150]** Nymand M, Andersen MA. High-efficiency isolated boost DC–DC converter for high-power low-voltage fuel-cell applications. *Industrial Electronics, IEEE Transactions on* 2010, **57(2)**, 505-514.

**[151]** Helioslite. http://helioslite.com/site/wp-content/uploads/2015/06/H%C3%A9liosLite-datasheet-35m2-2014-12.pdf. Date retrieved: 16-11-2015.

**[152]** Ulleberg Ø. Stand-Alone Power Systems for the Future: Optimal Design, Operation & Control of Solar-Hydrogen Energy Systems. *Ph.D. Thesis, Department of Thermal Energy and Hydropower, Norwegian University of Science and Technology, Trondheim, Norway* 1998.

**[153]** Li CH, Zhu XJ, Cao GY, Sui S, Hu MR. Dynamic modeling and sizing optimization of stand-alone photovoltaic power systems using hybrid energy storage technology. *Renewable Energy* 2009, **34(3)**, 815-826.

**[154]** REFPROP Reference Fluid Thermodynamic and Transport Properties, National Institute of Standards and Technology (NIST) Standard Reference Database 23, Version 8.0, http://www.nist.gov

**[155]** Guinot B, Champel B, Montignac F, Lemaire E, Vannucci D, Sailler S, Bultel Y. Techno-economic study of a PV-hydrogen-battery hybrid system for off-grid power supply: Impact of performances' ageing on optimal system sizing and competitiveness. International Journal of Hydrogen Energy 2015, **40**, 623-632.

**[156]** Simbeck D, Chang E. Hydrogen Supply: Cost Estimate for Hydrogen Pathways - Scoping Analysis. SFA Pacific, Inc. Mountain View, California, 2002 NREL.

**[157]** PV Magazine, Concentrated PV solar set to boom. http://www.pv-magazine.com/news/details/beitrag/concentrated-pv-solar-set-to-boom_100013699/#axzz3j DrxpxEr. Date Retrieved: 19-08-2015.

**[158]** Ghosh PC, Emonts B, Janßen H, Mergel J, Stolten D. Ten years of operational experience with a hydrogen-based renewable energy supply system. *Solar Energy* 2003, **75(6)**, 469-478.

**[159]** Granovskii M, Dincer I, Rosen MA. Economic and environmental comparison of conventional, hybrid, electric and hydrogen fuel cell vehicles. *Journal of Power Sources* 2006, **159(2)**, 1186-1193.

**[160]** Rehman S, Al-Hadhrami LM. Study of a solar PV–diesel–battery hybrid power system for a remotely located population near Rafha, Saudi Arabia. *Energy* 2010, **35(12)**, 4986-4995.

**[161]** Deb K. Genetic algorithm in search and optimization: the technique and applications. In *Proceedings of International Workshop on Soft Computing and Intelligent Systems,(ISI, Calcutta, India)* 1998, 58-87.

**[162]** Konak A, Coit DW, Smith AE. Multi-objective optimization using genetic algorithms: A tutorial. *Reliability Engineering & System Safety* 2006, **91(9)**, 992-1007.

**[163]** Bai Q. Analysis of particle swarm optimization algorithm. *Computer and information science* 2010, **3(1)**, 180.

**[164]** Aote SS, Raghuwanshi MM, Malik LA. Brief Review on Particle Swarm Optimization: Limitations & Future Directions. *International Journal of Computer Science Engineering (IJCSE)* 2013, **2(5)**, 196-200.

**[165]** Shukla M, Dhaliwal BS. Review of Multi-objective Optimization using Genetic Algorithm and Particle Swarm Optimization. *IP Multimedia Communications, A Special Issue from IJCA*. 72-74.

**[166]** Rajendra R, Pratihar DK. Particle Swarm Optimization Algorithm vs. Genetic Algorithm to Solve Multi-Objective Optimization Problem in Gait Planning of Biped Robot. In *Proceedings of the International Conference on Information Systems Design and Intelligent Applications 2012 (INDIA 2012) held in Visakhapatnam, India, January* 2012, 563-570). Springer Berlin Heidelberg.

**[167]** Boeringer DW, Werner DH. Particle swarm optimization versus genetic algorithms for phased array synthesis. *Antennas and Propagation, IEEE Transactions on* 2004, **52(3)**, 771-779.

**[168]** Rajendra R, Pratihar DK. Particle swarm optimization algorithm vs genetic algorithm to develop integrated scheme for obtaining optimal mechanical structure and adaptive controller of a robot. *Intelligent Control and Automation* 2011, **2(04)**, 430.

**[169]** Hassan R, Cohanim B, De Weck O, Venter G. A comparison of particle swarm optimization and the genetic algorithm. In *Proceedings of the 1st AIAA multidisciplinary design optimization specialist conference* 2005, 1-13

**[170]** Panda S, Padhy NP. Comparison of particle swarm optimization and genetic algorithm for FACTS-based controller design. *Applied soft computing* 2008, 8**(4)**, 1418-1427.

**[171]** Jones KO. Comparison of genetic algorithm and particle swarm optimization. In *Proc. Int. Conf. Computer Systems and Technologies*2005. 1-6.

**[172]** Yu X, Gen M. *Introduction to evolutionary algorithms*. Springer Science & Business Media. 2010.

**[173]** Senecal PK. Numerical optimization using the GEN4 micro-genetic algorithm code. *University of Wisconsin-Madison*. 2000.

**[174]** Abu-Lebdeh G, Benekohal RF. Convergence variability and population sizing in micro-genetic algorithms. *Computer-aided civil and infrastructure engineering* 1999, **14(5)**, 321-334.

**[175]** Krishnakumar K. Micro-genetic algorithms for stationary and non-stationary function optimization. In *1989 Advances in Intelligent Robotics Systems Conference, International Society for Optics and Photonics* 1990, 289-296.

**[176]** Srinivas N, Deb K. Muiltiobjective optimization using nondominated sorting in genetic algorithms. *Evolutionary computation* 1994, **2(3)**, 221-248.

**[177]** Deb K, Pratap A, Agarwal S, Meyarivan TAMT. A fast and elitist multiobjective genetic algorithm: NSGA-II. *Evolutionary Computation, IEEE Transactions on* 2002, **6(2)**, 182-197.

**[178]** Choi S. Speedups for Efficient Genetic Algorithms: Design optimization of low-boom supersonic jet using parallel GA and micro-GA with external memory. *Genetic Algorithms and Genetic Programming at Stanford* 2003, 21-30.

**[179]** Coello CC, Lamont GB, Van Veldhuizen DA. *Evolutionary algorithms for solving multi-objective problems*. Springer Science & Business Media. 2007.

**[180]** Coello CC, Pulido GT. Multiobjective structural optimization using a microgenetic algorithm. *Structural and Multidisciplinary Optimization* 2005, **30(5)**, 388-403.

# Appendix A: Parts of Tracker Control Box

## A.1 Atmega2560 Microcontroller Developing Board:

Manufacturer: Newtc Corp.

Website: www.newtc.co.kr

Development Board and Pin Configuration:

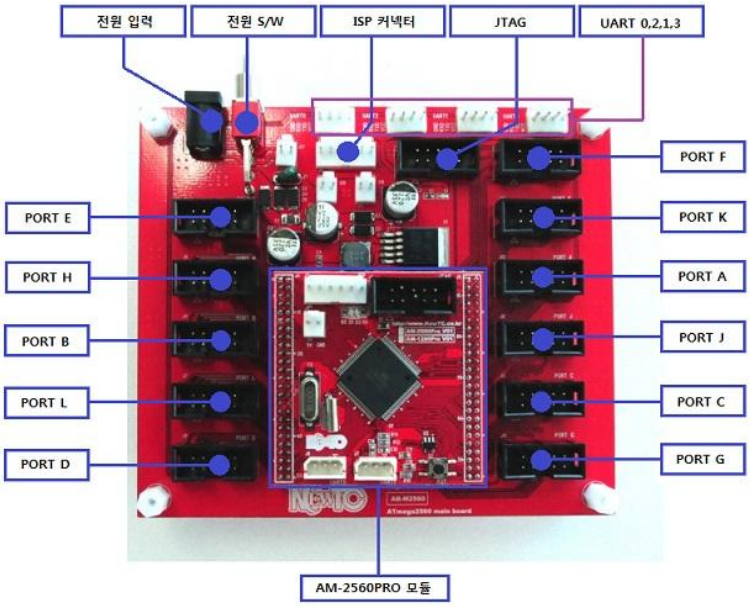


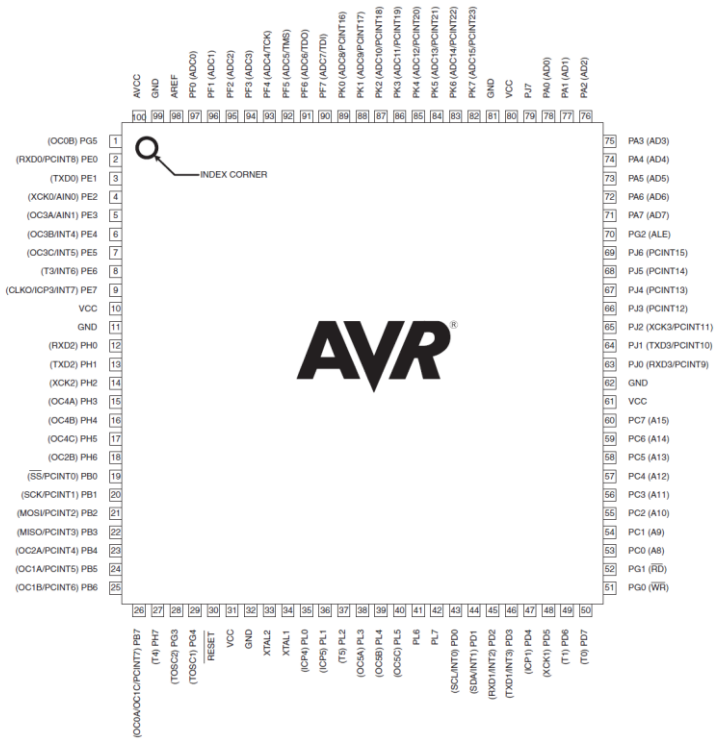

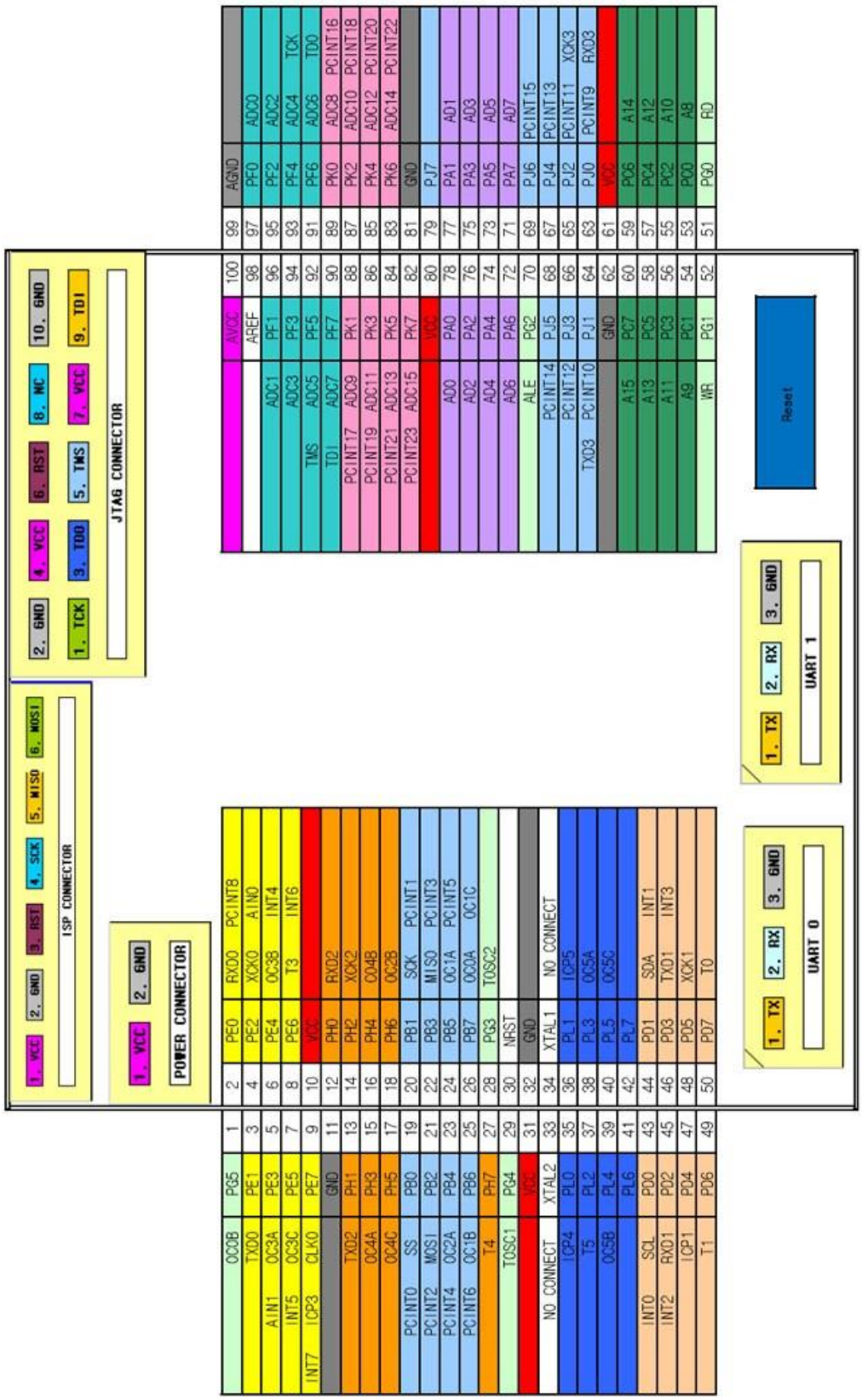
1. VCC
2. GND
3. RST
4. SCK
5. MISO
6. MOSI
ISP CONNECTOR
1. VCC
2. GND
POWER CONNECTOR
2. GND
4. VCC
6. RST
8. NC
10. GND
1. TCK
3. TDO
5. TMS
7. VCC
9. TDI
JTAG CONNECTOR
1. TX
2. RX
3. GND
UART 0
1. TX
2. RX
3. GND
UART 1
Reset

## A.2 ISP-USB Converter:

Manufacturer: Newtc Corp.

Website: www.newtc.co.kr

## A.3 UART-USB Converter:

Manufacturer: Newtc Corp.

Website: www.newtc.co.kr

# A.4 Stepper Motors:

Manufacturer: Newtc Corp.

Website: www.newtc.co.kr

SE-SM9K (9kg.cm Holding Torque):

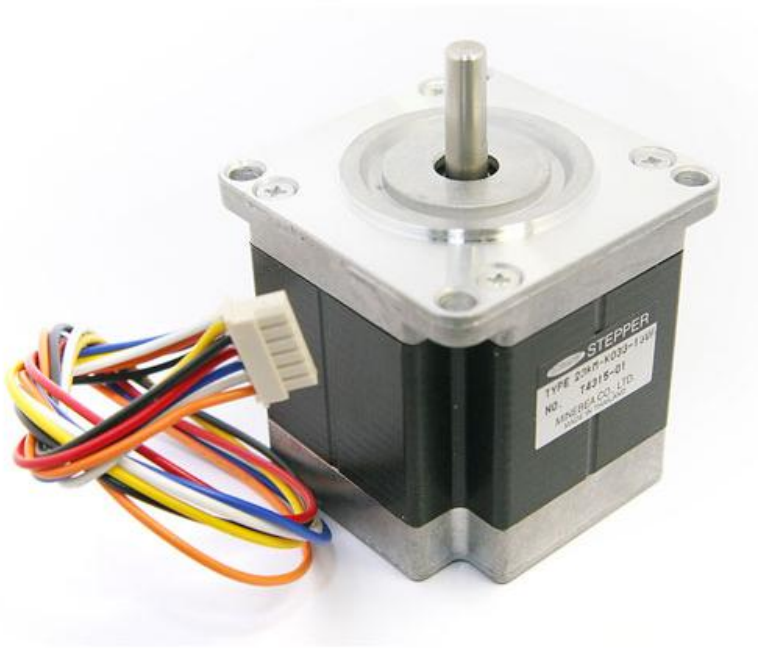


SE-SM243 (1.7kg.cm Holding Torque):

## A.5 Stepper Motor Driver:

Manufacturer: Newtc Corp.

Website: www.newtc.co.kr

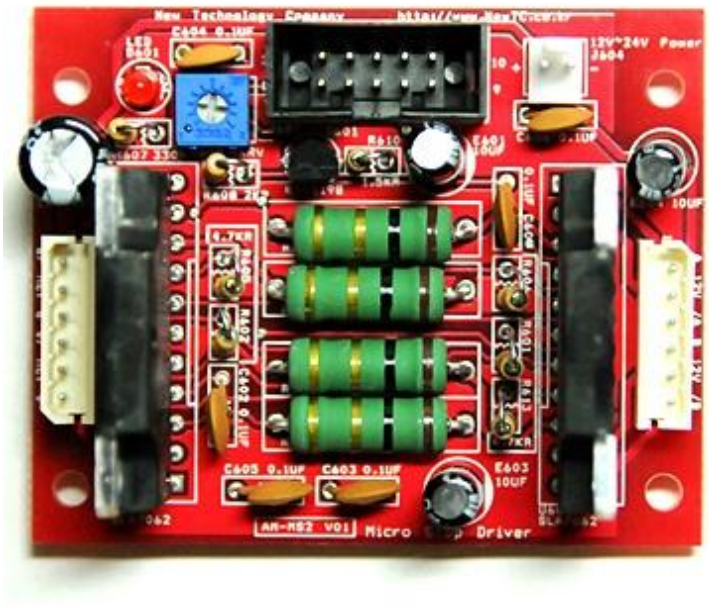

## A.6 Display LCD:

Manufacturer: Newtc Corp.

Website: www.newtc.co.kr

# A.7 Real Time Clock (RTC) Module for DS1307:

Manufacturer: Newtc Corp.

Website: www.newtc.co.kr

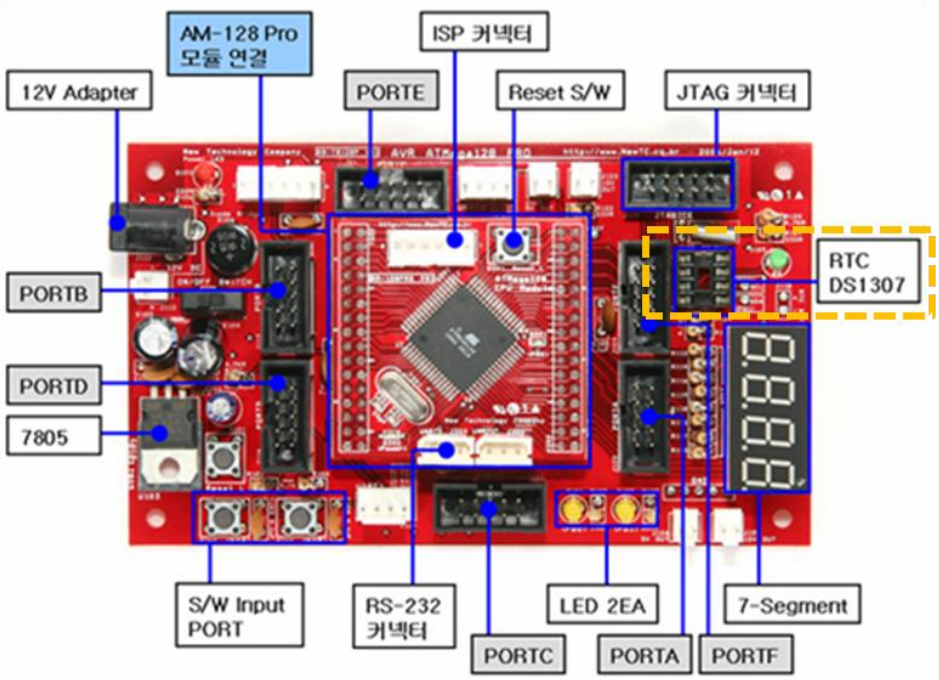


# A.8 GPS Module:

Manufacturer: UI Good Mall.

Website: www.uigoods.com

# A.9 Color Tracking Sensor (CTS) Camera:

Manufacturer: VARRAM SYSTEM

Website: www.varram.com

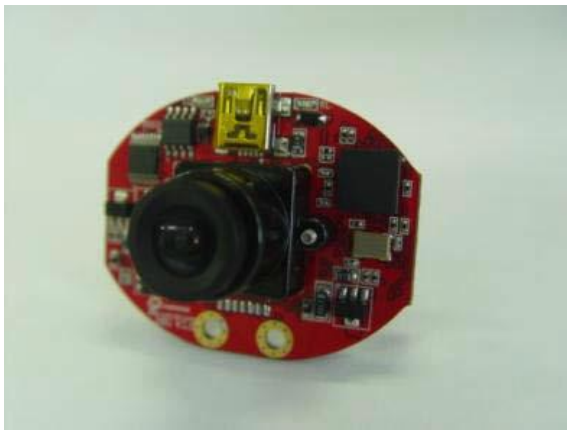

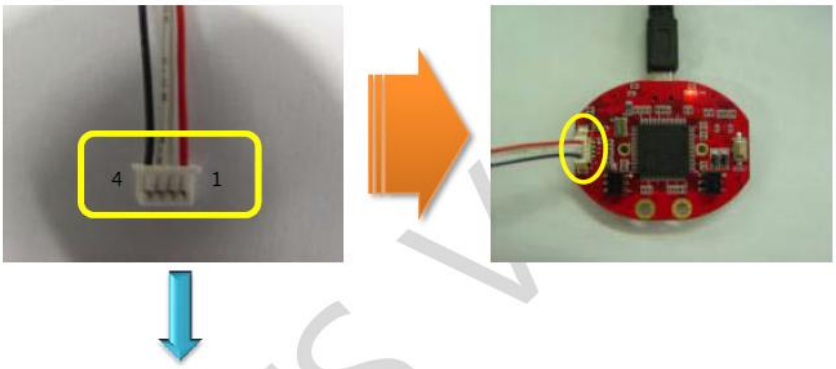


| Pin # | Signal Name | Signal Description |
|---|---|---|
| 1 | VCC | Input Voltage : 5V |
| 2 | 232_TXD | 232 level Transmit Data |
| 3 | 232_RXD | 232 level Receive Data |
| 4 | GND | Voltage Ground |

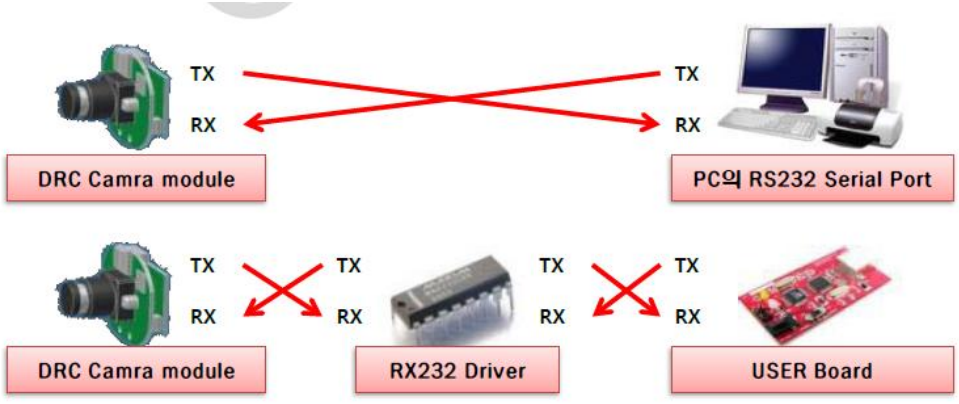

# A.10 Zigbee Module:

Manufacturer: Digi International

Website: www.digi.com

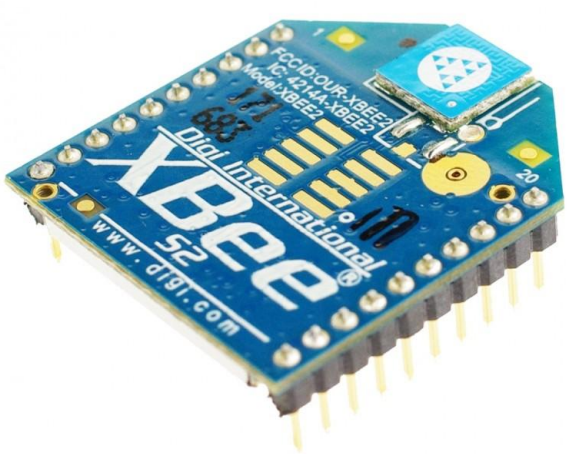

# Appendix B: Hydrogen Compression Unit Layout and Components Description

## B.1 System Layout:

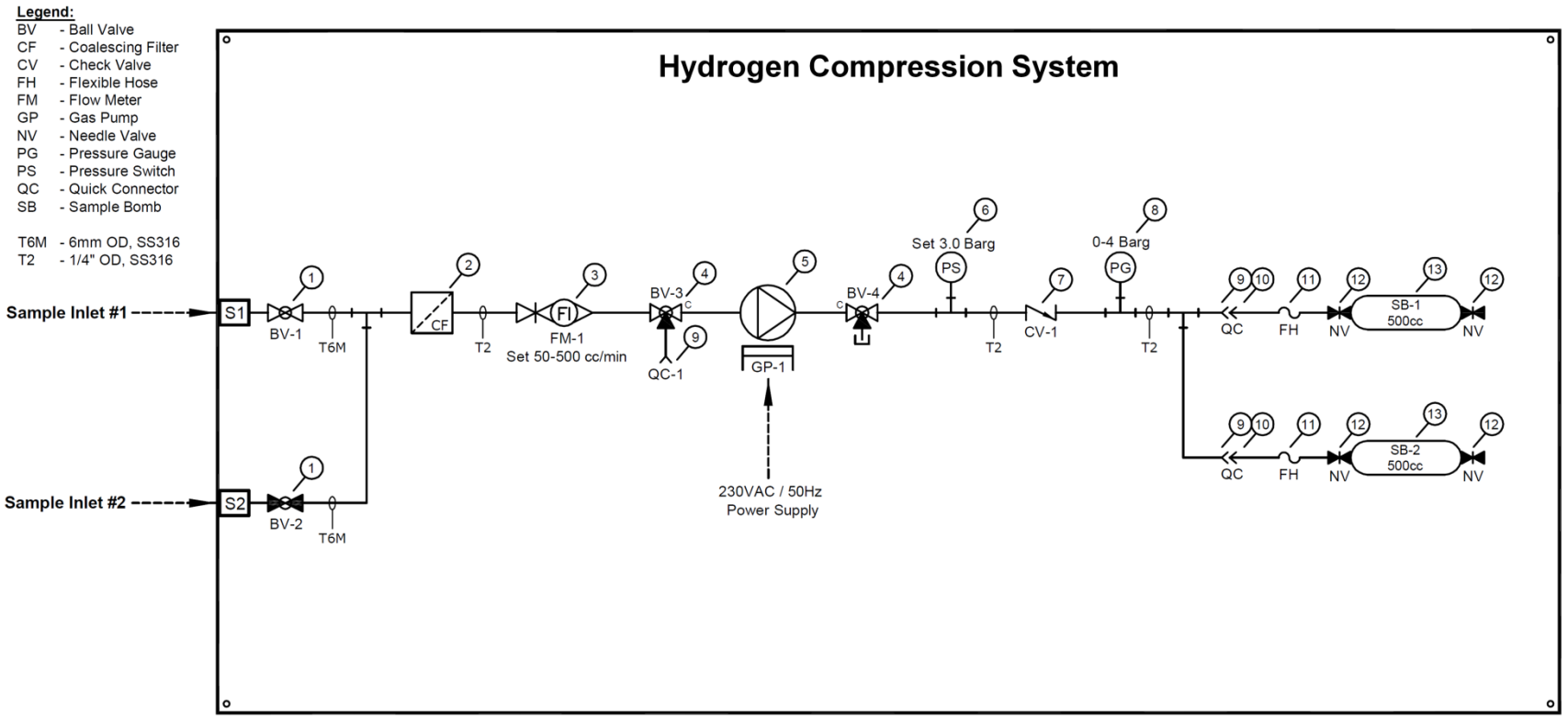

## B.2 Bill of Material:

| Bill of Material | | | | |
|---|---|---|---|---|
| **Item** | **Description** | **Manufacturer** | **Part No.** | **Qty** |
| 1 | 6mm O.D., 2-Way Ball Valve, SS316 | Hamlet | H6800-SSL-6MM-PSS | 2 |
| 2 | 1/4" NPTF Filter with SS316 Housing and Coalescing Filter Element | ASE | 4135999/12-57-50K | 1 |
| 3 | 1/8" NPTF Flowmeter Meter with Valve, Polycarbonate Body, Range: 0.05-0.5 LPM (Air) | KI | MR-3A12-SVVT | 1 |
| 4 | 1/4" O.D., 3-Way Ball Valve, SS316 | Hamlet | H6800-SSL-1/4"-PST | 2 |
| 5 | G1/8" Ex-Proof Gas Diaphragm Pump, 230VAC/50Hz/IP54 | KnF | N87TTE-Ex | 1 |
| 6 | 1/4" NPTF Ex-Proof Pressure Switch, Set Pressure 3.0 BarG | New-Flow | PS2100X-40RA2F1 | 1 |
| 7 | 1/4" O.D. Non-Return Valve, 1/3 PSIG Cracking Pressure, SS316 | Hamlet | H400-SSL-1/4"-1/3 | 1 |
| 8 | 1/4" NPTM Bottom Connection, Pressure Gauge, 63mm Dial Size, Range: 0-4 Barg, SS316 | Baumer | MEX3-D50-B19/0751 | 1 |
| 9 | 1/4" O.D. Quick Connect Coupling Body, SS316 | Swagelok | QC4-B-400 | 3 |
| 10 | 1/4" O.D. Quick Connect Coupling Stem, Double Shut-Off, SS316 | Swagelok | QC4-D-400 | 2 |
| 11 | 1/4" O.D., PTFE Lined SS Braided Flexible Hose, Length 24" | Swagelok | SS-4BHT-24 | 2 |
| 12 | 1/4" O.D., Needle Valve, SS316 | Hamlet | H300-SSL-R-1/4" | 4 |
| 13 | 1/4" NPTF Double Ended Cylinder, 500cc Capacity, SS304 | Swagelok | 304L-HDF4-500 | 2 |

## B.3 Hydrogen Compressor:

Mini-Diaphragm pump N 87 TTE Ex - for use in potentially explosive atmospheres

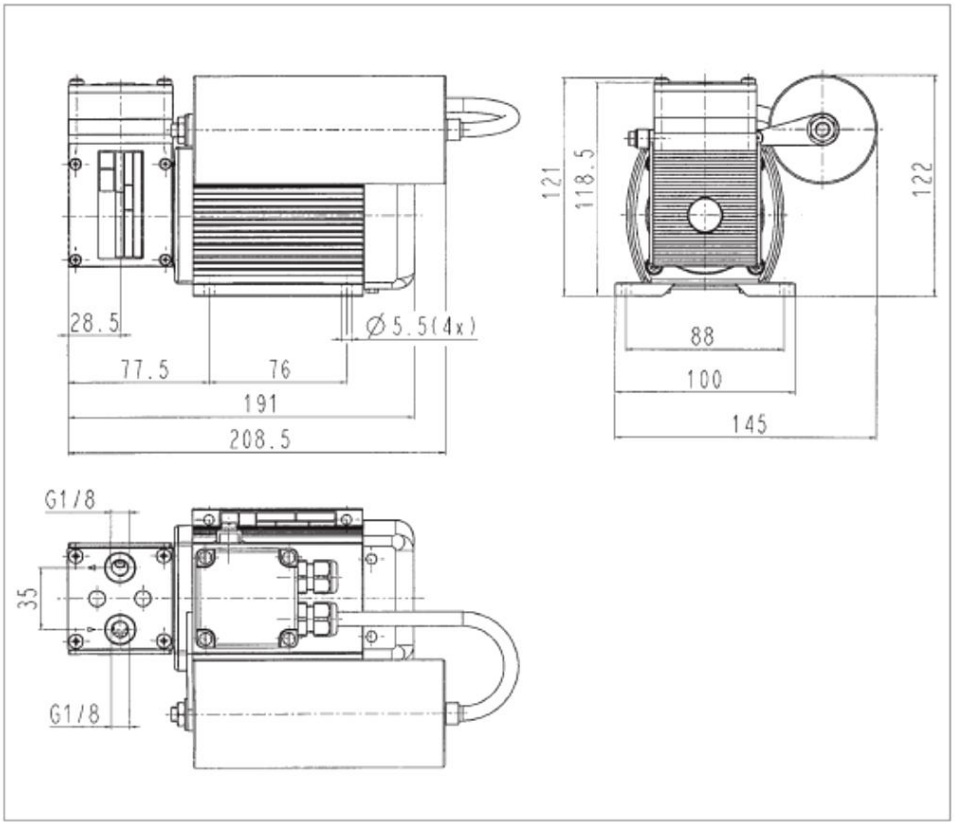


Dimensions mm (All dimensional tolerances conform to DIN ISO 2768-1, Tolerance Class V

## PERFORMANCE DATA

| Type and Order No. [2] | Delivery at atm. pressure **(l/min)** [1] | Max. operating pressure **(bar g)** | Ultimate vacuum **(mbar abs.)** |
|---|---|---|---|
| **N 87 TTE Ex** | 7.5 | 1.5 | 140 |

[1] Litre at STP

## MODEL CODES AND MATERIALS

| Type and Order No. [2] | **Pump head** | **Diaphragm** | **Vavles** |
|---|---|---|---|
| **N 87 TTE Ex** | PVDF | PTFE besch. | FFPM |

[2] See also „MODEL CODES FOR EASY ORDERING“

## MOTOR DATA

| | | | |
|---|---|---|---|
| Protection class | **IP 54** | | |
| Voltage/Frequencies (V/Hz) | 230/50 | | |
| Motor rating (W) | 60 | | |
| Rated motor current (A) | 0.35 | | |

Motors with other voltages and frequencies on request.

## Explosion protected

| Type and Order No. | Pump parts | A.C. motor | |
|---|---|---|---|
| **N 87 TTE Ex** | **Ex II 2G c IIB T4 X** | **Ex II 2G Ex de IIC T4** | |

Pumps for gases the Group of IIC on request.

## Performance characteristic

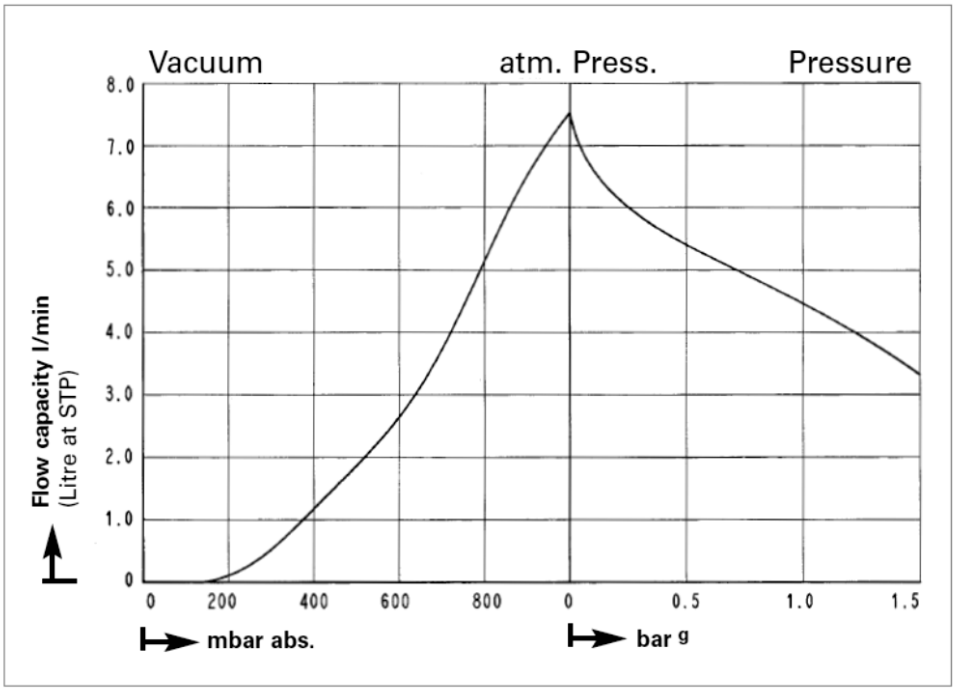

## B.4 Level Sensor Datasheet:

# eTape™ Continuous Fluid Level Sensor PN-12110215TC-12

### • Description

The eTape sensor is a solid state, continuous (multi-level) fluid level sensor for measuring levels in water, non-corrosive water based liquids and dry fluids (powders). The eTape sensor is manufactured using printed electronic technologies which employ additive direct printing processes to produce functional circuits.

### • Theory of Operation

The eTape sensor's envelope is compressed by hydrostatic pressure of the fluid in which it is immersed resulting in a change in resistance which corresponds to the distance from the top of the sensor to the fluid surface. The eTape sensor provides a resistive output that is inversely proportional to the level of the liquid: the lower the liquid level, the higher the output resistance; the higher the liquid level, the lower the output resistance.

### • Specifications

**Sensor Length:** 14.1" (358 mm)
**Thickness:** 0.015" (0.381mm)
**Width:** 1.0" (25.4 mm)
**Active Sensor Length:** 12.4" (315 mm)
**Sensor Output:** 2250Ω empty, 400Ω full, ±10%
**Resistance Gradient:** 150Ω /inch (59Ω/cm), ±10%
**Resolution:** < 0.01"(0.25 mm)
**Actuation Depth:** Nominal 1" (25.4 mm)
**Reference Resistor (Rref):** 2250Ω, ±10%
**Connector:** Crimpflex Pins
**Temperature Range:** 15°F - 150°F (-9°C - 65°C)
**Power Rating:** 0.5 Watts (VMax = 10V)

### • Sensor Output

The eTape can be modeled as a variable resistor (400 – 2250 Ω ± 10%). The typical output characteristics of the eTape sensor are show in the figure below:

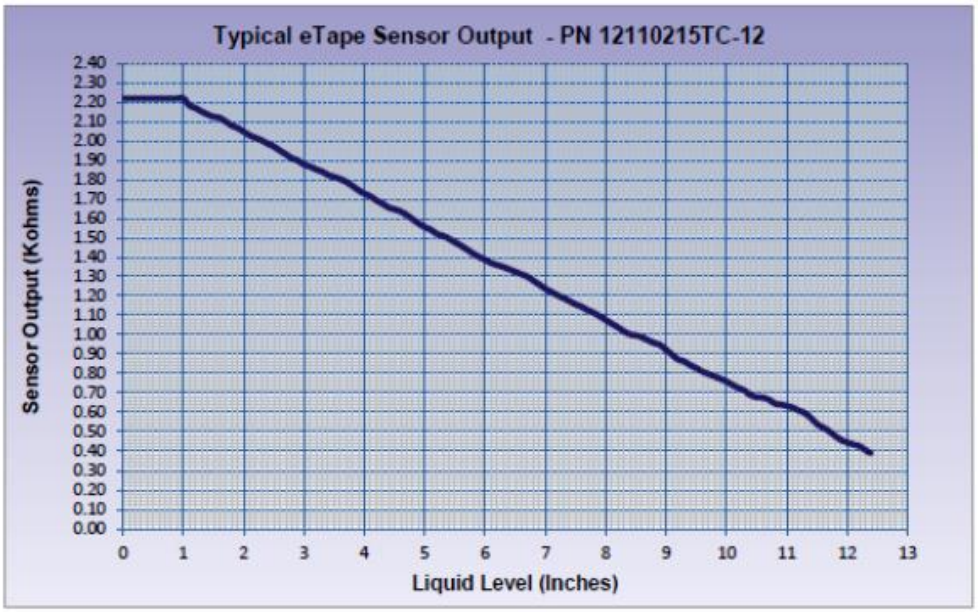


Milone Technologies, Inc - 17 Ravenswood Way - Sewell, New Jersey 08080 - Phone: (856) 270-2688
Email: info@milonetech.com Web: www.milonetech.com

# eTape™ Continuous Fluid Level Sensor PN-12110215TC-12

## Connection and Installation

Connect to the eTape by attaching a 4 pin connector with pre-soldered wires to the Crimpflex pins. Do not solder directly to the Crimpflex pins. The inner two pins (pins 2 and 3) are the sensor output (Rsense). The outer pins (pins 1 and 4) are the reference resistor (Rref) which can be used for temperature compensation. Suspend the eTape sensor in the fluid to be measured. To work properly the sensor must remain straight and must not be bent vertically or longitudinally. For best results install the sensor inside a section of 1-inch diameter PVC pipe. Double sided adhesive tape may be applied to the upper back portion of the sensor to suspend the sensor in the container to be measured. However, the liquid must be allowed to interact freely with both sides of the sensor. The vent hole located above the max line allows the eTape to equilibrate with atmospheric pressure. The vent hole is fitted with a hydrophobic filter membrane to prevent the eTape from being swamped if inadvertently submerged.

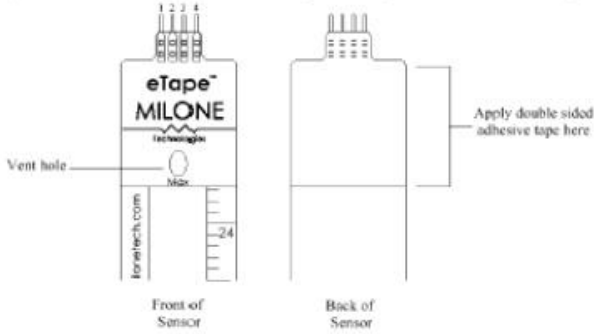


## Sample Circuits

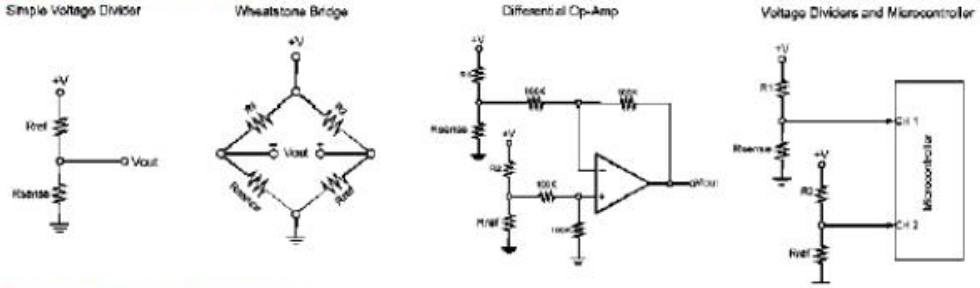


## Custom Applications

The eTape sensor can be manufactured in custom lengths to fit any application. Contact Milone Technologies if you have an application that requires specific length, configuration or output characteristics.

## Technical Support

If you require technical support for the eTape liquid level sensor, please contact our technical support department by email at: techsupport@milonetech.com.

**Innovative Fluid Sensing**

MILONE Technologies

Milone Technologies, Inc - 17 Ravenswood Way - Sewell, New Jersey 08080 - Phone: (856) 270-2688
Email: info@milonetech.com Web: www.milonetech.com

# Appendix C: MJC Characteristics

## C.1 MJC Datasheet:

Arima Photovoltaic & Optical Corp.
華 宇 光 能

*III-V Triple-Junction Solar Cell For HCPV*

### Product Features

- Triple junction solar cell (InGaP/InGaAs/Ge)
- Front and back contacts are weldable or solderable
- Cells are fully tested under concentrated illumination

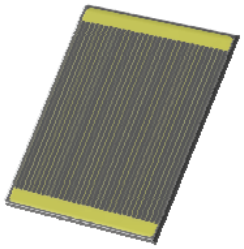

### Typical Characteristics

| Product | Aperture Area | Sun Concentration | $I_{sc}$ [A] | $V_{oc}$ [V] | $I_{mp}$ [A] | $V_{mp}$ [V] | $P_{mp}$ [W] | FF [%] | EFF [%] |
|---|---|---|---|---|---|---|---|---|---|
| T3JG7F040 | 0.1624 $cm^2$ | 500 X | 1.16 | 3.15 | 1.13 | 2.84 | 3.21 | 87.7 | 39.5 |
| | | 1000 X | 2.32 | 3.17 | 2.25 | 2.82 | 6.35 | 86.3 | 39.1 |
| T3JG7F055 | 0.3014 $cm^2$ | 500 X | 2.16 | 3.15 | 2.09 | 2.84 | 5.95 | 87.6 | 39.5 |
| | | 1000 X | 4.31 | 3.17 | 4.18 | 2.81 | 11.8 | 85.9 | 39.0 |
| T3JG7F100 | 1.006 $cm^2$ | 500 X | 7.12 | 3.16 | 6.90 | 2.83 | 19.5 | 86.9 | 38.9 |
| | | 1000 X | 14.2 | 3.19 | 13.8 | 2.80 | 38.6 | 85.0 | 38.3 |

Typical G7 Eff Distribution in Production

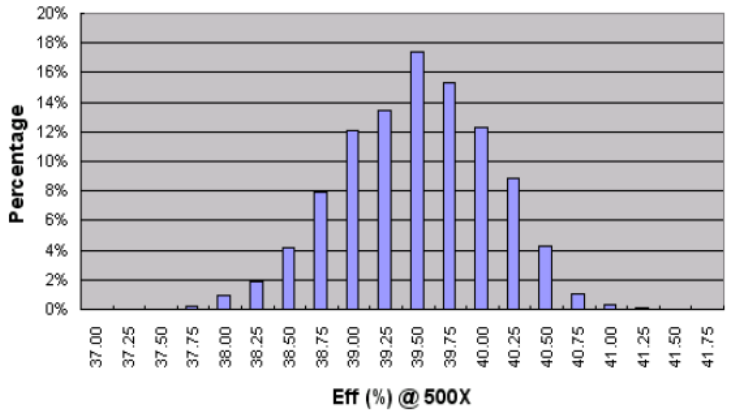


Arima PV&O W: www.arima.com.tw T: +886-3-3908877 F: +886-3-3908801 E: info-PV@arima.com.tw

Arima Photovoltaic & Optical Corp.
華 宇 光 能

**III-V Triple-Junction Solar Cell For HCPV**

## Typical I-V Characteristics

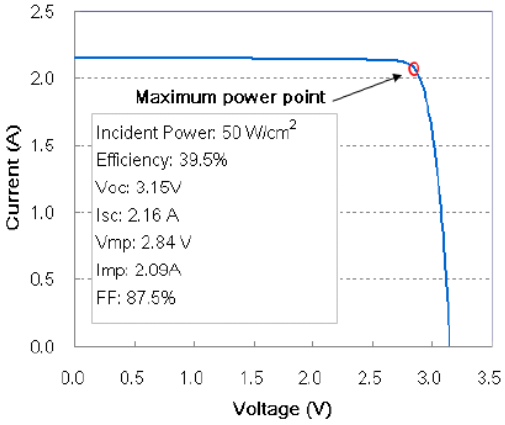


## Spectral Response

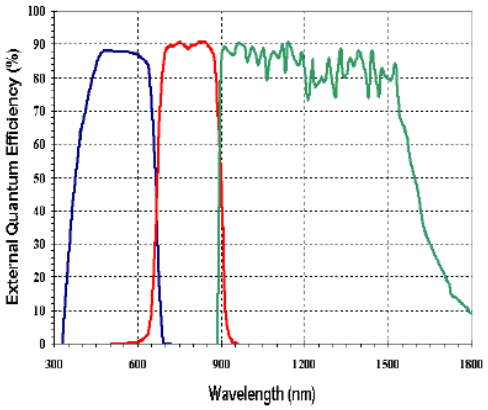


## Typical Characteristics over Temperature

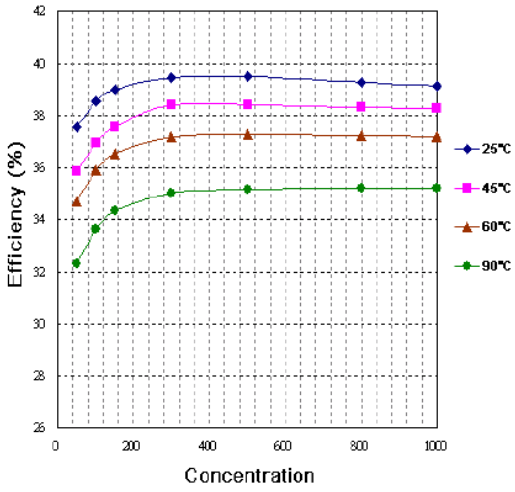


## Typical Characteristics over Temperature

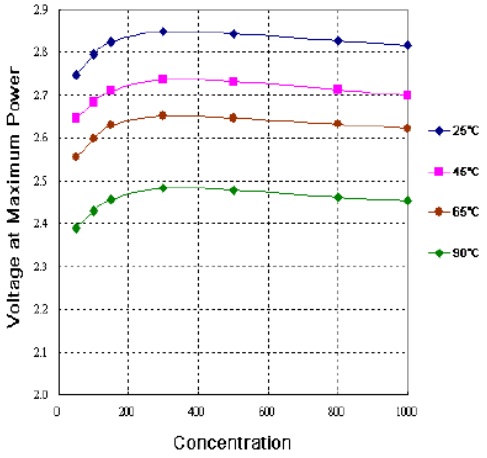


Arima PV&O W: www.arima.com.tw T: +886-3-3908877 F: +886-3-3908801 E: info-PV@arima.com.tw

## C.2 MJC Characteristics vs Concentration and Temperature:

| Temperature | CR | Isc(mA) | $V_{OC}$(V) | $P_{mp}$(mW) | $I_{mp}$(mA) | $V_{mp}$(V) | F.F(%) | Eff.(%) |
|---|---|---|---|---|---|---|---|---|
| | 1000 | 4379 | 3.183 | 11792 | 4185 | 2.818 | 84.6 | 39.1 |
| | 800 | 3503 | 3.166 | 9470 | 3349 | 2.828 | 85.4 | 39.3 |
| | 500 | 2190 | 3.131 | 5953 | 2094 | 2.844 | 86.8 | 39.5 |
| **25°C** | 300 | 1314 | 3.092 | 3570 | 1253 | 2.848 | 87.8 | 39.5 |
| | 150 | 657 | 3.040 | 1763 | 624 | 2.826 | 88.2 | 39.0 |
| | 100 | 439 | 3.009 | 1162 | 415 | 2.796 | 88.0 | 38.5 |
| | 50 | 220 | 2.957 | 566 | 206 | 2.747 | 87.1 | 37.5 |
| | 1000 | 4535 | 3.104 | 11528 | 4268 | 2.701 | 81.9 | 38.2 |
| | 800 | 3628 | 3.086 | 9239 | 3405 | 2.713 | 82.5 | 38.3 |
| | 500 | 2267 | 3.049 | 5790 | 2119 | 2.732 | 83.7 | 38.4 |
| **45°C** | 300 | 1360 | 3.009 | 3471 | 1268 | 2.737 | 84.8 | 38.4 |
| | 150 | 680 | 2.954 | 1697 | 626 | 2.711 | 84.5 | 37.5 |
| | 100 | 453 | 2.922 | 1114 | 415 | 2.685 | 84.1 | 37.0 |
| | 50 | 227 | 2.867 | 541 | 204 | 2.646 | 83.2 | 35.9 |
| | 1000 | 4658 | 3.045 | 11199 | 4273 | 2.621 | 79.0 | 37.2 |
| | 800 | 3726 | 3.026 | 8973 | 3407 | 2.634 | 79.6 | 37.2 |
| | 500 | 2329 | 2.986 | 5617 | 2122 | 2.648 | 80.8 | 37.3 |
| **60°C** | 300 | 1397 | 2.943 | 3363 | 1268 | 2.652 | 81.8 | 37.2 |
| | 150 | 699 | 2.884 | 1651 | 628 | 2.630 | 81.9 | 36.5 |
| | 100 | 466 | 2.850 | 1082 | 417 | 2.598 | 81.5 | 35.9 |
| | 50 | 233 | 2.791 | 523 | 205 | 2.555 | 80.5 | 34.7 |
| | 1000 | 4894 | 2.923 | 10613 | 4326 | 2.453 | 74.2 | 35.2 |
| | 800 | 3915 | 2.902 | 8490 | 3447 | 2.463 | 74.7 | 35.2 |
| | 500 | 2447 | 2.859 | 5300 | 2138 | 2.479 | 75.8 | 35.2 |
| **90°C** | 300 | 1468 | 2.812 | 3169 | 1275 | 2.485 | 76.8 | 35.0 |
| | 150 | 734 | 2.748 | 1552 | 632 | 2.455 | 77.0 | 34.3 |
| | 100 | 489 | 2.710 | 1014 | 417 | 2.429 | 76.4 | 33.6 |
| | 50 | 245 | 2.646 | 487 | 204 | 2.389 | 75.2 | 32.3 |